



City Research Online

City, University of London Institutional Repository

Citation: Owen, C. (1998). Quantitative Analysis of Conjunctival Vasculature. (Unpublished Doctoral thesis, City, University of London)

This is the accepted version of the paper.

This version of the publication may differ from the final published version.

Permanent repository link: <https://openaccess.city.ac.uk/id/eprint/31135/>

Link to published version:

Copyright: City Research Online aims to make research outputs of City, University of London available to a wider audience. Copyright and Moral Rights remain with the author(s) and/or copyright holders. URLs from City Research Online may be freely distributed and linked to.

Reuse: Copies of full items can be used for personal research or study, educational, or not-for-profit purposes without prior permission or charge. Provided that the authors, title and full bibliographic details are credited, a hyperlink and/or URL is given for the original metadata page and the content is not changed in any way.

QUANTITATIVE ANALYSIS OF CONJUNCTIVAL VASCULATURE

A Thesis submitted by

CHRISTOPHER GRANT OWEN

for the degree of
DOCTOR OF PHILOSOPHY

ADVISORS

Dr T J Ellis, Reader in Machine Vision, Department of
Electrical and Electronic Engineering, City University,
London, UK.

Professor E G Woodward, Professor of Optometry and
Visual Science, Department of Optometry and Visual
Science, City University, London, UK.

Applied Vision Research Centre, City University, London,
UK.

December 1998

Table of contents

QUANTITATIVE ANALYSIS OF CONJUNCTIVAL VASCULATURE	1
TABLE OF CONTENTS	2
LIST OF TABLES	7
LIST OF FIGURES	11
ACKNOWLEDGEMENTS	20
DECLARATION	21
ABSTRACT	22
KEY OF ABBREVIATIONS / SYMBOLS	24
CHAPTER 1	25
1. CONJUNCTIVAL VASCULATURE	25
1.1 <i>Introduction</i>	25
1.2 <i>Anatomy of conjunctiva</i>	25
1.2.1 Conjunctival arterial blood supply	26
1.2.2 Conjunctival venous drainage	28
1.2.3 Comparative vascular structure and function of retinal and conjunctival vessels	28
1.3 <i>Clinical relevance of conjunctival vasculature examination</i>	28
1.3.1 Diabetic angiopathy	29
1.3.2 Diabetic retinopathy	29
1.3.3 Conjunctival diabetic angiopathy	32
1.3.4 Conjunctival blood flow	34
1.3.5 Age related retinal vessel changes	35
1.3.6 Age related conjunctival angiopathy	36
1.3.7 Hypertensive retinopathy	36
1.3.8 Hypertensive conjunctival angiopathy	37
1.3.9 Glaucomatous conjunctival angiopathy	38
1.3.10 Effects of Sickle Cell disease and acquired immunodeficiency syndrome (AIDS) on conjunctival vasculature	39
1.3.11 Conjunctival vessels in renal failure	40
1.3.12 Conjunctival inflammation and hypersensitivity	41
1.3.13 Conjunctival effects of contact lens wear	42
1.3.14 Drug induced changes of the conjunctiva	43
1.3.15 Miscellaneous factors effecting conjunctival vasculature	44
1.4 <i>Methods of quantifying vasculature</i>	45
1.4.1 Subjective methods of assessing vascularity	47
1.4.2 Objective methods of assessing vascularity	48
1.4.3 Automated methods of determining vascularity	48
1.4.4 Manual techniques of assessing vessel width	50
1.4.5 Semi-automated densitometric techniques of determining width	51
1.4.6 Automated methods	59
1.4.7 Applications of automated vascular imaging	66
1.5 <i>Summary</i>	67
CHAPTER 2	68
2. RATIONALE FOR RESEARCH	68
2.1 <i>Aims</i>	68

4. METHOD OF CONJUNCTIVAL VASCULAR IMAGE ANALYSIS	117
4.1.1 Aim.....	117
4.1.2 Introduction	117
4.2 <i>Capillary tube width determination</i>	117
4.2.1 Method	117
4.2.2 Results	120
4.2.3 Discussion	121
4.3 <i>Vessel width determination</i>	122
4.3.1 Method	122
4.3.1.1 Image acquisition	122
4.3.1.2 Manual methods	123
4.3.1.3 Semi-automated methods	124
4.3.1.4 Automated methods	124
4.3.1.5 Intra-session analysis.....	125
4.3.1.6 Inter-method analysis	125
4.3.2 Results	125
4.3.2.1 Intra-session repeatabilities	125
4.3.2.2 Inter-method repeatabilities compared to manual photographic method	128
4.3.2.3 Inter-method repeatabilities compared to mouse driven method	135
4.3.3 Discussion	139
4.3.3.1 Sigma selection	139
4.3.3.2 Intra-session repeatabilities for large ($\geq 40\mu\text{m}$) and small vessels ($40\mu\text{m}$).....	140
4.4 <i>Vascular tortuosity measurement</i>	143
4.4.1 Introduction	143
4.4.2 Method	144
4.4.2.1 Vessel tortuosity model	144
4.4.3 Results	146
4.4.4 Discussion of vessel tortuosity measures	148
4.5 <i>Measurement of vascular indices</i>	149
4.5.1 Introduction	149
4.5.2 Method	150
4.5.3 Results and discussion.....	154
4.5.4 Summary	163
CHAPTER 5	164
5. NORMAL CONJUNCTIVAL VASCULATURE	164
5.1 <i>Aim</i>	164
5.2 <i>Introduction</i>	164
5.3 <i>Method</i>	165
5.4 <i>Statistical analysis</i>	166
5.4.1 Intra session repeatability	166
5.4.2 Inter session repeatability	166
5.4.3 Variability in measurement	166
5.5 <i>Results</i>	168
5.5.1.1 Vessel width	171
5.5.1.2 Vessel width variance.....	171
5.5.1.3 Curve energy	172

5.5.1.4 Curve energy variance	172
5.5.1.5 Density	172
5.5.2 Intra session repeatability	172
5.5.3 Inter session repeatability	173
5.5.4 Diurnal variation and association with other variables	177
5.5.4.1 Pooled data from all vessels	178
5.5.4.2 Data from vessels less than 25 μ m in diameter	181
5.5.4.3 Data from vessels \geq 25 μ m and < 40 μ m in diameter	182
5.5.4.4 Data from vessels \geq 40 μ m and < 80 μ m in diameter	182
5.5.4.5 Data from vessels \geq 80 μ m in diameter.....	182
5.5.4.6 Diurnal variation in MAP.....	183
5.5.4.7 Relative humidity and temperature	184
5.6 Discussion	184
CHAPTER 6	186
6. DIABETIC CONJUNCTIVAL VASCULATURE	186
6.1 Aim	186
6.2 Introduction.....	186
6.3 Method.....	187
6.4 Statistical analysis.....	188
6.5 Results	190
6.5.1.1 Univariate analysis of data from vessels less than 25 μ m in diameter	192
6.5.1.2 Multivariate analysis of data from vessels less than 25 μ m in diameter	194
6.5.1.3 Univariate analysis of data from vessels 25 μ m to < 40 μ m in diameter	194
6.5.1.4 Multivariate analysis of data from vessels 25 μ m to < 40 μ m in diameter	197
6.5.1.5 Univariate analysis of data from vessels 40 μ m to < 80 μ m in diameter	197
6.5.1.6 Multivariate analysis of data from vessels 40 μ m to < 80 μ m in diameter	198
6.5.1.7 Univariate analysis of pooled data from all vessels	199
6.5.1.8 Multivariate analysis of data from all vessels	200
6.6 Discussion	201
6.6.1 Tortuosity changes	201
6.6.2 Effects of diabetes on vessel width and vascular density.....	202
6.6.3 Effects of blood pressure on vascular density	202
6.6.4 Effects of age on vascular density	203
6.6.5 Effect of retinopathy and duration of diabetes on vessel indices	203
6.6.6 Summary	203
CHAPTER 7	204
7. CONCLUSION, SUMMARY OF RESULTS, AND FUTURE WORK	204
7.1 Conclusion and summary of results	204
7.2 Future work.....	206
APPENDICES	208
APPENDIX A.1	208

APPENDIX A2	215
SUPPORTING PUBLICATIONS	222
REFEREED PAPERS	222
REFEREED CONFERENCE ABSTRACTS	222
REFERENCES	223

List of tables

<i>Table 1.1 lists the vascular terminology used to classify vessels according to their size and structure, where IELM refers to the internal elastic limiting membrane. .</i>	<i>26</i>
<i>Table 3.1 shows characteristic points of Hb and HbO₂ where, ϵ^λ is absorptivity (litres mmol⁻¹ cm⁻¹), Isob Hb means isobestic with Hb, and Isob HbO₂ means isobestic with HbO₂ (from van Kampen et al, 1983).</i>	<i>78</i>
<i>Table 3.2 shows a selection of results of SER for conjunctiva and blood and the calculated SERD for images captured on HP5 plus film.</i>	<i>86</i>
<i>Table 3.3 shows a selection of results of SERD values for each sensor for a selection of filters, in descending order of value for the green CCD sensor.</i>	<i>89</i>
<i>Table 3.4 shows an analysis of variance table corresponding to the ability of the Gaussian model to predict the densitometric profile shown in figure 3.17. Note the R² value was 0.968.</i>	<i>92</i>
<i>Table 3.5 shows an analysis of variance table corresponding to the ability of the Gaussian model to predict the densitometric profile shown in figure 3.19. Note the R² value was 0.999.</i>	<i>95</i>
<i>Table 3.6 shows the σ needed to Gaussian blur a theoretical step edge, to give a least squares fit to the densitometric profile of each of the 30 images.</i>	<i>96</i>
<i>Table 3.7 shows an analysis of variance table corresponding to the ability of the Gaussian blurred cylindrical model to predict the densitometric profile shown in figure 3.22. Note the R² value was 0.975.</i>	<i>99</i>
<i>Table 3.8 lists the mean \pm standard deviation, depth, internal and external diameter of the 7 arterioles and 8 veins measured. The calculated ratio of wall size to lumen size is shown in the final column.</i>	<i>100</i>
<i>Table 3.9 shows an analysis of variance table corresponding to the ability of the Gaussian blurred tubular model to predict the densitometric profile shown in figure 3.24. Note the R² value was 0.977.</i>	<i>102</i>
<i>Table 3.10 shows an analysis of variance table corresponding to the ability of the Gaussian blurred tubular model to predict the densitometric profile shown in figure 3.24. Note the R² value was 0.974.</i>	<i>103</i>
<i>Table 3.11 shows the mean R² and standard deviation of each model for the 108 densitometric profiles measured. Note that the differences between R² values was not significant.</i>	<i>104</i>
<i>Table 3.12 shows the five green filters used and the neutral density filter needed to achieve optimal perceived contrast.</i>	<i>108</i>
<i>Table 3.13 lists the mean and standard deviations of the 10 estimates of vessel amplitude and width for the 3 vessel locations measured.</i>	<i>109</i>
<i>Table 3.14 lists the mean and standard deviations of the 50 estimates of vessel amplitude and width for the 3 vessel locations measured.</i>	<i>110</i>
<i>Table 3.15 lists the mean and standard deviations of the 10 estimates of vessel amplitude and width for the 3 vessel locations measured through each filter used.</i>	<i>112</i>
<i>Table 3.16 lists the mean and standard deviations of the 10 estimates of vessel amplitude and width for the 3 vessel locations measured on the G-CCD and C-CCD with and without Wratten 99 filtration.</i>	<i>113</i>
<i>Table 4.1 lists the 12 column widths obtained from the 2 capillary tubes using each of the 5 shape models. Note that widths are given in pixels where 188.494 pixels equals 1mm.</i>	<i>120</i>

Table 4.2 shows the MD, $\pm 95\%$ confidence limits of repeatability (± 1.96 SD), minimum and maximum values for each method used to measure vessel width on sessions 1 and 2, shown in ascending order or coefficient of repeatability (2×1.96 SD).....	126
Table 4.3 shows the MD and $\pm 95\%$ confidence limits of inter-method repeatability (± 1.96 SD) for each method used against measurement from digitally created photographs using electronic callipers, shown in ascending order of coefficient of repeatability (2×1.96 SD).....	128
Table 4.4 shows the best σ to be used, in increments of 0.5 pixels, which gives the nearest MD of zero when compared to digital photographic measurement of width. MD $\pm 95\%$ confidence interval (CI) of inter-method repeatability, and coefficient of repeatability (C of R) are given, for differing vessel bin sizes.....	134
Table 4.5 shows the MD and $\pm 95\%$ confidence limits of inter-method repeatability (± 1.96 SD) for each method used against mouse driven measurement from digital images, shown in ascending order or coefficient of repeatability (2×1.96 SD)...	135
Table 4.6 shows the best σ to be used, in increments of 0.5 pixels, which gives the nearest MD of zero when compared to mouse driven determination of width. MD $\pm 95\%$ confidence interval (CI) of inter-method repeatability, and coefficient of repeatability (C of R) are given, for differing vessel bin sizes.....	139
Table 4.7 shows the MD, $\pm 95\%$ confidence limits of repeatability (± 1.96 SD), minimum and maximum values for each method used to measure vessel width on sessions 1 and 2, for values less than $40\mu\text{m}$ in width as measured with $\sigma = 2$ ($n=67/101$ profiles), shown in ascending order of coefficient of repeatability (2×1.96 SD).....	141
Table 4.8 shows the MD, $\pm 95\%$ confidence limits of repeatability (± 1.96 SD), minimum and maximum values for each method used to measure vessel width on sessions 1 and 2, for values $\geq 40\mu\text{m}$ in width as measured with $\sigma = 2$ ($n=34/101$ profiles), shown in ascending order of coefficient of repeatability (2×1.96 SD).	141
Table 4.9 lists vessel /chord length ratio, mean curvature estimate, and curve energy values for the non tortuous and tortuous waveforms in figure 4.23.	149
Table 4.10 lists vascular indices for the 2 patients, measured with sigma's 2/4 and 3, where W is measured in μm , WV in μm^2 , T in units of curve energy (CE), TV in units of CE^2 , and Density in mm^2 of vessel per mm^2 of conjunctiva. The $\% \Delta$ represent the percentage difference between patient 1 and 2.....	162
Table 5.1 lists the demographic details of the sample.	168
Table 5.2 shows the sample mean, SD, maximum and minimum values for all indices, for each session of measurement, where W and WV are measured in μm and μm^2 respectively, T and TV in units of curve energy and curve energy ² . Density was measured in mm^2 of vessel per mm^2 of conjunctiva and hence can be regarded as a proportion.....	171
Table 5.3 lists the intra session repeatabilities of the 25 indices measured. The MD, 95% CI columns show mean difference, and 95% confidence interval in μm for W and μm^2 for WV, units of curve energy for T and curve energy squared for TV, and mm^2 of vessel per mm^2 of conjunctiva for Density. Columns $\% \text{ MD}$, and $\% \text{ CI}$, give repeatabilities as a percentage of the mean measurement. Shaded areas show those indices with an acceptable repeatability value ($\sim \pm 10\%$).....	173

Table 5.4 lists the inter session repeatabilities of the 25 indices measured. The MD, 95% CI columns show mean difference, and 95% confidence interval in μm for W and μm^2 for WV, units of curve energy for T and curve energy squared for TV, and mm^2 of vessel per mm^2 of conjunctiva for Density. Columns %MD, and % CI, give repeatabilities as a percentage of the mean measurement. Shaded areas show those indices with an acceptable repeatability value ($\sim\pm 10\%$).	174
Table 5.5 the effect size of the 95% CI of repeatability on the actual measurement of vascular density.....	177
Table 5.6 the effect size of the 95% CI of repeatability on the actual measurement of WV.....	177
Table 5.7 the effect size of the 95% CI of repeatability on the actual measurement of TV.....	177
Table 5.8 lists the diurnal variation in pooled values of WV expressed as a percentage change from baseline measurement. P values and 95% CI are also given.	179
Table 5.9 lists the diurnal variation in pooled values of T expressed as a percentage change from baseline measurement. P values and 95% CI are also given.	179
Table 5.10 lists the diurnal variation in pooled values of TV expressed as a percentage change from baseline measurement. P values and 95% CI are also given.	180
Table 5.11 lists the diurnal variation in MAP expressed as a percentage change from baseline measurement. P values and 95% CI are also given.	183
Table 6.1 lists the demographic details of the sample. Note mean \pm SD are quoted where applicable	190
Table 6.2 lists the mean, SD, minimum and maximum values for each index measured on 60 normal patients.....	191
Table 6.3 lists the mean, SD, minimum and maximum values for each index measured on 17 TI diabetic patients.....	191
Table 6.4 lists the mean, SD, minimum and maximum values for each index measured on 36 TII diabetic patients.....	191
Table 6.5 shows the age range, mean age, SD, and patient numbers for each quartile	192
Table 6.6 shows the MAP range, average MAP, SD, and patient numbers for each quartile	192
Table 6.7 lists the effect size, 95% confidence interval (CI), and P value for each index measured on TI and TII diabetics compared to normal data. Shaded areas indicate those indices which are statistically significantly different from normals ($P < 0.05$).	193
Table 6.8 lists the effect size, 95% CI, and P value for each index measured on TI and TII diabetics compared to baseline - normal data. Shaded areas indicate those indices which are statistically significantly different from baseline ($P < 0.05$).	195
Table 6.9 lists the effect size, 95% CI, and P value for each index measured on TI and TII diabetics compared to baseline - normal data. Shaded areas indicate those indices which are statistically significantly different from baseline ($P < 0.05$).	197
Table 6.10 list the percentage drop in each index per 10mmHg rise in MAP. Shaded areas indicate those indices which show statistically significantly change with increasing MAP ($P < 0.05$).	198

Table 6.11 summarises the multivariate analysis of the effects of diabetes, and MAP on indices W, T, and TV for vessels 40µm to <80µm in diameter. 198

Table 6.12 lists the effect size, 95% CI, and P value for each index measured on TI and TII diabetics compared to baseline - normal data. Shaded areas indicate those indices which are statistically significantly different from baseline (P<0.05) 199

Table 6.13 list the percentage drop in each index per 10mmHg rise in MAP. Shaded areas indicate those indices which show statistically significantly change with increasing MAP (P<0.05) 200

Table 6.14 summarises the multivariate analysis of the effects of diabetes, and MAP on indices W, T, TV, and Density for all vessels. 200

List of figures

- Figure 1.1 shows the dimensions (in millimetres) of human bulbar conjunctiva measured from the limbus (with an assumed corneal diameter of 12 mm) to the conjunctival sac (From Whitnall SE: *The anatomy of the Human Orbit*, p 195. Oxford University Press 1932; cited from Ruskell, 1991).26
- Figure 1.2 shows telangiectasia of a bulbar conjunctival blood vessel with a saccular like aneurysm in a 'normal' 67 year old individual. The square represents an area of approximately 1mm^234
- Figure 1.3 shows a point (x,y) on a conjunctival vessel, its direction, and the location where vessel width would be measured perpendicular to the vessels direction. Note that the width of the vessel shown is $100\mu\text{m}$46
- Figure 1.4 (a) shows a digital camera image of the vasculature emanating from the optic nerve head. Thinner, lighter vessels represent branches of the central retinal arteries, and thicker, darker vessels branches of the central retinal vein. White arrows (numbered 1 to 3) show the location where densitometric profiles were measured perpendicularly across arteries, and grey arrows (numbered 4 to 6) across veins.52
- Figure 1.4 (b) shows densitometric profiles measured perpendicularly across arteries (1 to 3). Note the magnitude of the central reflex for profile number 1.53
- Figure 1.4 (c) shows densitometric profiles measured perpendicularly across veins (4 to 6). Note the presence of the central reflex is less marked than those found on some of their arterial neighbours.53
- Figure 1.5 (a) shows a digital camera image of vasculature on the conjunctiva. White arrows (numbered 1 to 4) show the location where densitometric profiles were measured and are shown in figure 1.5 (b). Locations 1 and 2 were measured perpendicularly across an anterior ciliary artery, 3 and 4 across conjunctival venules or arterioles. The image represents 300 pixels^2 equivalent to 1.6mm^2 of conjunctiva.54
- Figure 1.5 (b) shows densitometric profiles measured perpendicularly across conjunctival vessels (1 to 4). Note that the central reflex evident with retinal vessels is absent. One pixel is equivalent to $\sim 5\mu\text{m}$ in object space.55
- Figure 1.6 (a) shows a digital image of a conjunctival vessel. A horizontal densitometric profile across this vessel is shown in figure 1.6 (b). The densitometric half height width is shown between the vertical white lines (width = $18.91\text{ pixels} \approx 100\mu\text{m}$).55
- Figure 1.6 (b) shows a densitometric profile taken across the vessel shown in figure 1.6 (a), the upper dashed line is the mean background intensity, the lower dashed line the minimum intensity value recorded near the centre of the vessel. The horizontal solid line marks the position of the half height width.56
- Figure 1.7 shows the densitometric profile taken from figure 1.6, across an anterior ciliary artery. The densitometric half height width is shown by the horizontal solid line, and the vertical arrows indicate the observers interpretation of Rassam's 'kick points'58
- Figure 1.8 shows 3 profiles where the top is a densitometric intensity function of an idealised vessel, middle the first differential, and bottom the second differential. Vertical lines show the zero crossing point of the second differential, inflection points of the first differential, and maximum gradient on the vessels edge.60

Figure 1.9 (a) shows the configuration of a simple Laplacian mask and its application to the raw conjunctival image shown in figure 1.9 (b), to give the image in figure 1.9 (c).....	61
Figure 1.10 shows lines and their width detected (a) in an aerial images of resolution 1m with the bias removed. A $\times 4$ enlarged detail (b) superimposed onto the original image of resolution 0.25m and (c) comparison to the line extraction without bias removal. (From Steger, C. {1996}. An unbiased detector of curvilinear structures. Technical Report FGBV-96-03. Forschungsgruppe Bilderverstehen (FG BV), Informatik IX, Technische Universität München, Figure 16).	63
Figure 1.11 shows lines detected in a coronary angiogram (a). Since this image has very low contrast, the results (c) extracted from (a) are superimposed onto a version of the image with better contrast (b). A magnified ($\times 3$) image of (c) is displayed in (d). (From Steger, C. {1996}. An unbiased detector of curvilinear structures.....	63
Technical Report FGBV-96-03. Forschungsgruppe Bilderverstehen (FG BV), Informatik IX, Technische Universität München, Figure 20).	63
Figure 1.12 shows a densitometric profile of a conjunctival vessel (closed circles) with a least squares fitted Gaussian curve (open squares), where A is the background intensity, and d is the perpendicular distance between the point (x,y) and the straight line passing through the centre of the blood vessel. The Gaussian curve shown has a $\sigma = 7.53$ pixels and is given by the equation above.	64
Figure 3.1 shows the relative spectral intensity distribution of low pressure xenon flash tube (from Philips Lighting catalogue, 1994).	75
Figure 3.2 shows the spectral transmittance of system optics, including illumination and imaging lenses measured with a Perkin Elmer Lambda 2 UV/Vis spectrophotometer.....	76
Figure 3.3 shows different paths of photons emitted by the source and emerging at the detector for the measurement of blood reflectance.	77
Figure 3.4 shows light absorption spectra of oxyhaemoglobin (solid line) and deoxyhaemoglobin (broken line) (from Zijlstra et al, 1991).	78
Figure 3.5 shows the mean reflectance (n=10) of nasal fundus (solid line), periphery (long dashed line), and fovea (short dashed line) (from Delori and Pflibsen, 1989).	79
Figure 3.6 shows spectral reflectance of oxygenated haemoglobin freshly obtained by venipuncture measured on a white background of magnesium carbonate.	80
Figure 3.7 shows the average spectral reflectance of the bulbar conjunctiva for 6 subjects, where the error bars represent \pm standard deviations.....	81
Figure 3.8 shows spectral sensitivity of HP5 plus film. Reciprocal of exposure required to produce constant density in negative.	82
Figure 3.9 shows the pixel arrangement on the DCS 100 where green pixels are the unfilled squares (75%), red pixels (12.5%) diagonal chequered squares, and blue pixels (12.5%) horizontally chequered squares. Note that the entire CCD array is 1280 pixels wide and 1024 pixels tall.	83
Figure 3.10 shows the spectral sensitivity of the DCS 100 CCD array, where open squares represents response of blue pixels, open circles green pixels, open triangles red pixels, and crosses the response of the combined colour channels (data courtesy of Kodak Eastman, Rochester, New York, USA).	84
Figure 3.11 shows the densitometric profile obtained along an image of a vernier scale, local minima equate to 0.1mm graduations in the vernier scale.	85

<i>Figure 3.12 shows the transmission characteristics of a Wratten 47B - open square symbols, Wratten 58 open triangular symbols, Wratten 96 open circular symbols, and Wratten 99 crossed symbols.</i>	86
<i>Figure 3.13 shows a selection of results of SER for conjunctiva (open triangular symbols) and blood (open square symbols) and the calculated SERD (open circular symbols) for images captured on HP5 plus film.</i>	87
<i>Figure 3.14 shows images digitised from consecutive photographs of the bulbar conjunctiva taken (a) without filtering, power setting 1, and (b) with a Kodak Wratten 35 filter, power setting 4. The increased information content in terms of image contrast is visible. The square represents $\sim 3.4\text{mm}^2$ of conjunctiva.</i>	88
<i>Figure 3.15 shows microdensitometer traces over the same blood vessel imaged without filtering (dashed line); and with a Wratten 35 filter over the light source (solid line).</i>	89
<i>Figure 3.16 shows the SERD values for the CCD sensor combined (solid line with no symbols), red sensor (open circles), green sensor (open squares), and blue sensor (open triangles), for differing filters, in descending order of green sensor response.</i>	90
<i>Figure 3.17 shows a densitometric profile taken across an arterial vessel of the conjunctiva (solid circles), and a least squares fitted Gaussian curve (open squares), where A is the amplitude of the Gaussian curve, B is the midpoint of the curve, and C is the background intensity. Note σ equals 7.53 pixels.</i>	91
<i>Figure 3.18 shows a plot of residuals against the least squares fitted Gaussian model for the raw data shown in figure 3.17.</i>	92
<i>Figure 3.19 shows a truncated linearly interpolated 25 pixel slice across a step edge (solid line), a theoretical step edge (dotted line), and Gaussian blurring of the theoretical step edge to give a least squares fit to the densitometric profile (open circles).</i>	94
<i>Figure 3.20 shows a plot of residuals against the least squares fitted Gaussian blurred step edge model for the raw data shown in figure 3.19.</i>	95
<i>Figure 3.21 shows σ blurring of step edge with defocus of Nikon FS-2 photo slit-lamp observation optics where negative defocus represents movement towards the step edge and positive movement away from the step edge. Open bars represents session one, solid bars session 2.</i>	97
<i>Figure 3.22 shows a densitometric profile across an arterial vessel of the conjunctiva (solid circles), cylindrical profile (open circles), and a blurred cylindrical profile convoluted with a Gaussian function with $\sigma = 1.655$ (open squares), where B is the midpoint of the curve, C is the background intensity, and r is the radius of the cylinder.</i>	98
<i>Figure 3.23 shows a plot of residuals against the least squares fitted Gaussian blurred cylindrical model for the raw data shown in figure 3.22.</i>	98
<i>Figure 3.24 shows a densitometric profile across an arterial vessel of the conjunctiva (solid circles), tubular profile, with wall size one sixth lumen diameter (open circles), and a blurred tubular profile convoluted with a Gaussian function with $\sigma = 1.655$ (open squares), where B is the midpoint of the curve, C is the background intensity, and r is the predicted radius of the lumen.</i>	101
<i>Figure 3.25 shows a plot of residuals against the least squares fitted Gaussian blurred tubular model for the raw data shown in figure 3.24.</i>	101

Figure 3.26 shows a densitometric profile across an arterial vessel of the conjunctiva (solid circles), tubular profile, (with wall size one tenth lumen diameter (open circles), and a blurred tubular profile convoluted with a Gaussian function with $\sigma = 1.655$ (open squares), where B is the midpoint of the curve, C is the background intensity, and r is the predicted radius of the lumen.	103
Figure 3.27 shows a plot of residuals against the least squares fitted Gaussian blurred tubular model for the raw data shown in figure 3.26.	103
Figure 3.28 shows the R^2 values for the Gaussian curve model plotted against Gaussian half height width for the 108 vessels measured. The fitted linear regression line indicates a near constant ability of the Gaussian curve model to predict densitometric data across vessels of different widths.	105
Figure 3.29 shows the R^2 values for the Gaussian blurred tubular model for veins against blood column width for the 108 vessels measured. The linear regression line indicates an improvement in the model to predict densitometric data across larger vessels.	105
Figure 3.30 shows the location where 3 densitometric profiles were measured for each image taken under differing optical configurations. The dimensions of the image shown is 250×450 pixels, equivalent to 1.33×2.39 mm in object space.	106
Figure 4.1 shows a densitometric profile taken across a glass capillary tube with internal diameter 0.340 mm (~ 64 pixels in width) and external diameter 1.092 mm (~ 206 pixels in width). Raw densitometric profile shown by closed circles, and averaged data open squares.	118
Figure 4.2 shows a densitometric profile taken across a glass capillary tube with internal diameter 0.578 mm (~ 109 pixels in width) and external diameter 1.346 mm (~ 254 pixels in width). Raw densitometric profile shown by closed circles, and averaged data open squares.	119
Figure 4.3 shows difference between paired values of vessel width for sessions 1 and 2 plotted against their mean ($n=101$) using the Steger's algorithm at $\sigma = 3$. Thick solid line represents mean difference, and thin lines $\pm 95\%$ CI. The dashed line with a slight positive gradient is a linear regression line of the data points showing insignificant measurement error.	127
Figure 4.4 shows difference between paired values of vessel width for sessions 1 and 2 plotted against their mean ($n=101$) using manual measurement from digital slide images. Thick solid line represents mean difference, and the thin lines $\pm 95\%$ CI. The dashed line with a slight negative gradient is a linear regression line of the data points showing insignificant measurement error.	127
Figure 4.5 shows differences between paired values of vessel width for average measurements taken from photographs and digitally created photographs using callipers, plotted against their mean ($n=101$). Thick solid line represents the mean difference, thin lines $\pm 95\%$ CI. Dashed line with a very slight positive gradient is a linear regression line of the data points.	129
Figure 4.6 shows differences between paired values of vessel width for average measurements taken mouse driven methods and digitally created photographs using callipers, plotted against their mean ($n=101$). Thick solid line represents the mean difference, thin lines $\pm 95\%$ CI. Dashed line with a very slight positive gradient is a linear regression line of the data points.	130
Figure 4.7 shows differences between paired values of vessel width for average measurements of Gaussian half height and digitally created photographs using	

- callipers, plotted against their mean ($n=101$). Thick solid line represents the mean difference, thin lines $\pm 95\%$ CI. Dashed line with a very slight negative gradient is a linear regression line of the data points. 130
- Figure 4.8 shows differences between paired values of vessel width for average measurements of cylinder model and digitally created photographs using callipers, plotted against their mean ($n=101$). Thick solid line represents the mean difference, thin lines $\pm 95\%$ CI. Dashed line with a steep negative gradient is a linear regression line of the data points. 131
- Figure 4.9 shows differences between paired values of vessel width for average measurements of automated width ($\sigma = 3$) and digitally created photographs using callipers, plotted against their mean ($n=101$). Thick solid line represents the mean difference, thin lines $\pm 95\%$ CI. Dashed line with a steep positive gradient is a linear regression line of the data points. 132
- Figure 4.10 shows a 3 dimensional plane surface of the mean difference of the manual calliper method minus the automated method, for differing sigma's of Steger algorithm, plotted against differing vessel bins varying from less than $20\mu\text{m}$ ($n=3$) to less than $110\mu\text{m}$ ($n=93$) as measured from digitally created photographic slides with electronic callipers. 133
- Figure 4.11 shows a 3 dimensional plane surface of the mean difference of the manual calliper method minus the automated method, for differing sigma's of Steger algorithm, plotted against differing vessel bins varying from greater than $20\mu\text{m}$ ($n=98$) to greater than $110\mu\text{m}$ ($n=8$) as measured from digitally created photographic slides with electronic callipers. 133
- Figure 4.12 shows differences between paired values of vessel width for average measurements of the mouse driven and shape modelled Gaussian half height measures of width plotted against their mean ($n=101$). Thick solid line represents the mean difference, thin lines $\pm 95\%$ CI. Dashed line with a slight negative gradient is a linear regression line of the data points. 136
- Figure 4.13 shows differences between paired values of vessel width for average measurements of automated width ($\sigma = 2.5$) and mouse driven determination, plotted against their mean ($n=101$). Thick solid line represents the mean difference, thin lines $\pm 95\%$ CI. Dashed line with a steep positive gradient is a linear regression line of the data points. 137
- Figure 4.14 shows a 3 dimensional plane surface of the mean difference of the mouse driven method minus the automated method, for differing sigma's of Steger algorithm, plotted against differing vessel bins varying from less than $20\mu\text{m}$ ($n=16$) to less than $110\mu\text{m}$ ($n=96$) as measured from digitally created photographic slides with electronic callipers. 138
- Figure 4.15 shows a 3 dimensional plane surface of the mean difference of the mouse driven method minus the automated method, for differing sigma's of Steger algorithm, plotted against differing vessel bins varying from greater than $20\mu\text{m}$ ($n=85$) to greater than $110\mu\text{m}$ ($n=5$) as measured from digitally created photographic slides with electronic callipers. 138
- Figure 4.16 shows difference between paired values of vessel width for sessions 1 and 2 plotted against their mean ($n=67/101$) using Steger's algorithm at $\sigma = 2$ for vessels $<40\mu\text{m}$. Thick solid line represents mean difference, and thin lines $\pm 95\%$ CI. The solid line also indicates a linear regression line of the data points showing insignificant measurement error. 142

Figure 4.17 shows difference between paired values of vessel width for sessions 1 and 2 plotted against their mean ($n=34/101$) using Steger's algorithm at $\sigma = 4$ for vessels $<40\mu\text{m}$ (as measured by $\sigma = 2$). Thick solid line represents mean difference, and thin lines $\pm 95\%$ CI. The dashed line with a slight negative gradient is a linear regression line of the data points showing insignificant measurement error.	142
Figure 4.18 shows a 20 unit portion of a sinusoidal wave form 360 units in length and the circular model fitted to the amplitude and chord length, where $A =$ amplitude (5 units) and chord length = $180/2C$	145
Figure 4.19 shows 20 sinusoidal waveforms with varying cycles (0 to 20 cycles per 360 unit of length), with amplitude of 5 units.	146
Figure 4.20 shows the relationship between vessel to chord length ratio and cycles per 360 unit length. A third order polynomial trendline is shown with equation of the line and regression value.	147
Figure 4.21 shows the relationship between mean curvature estimates and cycles per 360 unit length. A powered trendline is shown with equation of the line and regression value.	147
Figure 4.22 shows the relationship between mean curve energy (based on the square of the radian change between wave increments) and cycles per 360 unit length. A third order polynomial trendline is shown with equation of the line and regression value.	148
Figure 4.23 shows two sinusoidal waveforms which would give the same vessel to chord length ratio, but are clearly dissimilar in tortuosity.....	149
Figure 4.24 shows a 900×900 pixel portion of the 1024×1280 pixel image of patient 1.....	153
Figure 4.25 shows a 900×900 pixel portion of the 1024×1280 pixel image of patient 2.....	154
Figures 4.26 shows the output of Steger's algorithm, used with $\sigma = 2$, with the vessel boundary and axis points overlaid on the image of patient 1.	155
Figures 4.27 shows the output of Steger's algorithm, used with $\sigma = 4$, with the vessel boundary and axis points overlaid on the image of patient 1.	156
Figures 4.28 shows the output of Steger's algorithm, used with $\sigma = 2$, with the vessel boundary and axis points overlaid on the image of patient 2.	157
Figures 4.29 shows the output of Steger's algorithm, used with $\sigma = 4$, with the vessel boundary and axis points overlaid on the image of patient 2.	158
Figure 4.30 shows a 230×230 pixel portion of figure 4.25 of an anterior ciliary artery and underlying vascular network. All images are shown in negative to help visualisation. The raw image is shown top left, the raw image with the output of the algorithm run at $\sigma = 2$ top right, $\sigma = 3$ bottom left, and $\sigma = 4$ bottom right.	159
Figures 4.31 shows the output of Steger's algorithm, used with a $\sigma = 3$, with the vessel boundary and axis points overlaid on the image of patient 1.	160
Figures 4.32 shows the output of Steger's algorithm, used with a $\sigma = 3$, with the vessel boundary and axis points overlaid on the image of patient 2.	161
Figure 5.1 shows the differences between session 1 and session 3 for W, WV, T, TV and Density against their mean, for vessels $<25\mu\text{m}$ in diameter. Horizontal lines represent the mean and the 95% CI of inter session repeatability.	175
Figure 5.2 shows the differences between session 1 and session 3 for W, WV, T, TV and Density against their mean, for vessels 25 to $<40\mu\text{m}$ in diameter. Horizontal lines represent the mean and the 95% CI of inter session repeatability.....	176

Figure 5.3 shows mean W index for all vessels at each 2 hour interval of measurement, error bars represent $\pm SD$	178
Figure 5.4 shows separate graphs of WV plotted against the hour of measurement for each of the 31 subjects.....	179
Figure 5.5 shows a scatter plot of MAP against total vascular density and a linear trend line which shows a slight positive gradient.	180
Figure 5.6 shows a scatter plot of MAP against TV for vessels less than $25\mu m$ in width and a linear trendline showing a slight positive gradient.....	181
Figure 5.7 shows mean vessel widths for the above $80\mu m$ category plotted against hour for each subject separately.....	183
Figure 6.1 shows a scatter plot of MAP against Density for vessels $<25\mu m$ in diameter.....	193
Figure 6.2 shows a scatter plot of MAP against the logarithm of Density for vessels $<25\mu m$ in diameter. The linear regression line shows decreasing density with increasing MAP	194
Figure 6.3 shows a scatter plot of age against MAP where open squares represent normals, closed squares TI diabetics, and crossed symbols TII diabetics.....	195
Figure 6.4 shows a scatter plot of MAP against Density for vessels $25\mu m$ to $<40\mu m$ in diameter.	196
Figure 6.5 shows a scatter plot of MAP against the logarithm of Density for vessels $25\mu m$ to $<40\mu m$ in diameter. The linear regression line shows decreasing density with increasing MAP	196
Figure A1.1. W plotted against age at 0, 2, 4, 6 and 8 hours for vessels $<25\mu m$ in diameter, where W is in microns and age in years	208
Figure A1.2. WV plotted against age at 0, 2, 4, 6 and 8 hours for vessels $<25\mu m$ in diameter, where WV is in microns ² and age in years.....	208
Figure A1.3. T plotted against age at 0, 2, 4, 6 and 8 hours for vessels $<25\mu m$ in diameter, where T is in units of curve energy and age in years.....	209
Figure A1.4. TV plotted against age at 0, 2, 4, 6 and 8 hours for vessels $<25\mu m$ in diameter, where TV is in units of curve energy ² and age in years.....	209
Figure A1.5. Density plotted against age at 0, 2, 4, 6 and 8 hours for vessels $<25\mu m$ in diameter, where Density is in mm^2 of vessel per mm^2 of conjunctiva and age in years	209
Figure A1.6. W plotted against age at 0, 2, 4, 6 and 8 hours for vessels $25\mu m$ to $40\mu m$ in diameter, where W is in microns and age in years.....	209
Figure A1.7. WV plotted against age at 0, 2, 4, 6 and 8 hours for vessels $25\mu m$ to $40\mu m$ in diameter, where WV is in microns ² and age in years	210
Figure A1.8. T plotted against age at 0, 2, 4, 6 and 8 hours for vessels $25\mu m$ to less than $40\mu m$ in diameter, where T is in units of curve energy and age in years	210
Figure A1.9. TV plotted against age at 0, 2, 4, 6 and 8 hours for vessels $25\mu m$ to $<40\mu m$ in diameter, where TV is in units of curve energy ² and age in years.....	210
Figure A1.10. Density plotted against age at 0, 2, 4, 6 and 8 hours for vessels $25\mu m$ to $40\mu m$ in diameter, where Density is in mm^2 of vessel per mm^2 of conjunctiva and age in years	211
Figure A1.11. W plotted against age at 0, 2, 4, 6 and 8 hours for vessels $40\mu m$ to $80\mu m$ in diameter, where W is in microns and age in years.....	211

Figure A1.12. WV plotted against age at 0, 2, 4, 6 and 8 hours for vessels $40\mu\text{m}$ to $80\mu\text{m}$ in diameter, where WV is in microns ² and age in years	211
Figure A1.13. T plotted against age at 0, 2, 4, 6 and 8 hours for vessels $40\mu\text{m}$ to less than $80\mu\text{m}$ in diameter, where T is in units of curve energy and age in years	212
Figure A1.14. TV plotted against age at 0, 2, 4, 6 and 8 hours for vessels $40\mu\text{m}$ to $<80\mu\text{m}$ in diameter, where TV is in units of curve energy ² and age in years.....	212
Figure A1.15. Density plotted against age at 0, 2, 4, 6 and 8 hours for vessels $40\mu\text{m}$ to $80\mu\text{m}$ in diameter, where Density is in mm ² of vessel per mm ² of conjunctiva and age in years	212
Figure A1.16. W plotted against age at 0, 2, 4, 6 and 8 hours for all vessels, where W is in microns and age in years	213
Figure A1.17. WV plotted against age at 0, 2, 4, 6 and 8 hours for all vessels, where WV is in microns ² and age in years.....	213
Figure A1.18. T plotted against age at 0, 2, 4, 6 and 8 hours for all vessels, where T is in units of curve energy and age in years.....	213
Figure A1.19. TV plotted against age at 0, 2, 4, 6 and 8 hours for all vessels, where TV is in units of curve energy ² and age in years.....	214
Figure A1.20. Density plotted against age at 0, 2, 4, 6 and 8 hours for all vessels, where Density is in mm ² of vessel per mm ² of conjunctiva and age in years.....	214
Figure A2.1. W plotted against MAP at 0, 2, 4, 6 and 8 hours for vessels $<25\mu\text{m}$ in diameter, where W is in microns and MAP in mmHg.....	215
Figure A2.2. WV plotted against MAP at 0, 2, 4, 6 and 8 hours for vessels $<25\mu\text{m}$ in diameter, where WV is in microns ² and MAP in mmHg.....	215
Figure A2.3. T plotted against MAP at 0, 2, 4, 6 and 8 hours for vessels $<25\mu\text{m}$ in diameter, where T is in units of curve energy and MAP in mmHg	215
Figure A2.4. TV plotted against MAP at 0, 2, 4, 6 and 8 hours for vessels $<25\mu\text{m}$ in diameter, where TV is in units of curve energy ² and MAP in mmHg	216
Figure A2.5. Density plotted against MAP at 0, 2, 4, 6 and 8 hours for vessels $<25\mu\text{m}$ in diameter, where Density is in mm ² of vessel per mm ² of conjunctiva and MAP in mmHg.....	216
Figure A2.6. W plotted against MAP at 0, 2, 4, 6 and 8 hours for vessels $25\mu\text{m}$ to $<40\mu\text{m}$ in diameter, where W is in microns and MAP in mmHg.....	216
Figure A2.7. WV plotted against MAP at 0, 2, 4, 6 and 8 hours for vessels $25\mu\text{m}$ to $<40\mu\text{m}$ in diameter, where WV is in microns ² and MAP in mmHg	217
Figure A2.8. T plotted against MAP at 0, 2, 4, 6 and 8 hours for vessels $25\mu\text{m}$ to $<40\mu\text{m}$ in diameter, where T is in units of curve energy and MAP in mmHg	217
Figure A2.9. TV plotted against MAP at 0, 2, 4, 6 and 8 hours for vessels $25\mu\text{m}$ to $<40\mu\text{m}$ in diameter, where TV is in units of curve energy ² and MAP in mmHg ...	217
Figure A2.10. Density plotted against MAP at 0, 2, 4, 6 and 8 hours for vessels $25\mu\text{m}$ to $<40\mu\text{m}$ in diameter, where Density is in mm ² of vessel per mm ² of conjunctiva and MAP in mmHg	218
Figure A2.11. W plotted against MAP at 0, 2, 4, 6 and 8 hours for vessels $40\mu\text{m}$ to $<80\mu\text{m}$ in diameter, where W is in microns and MAP in mmHg.....	218
Figure A2.12. WV plotted against MAP at 0, 2, 4, 6 and 8 hours for vessels $40\mu\text{m}$ to $<80\mu\text{m}$ in diameter, where WV is in microns ² and MAP in mmHg.....	218
Figure A2.13. T plotted against MAP at 0, 2, 4, 6 and 8 hours for vessels $40\mu\text{m}$ to $<80\mu\text{m}$ in diameter, where T is in units of curve energy and MAP in mmHg	219

Figure A2.14. TV plotted against MAP at 0, 2, 4, 6 and 8 hours for vessels $40\mu\text{m}$ to $<80\mu\text{m}$ in diameter, where TV is in units of curve energy² and MAP in mmHg ...219

Figure A2.15. Density plotted against MAP at 0, 2, 4, 6 and 8 hours for vessels $40\mu\text{m}$ to $<80\mu\text{m}$ in diameter, where Density is in mm^2 of vessel per mm^2 of conjunctiva and MAP in mmHg219

Figure A2.16. W plotted against MAP at 0, 2, 4, 6 and 8 hours for all vessels, where W is in microns and MAP in mmHg220

Figure A2.17. WV plotted against MAP at 0, 2, 4, 6 and 8 hours for all vessels, where WV is in microns² and MAP in mmHg220

Figure A2.18. T plotted against MAP at 0, 2, 4, 6 and 8 hours for all vessels, where T is in units of curve energy and MAP in mmHg220

Figure A2.19. TV plotted against MAP at 0, 2, 4, 6 and 8 hours for all vessels, where TV is in units of curve energy² and MAP in mmHg.....221

Figure A2.20. Density plotted against MAP at 0, 2, 4, 6 and 8 hours for all vessels, where Density is in mm^2 of vessel per mm^2 of conjunctiva and MAP in mmHg221

Acknowledgements

I gratefully acknowledge my advisors Dr Tim Ellis and Professor Geoffrey Woodward. I would particularly like to thank Geoff for giving me the opportunity to pursue this self-initiated project, especially when it is an area somewhat removed from our departments expertise. His advice and friendship has extended well beyond the bounds of this thesis.

Without the assistance of Tim Ellis this project would never have got off the ground. He has added the imaging clout to this work making it worthy of submission. I know that he has given more time to this thesis than he ever expected and I will be eternally grateful to him for his contagious enthusiasm, and for explaining various aspects of computer vision which were far beneath him.

I am indebted to Dr Alicja Rudnicka, who I met in the infancy of this thesis, and has been my 'statistical guru' throughout the duration of this project. In addition she agreed to marry me during this work which was a perk far beyond my expectation of any research project. She has always had the confidence in me that I sometimes lacked.

I also wish to thank various members of the academic and technical staff within the Optometry Department of City University. Professor John Barbur for giving me the space to work, Stuart Brundritt for endless computational advice, Alf Goodbody and Colin Longhurst for their technical skills. Also Professor Gordon Ruskell and Dr John Lawrenson for their anatomical input, and especially to Gordon who allowed me to image his congested conjunctival vascular bed on numerous occasions. I would also like to thank Dr Fred Fitzke for allowing me to use computer facilities at the Institute of Ophthalmology, and Dr Jake Palmer (University of Westminster, London, UK), Professor Dave Delby (University College London, London, UK) and Dr Ron Douglas for their assistance in matters concerning the reflectance of haemoglobin.

Finally, I would like to thank my mother for her endless care, and father whose dedication to work gave me the impetus to see this project to its end.

Declaration

I grant the powers of discretion to the University Librarian to allow this thesis to be copied in whole or in part without further reference to me. This permission covers only single copies made for study purposes, subject to normal conditions of acknowledgement.

Abstract

The purpose of this project was to investigate the utility of an automated means of quantifying the conjunctival bed. To simplify the task of any image processing system, it is important that the original image capture stage is optimised, this is an aspect that is often overlooked on the assumption that sophisticated computational techniques can be used to enhance the image. Hence, the concept of exposure density was used to achieve optimal images of bulbar conjunctival vessels using a digital camera (Kodak DCS 100 camera). A database of filters predicted a 6.5 times increase in vessel contrast when recording on the green channel of the charge coupled device (CCD) camera with a Wratten 99 (green) filter over the illumination optics, compared to recording without a filter.

With knowledge of the optical transfer characteristics of the imaging system a vascular model was derived. The tubular model, corrected for optical distortions, was fitted to densitometric profiles across conjunctival vessels repetitively imaged under different optical configurations. Although vessel contrast did not increase by the predicted amount, a ~30% increase in the amplitude was observed in comparison to images recorded on the green CCD alone. Hence, this became the method of choice when imaging vessels of the conjunctiva.

Often automated methods of image segmentation are used without quantification of what is actually being measured, however, this is complicated when no accepted gold standard of measurement exists. Manual methods of determining widths using electronic callipers from projected digitally created photographs were used as the gold standard as they demonstrated a good intra session repeatability and range of measurement when 101 sample vessel widths were measured (95% confidence interval from +10.12 to -9.29 μ m, ranging from 14.4 to 140.0 μ m). To best agree with the automated measure of width, the algorithm was run at sigma (σ) = 3, to give a 95% confidence interval of inter method repeatability of +9.41 to -8.48 μ m. However, it was acknowledged that this algorithm overestimates small vessel widths, and underestimates larger widths.

The use of an automated approach of vessel recognition results in a vast amount of data concerning vessel axis and vessel edge locations. Five indices were derived to describe the vascular bed including mean vessel width, width variance, tortuosity, tortuosity variance and density, for vessels as a whole and for sub-groups of vessels classified on the basis of size. These indices were a novel way of describing the conjunctival vascular complex. The inter session repeatabilities of these indices were investigated on 31 normal patients and were acceptable in all cases. Also the diurnal variation in these indices on this population showed negligible changes.

The angiopathic consequence of diabetes are well known in a variety of organs. However, these have never been adequately quantified in conjunctival vasculature. Seventeen Type I (TI) diabetics, 36 Type II (TII) diabetics, and 60 normals were analysed. Although several indices showed a difference between normals and diabetics for all vessels and sub-categories of vessels, by far the most remarkable was the dramatic change in density at a capillary level (vessels less than 25 μ m in diameter). A -57.12% (95% confidence interval from -71.96 to -36.76%, $P < 0.0001$) reduction in

capillary density was found in TI diabetics compared to normals and a reduction of -17.5% (95% confidence interval from -41.02 to 16.64%) in TII diabetics compared to normals, however this was not statistically significant ($P=0.273$). A similar phenomenon was found in venular density (vessel 25 to less than 40 μ m in diameter). Hence, diabetes principally exerts its affect on the microvasculature of the conjunctival bed. In addition a statistically significant association between mean arterial pressure and vascular density was found, even though our sample did not contain anyone diagnosed with hypertension. A -13.82% (95% confidence interval from -23.71 to -2.65%, $P=0.017$) reduction in capillary density per 10mmHg rise in mean arterial pressure was established. Hence raised mean arterial pressure exerts an effect on smaller vessels of the conjunctiva.

Key of abbreviations / symbols

ACV	Aneurysms of conjunctival vessels
AIDS	Acquired immunodeficiency syndrome
AION	Anterior ischaemic optic neuropathy
ANOVA	Analysis of variance
BC	Bulbar conjunctiva
BDR	Background diabetic retinopathy
CCD	Charge coupled device
CI	Confidence interval
CRA	Central retinal artery
CRV	Central retinal vein
DCS	Digital camera system
DSU	Digital storage unit
EDV	End diastolic velocity
GEE	General estimating equations
HIV	Human immunodeficiency virus
IOP	Intra ocular pressure
IR	Infra red
IRMA	Intraretinal microvascular abnormalities
MAP	Mean arterial pressure
MD	Mean deviation
NDR	No diabetic retinopathy
NTG	Normal tension glaucoma
OA	Ophthalmic artery
ONH	Optic nerve head
PCA	Posterior ciliary artery
P _D	Diastolic blood pressure
PMN	Polymorphonuclear leukocytes
POAG	Primary open angle glaucoma
POBF	Pulsatile ocular blood flow
PPR	Pre-proliferative retinopathy
PR	Proliferative retinopathy
PRP	Pan retinal photocoagulation
P _S	Systolic blood pressure
PSV	Peak systolic velocity
RGP	Rigid gas permeable
ROI	Region of interest
RR	Relative redness
σ	Sigma
SCL	Soft contact lens
SD	Standard deviation
SER	System exposure response
SERD	System exposure response difference
SLO	Scanning laser ophthalmoscope
UV	Ultra violet
VA	Vessel area
VV	Vortex vein

CHAPTER 1

1. Conjunctival vasculature

1.1 Introduction

In general, the vascular supply of humans is obscured beneath a semiopaque skin or lies deep within the body. However, vessels of the bulbar conjunctiva offer a superficial three dimensional vascular bed, which can be viewed without invasion. It represents a complex network which cannot be adequately described by a human observer. With the increasing development of computer vision, the conjunctival vascular arrangement presents an interesting structure for image segmentation and analysis. Any angiopathic change could then be computed and studied on a sequential or cross sectional basis. However, knowledge of what computationally advanced algorithms measure is paramount before such systems can be advocated. The purpose of this thesis is not to linger on the complexities of image algorithms but to verify their use, and investigate whether they can delineate between a normal and challenged vasculature. Within this chapter we will discuss the anatomy and physiology of conjunctival circulation and methods of computational vascular measurement.

1.2 Anatomy of conjunctiva

The conjunctiva represents a thin, microvillus covered, translucent mucous membrane which joins the eyeball to the lids. It can be conveniently divided into three zones, palpebral, bulbar and forniceal. The palpebral conjunctiva can be further subdivided into marginal, tarsal, and orbital zones. Tarsal conjunctiva is thin, adherent, very vascular and readily observed on lid eversion. Its reddish colour is a gross clinical indicator however, it is often blanched to differing degrees on lid eversion. The forniceal conjunctiva represents an envelope from the tarsus to the orbital margin (conjunctival sac), from which the bulbar conjunctiva begins. It is only clinically examined on double eversion. Bulbar conjunctiva represents a thin (~80 μ m in thickness), translucent mucous membrane, which allows visualisation of the underlying 'white sclera'. It is this structure which is readily observed (not in its entirety) beyond the iris of the open eye, and hence will be considered in greater detail. Dimensions of the bulbar conjunctiva are shown in figure 1.1 and are evidently bigger than the palpebral fissure.

Unlike the tarsus, bulbar conjunctiva is loosely adhered to underlying structures by areolar tissue allowing ocular movement. Underlying structures include fascia bulbi (Tenon's capsule) of the recti muscles and sclera. The episclera is found between the conjunctiva and sclera and contains a rich blood supply including anterior ciliary arteries, forming a pericorneal plexus. This vascular system spills over into the lymphoid layer of the conjunctival submucosa forming a vessel network. At the limbus, near the cornea, the conjunctival dermis, fascia bulbi, episcleral connective tissue, and sclera fuse to become limbal conjunctiva. It is the blood supply contained within the episclera and submucosa which is of most interest as it offers an open window to a peripheral vascular bed, hence is worthy of further investigation. An understanding of this vasculature is paramount to the importance of this work. Table

1.1 lists the vascular terminology used to broadly classify vessels according to their size and structure (Junqueira and Carneiro, 1983).

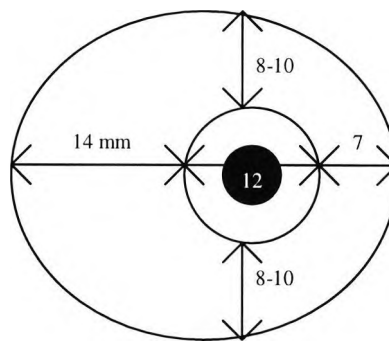


Figure 1.1 shows the dimensions (in millimetres) of human bulbar conjunctiva measured from the limbus (with an assumed corneal diameter of 12 mm) to the conjunctival sac (From Whitnall SE: *The anatomy of the Human Orbit*, p 195. Oxford University Press 1932; cited from Ruskell, 1991).

Vessel group	Diameter (μm)	Tunica intima	Tunica media	Tunica adventitia
Elastic arterioles	>500	Present, complete IELM	Thick, rich in elastin and elastic membranes	Contains elastic and collagen fibres
Muscular arteries	>500	Present, incomplete or complete IELM	Includes ~40 layers of smooth muscle cells	Thicker than arterioles
Arterioles	<500	Present but incomplete IELM	Includes 1 to 5 layers of smooth muscle cells	Narrow
Capillaries	9 to 10	One layer of endothelial cells, surrounded by a basement membrane and a partial layer of pericytes		
Post capillary venules	10 to 30	Present	Thin	Thin
Collecting venules	30 to 50	Present	Contains cells similar to smooth muscle cells	Thin
Venules	50 to 1000	Present	Thin, none to a few layers of smooth muscle cells	Thin, contains connective tissue rich in collagenous fibres
Veins	1000 to 9000	Present, well developed	Thin, a few layers of smooth muscle cells	Thicker than venules, rich in collagenous fibres

Table 1.1 lists the vascular terminology used to classify vessels according to their size and structure, where IELM refers to the internal elastic limiting membrane.

1.2.1 Conjunctival arterial blood supply

The anterior segment has deep and superficial circulations which both arise from the ophthalmic artery via the palpebral arcades and anterior ciliary arteries, this was described by Leber in 1903 (cited from Meyer, 1989). The supply can be divided into 4 arterial sources.

- Peripheral tarsal arcades
- Marginal tarsal arcades
- Anterior ciliary arteries
- Deep ciliary system

The peripheral tarsal arcade supplies the tarsus, fornix, and proximal bulbar conjunctiva. After passing above the tarsal plate and piercing the palpebral muscle the arcade bifurcates into ascending and descending branches. Ascending branches pass over the fornix to the globe to become posterior conjunctival arteries and anastomose with the anterior ciliary arteries to supply the proximal bulbar conjunctiva. A peripheral arcade is often missing from the lower eyelid and the palpebral conjunctiva receives vessels exclusively from the marginal arcade. Marginal arcades send branches through the tarsus at the subtarsal fold feeding the lid margin and palpebral conjunctiva. The supply to the corneoscleral perilimbal conjunctiva is elaborate, rich and complex, and has been an area of some debate. The need for a rich blood supply in this area is paramount as corneal epithelium is renewed from limbal stem cells located within this region, also for the metabolic demands of aqueous drainage. A number of methods have been used to investigate this complex system using Indian ink injections (Kiss 1943; cited from Meyer and Watson, 1987), vascular casting (Ashton, 1951 and 1952; Ashton and Smith, 1953), and *in vivo* anterior segment fluorescein angiography (Bron and Easty, 1970; Marsh and Ford, 1980; Meyer and Watson, 1987; Meyer, 1988 and 1989). The perilimbal bulbar conjunctiva is served by the anterior ciliary arteries which are forward extensions of muscular arteries (a branch of the ophthalmic artery) emanating from the 4 rectus muscle tendons. Conjunctival anterior ciliary arteries have been observed by fluorescein angiography and are said to carry blood with pulsatile flow with velocities from 1.6mm/sec to 10cm/sec (Meyer 1988). There can be a great deal of variation in flow dynamics between individuals and pulsatility may not be present. Usually there are 7 anterior ciliary arteries destined for the major iridic circle, one travels from the lateral rectus, and two from each of the other recti muscles.

The appearance of anterior ciliary arteries on the bulbar conjunctiva is easily recognisable (with and without the use of slit-lamp biomicroscopy) as large, deeply coloured (because of their depth), meandering, vessels, and are usually located laterally and / or vertically to the iris. They appear to terminate abruptly but in fact dive into the sclera often through a pigmented ring, and along with the deeper long ciliary arteries form the major arterial (iridic) circle, which supplies the iris, anterior choroid and ciliary apparatus (Ashton and Smith, 1953). Low dose fluorescein videoangiography has shown that episcleral branches from the anterior ciliary artery meet each other in the episcleral arterial circle, lying 1-5mm behind the limbus (Meyer and Watson, 1987; Meyer, 1988 and 1989) thus allowing an elaborate shunt system between the inner major arterial and outer episcleral arterial circle. Branches emanate from the episcleral arterial circle and fold back to form the perilimbal vascular plexus of the anterior conjunctiva and episcleral capillary bed (Meyer and Watson, 1987). Limbal loops emanate from these episcleral arterial folds. The anterior conjunctival arteries which form the perilimbal blood supply spans some 4 to 6mm from the limbus (Marsh and Ford, 1980; Bron *et al*, 1985). Arterial supply to the episclera is complex especially when considering flow dynamics.

1.2.2 Conjunctival venous drainage

Venous drainage of the tarsus, fornix, and posterior bulbar conjunctiva is principally by palpebral veins (Marsh and Ford, 1980). Within close proximity of the episcleral arterial circle lies a perilimbal venous circle which collects from the limbus, corneal arcades, and anterior conjunctival veins (Meyer, 1988 and 1989). This drains into radial episcleral collecting veins and flows towards the rectus muscles. On its journey across the anterior sclera, radial veins marry with episcleral veins and veins which emerge from the sclera which drain deeper limbal structures. 'Emissary veins' emerging from scleral foramina also join collecting veins destined for the rectus muscle. Rectus muscle veins eventually join the ophthalmic vein.

1.2.3 Comparative vascular structure and function of retinal and conjunctival vessels

Capillary density is relatively high in the perilimbal region (4 to 6mm from the limbus), curtails in the proximal conjunctiva, increases slightly in the orbital region, and reaches a maximum at the tarsus. The rich vascular monolayer of the tarsal conjunctiva is sufficient to maintain corneal metabolism during sleep when atmospheric oxygen is unavailable due to eyelid closure (Ruskell, 1991). The difference in vascular density have ramifications in vascular structure. Capillaries of the limbus have thicker endothelium and fewer fenestrations than those of the conjunctiva (Iwamoto and Smelser, 1965; cited from Ruskell, 1991). Hence limbal capillaries have less leakage than those found in the conjunctiva which is evident when performing fluorescein angiography (Meyer and Watson, 1987). The low molecular weight of sodium fluorescein (376.3 daltons) is ideal to test the integrity of tight junctions between retinal capillary endothelial cells, retinal pigment epithelial cells, and the permeability of Bruch's membrane. It is also of use to test the integrity of tight junctions of endothelial cells in iris capillaries (Jensen and Lundback, 1968). Note that it is the tight junctions (zonulae occludentes) between endothelial cells which form the major constituent of the blood retinal barrier, which is imperative for retinal function. In contrast, episcleral and conjunctival capillaries leak molecules smaller than serum albumin allowing fluorescein to rapidly extravate, obliterating the angiogram. To overcome this problem Meyer and Watson (1987) used a low dosage of sodium fluorescein to allow ionic binding with macro moleculated albumin. The difference in vascular structure between conjunctival / episcleral and retinal vessels may result in differing responses to disease and angiopathic challenge.

1.3 Clinical relevance of conjunctival vasculature examination

Conjunctival, episcleral, scleral hyperaemia and ciliary flush are readily observed with the naked eye. One can also see the pale conjunctiva of anaemia, the massively congested conjunctival vessels of a carotid-cavernous fistula, and injected vessels over the lateral and medial rectus muscles in endocrine exophthalmous. In addition systemic conditions such as diabetes (Ditzel and Saglid, 1954; Coget *et al*, 1989), hypertension (Davis and Landau, 1957; Harper *et al*, 1978; Albanese and de Nicola, 1987), sickle cell disease (Paton, 1961; Serjeant *et al*, 1972), renal failure (Klassen-Broekema and van Bijsterveld, 1992), and ocular conditions such as primary open angle glaucoma (Orgül and Flammer, 1995), are all known to effect the morphological and morphometric characteristics of conjunctival vasculature (similar effects have also been reported in retinal vessels). Also contact lens wear (McMonnies and Chapman-

Davies, 1982; McMonnies and Chapman-Davies, 1987a, 1987b), contact lens wearing time (Holden *et al*, 1986), *in vivo* ocular irritancy of contact lens cleaning solutions (Sivak *et al*, 1995) have all been shown to effect conjunctival vasculature. Biocompatibility of ocular medications, and therapeutic effectiveness of ocular medications in the treatment of conjunctivitis, episcleritis, scleritis, uveitis, and other non infective conditions such as allergic eye disease (GPC/CLAPC), and acute closed angle glaucoma are all known to effect conjunctival vascularity. Also the success of certain surgical treatments are gauged by monitoring the vascular response for example glaucomatous bleb surgery (Chew *et al*, 1994; Wilkins *et al*, 1996). It is the angiopathic changes observed in diabetes and age which will be principally considered within this thesis, and hence are discussed in some detail. Where the literature concerning conjunctival vasculature is scarce the abundant literature on retinal vessels is summarised, which may relate to conjunctival vessel changes.

1.3.1 Diabetic angiopathy

The effects of diabetes on retinal vasculature were known soon after Helmholtz invented the ophthalmoscope in 1851. However diabetes is a systemic disorder having numerous complications which are caused by vascular angiopathy. Diabetic microangiopathy has its greatest effect in the retina and kidney, leading to retinopathy and nephropathy. Effects on other capillary beds lead to peripheral vascular disease. An understanding of the sequential micro and macroangiopathy is required, to help in the formulation of vascular indices which are pathognomonic of this condition.

1.3.2 Diabetic retinopathy

Diabetes is known to cause abnormalities of retinal vessels and blood rheology. The occurrence of retinal microaneurysms in early diabetic retinopathy was first described by MacKenzie in 1877 (cited from Ditzel, 1954) and has since been advocated as a clinicopathological hallmark of diabetic retinopathy (Stitt *et al*, 1995). Spencer *et al* (1992) state that the 'presence of microaneurysms is the first unequivocal indication of early diabetic retinopathy'. A positive correlation has been shown between the number of microaneurysms and progression of the disease (Klein *et al*, 1989, Kohner *et al*, 1986). Macroangiopathy is less marked in the early stages of the condition amounting to minor dilation (Mendívil *et al*, 1995a; Patel *et al*, 1992). As the retinopathy progresses capillary occlusion, exudates, haemorrhages, and new vessel formation begin (Mendívil *et al*, 1995a; Patel *et al*, 1992). Such findings enable classification of the retinopathy.

- Background retinopathy (BR) defines the presence of one or all of the following; microaneurysms, lipoidal exudates, macular oedema, dot and blot haemorrhages. The presence of macular oedema is often reserved for the term diabetic maculopathy.
- Pre-proliferative retinopathy (PPR) features include; cotton wool spots, intraretinal microvascular abnormalities (IRMA), venous beading / looping, clusters of deep retinal haemorrhages, and arteriolar abnormalities.
- Proliferative retinopathy (PR) include features such as neovascularisation of the disc, neovascularisation elsewhere, vitreous haemorrhage, and tractional retinal detachment.

Diabetic retinopathy is a leading cause of blindness among the working age. The yearly incidence of blindness due to diabetes mellitus was found to be 3.3 per 100,000 population, or around 1600 cases for England and Wales (Moss *et al*, 1988). Javitt *et al* (1990) used a computer simulation model to predict that 72% of Type I (TI) diabetics will develop PR and require pan retinal photocoagulation (PRP), whilst 42% of TI will develop macular oedema. They propose that treatment costs are far less than the cost of visual disability payments. Screening for and treating retinopathy in patients with TI diabetes mellitus was found to be cost effective (Javitt *et al*, 1989). Annual examination of all diabetics and semi-annual examination of those with retinopathy was advocated. A method which can improve the specificity of detecting angiopathic change will help reduce the alarming incidence of blindness from this disease. Indeed, Rohan *et al* (1989) showed that effective community based screening, detection, referral, treatment, and follow up could prevent approximately 270 new cases of blindness in diabetics less than 70 years of age per year in England and Wales, equivalent to 10% of all cases of blindness in adults of this age group.

Since the application of bi-directional laser Doppler velocimetry to retinal vessels (Riva *et al*, 1981) a great deal of work has studied retinal vessel velocity in a variety of different contexts (Aburn and Sergott, 1993; Béchettille, 1996; Butt *et al*, 1995; Chen *et al*, 1994; Feke *et al* 1989; Grunwald *et al*, 1986, 1993; Newsom, 1994; Mendívil *et al*, 1995b; Patel *et al*, 1992; Ravalico *et al*, 1996; Riva *et al*, 1985; Williamson and Lowe *et al*, 1995, Williamson and Baxter *et al*, 1995, Williamson *et al*, 1994; Williamson and Harris 1996). To determine volumetric blood flow in a vessel the general formula, shown below, is used where Q indicates volumetric flow, V indicates blood velocity (derived from red cell velocity using laser Doppler velocimetry), and A is the cross sectional area of the vessel.

$$Q = V \times A$$

Assuming a circular cross sectional area of the vessel the formula may be written as in the following format, where R is the vessels radius.

$$Q = V \times \pi R^2$$

The prediction of volumetric blood flow in retinal vessels from their diameter without measuring velocity has been proposed using Poiseuille's formula (shown below), where ΔP is the pressure change along a vessel, L is the vessel length and η is the viscosity of the fluid.

$$Q = \frac{\pi R^4 \Delta P}{8L\eta}$$

Flow is proportional to the fourth power of vessel radius, hence, an error in measurement will have a profound effect on the calculation of flow. Poiseuille's formula relies on laminar flow, but vessels demonstrate turbulent flow at vessel branching and narrowing, and due to biphasic circulation. In addition, diabetes affects blood rheology causing an increase in blood and plasma viscosity (Mendívil *et al*, 1995a), especially in poorly controlled diabetics (Oughton 1981, cited from Newsom 1994). Kaba *et al* (1986) demonstrated an increase in blood and plasma viscosity 60

minutes after subcutaneous insulin administration in both TI and TII diabetics. Whilst Su *et al* (1996) found that intraluminal application of insulin dilates potassium-contracted retinal arteries of the pig. Hence, the application of Poiseuille's law in the assessment of diabetic retinal vessels is of dubious validity.

A number of studies have proposed that retinal blood flow is affected by diabetes (Grunwald *et al*, 1986; Mendivil *et al*, 1995a; Newsom, 1994; Patel *et al*, 1992). Colour Doppler imaging of the ophthalmic artery (OA), central retinal artery (CRA), central retinal vein (CRV), vortex veins (VV), and posterior ciliary artery (PCA) have showed a reduction in diabetic blood velocities compared to normals (Mendivil *et al*, 1995a). Patel *et al* (1992) used bi-directional laser Doppler velocimetry and fundus photography to determine blood flow in the temporal CRV. Diabetics with retinopathy showed statistically significant vein dilation compared to controls ($P < 0.005$) with $143.9 \pm 17.8 \mu\text{m}$ (mean \pm SD) for normals, 160.0 ± 24.3 for diabetics with no diabetic retinopathy (NDR), $174.8 \pm 17.7 \mu\text{m}$ for diabetics with PPR, and $162.6 \pm 21.6 \mu\text{m}$ for those with PR. No statistical differences in V_{MAX} velocities were found with $1.53 \pm 0.30 \text{ cm/sec}$ for normals, $1.49 \pm 0.22 \text{ cm/sec}$ for NDR, $1.57 \pm 0.27 \text{ cm/sec}$ for BDR, $1.67 \pm 0.55 \text{ cm/sec}$ for PPR, and $1.78 \pm 0.45 \text{ cm/sec}$ for those with PR. This suggests a non significant increase in velocities contesting the findings of Mendivil *et al* (1995a). Calculated flow values were $9.52 \pm 3.18 \mu\text{l/min}$ in controls, $9.12 \pm 3.83 \mu\text{l/min}$ NDR, compared to $12.13 \pm 3.92 \mu\text{l/min}$ for BR, $15.27 \pm 5.88 \mu\text{l/min}$ for PPR, and $13.88 \pm 4.51 \mu\text{l/min}$ in diabetics with PR. Analysis of variance showed that the observed increase in blood flow for those with retinopathy was statistically significant ($P < 0.005$). Grunwald *et al* (1986) found no statistical differences in calculated temporal CRV blood flow with values of $11.3 \pm 3.4 \mu\text{l/min}$ for normals, $10.6 \pm 3.2 \mu\text{l/min}$ for diabetics without retinopathy, $12.3 \pm 5.5 \mu\text{l/min}$ for diabetics with BDR, and $10.4 \pm 3.0 \mu\text{l/min}$ with PDR. However, velocities in the temporal CRV were statistically reduced in diabetic patients with retinopathy compared to normals and diabetics without retinopathy ($P < 0.05$, Bonferroni test) with $1.7 \pm 0.4 \text{ cm/sec}$ for normals, $1.6 \pm 0.5 \text{ cm/sec}$ for diabetics with NDR, $1.4 \pm 0.4 \text{ cm/sec}$ for diabetics with BDR, $1.2 \pm 0.1 \text{ cm/sec}$ for diabetics with PDR. Which is in agreement with Mendivil's (1995a) findings. In addition, statistically significant CRV dilation was found in diabetic retinopathy patients compared to controls and diabetics without retinopathy ($P < 0.05$, Bonferroni test), with $152 \pm 14 \mu\text{m}$ for normals, $151 \pm 12 \mu\text{m}$ for NDR, $167 \pm 25 \mu\text{m}$ for BDR, and $170 \pm 21 \mu\text{m}$ for diabetics with PDR. Similar findings were reported in the CRA. Skovborg *et al* (1969) measured the diameter of the CRA and CRV using a travelling microscope from fundus photographs of 266 TI diabetics and 129 normals. Mean arterial width (right eye only) was $274.4 \pm 31.80 \mu\text{m}$ for normals, and 288.3 ± 32.62 for diabetics. This 6.22% increase was statistically significant ($P < 0.001$, statistical method not quoted). Mean venule width (right eye only) was $361.6 \pm 34.07 \mu\text{m}$ for normals, and $392.0 \pm 42.40 \mu\text{m}$ for TI diabetics. This 8.41% increase in diameter was statistically significant ($P < 0.001$). Similar findings were found in the left eye. Note that these diameters are larger than those quoted by Grundwald (1986) and Patel (1992) and are larger than the range quoted by Taylor *et al* (1993) who directly measured vessel diameters from anatomical sections and found the CRA diameter to vary from 157 to $173 \mu\text{m}$, and the CRV from 110 to $252 \mu\text{m}$. Skovborg *et al* (1969) used a fixed object to film plane magnification for all subjects which may have overestimated the true magnification. However, the finding of vessel

dilation is still valid. Skovborg *et al* (1969) concluded that 'beading of the {retinal} veins is a rare phenomenon, while a general dilation is frequently seen' and that 'dilation seems to appear before other elements of diabetic retinopathy'.

Diabetic subjects in term 1 of their pregnancy showed significantly smaller retinal vessels (143.5 μ m) compared with measurements taken post partum (157.5 μ m) by 10.9% (P=0.003, Student's t test) (Chen *et al*, 1994). However, non diabetic pregnant controls showed smaller retinal vessels for terms 1, 2 and 3 compared to post partum widths with a reduction of 11.2% (from 143.5 to 157.5 μ m, P=0.001), 6.2% (from 155.2 to 156.6 μ m, P=0.005), and 7.4% (from 148.7 to 149 μ m, P=0.01) respectively. Hyperdynamic circulation present in pregnancy led to constriction of retinal blood vessels in the normal group. However, this mechanism is absent in pregnant women with diabetes. These findings point towards a lack of haemodynamic control in diabetic patients.

Interestingly, a statistically significant reduction in venous velocity, diameter, and flow for diabetic patients with PR treated with PRP, compared to normals has been reported suggesting an attempt to return to normal haemodynamics after PRP treatment (Grunwald *et al*, 1986; Patel *et al*, 1992). Diabetes also effects blood rheology with an increase in blood and plasma viscosity along with red blood cell / plasma aggregation which contributes to blood flow changes (Isogai *et al*, 1996; Mendivil *et al*, 1995a). This may explain the reduction in red blood cell velocity observed by Grunwald *et al* (1986) and Mendivil *et al* (1995a) in diabetics compared to normals. There appears to be some dispute over the precise effects of diabetes on retinal blood flow. However there appears to be a consensus of macrovascular dilation.

1.3.3 Conjunctival diabetic angiopathy

Dilation of conjunctival venous capillaries due to diabetes was first described by Zeller in 1921 (cited from Ditzel, 1954). Whether conjunctival microaneurysms are a pathognomonic sign of diabetes is less clear than their retinal equivalent. Friedenwald in 1950 (cited from Ditzel, 1954) studied 60 patients with DR and found only 1 microaneurysm, he stated that 'since such aneurysms are occasionally seen in non-diabetics, no significance is attached to this finding'. However, McCulloch and Pashby (1950) reported a higher incidence of microaneurysms and concluded that their presence warranted further investigation. Landau and Davis (1960) examined the conjunctival vasculature of 75 diabetic patients and found a 25% incidence of 'micropools', but noted that this findings was also common in patients with arteriosclerosis or hypertension. Sixty percent of these diabetic patients also exhibited conjunctival venous congestion (n=45/75), which was often accompanied by a congested venous limb of the capillary nailbed. Landau and Davis (1960) also report that conjunctival capillary narrowing was frequently seen in diabetic patients, contesting the findings of Zeller (1921). Literature concerning the effect of diabetes on conjunctival vasculature is somewhat confused, inadequate, and largely anecdotal. However a pattern of findings appears to emerge. Interpretation of these findings is confounded by a lack of good methodologies to quantify or qualitate conjunctival vascular networks. Dexel *et al* (1976) studied 60 diabetic patients (20 without retinopathy, 20 with BR, 20 with PPR or PR) and 20 normals. A microvascular subjective index was derived, where the presence of certain clinically observed

phenomenon were awarded points. The point system was proportional to the authors' interpretation of the likelihood of a clinical observation in a diabetic or non-diabetic patient, for instance venous sludging was observed in both diabetic and non-diabetic patients hence given a score of 2. Microaneurysms and focal narrowing were said to be more specific to diabetic individuals and given a higher score of 9. In total 12 observations were scored, but no statistical difference between the 2 populations was found (details of statistical analysis omitted). It was concluded that there was no correlation between diabetic retinopathy and conjunctival diabetic angiopathy. In contrast, Coget *et al* (1989) were so convinced of the effect of diabetes on the conjunctiva that they anecdotally advocated annual capillaroscopy by trained and experienced observers for those at risk of diabetes. Ditzel and Saglid (1954) performed capillary microscopy on 150 diabetics and 90 non-diabetics, but the observer was unaware of the individuals status. They observed that diabetics had a great number of arteriolar constrictions, larger number of capillaries, elongation of venules with focal nodularities, sacculation, greater tortuosity and angularities. Also diabetics had aggregated red blood cells in their blood stream, haemorrhages or post haemorrhage pigmentary artefacts. Interestingly, aneurysms were seen in 4% of diabetics, and 4% of normals and were not considered as pathognomonic. They concluded that 'none of these findings specifically correlated with the disease, but the combined morphological and haemodynamic pattern in the young diabetic patient appears to be characteristic'. Indeed they believed venules 12 to 60 μm in diameter show the greatest change. Worthen *et al* (1981) used a more objective method of studying conjunctival vasculature by superimposing a grid pattern over digitised photographic images, and measuring vessel area, as determined by the number of intersections vessels had with a grid-like pattern. They objectively concluded that diabetic conjunctival microvessels, less than 20 μm in diameter (capillaries and post capillaries) showed a 25% decrease in area, whereas vessels over 25 μm (post capillaries and venules) showed a 15% increase in diameter. Also that capillary diffusion distance (distance between capillaries) was greater in diabetics. Unfortunately no statistical analysis verified this finding. The authors claim a 90% specificity of diagnosing diabetes from conjunctiva, but such a claim is of dubious statistical validity. These findings appear to agree with those of Greer *et al* (1996) who using an unspecified automated video technique, observed that diabetics had significantly ($P < 0.05$) 'larger vessels (venules)' as well as 'abnormal vascular organisation', with a mean size of 76.2 μm compared to normals with 54 μm . Vessel density was less in type two (T II) ($n=19$) diabetic patients (mean 33 μm per unit area) than ($n=50$) controls (mean 44.6 μm per unit area). An incomplete abstract by Chen *et al* (1986) states that diabetics show a 20% increase in vascularity, while hypertensives show a 10% decrease in vascularity, compared to normals. Fenton (1980) demonstrated that there was a significant difference in vascular length per unit area between a diabetic ($n=5$) and non-diabetic cohort ($n=5$). Age was said 'to exert a dramatic influence on overall vascularity'. From this small sample they concluded that geometrical variations associated with diabetes and old age lead to significant changes in vascular mean pressure and flow, particularly at a capillary level. Electron microscopic studies conducted by Schwenk *et al* (1986) of conjunctival capillaries, venules, and arterioles, revealed a $\times 20$ increase in manually measured thickness of the basal lamina of 12 chronic diabetics compared to 12 normals. Thickening of the

vascular basement membrane in diabetics has also been reported in skeletal muscle, retina, pituitary, peripheral nerves, and cortex.

It is difficult within the current literature to decide what parameters to measure to best describe differences between normal and diabetic conjunctiva, however, Chen *et al* (1987) and Fenton (1980) advocate exact morphometric conjunctival vascular analysis as an important tool. In conclusion, microvascular dropout (capillary), macrovascular (venule) dilation accompanied with calibre variation and increased tortuosity are the likely effects of diabetes on the conjunctiva, and that conjunctival microaneurysms are unlikely to be pathognomonic of diabetes because they often occur in healthy subjects (Sakai *et al*, 1990). Figure 1.2 shows telangiectasia of a bulbar conjunctival blood vessel with a saccular like aneurysm in a normal 67 year old individual.

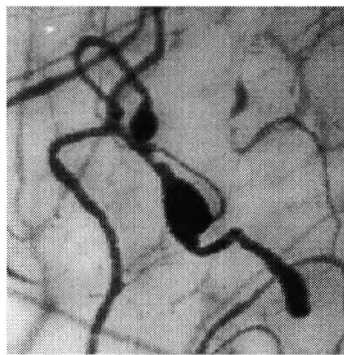


Figure.1.2 shows telangiectasia of a bulbar conjunctival blood vessel with a saccular like aneurysm in a 'normal' 67 year old individual. The square represents an area of approximately 1mm^2 .

1.3.4 Conjunctival blood flow

Although a vast literature exists on the measurement of retinal blood flow with the introduction of Doppler imaging, the conjunctiva has received less attention. However the bulbar conjunctiva is one of the few regions of the body in which the circulation of blood can be directly and non-invasively observed in the human. Flow in retinal vasculature is affected by extrinsic factors such as IOP. By contrast conjunctival vasculature is relatively unaffected by IOP due to its peripheral anatomical position. Lee (1955; cited from Mayrovitz *et al*, 1981) visually tracked individual red blood cells over a long distance and timed, with a stop watch, mean venular velocity as 0.06mm/sec , mean arterial velocity as 0.11mm/sec , and noted that velocities decreased in hypertensive patients. Wells and Egerton (1967) used microcinematography and strobe lighting to observe specific cell groups or plasma gaps giving a venule velocity of 0.375 to 0.425mm/sec . Jung *et al* (1983) used red-free slit-lamp (U-matic) video microscopy to manually estimate erythrocyte velocity. Values ranged from $0.205 \pm 0.091\text{mm/sec}$ to $0.349 \pm 0.155\text{mm/sec}$ for a conjunctival vessel of $22\mu\text{m}$ and $5.3\mu\text{m}$ in diameter respectively. Temporal variation in vessel opacity due to the differences in red blood cell and plasma optical density allowed Mayrovitz *et al* (1981) to record a characteristic 'signature' at 2 locations, of known distance apart, using an electro-optical sensor. Cross correlation was used to find similar 'signatures' on consecutive video still-images allowing velocity to be calculated. Diametric values were obtained from the video images and hence blood flow could be established.

Values quoted for one vascular tree of a 25 year old patient varied from a velocity of 0.71mm/sec for a 20 μ m diameter vessel (flow = 22.9×10^{-8} ml/sec) to 0.93mm/sec for a vessel diameter of 33 μ m (flow = 79.6×10^{-8} ml/sec). The paper shows a large reduction in blood flow for one patient after inhalation of amyl nitrate and an increase in flow for a patient suffering from a myocardial infarction after treatment with β -blockers. These figures contrast with those quoted by Meyer (1988) who using anterior segment fluorescein angiography found a huge variation in velocities from 0.16mm/sec to 10cm/sec in the anterior ciliary artery. This variability was accounted for by the large variation in vessel sizes, with the anterior ciliary artery being approximately 100 μ m in diameter. The diversity of vessel sizes, complexity of conjunctival network, and likely differences in vessel flow does not lend itself to study. Hence unlike retinal vessels no papers were found on the direct effect of diabetes on conjunctival blood flow.

1.3.5 Age related retinal vessel changes

The angiopathies described may not be specific to diabetes, indeed post-mortem plastic casts of human retinal vessels show microaneurysms, arterio-venous crossing defects, and areas of capillary non perfusion in hypertensive, atherosclerotic, as well as diabetic patients (Fryczkowski *et al*, 1985). Retinal vascular abnormalities have been associated with age. Studies on retinal vascular casts of Wistar Kyoto rats (aged 6, 18 and 24 months) using scanning electro microscopy showed straight parallel arteries and veins with perpendicular bifurcations in the young age group, but a significant ($P=0.036$) reduction in vessel diameter, increased tortuosity, irregular calibre's, sacculation, local narrowing, and acute angled bifurcation in the oldest group (Bhutto and Amemiya, 1995). Histological disappearance of cellular nuclear components, development of microaneurysms, and thickening of vessel walls in elderly humans was shown by Leishman in 1957 (cited from Bhutto and Amemiya, 1995). Angular tortuosity, calibre variations, arterio-venous constrictions are a sign of ageing and arteriosclerosis. Hypertension, diabetes, ageing are all related and inter-related to angiopathy. Vascular impairment of choroidal circulation has been hypothesised by Grunwald *et al* (1993) as part of the mechanism that leads to age related maculopathy. They suggested that this was related to foveal capillary occlusion with age. Thirty three normals, aged 20 to 78 had macular circulation assessed with a blue field simulation technique, based on the blue field entopic phenomenon. A statistically significant negative linear correlation was observed between leukocyte velocity and age ($R=-0.67$, $P=0.0001$, Spearman correlation), and leukocyte density and age ($R=-0.46$, $P=0.009$). Older subjects (50-78 years) had significantly lower leukocyte velocities (0.61 ± 0.21 mm/s), and smaller leukocyte densities (90 ± 43 particles per field of view) than younger subjects (0.92 ± 0.12 mm/s, 135 ± 65 particles), with unpaired Student's t test probabilities of $P=0.001$, $P=0.01$ respectively. This could be due to a decrease in metabolic demand (due to loss of ganglion cells with age), and / or decreased transmission of blue light with age. This paper cites the work of Laatikainen and Larinkari (1977) who found an increase in the measured diameter of the foveal capillary free zone, as shown by fluorescein angiography, with age. Hence, capillary drop out, and decreased choroidal blood flow may occur in those greater than 50 years of age. Ravalco *et al* (1996) studied the effect of age on pulsatile ocular blood flow (POBF) and pulse amplitude in 105 normal subjects aged from 10 to 80 years, with 15 subjects per decade. POBF in those 10 to 20 years of age was

found to be $819 \pm 212 \mu\text{l}/\text{min}$ compared to $630 \pm 194 \mu\text{l}/\text{min}$ for those aged between 71 to 80, as assessed in the sitting position. A significant negative correlation between POBF and age was found ($R = -0.36$, $P < 0.001$, linear regression analysis). However, such changes could be explained by a reduction in scleral rigidity with age. Williamson and Lowe *et al* (1995) used colour Doppler imaging to obtain a spectral waveform of the velocity of blood from the OA from 95 healthy volunteers. The influence of age, systemic blood pressure, smoking, and arteriopathy was assessed. Weak negative correlations between age and peak systolic velocity and end diastolic velocity of the OA were found ($R = -0.31$, $P = 0.003$, linear regression analysis, for both PSV and EDV). The paper accounted for this by a reduction in peripheral perfusion due to an increase in resistance to flow. These findings are similar to those of Béchetoille (1996). In summary there appears to be an increase in resistance to blood flow, retinal capillary / vascular constriction and deformation associated with age.

1.3.6 Age related conjunctival angiopathy

Photographic studies of conjunctival vasculature in 143 'normal' individuals aged 5 to 70 years revealed that the frequency of capillary and venule meandering increased with age (Kovalcheck *et al*, 1984). Also arteriole, venule, and capillary surface area increased with the onset of years. Although these are described as quantitative findings no statistical nor methodological data was given. These findings agree with McMonnies and Ho (1991) who using a photographic scale (0 for none to 5 for severe) to grade 252 females (aged 1 to 82 years) and 227 males (aged 1 to 89 years) for conjunctival vascularity showed a small increase in hyperaemia with age ($R = 0.73$, $P < 0.0001$, Spearman rank correlation), and that males exhibit greater hyperaemia than females ($P < 0.0001$, Mann Whitney U test). However such differences were classed as insignificant and such a technique is open to observer bias. Aliò and Padron (1982) investigated the mean absolute temperature of the anterior segment in 96 normals, aged 15 days to 80 years, and found a mean temperature of $34.06 \pm 0.56^\circ$, but a negative correlation with age. This may indicate a decreased perfusion with age, in contrast with the findings of Kovalcheck *et al* (1984) and McMonnies and Ho (1991), but ocular thermography is riddled with experimental artefacts. An anecdotal assessment of bulbar conjunctival vasculature using capillaroscopy on a geriatric population (Tassi *et al*, 1985) revealed an increase in microvessel tortuosity, microvessel serpentine shaped deformations, and increased red blood cell aggregation. The paper concludes that these findings are also indicative of arteriosclerotic changes.

1.3.7 Hypertensive retinopathy

In a comprehensive review Hayreh (1996) defined hypertensive retinopathy as retinal arteriolar changes, focal intraretinal periarteriolar transudates (a type of exudate associated with arteries), inner retinal ischaemic spots (cotton wool spots), retinal capillary changes (including aneurysm, arterio venous shunts, and looping), retinal venous changes, increased permeability of the retinal vascular bed, retinal haemorrhages, macular oedema, lipid deposits (hard exudates), nerve fibre loss, and vasospasm. The blood-ocular barrier is formed by tight endothelial junctions in retinal vessels and between cells of the retinal pigment epithelium which are disturbed by arterial (malignant) hypertension and diabetes, leading to vascular changes and leakage. He also indicates that prolonged hypertension leads to arteriosclerosis. These morphological changes have been observed using high resolution images obtained by scanning electron microscopy of vascular casts from 10 hypertensive, and 10 normal

subjects (Kaupp *et al*, 1991). By the implementation of a vascular algorithm based on the work of Pappas and Lim (1988), hypertensive retinal vessels demonstrated decreased width, and increased tortuosity. Vascular endothelium derives vasoactive agents such as vasoconstrictors including endothelin-1, thromboxane A₂, prostaglandin, and vasodilators such as nitric oxide which modulate vascular tone (Haefliger *et al*, 1994; cited from Hayreh 1996). Changes in vascular endothelial function with hypertension affects basal cell production of nitric oxide leading to less vasodilation (Luescher, 1994; cited from Hayreh 1996). Damaged endothelial cells are also seen in arteriosclerosis, atherosclerosis, hypercholesterolaemia, ageing, diabetes mellitus, and ischaemia, leading to well documented angiopathy. Wolf *et al* (1994) propose that hypertension is an important risk factor for cerebral, coronary and peripheral arterial disease. Changes in both capillary density and vessel diameter contribute to increased vascular resistance in hypertensive patients. This was demonstrated by Wolf *et al* (1994) who compared the macular blood flow of 17 hypertensive patients (blood pressure more than 145/95 mmHg) with stage 1 retinopathy, and 17 age matched normals, using fluorescein angiography and scanning laser ophthalmoscopy. Digital images were used to record mean perifoveal (5° around macular) intercapillary area (using digital image processing for which details were omitted), and perifoveal capillary flow velocity (by tracking fluorescence through capillaries). Intercapillary area significantly increased by 50% in the hypertensive group with 5591 ± 838 and $3742 \pm 391 \mu\text{m}^2$ respectively ($P < 0.01$, Student's t-test). Capillary blood flow velocity significantly reduced in the hypertensive group with 2.23 ± 0.33 and $2.87 \pm 0.53 \text{mm/s}$ in normals ($P < 0.01$). The paper concludes that 'retinal vascular alterations in hypertension provide a clue to the status of various organs, especially the central nervous system, cardiovascular system, and kidneys. Because of the similarities between retinal and cerebral vessels these findings indicate a 'global capillary loss in the perifoveal capillary network'.

1.3.8 Hypertensive conjunctival angiopathy

Unlike the effects of hypertension on retinal vasculature, conjunctival vasculature has received less attention. Davis and Landau (1957) briefly mention hypertensive effects on conjunctival vessels, while Harper *et al* (1978) anecdotally report a reduction in the number of bulbar conjunctival arterioles in hypertensive patients. Albanese and de Nicola (1987) conducted microscopic (magnification $\times 30$) capillary examination of the bulbar conjunctival of 20 elderly hypertensive patients, before and after administration of Captopril (angiotensin converting enzyme inhibitor). Arterial, venous, and capillary diameters, terminal capillary network, and intra vascular red cell aggregation were subjectively scaled from 1 to 3 (where 1 is normal and 3 represents a character in the extreme). After Captopril administration arterial, venular, capillary diameters increased. However, no statistical methods were quoted, although convincing photographs were published. In a brief abstract by Chen *et al* (1986) vessel length, diameter, and capillary perfusion distance were measured from photographs. They comment that diabetics and hypertensives showed diametrically opposite trends, with a 20% increase in vascularity in diabetic patients, a 10% decrease in vascularity in hypertensive patients, and that the vasodilatory effects of diabetes predominate in patients suffering from both diabetes and hypertension. However, there was no methodological or statistical verification of these findings.

Although it is the effects of age, hypertension and diabetes on conjunctival vasculature which are the main areas of interest within this thesis, an understanding of the effects of other diseases on conjunctival vasculature is useful in building up a picture of the type morphometric or morphological change likely to be seen. Hence these are dealt with under the following headings.

1.3.9 Glaucomatous conjunctival angiopathy

Pathogenesis of glaucoma can be divided into mechanical and/or vasogenic mechanisms. Increased intra ocular pressure (IOP) leads to glaucomatous damage, hence glaucoma is often described as a fault of aqueous humour dynamics, however, normal tension glaucoma (NTG) confounds this. Hence increased sensitivity to IOP was postulated as a causation of NTG. Increased IOP alters structural and neural elements of the optic nerve head (ONH) whether increased IOP impairs blood perfusion to ONH or causes primary damage to the glial cells or axons of the ONH is unclear. Jonas *et al* (1989) believed that 'retinal blood vessels serve for nutrition of retinal ganglion cells and their axons'. They manually measured the diameter of the superior and inferior arcades from colour stereo photographs. Mean retinal vessel diameter was significantly reduced in POAG patients (n=473 eyes from 281 patients) compared to normals (n=275 from 173 patients), especially for the inferior temporal artery. A similar study (Jonas *et al*, 1991) found decreased retinal vessel diameters in patients with both POAG and non-glaucomatous optic nerve atrophy compared to normals. Hence, eyes with small vessels should be screened for optic nerve atrophy. They advocate that decreased retinal vessel diameter is not primarily due to ganglion cell loss, but secondary to a diminished retinal ganglion cell population. Jonas *et al* (1991) conclude that 'parapapillary chorioretinal atrophy and decreased retinal vessel diameter occurs in glaucomatous eyes'. The occurrence of disc haemorrhages, and retinal vein occlusion has been associated with glaucoma (Sonnsjö and Krakau, 1993). Flammer (1996) also proposes a vasospastic aetiology of glaucoma which can have systemic effects. He suggests verification of vasospasm by viewing capillaries of the nail fold or in the conjunctiva. Stroman *et al* (1995) used magnetic resonance imaging to show that cerebral microvascular ischaemia was more common in NTG patients than normals. These sentiments of a vasospastic aetiology of glaucoma are echoed by Béchetoille (1996) who believes that conjunctival endoscopy may play a role in conjunction with ophthalmoscopy in assessing vascular spasm. Indeed local constrictions, aneurysms and dilations of conjunctival and perilimbal vasculature are said to be typical of patients with vasospasm (Orgül and Flammer, 1995). Aneurysms of conjunctival vessels (ACV) were assessed in 20 NTG, 20 POAG, and 60 non-glaucomatous normals. Patients with systemic hypertension, diabetes, uveitis, acquired immunodeficiency syndrome (AIDS), ocular vascular events, or eye surgery were excluded due to the possibility of vascular dysregulation. ACV were counted and graded by 2 observers, on 1 eye within 5mm from the limbus. Grades included none, faint (1-2 ACV), moderate (3-5 ACV), and copious (≥ 6 ACV). Differences in incidence were measured using a Kruskal-Wallis test, differences between groups were measured using a Mann-Whitney U-test. All ACV were observed in interpalpebral area or slightly below. Significantly higher copious ACV were found in the NTG group than POAG patients or controls, with the incidence in POAG patients being similar to controls (Orgül and Flammer, 1995). These differences could not be explained by climatic variations, age differences, nor medication regimes. The paper concludes that this maybe related to circulatory problems in NTG patients, but

alterations are not specific to glaucoma and have been reported in heavy smokers, arteriosclerotic or diabetic patients (Sakai *et al*, 1990). Interestingly, anterior ischaemic optic neuropathy (AION) is thought to be caused by occlusions of posterior ciliary arteries, due to arteriosclerosis, emboli or idiopathic in nature (Kaiser *et al* 1996). AION usually occurs in elderly patients but may occur in the young, ruling out arteriosclerosis and other risk factors. Five young patients (aged 12 to 44 years) with AION were extensively examined and showed vasospastic syndrome including cold hands, feet, low blood pressure, migraine, and abnormal conjunctival vessels. It was hypothesised that AION was due to local vasospasm. Vasospasm refers to reversible constriction of vascular smooth muscle cells without anatomical alteration. It is suggested that the diagnosis of vasospastic syndrome can be elucidated from a patient's history and validated by nailfold capillaroscopy, colour Doppler imaging, 24 hour blood pressure monitoring, and conjunctival capillaroscopy.

The success of glaucomatous bleb surgery is gauged by a minimal vascular response (Chew *et al*, 1994). Low-dose anterior segment fluorescein angiography was performed on 10 eyes before and after trabeculectomy surgery with a limbal based conjunctival flap. Post-trabeculectomy angiography in those with successful surgeries showed an area of decreased capillary perfusion over the bleb site. Hence, successful bleb surgery entails a limited healing response. Chew *et al* (1994) recommend fluorescein angiography as a method of determining the efficacy of surgery.

1.3.10 Effects of Sickle Cell disease and acquired immunodeficiency syndrome (AIDS) on conjunctival vasculature

Sickle cell disease is caused by a point mutation in the haemoglobin gene, causing sickle shaped red blood cells. Impaired microcirculatory blood flow leads to vaso-occlusive events which initiates ischaemic damage. McLeod *et al* (1993) found that vaso-occlusion of the peripheral retina caused areas of ischaemia, stimulating angiogenesis. Retinal angiogenesis occurs between perfused and non perfused retina, creating arteriovenous anastomoses, from which venous neovascularisation occurs in a characteristic 'sea fan' morphology. Traction causes schisis cavities, retinal detachment, iridescent spots, and haemorrhage. Microscopic studies of sickle cell diseased human retinae revealed unusual hair pin neovascular formations, and that vascular occlusion occurs at the precapillary level (McLeod *et al* 1993). Lieb *et al* in 1959 (cited from Paton, 1961) observed icterus, telangiectasis, vascular stasis, and sausage like dilations in bulbar conjunctival blood vessels in 22 out of 51 patients with Sickle cell disease. Paton (1961) believed that vascular stasis in bulbar conjunctival blood vessels, situated in the lower fornix, was indicative of this condition. Twenty three patients out of 99 Afro-Caribbean's with Sickle cell disease exhibited vascular stasis. A later study (Bachir *et al*, 1993) used a descriptive analysis of bulbar conjunctival blood vessels consisting of an itemised scoring system based on the assessment of arterial and capillary morphology, venous morphology, aneurysms, conjunctival tissue oedema, and subjective assessment of blood velocity flux. Each were scored from 0 (normal) to 2 (a character in the extreme) and summed to make a maximum of 10. However, this descriptive analysis failed to distinguish 11 Sickle cell patients from 100 normals.

Microvascular disease is also a frequent finding in patients with acquired immunodeficiency syndrome (AIDS) and other disorders associated with human

immunodeficiency virus infection (HIV) (Enstrom *et al*, 1990). Retinal lesions include cotton wool spots (focal ischaemia), haemorrhages, microaneurysms, and microvascular abnormalities. Such findings are similar to retinopathies found with diabetes mellitus, chronic myelogenous leukaemia, and systemic lupus erythematosus. Vasculopathy can also be found in conjunctiva of patients with HIV infection (Teich, 1987). Similar conjunctival changes occur in sickle cell disease, chronic myelogenous leukaemia, and ataxia-telangiectasia. Conjunctival biomicroscopic examination of 22 HIV patients subjectively graded for blood-flow sludging, based on the degree of granularity in blood column, speed of blood flow, presence, size and location of dilated limbal capillaries, microaneurysms, isolated vascular segments, and irregular calibres was performed (Enstrom *et al*, 1990). Conjunctival changes were found in all HIV patients, and were most prominent in the inferior perilimbal bulbar conjunctiva, similar to the findings of Paton (1961) observed with Sickle cell patients. The severity of conjunctival changes was associated with increased, red cell aggregation, fibrinogen levels, plasma viscosity, and elevated Ig G levels. The altered blood flow was thought to contribute to the observed vasculopathy. Similar findings were reported by Teich (1987), where 20 AIDS patients showed dilated, short, and curved conjunctival vessels. Vessels were globular or aneurysmal in configuration and exhibited comma like segments. Some arterioles were empty and grey in appearance and described as 'ghost vessels', similar to those seen in sickle cell and chronic granulocytic leukaemia patients. Findings suggest vaso-occlusion or ischaemia, similar to those advocated in sickle cell disease.

1.3.11 Conjunctival vessels in renal failure

Association between irritable red eyes, calcium deposits, and renal failure has been known for some 30 years (Klaassen-Broekema and van Bijsterveld, 1992). Klaassen-Broekema and van Bijsterveld (1992) recruited 57 patients with terminal kidney insufficiency, receiving regular haemodialysis, exhibiting deposition of calcium in the conjunctiva and corneal tissue, and monitored inflammatory complications of the anterior eye. Corneal / conjunctival calcium deposits were graded and levels of serum phosphate and calcium measured every 3 months, and compared to age matched normals (n=50). Inflammatory reactions were divided into 3 groups, 2 patients developed a brief episode of painful irritation and redness of the conjunctiva adjacent to erosions of the corneal epithelium as a consequence of exfoliation of their calcium concretions. Eight patients suffered from mild pingueculitis. However, 3 patients exhibited episcleral and conjunctival hyperaemia, which was waxy red, and diffuse in appearance, extending beyond the palpebral fissure. This latter group showed a significantly higher mean serum calcium concentration ($3.53 \pm 0.65 \text{ mmol/l}$) than patients with calcification without inflammatory signs ($2.49 \pm 0.28 \text{ mmol/l}$), and those with pingueculitis ($2.61 \pm 0.27 \text{ mmol/l}$) (ANOVA used but P values not quoted). Serum phosphate levels were significantly elevated in comparison to normals. It is suggested that 'red eyes of renal failure' be reserved for the waxy red type inflammation, which is associated with a disturbance of calcium metabolism resulting in high serum calcium concentration. It has been proposed that conjunctival precipitation of hydroxyapatite crystals may result in this inflammatory reaction mediated by enzymes liberated from polymorphonuclear leukocytes (PMN) (Klassen-Broekema *et al*, 1995). However, this 'suicide sac' hypothesis for conjunctival inflammatory reactions was rejected after histopathological examination of conjunctival biopsies failed to reveal

complement activation or crystal ingestion by PMN's despite the presence of small subepithelial hydroxyapatite crystals (Klassen-Broekema *et al*, 1995).

1.3.12 Conjunctival inflammation and hypersensitivity

The classic signs of inflammation include 'tumor, rubor, calor, and dolor'. In terms of conjunctival inflammation this is often described as oedema, hyperaemia, heat, and pain (Efron *et al*, 1988; Silbert, 1991; Ugomori *et al*, 1991). The association between 'rubor and calor' has been shown using ocular thermography and toxic challenge (Efron *et al* 1988). Conjunctival hyperaemia is commonly seen in inflammatory conditions such as conjunctivitis, episcleritis, uveitis (Phylactos, 1991), or in reactions to allergens (foreign bodies, contact lenses, etc.) or toxins (ophthalmic solutions, acids, alkali, etc.). It is the aspect of conjunctival hyperaemia which is of most interest within this thesis. Ocular inflammation first dilates blood vessels (Bron *et al*, 1985) allowing leakage of serum, C-reactive protein, immunoglobulins (Ig), macrophages, neutrophilic polymorphonuclear leukocytes, and lymphocytes into extra vascular spaces (Smolin, 1989). The inflammatory reaction is biphasic, with an immediate dilatatory response (maximal after 8-10 minutes), which levels off after a variable duration, mediated by histamine, or other mediators (plasmin activator factor). Histamine released from tissue mast cells (Bron *et al*, 1985; Stock *et al*, 1990) and Ig E sensitised basophils (Janssens, 1992; Stock *et al*, 1990), acts on H₁ and H₂ receptors causing vasodilation and increased permeability (Bron *et al*, 1985; Janssens, 1992; Stock *et al*, 1990). The sensation of itching is thought to be principally mediated by the interaction of histamine with H₁ receptors (Bron *et al*, 1985). Indeed, Janssens (1992) advocated that the interaction of histamine with H₁ receptors is responsible for vasodilation and itching seen in ocular allergy. By subjectively monitoring the conjunctival response in histamine provocation studies, the effects of levocabstine (a topical histamine H₁ antagonist) were found to significantly alleviate subjective symptoms of itching, and subjectively assessed redness, chemosis, lid oedema, and lacrimation. They suggest that one dose of levocabstine was more effective in preventing hyperaemia, lid oedema, chemosis, and tearing than 2 weeks of sodium cromoglycate four times a day. However, there is limited statistical and methodological data to support this statement. More recently elevated tear levels of plasmin activator factor (a polar phospholipid) have been implicated as a potent vasodilator (Berta *et al*, 1990). Elevated levels were observed by staining and spectrophotometric techniques in patients with corneal ulcers, superficial keratitis, superficial punctate epithelial erosions, recurrent epithelial erosions, band keratopathy, contact lens associated erosions, alkali burns, Mooren's ulcer, conjunctival pemphigoid, acute keratoconjunctivitis sicca, and corneal melanoma (Berta *et al*, 1990). Plasmin activator factor was found to be a potential mediator in hypersensitivity reactions, its effects are similar but thirty to forty times more potent than histamine (Stock *et al*, 1990). Eventually homeostasis is achieved and a second late stage of vessel dilation and increased permeability, allowing infiltration of blood elements (leukocytes, C-reactive protein, complement) is mediated by kinins and E-type prostaglandins (Williams and Peck, 1977; Bron *et al*, 1985). The phasic course of these inflammatory events has been demonstrated by Greiner *et al* (1985). Eye rubbing is known to cause conjunctival hyperaemia, hence, the upper lid of 20 rats were rubbed continuously for 5 minutes. Animals were sacrificed immediately post trauma, and after 4, 8, and 24 hours. Counts of mast cells, degranulated mast cells, inflammatory cells (eosinophils, neutrophils, lymphocytes, plasma cells, and

macrophages) were histologically recorded from upper lid. Immediately after eye rubbing conjunctival epithelium was histologically disrupted, 50% of the mast cells had degranulated. Four hours after a 2300% increase in the number of neutrophils was found, which had migrated into substantia propria and epithelium, and 24 hours post trauma a statistically significant increase in macrophages was observed. However lymphocytes, plasma cells, and eosinophils remained unchanged. A study by van Bijsterveld and Janssens (1981) showed high tear levels of serum albumin using radial immunodiffusion, in 17 patients with chronic keratoconjunctivitis sicca. It was proposed that the source of serum albumin was vascular because patients treated with calcium dobesilate (a synthetic angiotherapeutic agent used in vascular disorders such as diabetes mellitus) showed a reduction in conjunctival vascular permeability.

Inflammatory processes of the conjunctiva are complex and cannot be adequately described here. However, the importance of understanding this mechanism is paramount. The ability to monitor exact changes in vascular response will enable the time course of ocular allergy / inflammation to be studied in more detail and accounted for in terms of cellular changes. The efficacy of treatment modalities could be assessed more accurately instead of reliance on anecdotal subjective assessment.

1.3.13 Conjunctival effects of contact lens wear

Although a vast literature exists on corneal vascularisation associated with contact lens wear, the conjunctiva has received less attention. Bruce and Brennan (1990) conclude that 'superficial corneal vascularisation is one of the most common biomicroscopic signs associated with soft contact lens wear'. The mechanisms of corneal vascularisation have been extensively reviewed (Ashton and Cook, 1953; Cogan, 1949), especially in context of contact lens wear (Efron, 1987; McMonnies, 1983, Stevenson and Chawala, 1993). However, it is the vascular response of the conjunctiva to contact lens wear that we are most concern with. Holden *et al* (1986) studied the effect of chronic (69 ± 29 months) extended wear of soft contact lenses (SCL) in 27 monocular contact lens wearers. Subjective assessment of the extended wear SCL wearing eyes showed greater general conjunctival hyperaemia ($P < 0.001$, paired Student's *t* test), limbal hyperaemia ($P < 0.0001$), and limbal vessel penetration ($P < 0.001$) than non contact lens wearing eyes. Cessation of lens wear resulted in a reduction in general and limbal hyperaemia to baseline levels within 2 to 7 days. However, limbal vessel penetration was still significantly greater 33 days after cessation ($P < 0.05$). McMonnies and Chapman-Davies (1987a, 1987b) argued that assessment of conjunctival hyperaemia is associated with a large inter and intra-observer variation, which can often cloud the true effects of conjunctival challenge. Their paper advocates the use of a reference scale with 6 grades of hyperaemia. Fifty non contact lens wearers, 50 SCL wearers and 50 hard contact lens wearers were graded. Significantly less conjunctival vascularity was observed in the hard contact lens wearing group (mean grade 1.48 ± 0.814) compared to SCL wearers (mean grade 2.1 ± 0.953) ($P < 0.01$, Kruskal-Wallis one way ANOVA), and non contact lens wearers (mean grade 0.96 ± 0.669) had significantly less hyperaemia than SCL wearers ($P < 0.001$, Kruskal-Wallis one way ANOVA). Although the use of a photographic scale is said to be more repeatable than other subjective assessments of vascularity we argue that it is still associated with a large inter and intra-observer variation. This is discussed in more detail under the relevant heading. However, the increase in vascularity observed is in agreement with other findings.

1.3.14 Drug induced changes of the conjunctiva

The ocular compatibility of ophthalmic medications is often gauged by the conjunctival response after instillation. For the past 50 years, the ocular irritancy of new chemical products, including contact lens solutions, have been tested by placing high concentrations of the materials on the eyes of living animals and subjectively grading ocular damage at varying intervals (Sivak *et al*, 1995). Measuring the optical laser transmission of bovine crystalline lenses after exposure to ocular toxins has been suggested as an alternative (Sivak *et al*, 1995). However, exact quantification of conjunctival vasculature would enable ocular irritancy to be established on humans without exposing animals to unduly high concentrations of ophthalmic drugs. Obviously, minimal ocular irritancy is the goal with any ophthalmic medication. Villumsen and Alm (1989) studied the effect of prostaglandin $F_{2\alpha}$ - isopropylester eye drops on intra ocular pressure. Conjunctival hyperaemia was manually assessed using a pointwise counting technique where projected photographic images of the bulbar conjunctiva were overlaid with a 14×14 dot pattern. Dots in contact with vessels were counted to give a measure of vascularity. A dose dependant hyperaemia was seen 10 minutes after application, with doses of 0.1 to 0.5µg resulting in hyperaemia for 1 hour. This method was also used to compare the conjunctival vascular response to differing topically applied prostaglandin esters (Villumsen and Alm, 1990). The paper outlines the importance of conjunctival hyperaemia assessment, in determining the efficacy of ophthalmic medications. They concluded that de-esterfied prostaglandin preparations made no difference to the vascular response of the conjunctiva. Villumsen *et al* (1991) later rejected this method of vascular assessment, in favour of computerised edge detection of digitised vascular images, which showed a good correlation with laborious pointwise analysis ($R^2=0.92$). However as detailed in the relevant section the automated method although less labour intensive was far from perfect. Hence, in 1992 Villumsen and Alm used colour photographs to subjectively grade conjunctival vascularity on a scale from 0 to 3, to assess a new formulation for lowering intra ocular pressure (PhXA34). Using a parametric t-test statistical analysis on non-parametric data they found low doses of PhXA34 did not result in hyperaemia, and that doses in excess of 10µg caused slight hyperaemia. The paper recommended the use of PhXA34 in favour of prostaglandin $F_{2\alpha}$ - isopropylester which causes hyperaemia at all doses. Trew *et al* (1991) investigated the vasodilatory ocular effects of a α -adrenoreceptor blocking drug (bunazosin), used topically in the treatment of glaucoma. Conjunctival hyperaemia was assessed on a 0 to 3 subjective scale before and after drug administration. A Wilcoxon signed ranked test showed significantly more hyperaemia 10 minutes to 2 hours after administration compared to vehicle drops. Arend *et al* (1993) studied the vascular bed of temporal bulbar conjunctiva of 10 females using contraceptives (ethinyl estradiol) and 10 female controls, recorded on U-matic video tape through a direct light microscope (magnification ×300). Erythrocyte formation velocity through capillaries was calculated from frame to frame. Red blood cell velocity was assessed under normal and post ischaemic conditions, where ischaemia was induced by 7kPa (53mmHg) of pressure on the conjunctiva for 1 minute. Vessel diameter was not assessed due to apparent difficulties in deciding on the location of the vessel edge. Capillary red blood cell velocity was significantly lower in those taking contraceptives (35%, $P<0.05$, t test). In addition increases in haemocrit, plasma viscosity, erythrocyte aggregation, and spontaneous thrombocyte aggregation were reported in those using oral contraception.

They concluded that those taking ethinyl estradiol contraception might be at risk of microvascular pathologies.

The papers in this section show the importance of vascular measurement in the recommendation of ophthalmic drugs. The basis of subjective measurement is of dubious validity but offers a convenient form of assessment. Objective measurements would prevent inappropriate advice being given.

1.3.15 Miscellaneous factors effecting conjunctival vasculature

A diversity of vessel reactions are observed in the conjunctiva some of which are mentioned within this chapter, but not exhaustively. Carotid carvenous fistula typically occurs as a result of trauma or spontaneous rupture of an intracavernous carotid artery aneurysm (Wolansky *et al* 1997). Classically, patients present with sudden onset of pulsatile proptosis, with a marked engorgement or arterialisation of conjunctival vessels. Carotid carvenous fistula is a syndrome consisting of direct communication in the region of carvenous sinus with the carotid arterial system, involving the carvenous internal or dural branches of the internal carotid and / or external carotid arteries (Aburn and Sergott 1993). Congested dilated conjunctival vessels can also be associated with ciliary melanomas (Crawford, 1986).

Anaemia is said to give the conjunctiva a pink hue (Sanchez-Carrillo 1989). Anaemia results in a decrease in the oxygen carrying capacity per unit volume of blood (haemoglobin less than 10.0g/dl) and is non-specific sign of underlying disease. Sanchez-Carrillo (1989) examined 219 ambulatory patients, chosen at random, and classified their conjunctival hue as pink or red, where 'pink' was indicative of anaemia and 'red' normal. Haemoglobin levels were subsequently measured. Values between 7.0-9.9mg/dl were indicative of anaemia, and values above 10mg/dl were considered normal. A quarter of the test population were assigned with pink eyes (27.2%) while the remainder (72.8%) were normal. However, anaemia was detected in 5.4% of those classified as pink eyed, and 3.4% of 'normal red eyes'. Hence, subjective assessment of conjunctival hue cannot be regarded as a diagnostic or specific test of anaemia.

Familial amyloidotic polyneuropathy is a heterogenous collection of familial diseases characterised by systemic accumulation of amyloid fibrils in peripheral nerves and other organs (Ando *et al*, 1997). Amyloid deposit can be histologically recognised in the superficial propia of the conjunctiva and the wall / perivascular region of conjunctival vessels (Ando *et al*, 1997). In addition conjunctival vessel abnormalities are common with between 75.7% (n=28/37) to 86.1% (n=31/36) of patients with familial amyloidotic polyneuropathy showing angiopathy (Ando *et al*, 1997; Ando *et al*, 1992). Conjunctival vessel abnormalities include red spot, spindle, and 'spider like' vessel formations. However, 17.1% (n=48/280) showed these abnormalities in controls (Ando *et al*, 1992), but the difference in incidence was quoted as being statistically higher in the diseased group ($P < 0.001$, hypothesis test not specified). Other familial conditions such as Rendu-Osler-Weber syndrome, an autosomal dominant disease, and Louis-Bar syndrome, an autosomal recessive disease, cause telangiectasia of conjunctival blood vessels (Crawford, 1986). Sturge-Weber syndrome is a neuro-oculocutaneous disorder, typified by epilepsy, mental retardation, and neurological hemiplegia (Sullivan *et al*, 1992). Dermal effects typically include

port-wine stains. Ocular effects include glaucoma, vascular malformations of the conjunctiva, episclera, retina and choroid. Thirty five patients of 51 (69%) with this condition had conjunctival or episcleral haemangiomas (Sullivan *et al*, 1992).

Vascular abnormalities are frequently reported in lysosomal storage diseases (Libert and Toussaint, 1982). They include fusiform / saccular aneurysms of conjunctival vessels and tortuous retinal venules. However only 2 of 15 individuals with Fabry's disease (a deficiency in the enzyme α -galactosidase A) showed conjunctival aneurysms or venous tortuosity. These cases represented the 2 oldest (41,44 years) of the group measured and could merely indicate the effects of age.

The effect of cholesterol feeding in the rabbit model has been investigated using conjunctival capillary microscopy (Xiu *et al*, 1994). High resolution images of the lateral conjunctiva were evaluated by manually measuring segmental dilation, red blood cell aggregation, and stasis. Computer assisted digital image processing allowed microvessel diameter (using an unspecified autotracking method) and erythrocyte flow velocity (flying spot method) to be quantitatively measured. After 3 weeks of cholesterol feeding there was a dramatic decrease (30%) in blood flow velocity, in arterioles of the third order ($p < 0.0001$, parametric ANOVA), accompanied by aggregation of cells in 40-50% of microvessels ($P < 0.0001$, non-parametric ANOVA), and a decrease in measured arteriole diameter ($P < 0.005$, parametric ANOVA). These effects worsened after 7 weeks of cholesterol feeding. However, in a group where antioxidant (butylated hydroxytoluene) was used, such microcirculatory changes were avoided. Xiu *et al* (1994) conclude that a considerable part of the effects on microcirculation in hypercholesterolemia may be due to cholesterol induced oxidants and not cholesterol itself. They propose the use of antioxidants in the therapy and prophylaxis of atherosclerosis. An abstract by Stubiger *et al* (1995) investigated 285 patients with perilimbal alterations including vessel ectasia ($n=225/285$, 79%), aneurysms ($n=117/280$, 41%), vessel interruptions ($n=105/285$, 37%), and avascular zones ($n=34/285$, 12%), and compared them with 58 patients without conjunctival angiopathy. A higher incidence of peripheral vascular spasm, head aches, migraine, hypertension, vertigo, tinnitus, was found in the group with perilimbal vascular changes. Although there was no statistical basis for these conclusions they advocated internal medical examination for those with bulbar conjunctival vascular changes.

Conjunctival angiopathy has received less attention than its retinal neighbour. However, we have shown that conjunctival vessel examination is a valuable source of information in a variety of different contexts and diseases. Many believe that vessels in the conjunctiva are indicative of a systemic peripheral vascular circulation and hence are worthy of investigation. Anecdotal and subjective assessment of the conjunctival vascular network, although of use, could be enhanced by the application of image processing. This forms the subject of the following text.

1.4 Methods of quantifying vasculature

Numerous authors have used subjective gradings to quantify the extent of conjunctival vascularity (Bachir *et al*, 1993; Efron *et al*, 1988; Holden *et al*, 1986; McMonnies and Chapman-Davis, 1987a, 1987b; McMonnies and Ho, 1991; Trew *et al*, 1991; Villumsen and Alm, 1992) and conjunctival hue (Sanchez-Carrillo, 1989). Some authors have compared novel objective techniques of conjunctival vascular

assessment against subjective grades, in the absence of a 'gold standard' (Guillon and Shah, 1996; Willingham *et al*, 1995). More recently objective methods of quantifying conjunctival hyperaemia using computational techniques have emerged. However, automated methods of assessing conjunctival vasculature have received less attention than retinal vascular imaging. The reason for this lies with the known risk of visual impairment associated with retinal vascular compromise. In addition, image processing of coronary angiograms (Pappas and Lim, 1988) and vascular networks in the cochlea (Miles and Nuttall, 1993) are worthy of mention. Although these vascular beds differ in vessel characteristics the techniques of assessment can be divided into two generic methods: detection of vessel structure, or globally measuring vessels by redness. Both of these approaches will be discussed in this chapter.

One of the key parameters to obtain from any vessel is a measure of width as variations in width are indicative of vascular compromise. To accurately measure vessel width it is important to determine the local vessel direction and then determine the width as the perpendicular distance between edges of the vessel. This is illustrated in figure 1.3 which shows a point (x,y) on a conjunctival vessel (anterior ciliary artery), vessel direction, and width. The vessel direction shown in figure 1.3 is vertical but can be at any angle.

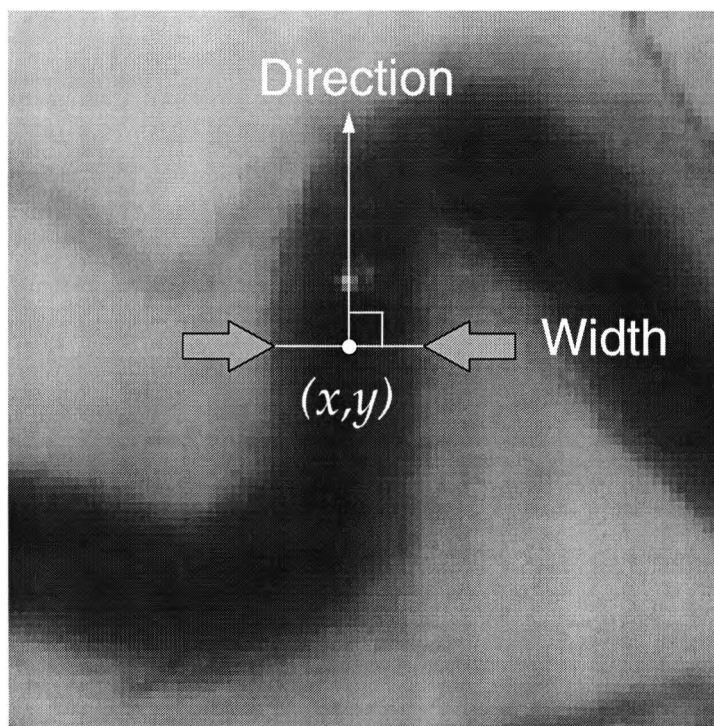


Figure 1.3 shows a point (x,y) on a conjunctival vessel, its direction, and the location where vessel width would be measured perpendicular to the vessels direction. Note that the width of the vessel shown is $100\mu\text{m}$.

There are a number of factors which confound the interpretation of a vessel's edge, which complicates the determination of width. Conjunctival vessels, for instance, exist in a three dimensional structure, hence when imaged in a two dimensional plane vessels change in contrast and become blurred along their length as they move anteriorly or posteriorly from the focal plane, hence, detecting edges is difficult. Vessels have an erratic, unpredictable path, and form random interconnections

(branches) in differing directions and angles. 'Normal' vessels have circular cross sections, however the vessel edges can vary significantly from the ideal due to optical distortions and blurring. Attenuations in contrast are not aided by imaging geometry, the bulbar conjunctiva exists as a semi-spherical surface, and directional flash, from the illumination turret of the photo slit-lamp, creates a non-uniform reflectance in the image. Direct reflections of a flash from the anterior tear layer are readily observed as brilliant patches in the image, which can mask underlying detail. Also the presence of iris, lids, and lashes introduce confusing structures. Because of these difficulties many papers utilise subjective grading to give an overview of vascularity to negate direct measurement of width.

1.4.1 Subjective methods of assessing vascularity

As quoted by Bailey *et al* (1991) 'the use of numeric scales to grade the severity or advancement of clinical signs is becoming widespread'. Instead of descriptive terminologies such as incipient, slight, moderate, mild, and severe, numeric scaling or grading systems are often used. However, problems of grading include whether the grades are too coarse or too broad. In addition it is difficult to discern whether scale increments are of equal steps or will be sensitive enough to identify an expected clinical effect.

Photographic reference scales have been used to aid subjective assessment of conjunctival vascularity in contact lens wear (McMonnies and Chapman-Davis, 1982; Terry *et al*, 1993) and are increasing in popularity. The assessment of conjunctival hyperaemia is associated with a large inter and intra observer variation (McMonnies and Chapman-Davis, 1987a, 1987b). McMonnies and Chapman-Davis (1987a, 1987b) used a reference scale with 6 grades of hyperaemia. The inter observer agreement measured with a Spearman P coefficient was 0.62 (t-test $P < 0.01$), and intra observer agreement 0.83 (t-test $P < 0.001$) for 19 observations. However, this approach is not considered a good way to study agreement (Bland and Altman, 1986; 1995). Hence we have reanalysed the data using the preferred method of Bland and Altman (1986, 1995) using the raw data quoted for session 1 and session 2. Inter observer agreement gave a mean difference of 0.056 between grades with a 95% confidence interval of +1.113 to -1.001, intra observer agreement gave a mean difference of -0.222 with a 95% confidence interval of +0.616 to -1.061. Hence, unless there is at least 1 grades difference between 2 successive examinations of conjunctival hyperaemia, it is likely to be statistically similar. However, this grading system showed statistically significant differences in conjunctival vascularity between contact lens wearers and those not wearing contact lenses. Although the 95% confidence limits of agreement are large, Bailey *et al* (1991) advocate that established grading systems can be made substantially more sensitive by finer scaling. However, if the degree of expected change is small, and likely to fall within the 95% confidence interval, differences are unlikely to be found.

The effects of diabetes on conjunctival vessels were considered to be small, and are unlikely to exert an effect on general vascularity. Vascularity measurements do not attempt to quantify vessel characteristics such as changes in calibre or tortuosity. Subjective determination of vessel area is also prone to the possibility of observer bias, hence, objective methods were considered more suitable. However, objective determination of vessel area is again unlikely to reveal useful data.

1.4.2 Objective methods of assessing vascularity

Objective assessment of conjunctival vascularity has been attempted by number of authors. Fenton (1980) exposed images of the lateral bulbar conjunctiva to film, under red-free (green) illumination, at a magnification of $\times 3$. This was exposed to print at a magnification of $\times 40$. Peripheral distortions on the print, caused by imaging a semi spherical surface, were ignored, by only considering the central 11mm^2 of print. Vascularity was estimated using a grid overlay and a well known stereological equation shown below, where N_T = number of intersections between vessels and grid, M = total magnification, L_T = total length of grid lines, L_A = estimate of vessel area.

$$L_A = \frac{\pi \times N_T \times M}{2 \times L_T}$$

However, this method was labour intensive, and suffered from the errors associated with 2 photographic developments. This method was used by Worthen *et al* (1981) to study the effects of diabetes on conjunctiva as indicated in a previous section. A similar pointwise method was used by Villumsen and Alm (1989) to study the effects of Prostaglandin $F_{2\alpha}$ - isopropylester eye drops on conjunctival hyperaemia. Film negative images of temporal bulbar conjunctiva were projected on to a screen at a magnification of $\times 25$. A square 14×14 dot overlay, with dots 1.5mm in diameter and 1cm apart was used to count the number of dots in contact with vessels. Differences between counts in eyes treated with Prostaglandin $F_{2\alpha}$ - isopropylester eye drops and vehicle drops were used to estimate drug induced hyperaemia. However, the paper comments on the tedious, and time consuming nature of this assessment. These methods also require considerable interpretation by the observer as to whether a vessel intersects with the 'point' used. For points incident on the centre of a vessel there is little difficulty, however, once the target nears the vessels edge so the interpretation of whether they are incident or not becomes more subjective and less certain. These labour intensive methods are tedious, hence, more recent attempts at vascular assessment have become more automated.

1.4.3 Automated methods of determining vascularity

Chen *et al* (1986) took photographic negatives of the lateral bulbar conjunctiva under red-free (green) illumination, with a film plane magnification of $\times 4.5$. Photographic prints, magnified to $\times 10$, were digitised to 128×128 pixels (equivalent to an object space of 6.7cm^2), averaged, and subtracted from the original to eradicate background illuminosity gradients. Images were then thresholded to achieve a binary representation of vasculature and the surround to give a percentage vessel area. Owen *et al* (1996) used a similar method. Photographic images of the dextro temporal conjunctiva were captured using a Nikon FS-2 photo slit lamp with a Xenon flash tube filtered with a Wratten 35 (purple) filter, on Ilford HP5 monochrome film. A purple filter was used to optimise vessel contrast (Palmer *et al*, 1996). Images were digitised using a Polaroid SprintScan 35mm Slide Scanner. A square region of interest (ROI) immediately lateral to the limbus (equivalent to 17mm^2 of object space) was manually selected tangential to the limbus. Images were scanned to an 8 bit, 256 grey level, 336×336 pixel square, at a resolution of 133 dots per inch. The image was repetitively averaged fifteen times (using a 3×3 pixel square) and then subtracted from the original image averaged once, similar to the pre-processing methodology of Chen *et al* (1986),

in photographic terms this method is called un-sharp masking. Spatially averaging in a repetitive sequence will smooth all high contrast gradients, such as vasculature, leaving low contrast gradients of the background relatively unchanged. When this is subtracted from an image averaged only once, the high contrast gradients (vasculature) remain. This is a well known phenomenon of image processing and tends towards Gaussian smoothing, and is similar to a Laplacian operator, and is often termed a difference of Gaussian (DOG) filter. This will be demonstrated in a later section. A frequency histogram of grey levels contained within the image was plotted. A bimodal histogram, with 2 grey level maxima, representing vessels and the scleral surround, would have enabled a minimum histogram value between the 2 mentioned maxima to be found, which would give optimal image segmentation. However, the distribution was multimodal and an arbitrary threshold for binary segmentation (10% below the peak grey level) was used to delineate between vasculature and the surround. As with Chen *et al* (1986) the decision of where to threshold the image will greatly effect vascularity, and hence is a major drawback of these techniques. This is demonstrated by the large 95% confidence limits for inter session repeatability which are +8.58% (+1.46mm²) to -3.95% (-0.67mm²) for the 17mm² of conjunctiva assessed. However, this method showed sufficient sensitivity in detecting increased hyperaemia in a RGP contact lens wearing group compared to a non lens wearing and SCL wearing. Villumsen *et al* (1991) abandoned their pointwise counting system (Villumsen and Alm, 1989) on the basis of time consumption and adopted an automated method. Colour transparencies were digitised to 512×480 pixels. The image was grabbed 8 times and averaged to reduce noise. A ROI (300×270 pixels) was averaged (using a 3×3 pixel square), and a simple 3×3 edge detector applied. Again a threshold was determined, and the image converted to a binary image, allowing vascular area to be measured. This method was shown to give a good correlation with pointwise analysis ($R^2=0.92$). However, the paper acknowledged errors with identifying vessels with blurred edges, edges of specular reflection were recorded as vessels, and despite averaging the background was often far from uniform.

Willingham *et al* (1995) used colour video images obtained using a Nikon FS-2 photo-slit lamp to measure hyperaemia induced with 0.5% dapiprazole hydrochloride, and hyporaemia with 2.5% phenylephrine hydrochloride. Using dedicated software a region of interest (ROI) was selected from the image (640×480 pixels) equivalent to 3.8 cm² in object space, which was automatically masked to exclude specular reflections, lashes, lids and non-illuminated regions. The red (R), green (G), and blue (B) colour content of each pixel was extracted. For each colour the intensity ranged from 0 (darkest) to 255 (brightest). The total intensity (I) of a pixel was the sum of the RGB components. Mean relative redness (RR) was calculated for each pixel from the ratio of the intensity of R to I. The measure of RR was the sum of these ratios divided by the number of active pixels multiplied by 100. This type of colour image analysis, using normalised colour space, is a well known imaging method.

To compute vessel area (VA), red free images (G) were selected on the basis of superior contrast. Five Gaussian spatial filters (standard deviation {SD} 1, $\sqrt{2}$, 2, $2\sqrt{2}$, and 8 pixels) were applied. Subtracting severely blurred images from originals compensates for illuminosity gradients. Vessel and non-vessel areas were manually labelled. A selection of densitometric profiles spanning vessel borders were modelled by multivariate Gaussian densities. These models were then used to isolate vasculature

over the ROI. Random sampling revealed 6% of pixels described as vessels were artefacts. In the absence of a 'gold standard' RR and VA area were compared with subjective gradings of hyperaemia, giving Pearson correlation coefficients of 0.98 and 0.99 respectively. A similar method was used by Wilkins *et al* (1996) but images were obtained by exposing images of the bulbar conjunctiva directly onto of a charged couple device (CCD) digital camera, avoiding the need to digitise the film. Cox (1994) bestowed the financial virtues of video analogue imaging and a video capture board (frame grabber) over direct CCD imaging. However, this financial argument is no longer valid.

Subjective, objective, and automated approaches to determine vascularity have been shown to be of use in a variety of clinical contexts. However, as indicated, the effects of diabetes on vasculature is unlikely to cause an overall change in vascularity, but to effect the morphological and morphometric properties of a vascular bed. Hence, determination of vessel characteristics must include more appropriate determination of width and tortuosity. The use of edge detection minimises global intensity variations, which global thresholding methods are always sensitive to, hence edge detectors were considered as a more appropriate method of segmenting vessels from their surround and will be discussed later.

1.4.4 Manual techniques of assessing vessel width

Unlike general assessment of conjunctival vascularity Guillon and Shah (1996) attempted to manually determine vessel width at referenced locations from the limbus. Digitised video images were viewed on a PC and after pseudocolouring to enhance the perception of vessels; the limbus was manually selected. Lines were drawn at 1 mm intervals from the limbus, and blood vessel width along each reference line was manually estimated using the mouse to mark vessel edges. However, this method did not correlate with subjective assessment of vascularity (graded 0 to 5 in 10 steps). The 95% confidence interval was quoted as being between 8.9 to 12.6 μ m (16.7 to 22.8%). This was the mean and 1.96 \times SD of 10 measurements of vascularity taken from 5 patients, and did not use the preferred method of Bland and Altman (1986). However, the paper reports greater vascularity in the morning and evening compared with during the day for SCL wearers ($P=0.048$, Turkey's multiple comparison's test), and non contact lens wearers ($P=0.014$).

Early methods on retinal vessel width determination involved: viewing photographic images via projection and using callipers to directly measure width (Hodge *et al*, 1969; Eberli *et al*, 1979; Behrendt, 1966), viewing through a microscope with a micrometer eyepiece (Hodge *et al*, 1969; Griffith *et al*, 1974), or using an image splitter to assist visual determination of a vessels edge (Bracher *et al*, 1979; Wilson *et al*, 1981). To quantify accuracy it is often the mean coefficient of variation which is quoted. It has been well argued that this is an inferior method of assessing agreement and gives no information about the association over a range of values (Bland and Altman, 1986; Bland and Altman, 1995). The coefficient of variation can often give spurious levels of accuracy depending on the location which is repeatedly measured, the number of measures, and the number of locations. Newsom *et al* (1992) projected photographic images of retinal vasculature onto a graphic digitising table allowing manual measurement of vessel width. They quote a coefficient of variation of 6 to 34% and also give the 95% confidence interval of measurement as being between

+14.6 to -27.1 μ m, based on the analysis of Bland and Altman (1986). Hodge *et al* (1969) and Bracher *et al* (1979) believed vessel width measurement, was best achieved using a travelling microscope and subjective interpretation of the vessels edge. However, large inter-observer differences were found, and 'apparent blood vessel width is dependant on focusing, resolution of the {imaging} optics, {film} exposure and development' (Bracher *et al*, 1979). Hodge *et al* (1969) advocate that vessels were manually measured 11 to 22% larger when measured during fluorescein angiography, indicating that vessel contrast can alter the subjective determination of width. Unfortunately the accuracy of all of these methods was not documented. However from the selection presented there is a great deal of variation in the reported accuracy.

1.4.5 Semi-automated densitometric techniques of determining width

Subjective determination of a parameter is open to observer bias and individuals may differ considerably in their interpretation of a particular measurement. Observers vary in their determination of vessel edge when assessing retinal vasculature, and are reported to overestimate the true width (Griffiths *et al*, 1974; Delori *et al*, 1977; Newsom *et al*, 1992; Suzuki, 1995). Hence densitometric methods, based on the intensity distribution of light perpendicular to a vessel direction, have become the main form of measurement. One difficulty in any densitometric assessment of width is to obtain the intensity profile perpendicular to a vessels direction. This is often achieved by manually taking densitometric profiles perpendicular to the perceived vessel direction.

A number of differing interpretations of the densitometric profile exist. The width taken at the densitometric half height is most commonly used to quantify retinal vasculature (Behrendt, 1966; Bracher *et al*, 1979; Chen *et al*, 1988; Chen *et al*, 1994; Dumskyj *et al*, 1996; Eaton and Hatchell, 1988; George *et al*, 1990; Griffiths and Hill, 1974; Hill and Crabtree, 1984; Hodge *et al*, 1969). Others describe vessel width as the distance between points of maximum gradient on the densitometric profile (Da-Ching *et al*, 1995; Suzuki, 1995). Difficulty arises with these methods in deciding local maxima / minima along the profile, especially when localised vascular light reflexes, background reflectance changes, and/or small signal-to-noise ratios exist. Figure 1.4 typifies the range of densitometric profiles across retinal arteries and veins obtained from a digital image of the fundus. Densitometric profiles were obtained by manually estimating vessel sections perpendicular to the vessels direction (acquired using Matlab for Windows © Version 4.2c1). Veins appear darker than arteries because deoxygenated haemoglobin absorbs more light than oxygenated haemoglobin (Manivannan *et al*, 1994). In addition arterial walls absorb less light (0.145 at 570nm) than venous walls (0.149 at 570nm) helping arterial walls to appear lighter (Flower *et al*, 1978). The presence of the central light reflex (especially for retinal arteries) and non-uniformity of vessel background confounds the apparent ease of attaining the width at the intensity half height or maximum gradient. Intra and inter retinal vessel differences in reflectance are well known. Bracher *et al* (1979) believe that this is due to differences in retinal pigment epithelium, blood filling of the choriocapillaries, and haemoglobin saturation, as well as imaging artefacts. Some authors have rejected densitometric analysis since it does not overcome the difficulty of locating boundaries between a vessel edge and retinal background (Hodge *et al*, 1969; Bracher *et al*, 1979). However, others believe that a substantial amount of information can be

gleaned from the intensity profile of a blood column, including the central light reflex (Brinchmann-Hansen and Engvold, 1986; Brinchmann-Hansen and Heir, 1986; Brinchmann-Hansen, Heir and Myhre, 1986; Brinchmann-Hansen, Myhre and Sandvik, 1986). An increase in the intensity of the central light reflex on both arteries and veins has been reported in older age groups (Brinchmann-Hansen, Myhre and Sandvik, 1986), and can be indicative of atherosclerosis, resulting in optical changes in the vessel wall.

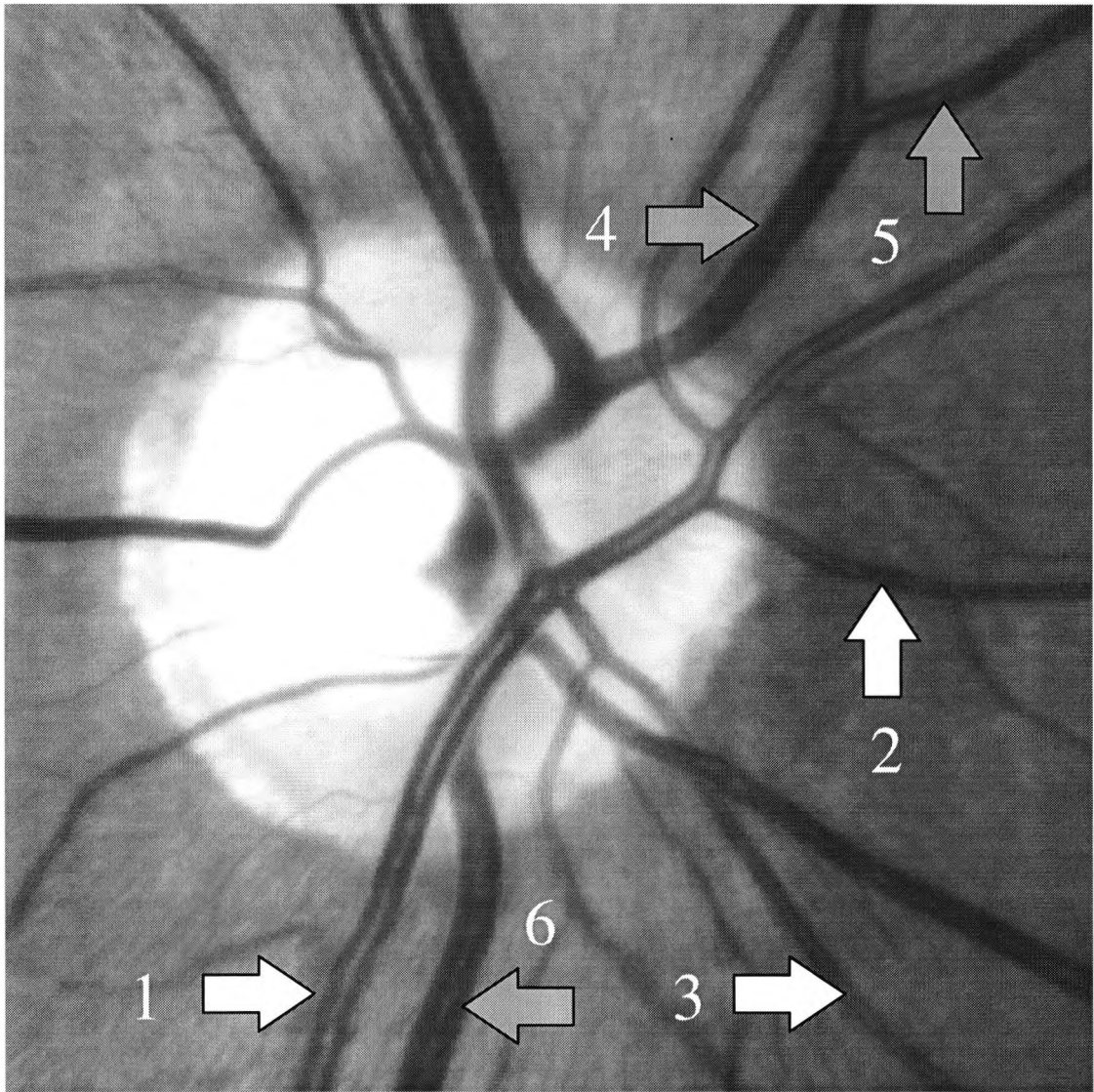


Figure 1.4 (a) shows a digital camera image of the vasculature emanating from the optic nerve head. Thinner, lighter vessels represent branches of the central retinal arteries, and thicker, darker vessels branches of the central retinal vein. White arrows (numbered 1 to 3) show the location where densitometric profiles were measured perpendicularly across arteries, and grey arrows (numbered 4 to 6) across veins.

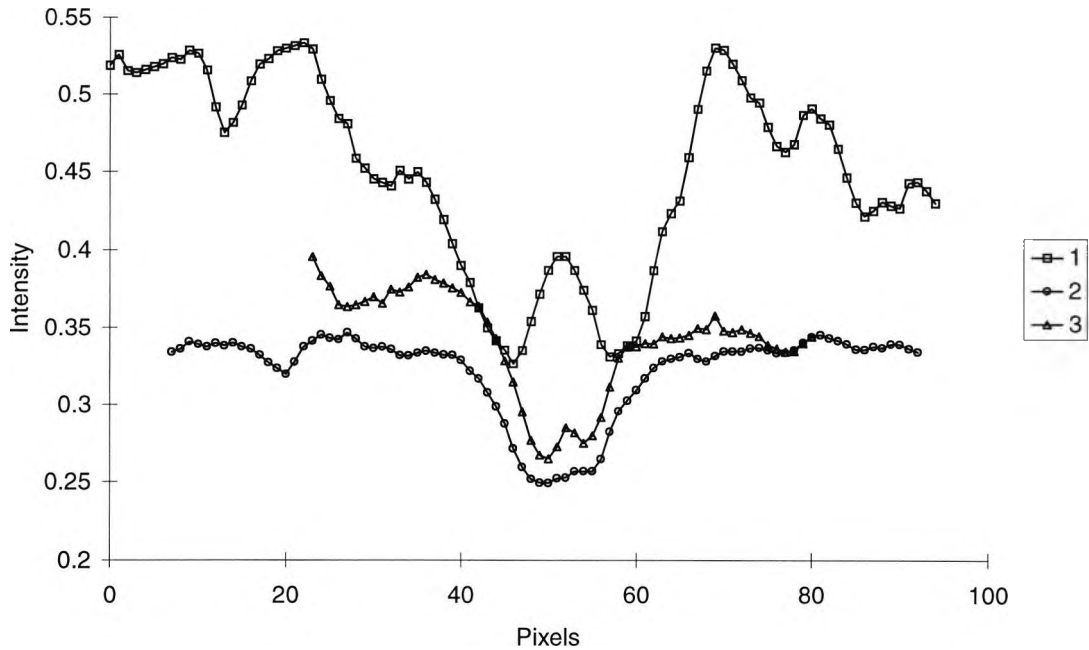


Figure 1.4 (b) shows densitometric profiles measured perpendicularly across arteries (1 to 3). Note the magnitude of the central reflex for profile number 1.

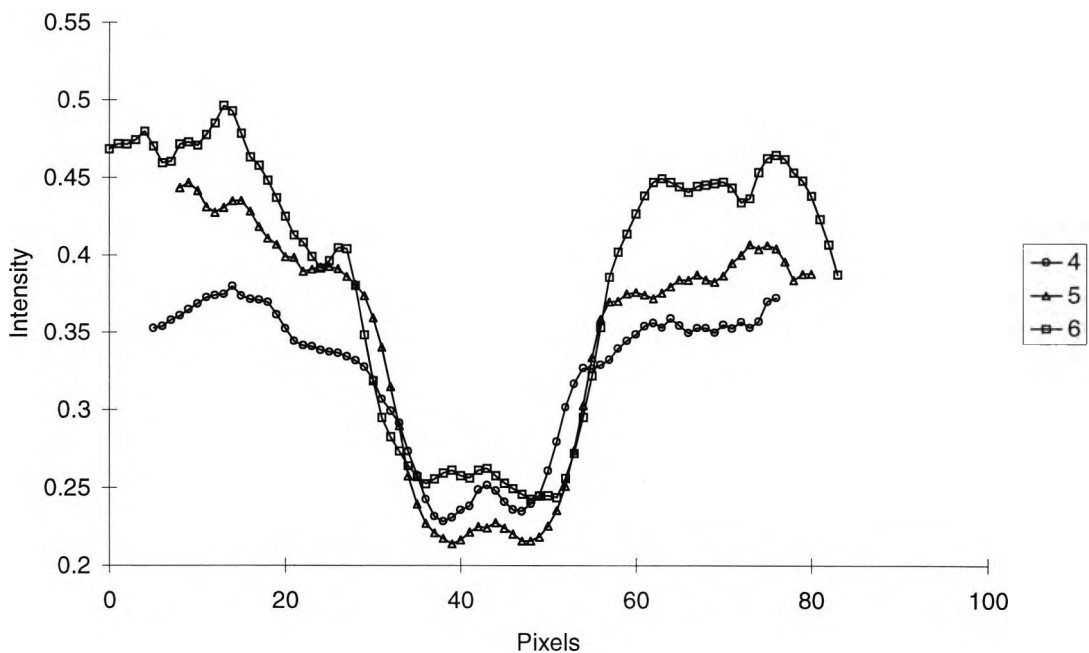


Figure 1.4 (c) shows densitometric profiles measured perpendicularly across veins (4 to 6). Note the presence of the central reflex is less marked than those found on some of their arterial neighbours.

The central reflex is rarely seen on conjunctival vessels indicating that its presence on retinal vessels may be related to the relationship between the refractive indices of vessel wall and vitreous. Figure 1.5 typifies the range of densitometric profiles across conjunctival vessels obtained from a digital image of the conjunctiva. Densitometric profiles were obtained by manually estimating vessel sections perpendicular to the vessels direction (acquired using Matlab for Windows © Version 4.2c1). Evidently,

there is a large intra conjunctival vessel variation in densitometric shape, and inter vessel variation when compared to retinal vessels. Densitometric profiles of deeper vessels (location 3 and 4) appear Gaussian in shape, explained by the blurring effects of overlying tissue, whilst those more anterior (location 1 and 2) appear to give a near cylindrical profile. Determination of width would appear easier on vessels with sharp edges (location 1 and 2), than estimates of deeper vessel blurred edges (location 3 and 4).

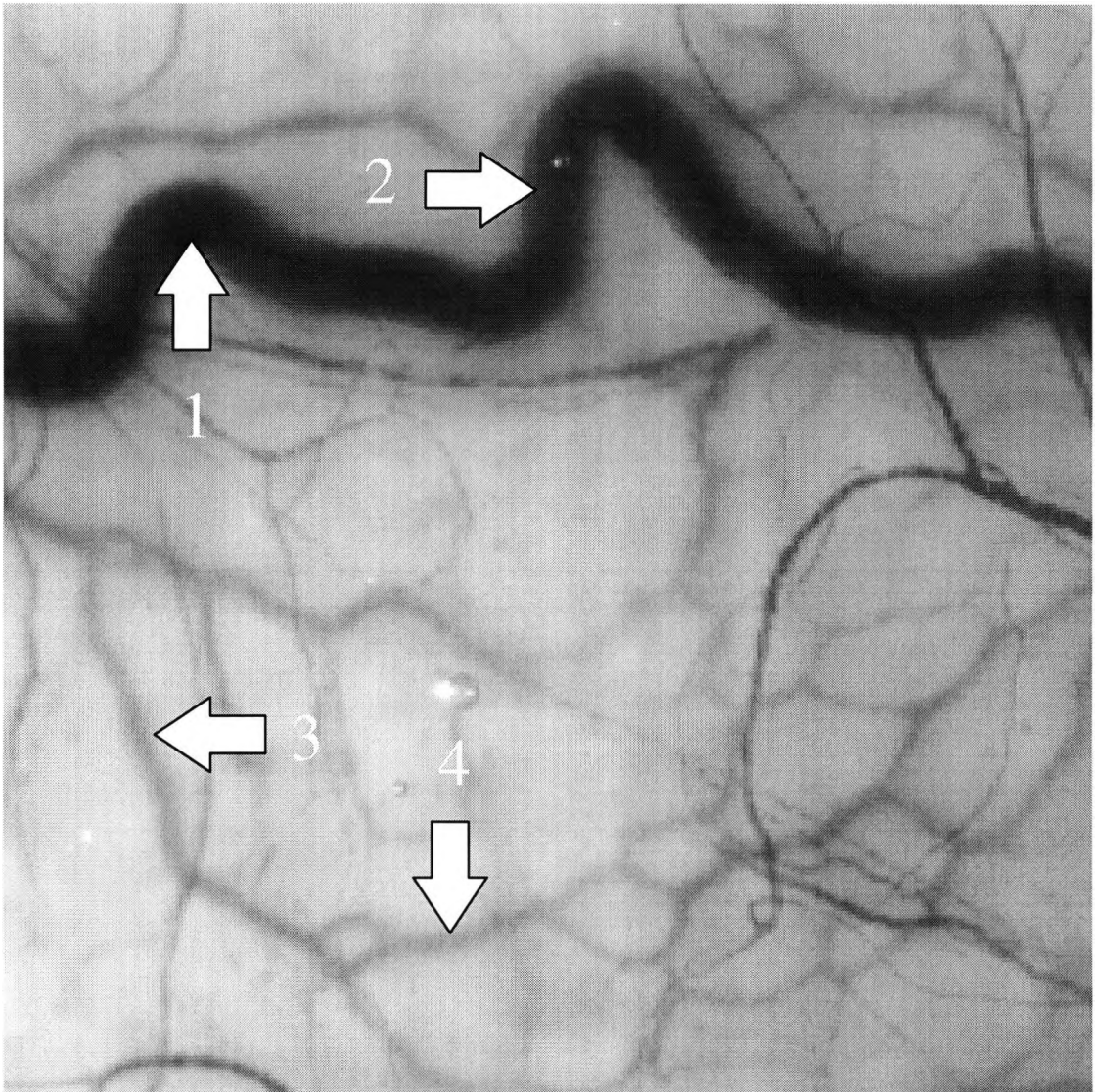


Figure 1.5 (a) shows a digital camera image of vasculature on the conjunctiva. White arrows (numbered 1 to 4) show the location where densitometric profiles were measured and are shown in figure 1.5 (b). Locations 1 and 2 were measured perpendicularly across an anterior ciliary artery, 3 and 4 across conjunctival venules or arterioles. The image represents 300 pixels² equivalent to 1.6mm² of conjunctiva.

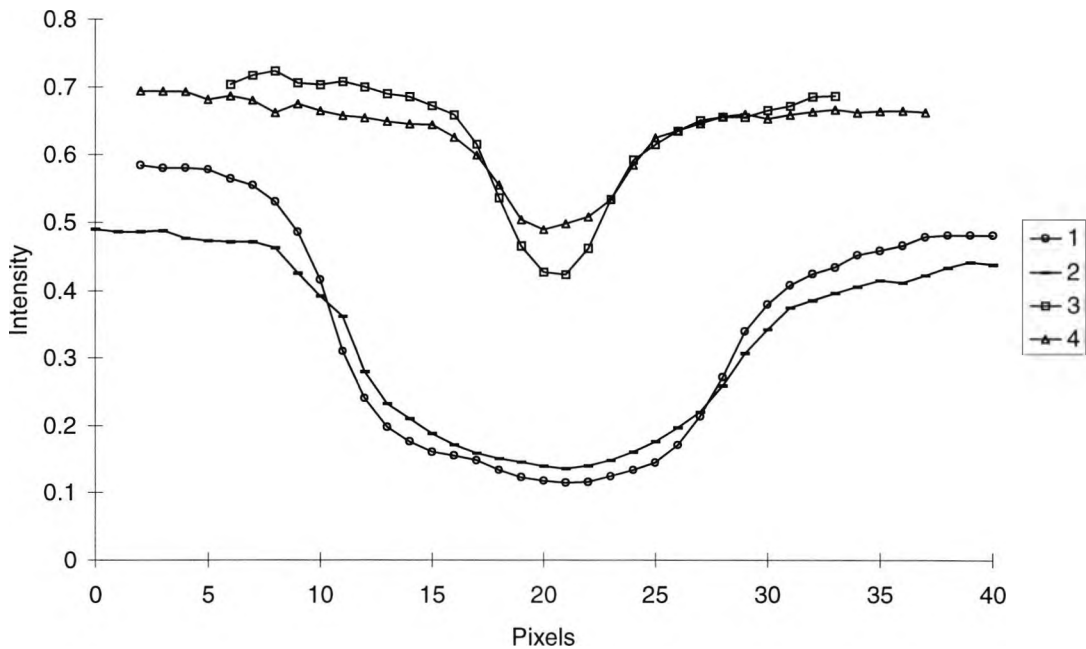


Figure 1.5 (b) shows densitometric profiles measured perpendicularly across conjunctival vessels (1 to 4). Note that the central reflex evident with retinal vessels is absent. One pixel is equivalent to $\sim 5\mu\text{m}$ in object space.

The absence of the central light reflex on conjunctival vessels enables the intensity minima, at the centre of the vessel, to be estimated more easily. However, the presence of background differences in illumination confounds the decision as to the appropriate intensity level of the surround.

Despite these inadequacies, determination of the densitometric half height vessel width has been used in a variety of contexts, to quantify vascular changes. Figure 1.6 shows how the densitometric half height width is obtained from a densitometric profile across a conjunctival vessel.

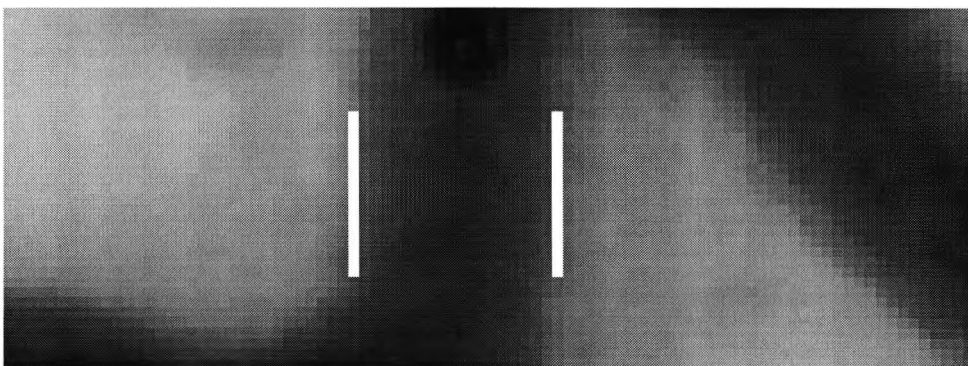


Figure 1.6 (a) shows a digital image of a conjunctival vessel. A horizontal densitometric profile across this vessel is shown in figure 1.6 (b). The densitometric half height width is shown between the vertical white lines (width = 18.91 pixels $\approx 100\mu\text{m}$).

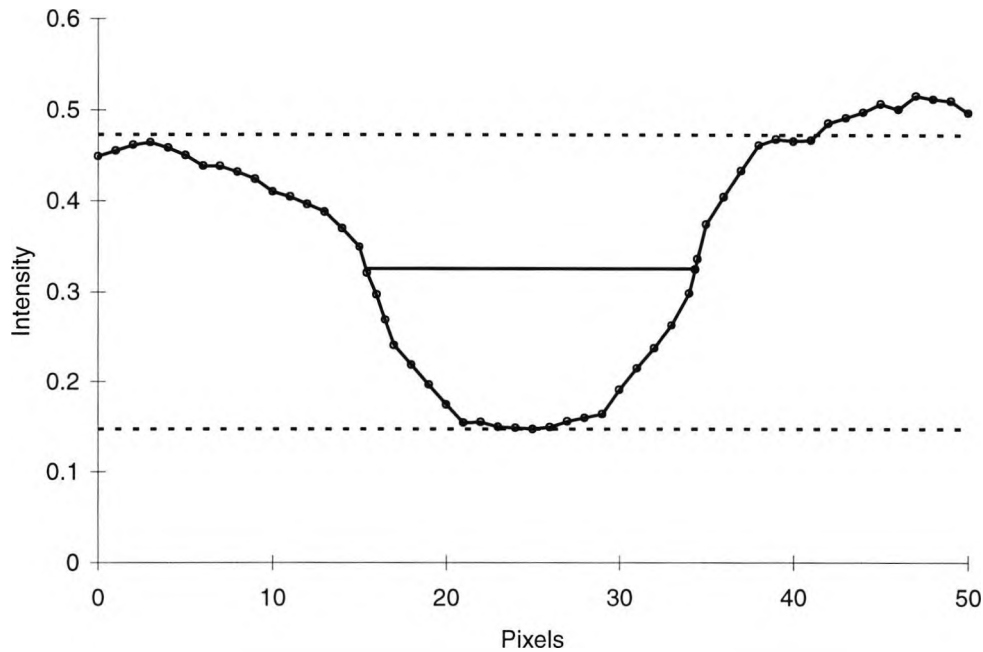


Figure 1.6 (b) shows a densitometric profile taken across the vessel shown in figure 1.6 (a), the upper dashed line is the mean background intensity, the lower dashed line the minimum intensity value recorded near the centre of the vessel. The horizontal solid line marks the position of the half height width.

Chen *et al* (1988) digitised green filtered photographic images (high contrast, Technical Pan Film, Kodak) of the fundus to 512 by 512 pixels. The camera shutter was synchronised with the electro cardiogram of 10 normal subjects. Three neighbouring intensity profiles were measured perpendicular to a referenced retinal vessels direction for each of the 8 images recorded during a cardiac cycle. The mean densitometric half height width of the 3 profiles was measured and ranged from $143.04 \pm 25.23 \mu\text{m}$ at one eighth after the R wave (early systole) to $149.93 \pm 27.95 \mu\text{m}$ five eighths after the R wave (early diastole). An analysis of variance revealed that these changes were statistically different ($F=4.98$, $P=0.0002$, $df=7$). This method was also used to study retinal vasculature in pregnant females with diabetes (Chen *et al*, 1994), and Dumskyj *et al* (1996) who found that retinal vessel width increased by 1.4% after isometric exercise, and decreased by 5.4% after breathing 100% oxygen.

Eaton and Hatchell (1988) quoted the mean coefficient of variation of densitometric half height vessel width determination, manually selected from digitised photographic images, as 0.45% for measuring the same vessels on separate days (40 vessel locations, from 20 fluorescein angiograms of cat retina), and 0.24% for measuring 40 vessel locations on the same day. They concluded that such methods are able to detect $1 \mu\text{m}$ changes in diameter. George *et al* (1990) digitised black and white negatives of human retinal vessels, taken under red-free illumination, and found that the coefficient of variation of densitometric half height width measurement ranged from 1.2 to 3.4%, with a mean of 2.2%, for 10 repeated measures of 6 vessel locations from 3 individuals. This is considerably more than the figure published by Eaton and Hatchell (1988). Suzuki (1995) found a similar coefficient of variation to George *et al* (1990) of $1.28 \pm 0.73\%$ for 38 intra session measures of width, and $4.04 \pm 4.61\%$ for 38 inter observer measures of width. However, neither of these methods use the Bland and

Altman (1986) method of inter and intra session repeatability. Re-analysis of the densitometric raw data published by Griffiths *et al* (1974) using data from session 1 and 2 only (ignoring session 3) for 14 measurements of width, showed an intra session repeatability mean difference of $3.21\mu\text{m}$, with a 95% confidence interval of $+16.86$ to $-10.43\mu\text{m}$. An inter method comparison of densitometric and manual micrometry methods, for 35 vessel locations, from 3 images, showed a mean difference of minus $9.74\mu\text{m}$, indicating that manual methods may overestimate in comparison to densitometric methods, with a 95% confidence interval of $+23.32$ to $-42.80\mu\text{m}$. Newsom *et al* (1992) measured the half height widths at 12 vessel locations (each measurement being the mean half height of 12 neighbouring parallel densitometric slices). The coefficient of variation ranged from 1.5 to 7.5%, more importantly the 95% confidence limit of intra session repeatability was $+3.2$ to $-6.0\mu\text{m}$. Evidently there is a great deal of variation in the quoted accuracy of these similar techniques. Newsom *et al* (1992), like the others mentioned above, used digitised photographic images and concluded that the true 'half height width of the intensity pattern corresponds more closely to vessel width than the half height width on film density'. Hence, this may explain the large variation in the repeatability of results, although this could also be related to the selection of vessel sizes measured, and the differing number of vessels measured. Rassam *et al* (1994) also believed that the characteristic photosensitivity curve of photographic film is likely to alter half height measures of width. Newsom *et al* (1992) advocated the use of a CCD camera where the response to light is linear unlike the 'characteristic curve' response of photographic film, and the input is direct, negating the need for subsequent film digitisation. Spencer *et al* (1992) state that an 'image should be acquired directly to avoid numerous non-linearities inherent with photography which can diminish the quality of the measurement'. Suzuki (1995) was amongst the first to use a 512 pixel digital array, which compared favourably with half height and mouse driven determinations of vessel width obtained from photographic digitisation.

As indicated densitometric half height width is associated with a number of inadequacies, and is often a difficult measure to obtain. Rassam *et al* (1994) considered that a hypothetical vessel could be described by 2 concentric circles, the inner circle representing the blood column and the outer circle the vessel wall. Anatomically, the thickness of an arterial wall is one sixth that of the blood column width, and the venous wall one tenth the width of the blood column (Williams *et al*, 1989). Hence, the presence of apparent kick points demarcating the blood column from a vessels wall were predicted. Monochrome film negatives images of retinal vessels were taken, and densitometric profiles were measured perpendicular to the perceived vessels direction. The presence of 'kick points' or inflections in the profile were shown, and the distance between them recorded as the vessels width. These measurements were compared to conventional half height measurements. Using densitometric profiles from tubular models of known width they concluded that the distance between kick points over estimated width by 0.34 to 1.4%, while half height measures under estimate by 6.46 to 7.33%. Monochrome digitised fundus images of retinal vessels revealed that half height determination of vessel width was between 15.86% (for arteries) and 16.67% (for veins) less than widths obtained between kick points. This paper concludes that kick points are rarely seen and are difficult to locate, hence despite the possibility of underestimation half height procedures are a more practical measure of width. Figure 1.7 shows the densitometric profile taken from

figure 1.6, across an anterior ciliary artery. The densitometric half height width is shown, and the vertical arrows indicate the observers interpretation of Rassam's 'kick points' which demarcates the reflective profile of the blood column from that of the vessel wall. Note that the densitometric half height width is 18.905 pixels (100 μ m), whilst the 'kick point' width is 23 pixels (122 μ m). Hence for this arterial example half height width is 17.8% less than 'kick point' width in agreement with retinal arterial findings (Rassam *et al*, 1994).

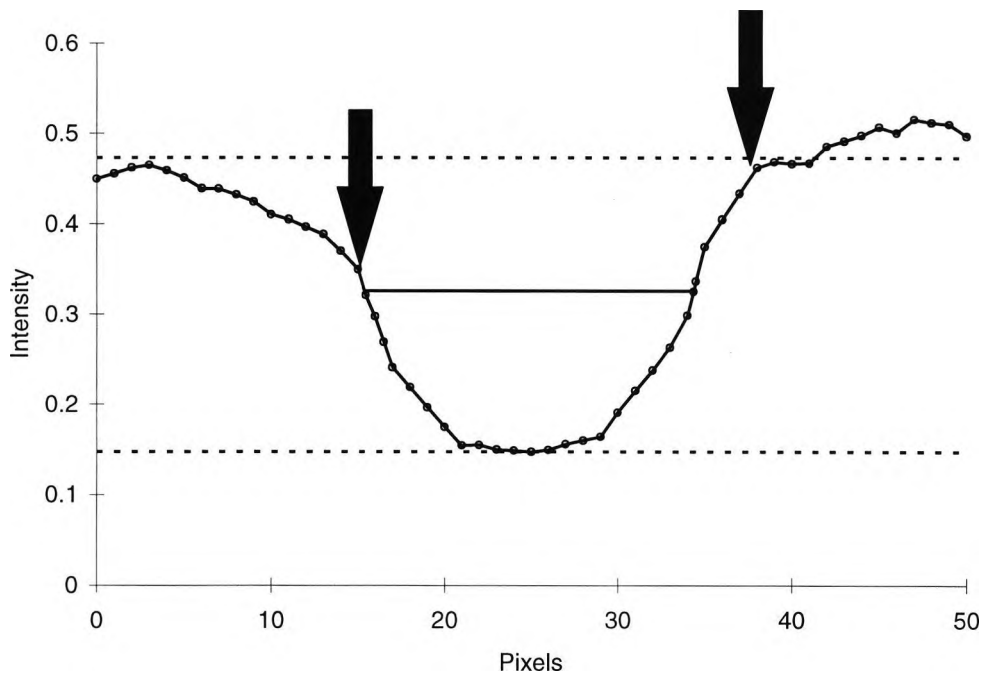


Figure 1.7 shows the densitometric profile taken from figure 1.6, across an anterior ciliary artery. The densitometric half height width is shown by the horizontal solid line, and the vertical arrows indicate the observers interpretation of Rassam's 'kick points'.

Densitometric profiles have also been modelled over their entirety using different shapes, to allow a global interpretation of vessel width. Formaz *et al* (1997) digitised green filtered black and white negatives of the fundus (Kodak TMAX 400) to 3072 \times 2048 pixels. Non tortuous vessels were rotated vertically and a series of 40 consecutive horizontal densitometric profiles (100 pixels long) were averaged. This densitometric average was fitted with a rectangular function by a least squares method. Pixel widths between rectangular edges were recorded as vessel width. This enabled a statistically significant $4.2\pm 2.2\%$ increase in arterial diameter ($P < 0.014$, 2 way ANOVA) and a $2.7\pm 1.7\%$ increase in venous diameter ($P < 0.0001$) to be found in response to a 10Hz flicker stimulus. Breathing 100% oxygen for 5 minutes resulted in a decrease in both arterial and venule diameters with a reduction of $10.1\pm 5.4\%$ and $11.6\pm 2.6\%$ respectively. Clearly fitting a rectangular function to the type of densitometric profiles shown in figure 1.5 (b) is far from ideal. The rapid development of image processing, especially edge detection, has lent itself to image segmentation of blood vessels and forms the subject of the next section.

1.4.6 Automated methods

Manual methods or those requiring operator control are time consuming, tedious, subjective, and not conducive to a large patient study. Hence the holy grail is to obtain fully automated image segmentation, which performs edge detection, identification of correct pairs of points on either side of the vessel, and measures the distance between them. Before discussing the numerous automated approaches of vascular imaging, a brief overview of the rudiments is needed.

A digital image is described as a function $f(x,y)$, m pixels wide and n pixels deep. Each pixel has a particular grey level value, hence, an image is often described by a matrix.

$$f(x,y) = \begin{bmatrix} f(0,0) & f(0,1) & \dots & f(0,m-1) \\ f(1,0) & f(1,1) & \dots & f(1,m-1) \\ \vdots & \vdots & \ddots & \vdots \\ f(n-1,0) & f(n-1,1) & \dots & f(n-1,m-1) \end{bmatrix}$$

Image analysis can be divided into a number of steps, image acquisition, pre-processing, and segmentation. Image pre-processing involves enhancement of contrast and removal of noise. Examples of pre-processing steps include grey level histogram processing, image subtraction, spatial filtering, image smoothing, averaging, or sharpening. Segmentation refers to the process of performing foreground / background separation, and is the first step in identifying regions of interest in the image. In our case image segmentation refers to the extraction of vessels from their surround. Note that there is a trade off between spatially averaging to reduce noise and the ability to localise the object of interest. If an image is smoothed too aggressively the ability to segment foreground from background will effect accuracy.

Edge detection plays an important role in a number of image processing applications and form a collection of important local image processing methods used to locate discontinuities in image luminance. Note that an edge is a local property of a pixel and its immediate neighbourhood, it has a vector given by a magnitude and direction. If an image is considered as a function then an edge is defined as pixels where this function changes abruptly, hence edge detectors are sometimes referred to as gradient operators because of what they compute. Gradient operators as a measure of edge sheerness can be divided into 3 categories: mask operators which approximate derivatives of the image function, operators based on the zero crossings of the images' second derivative, and operators which attempt to match an image function to a parametric profile. The top profile of figure 1.8 shows an idealised densitometric intensity function across a vessel in one dimension (based on those shown in figure 1.4 and 1.5). If this is considered as a function then the first differential will give the middle profile where 'inflection points' correspond to the maximum gradient of the vessel's edge, and second differential gives the position of the zero crossing points which correspond to 'inflection points' of the first differential, and maximum gradient of the vessels edge.

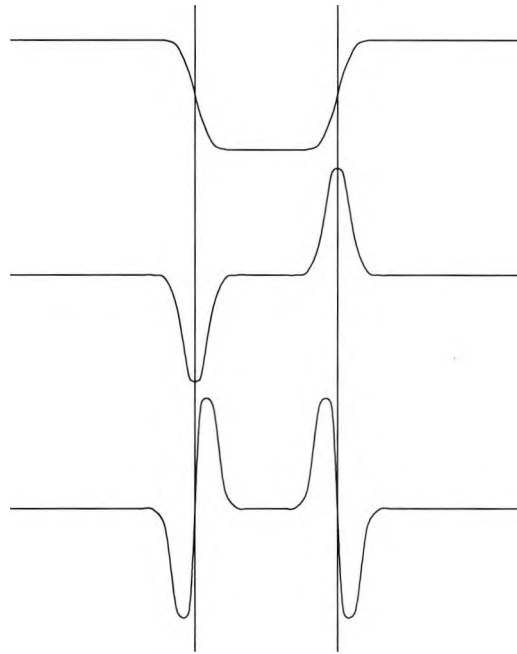


Figure 1.8 shows 3 profiles where the top is a densitometric intensity function of an idealised vessel, middle the first differential, and bottom the second differential. Vertical lines show the zero crossing point of the second differential, inflection points of the first differential, and maximum gradient on the vessels edge.

Differential operators are increasingly sensitive to noise, as their order increases. This is caused by using spatial filtering to suppress noise. Well designed filters suppress noise without changing the location of the edge gradient.

The first and second derivatives of an image function can be estimated in a number of ways. Mask operators offer an approximation to the derivative of an image function. The simplest type of differential operator, the Robert's operator, was introduced some 30 years ago (Chaudhuri *et al*, 1989). The Robert's operator is a 2×2 convolution kernel, whereas Prewitt and Sobel operators are 3×3 . Chaudhuri *et al* (1989) investigated the use of Sobel operators on smoothed images (using a 5×5 averaging filter) of retinal vasculature and concluded that their use was restricted to the detection of sharp edges, hence, they are not suited to vessel boundary gradients. Despite this their use is widespread in both retinal and conjunctival vascular imaging (Villumsen *et al*, 1991).

The application of a Laplacian operator gives an approximation to the second order derivative of an image function and can be implemented in its simplest form using a 3×3 mask. Figure 1.9 (a) shows the mask configuration and the application of the mask to the raw image given in figure 1.9 (b), to give figure 1.9 (c). However this simplification is unacceptably sensitive to noise (as shown in figure 1.9 (c)). A more general use of the Laplacian is in finding the location of edges using its zero crossings property. This concept is based on convolving an image with the Laplacian of a 2 dimensional, symmetric Gaussian function which combines edge detection and noise suppression. Chaudhuri *et al* (1989) developed convolution masks (16×15), which unlike the Laplacian operator were orientation specific. Twelve large convolution

masks at 15° intervals were used and gave superior performance at detecting retinal vessels than a Laplacian operator.

$$\begin{pmatrix} 1 & 1 & 1 \\ 1 & -8 & 1 \\ 1 & 1 & 1 \end{pmatrix}$$

Figure 1.9 (a)

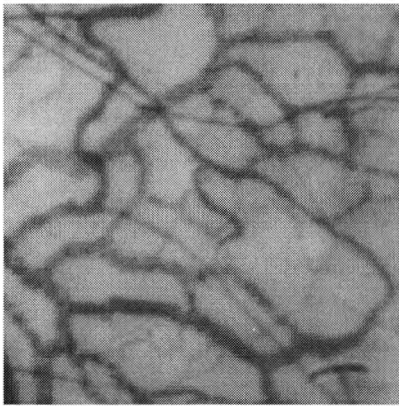


Figure 1.9 (b)

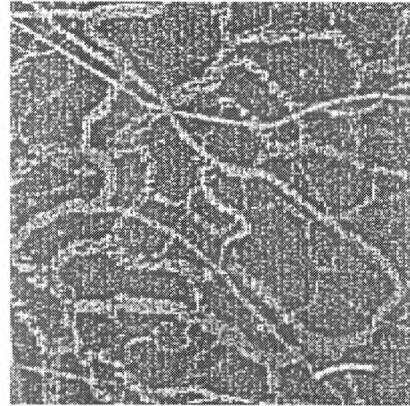


Figure 1.9 (c)

Figure 1.9 (a) shows the configuration of a simple Laplacian mask and its application to the raw conjunctival image shown in figure 1.9 (b), to give the image in figure 1.9 (c).

Gaussian smoothing kernels are a well proven method of estimating the derivatives of noisy functions, where vascular images are a prime example. The Gaussian kernels are given by the equations below.

$$g_{\sigma}(x) = \frac{1}{\sqrt{2\pi}\sigma} e^{-\frac{x^2}{2\sigma^2}} \quad \text{Gaussian function}$$

$$g'_{\sigma}(x) = \frac{-x}{\sqrt{2\pi}\sigma^3} e^{-\frac{x^2}{2\sigma^2}} \quad \text{First derivative}$$

$$g''_{\sigma}(x) = \frac{x^2 - \sigma^2}{\sqrt{2\pi}\sigma^5} e^{-\frac{x^2}{2\sigma^2}} \quad \text{Second derivative}$$

As indicated the positions of vessel edges are given by the maxima of the first differential or the zero crossings of the second differential. Tamura *et al* (1988) used fundus photographs digitised to an 8 bit, 512×512 pixel image. Detections of retinal blood vessels were made by convolving the second order derivative of the Gaussian function with the cross sectional profile of the blood vessel. From the convoluted profile the width of blood vessels was estimated from the zero-crossing point interval. Blood vessels were traced by performing this convolution at repeated intervals.

Tamura *et al* (1988) point out that correct sigma (σ) selection is paramount. High sigma's increase noise suppression but lead to over estimation of vessel width. Unduly low sigma's do not adequately smooth noise and lead to under estimation of vessel width and the detection of spurious detail. With prior knowledge of a hypothetical vessel width Tamura *et al* (1988) found that the zero crossing interval gave a good approximation of width when the σ value was $\times 0.6$ of the vessels' calibre. Steger (1998) considered the case in 2 dimensions where the maxima of any curve linear structure, such as a road or vessel, must have its gradient determined in a direction perpendicular to its path. By convolving an image with discrete 2 dimensional Gaussian partial derivative kernels the direction in which the second directional derivative takes on its maximum absolute value is used as the correct vessel direction. This gives the correct edge locations unless the curvature of the vessel is very high compared to σ , in which case the width will be underestimated. Steger (1998) found that the detected edges of a structure can never move closer than σ to the real edge position, hence, for instance the width of narrow vessels will be overestimated. Steger (1998) also points out that the position of a structures edge (e.g. vessel edge) will be wrong whenever the contrast is significantly different on both sides of the structure being measured. This is particularly true of conjunctival vessels where the asymmetry in the densitometric profile across vessels is shown in Figure 1.5. As the asymmetry increases so the line and edge positions are pushed towards the side with the smaller edge gradient. Failure to model the surroundings of a vessel will result in large errors in the estimated vessel position and width, hence Steger encompasses solutions to this problem within his algorithm. Tamura's (1988) use of the zero crossing interval will yield the position of a vessel edge with only pixel accuracy. Steger (1998) uses a second order Taylor polynomial to convolve the Gaussian derivative output, allowing sub pixel determination of width. By using a linking algorithm edge points are extended into lines representing vessel boundaries. Steger has applied his algorithm to a variety of images containing vessel like structures. Figure 1.10 shows the analysis of roads from aerial images before and after bias removal caused by profile asymmetry. Its application to a coronary angiogram in figure 1.11 offers the nearest equivalent to our application. This approach negates the need for operator intervention. The algorithm is self propagating and does not require the manual selection of a start and finishing point on a vessel.

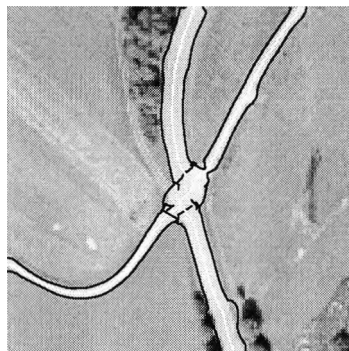


Figure 1.10 (a)

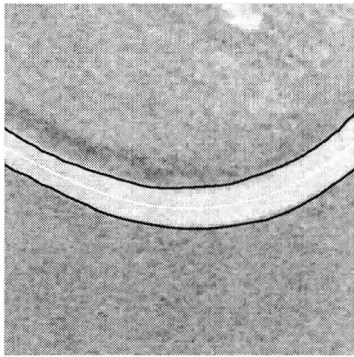


Figure 1.10 (b)

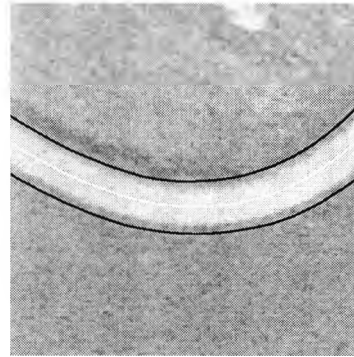


Figure 1.10 (c)

Figure 1.10 shows lines and their width detected (a) in an aerial images of resolution 1m with the bias removed. A $\times 4$ enlarged detail (b) superimposed onto the original image of resolution 0.25m and (c) comparison to the line extraction without bias removal. (From Steger, C. {1996}. An unbiased detector of curvilinear structures. Technical Report FGBV-96-03. Forschungsgruppe Bildverstehen (FG BV), Informatik IX, Technische Universität München, Figure 16).



Figure 1.11 (a)

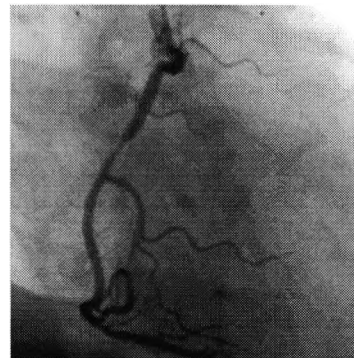


Figure 1.11(b)

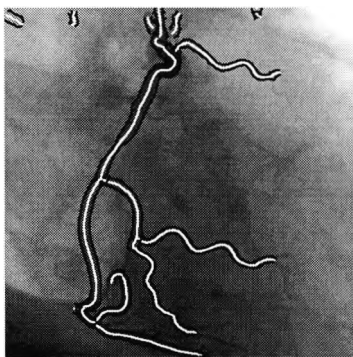


Figure 1.11 (c)

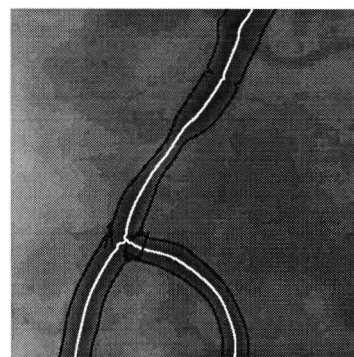


Figure 1.11 (d)

Figure 1.11 shows lines detected in a coronary angiogram (a). Since this image has very low contrast, the results (c) extracted from (a) are superimposed onto a version of the image with better contrast (b). A magnified ($\times 3$) image of (c) is displayed in (d). (From Steger, C. {1996}. An unbiased detector of curvilinear structures. Technical

Report FGBV-96-03. *Forschungsgruppe Bildeverstehen (FG BV), Informatik IX, Technische Universität München, Figure 20).*

Chaudhuri *et al* (1989) observed that densitometric profiles, across retinal vessels, were similar to a Gaussian curve, given by the following equation, where d is the perpendicular distance between the point (x,y) and the straight line passing through the centre of the blood vessel, σ defines the spread of the intensity profile, A is the grey level of the background, and k is a measure of reflectance of the blood relative to its neighbourhood. These parameters are shown in figure 1.12.

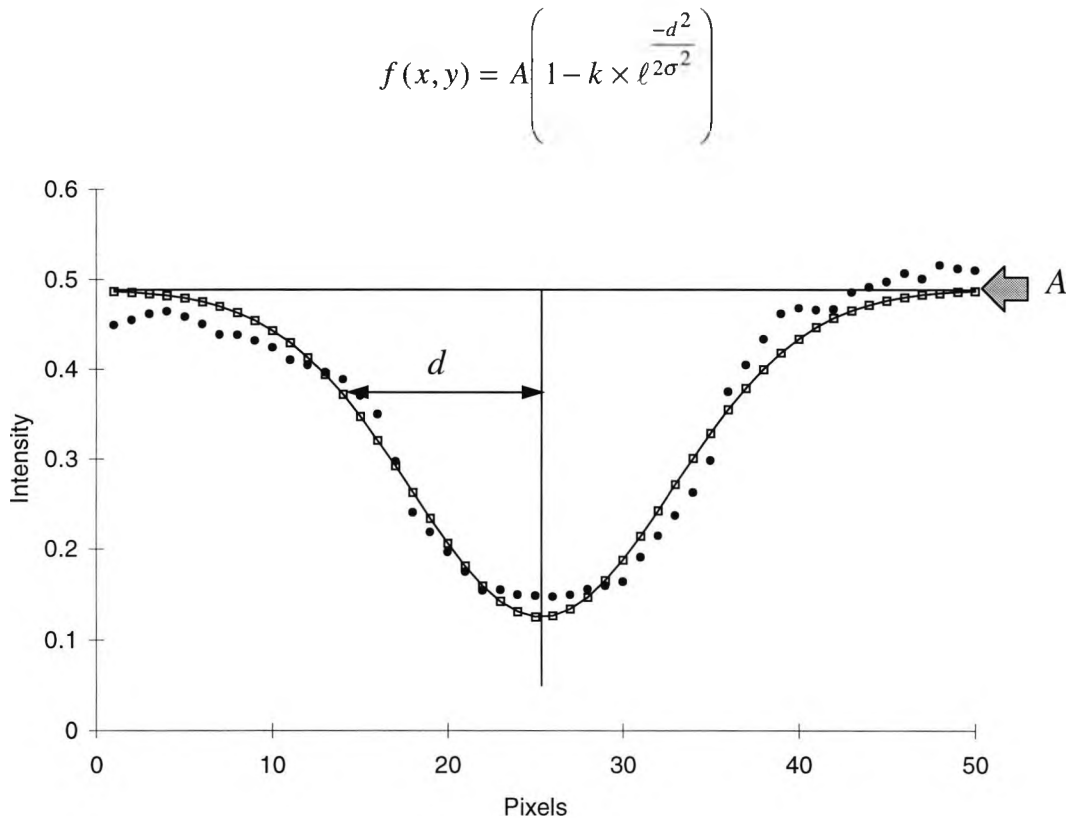


Figure 1.12 shows a densitometric profile of a conjunctival vessel (closed circles) with a least squares fitted Gaussian curve (open squares), where A is the background intensity, and d is the perpendicular distance between the point (x,y) and the straight line passing through the centre of the blood vessel. The Gaussian curve shown has a $\sigma = 7.53$ pixels and is given by the equation above.

A model based edge detector based on a Gaussian shape was derived. When this matched filter is extended to a 2 dimensional image, it must be appreciated that a vessel may be orientated at any angle ($0 \leq \theta \leq \pi$). The matched filter will have its peak response only when it is aligned at an angle $\theta \pm \pi/2$. Therefore the filter was rotated for all possible angles and only the maximum response retained. Vessels were considered as piecewise linear segments. Instead of matching a single intensity profile to the cross section of a vessel, a significant improvement was achieved by matching a number of cross sections (of identical profile) along its length simultaneously. Although the images published in this paper did show good performance without the

need for operator intervention, no means of quantitative analysis was presented i.e. widths were not measured.

Zhou *et al* (1994) also believed that a retinal blood vessel cross section could be approximated by a Gaussian shaped profile. Using an adaptive iterating procedure a retinal tracking algorithm was derived. The amount of iteration was proportional to the tortuosity of the vessel being tracked where increased tortuosity lead to fewer iterative steps. A photographic image was digitised to a 16 bit, 1024×1024 pixelated image. A least squares Gaussian curve was fitted to iterative densitometric profiles obtained at 90° from the vessels direction. As with Chaudhuri's paper a start point and end point on a vessel was manually selected. However, Zhou *et al* (1994) also measured vessel widths as $\pm 1.96 \times \sigma$ of the Gaussian fitted profile. Knowing the straight line distance between the manually selected start point and finish point along a vessel and the distance along the vessels centre line as measured by the iterative tracking algorithm, a 'curvature index' based on chord to curve length ratio was derived. Pappas and Lim (1988) believed that inflection points (extremes of the first derivative) equivalent to the zero crossing point of the second differential are close to what the eye perceives as the vessel edge. However their investigations of coronary angiograms led them to fit elliptical models to the densitometric profile of vessels using a least squares procedure. Unlike other computationally expensive methods of modelling a vessel's background using regression lines, they use a low order polynomial. Alas this method proceeds iteratively and requires the manual input of a start and finishing point. Interestingly the need to model the surround was negated by Shmueli *et al* (1983) who used image subtraction of coronary angiograms before and after fluorescein angiography to give a uniform background. Pappas and Lim's (1988) method was successfully implemented on high resolution SLO fundus images to demarcate retinal vessels from their surround. Miles and Nutall (1993) also observed that the densitometric profile of blood vessels in the cochlea were elliptical in shape. Gaussian blurred elliptical profiles were fitted to smoothed images which had undergone image smoothing with a 3×3 averaging filter followed by a truncated 3×3 Gaussian filter. A least squares fit between the blurred cylindrical profile and smoothed data was obtained iteratively from a manually selected start point and finish point. Iterative steps were completed at pixel (1.06µm) intervals in the direction of the next brightest pixel (indicative of the vessels centre). The densitometric profile used was taken perpendicular to the vessels direction.

Our initial studies on the conjunctiva will be mentioned in this section as it was our first attempt to apply some of the above methods to this type of vascular bed (Owen, Ellis, and Woodward, 1998). Filtered black and white negatives (Palmer *et al*, 1996) of conjunctivae (magnification ×3.11) were digitised to 512×512 pixels. A 'ravine finding algorithm was used to find local minima in the grey level image which defined the axis of a vessel. Edges were localised using a standard edge detector (Canny, 1986; Deriche, 1990), which performs Gaussian smoothing, gradient based edge detection, non-maximum suppression of proximal edges, and finally hysteresis thresholding. The Canny operator is widely used in computer vision, and its capability for accurate edge location and good detection performance are well known. Gaussian smoothing, with smaller σ sizes, produces an enhanced performance of the Canny edge detector. However, this is at a cost of the detection of spurious noise. Points

detected by the ravine finding algorithm were processed with a connectivity labelling algorithm, which linked adjacent pixels into strings, defining segments of the vessel. At each ravine point the orientation of the vessel was estimated by using a least squares filter on 7 adjacent ravine points. Tracking perpendicularly from the centre point outwards in both directions allowed the detection of the blood vessel boundaries using the previously extracted vessel edges. Genuine blood vessels are distinguished from other noise and artefacts in the image by recognising (within a given tolerance) symmetric pairs of boundary points. The use of a connectivity algorithm was used to enable spurious detail to be ignored. The performance of this approach was satisfactory except for the ability to detect small faint vessels and the incorrect detection of spurious noise at lower σ levels. The algorithm did not reliably extract long lengths of vessel, though it was able to measure a large number of short vessel segments. Similar investigations carried out by the authors using Steger's (1998) algorithm gave superior performance. Hence our initial method, although useful, was abandoned. Experience revealed that image optimisation, to improve contrast, considerably enhances the performance of image segmentation. In addition the use of digitised photographic film is associated with a number of exposure related artefacts. Image optimisation forms the subject of chapter 3.

1.4.7 Applications of automated vascular imaging

The application of image segmentation to vascular structures allows quantitative assessment which supersedes the inadequacies of subjective grading. An example lies in the assessment of vessel tortuosity, where the Steger algorithm (1998) gives a series of subpixel co-ordinates of a vessels axis, which can be analysed using dedicated software to give more accurate vascular indices. Vessel meandering forms the subject of chapter 4, where alternatives to the conventional chord versus curve length ratio are proposed using the output of Steger's algorithm. Automated determination of vessel edges also allows vascular areas and width changes to be monitored without the need for time consuming and tedious manual estimation. Other applications include the work of Spencer *et al* (1992) who derived matched filters to describe retinal microaneurysms. Fluorescein angiograms of 6 diabetic fundi were recorded to photographic film and digitised to a 512×512 pixel square. Microaneurysms were described by 2 dimensional Gaussian filters, where microaneurysms in sharp focus had sigma's between 0.5 to 1.5, and those of poorer focus had sigma's between 2 to 4 pixels. However, automated detection of retinal microaneurysms compared poorly against a manual 'gold standard'. The paper concludes that photographic images must be scanned to a higher resolution (1024×1024 pixels) to give an ROC performance similar to the gold standard. The paper reiterates the inadequacies of using photographic film and recommends that images should be recorded digitally. Recent work (Gardner *et al*, 1996) has employed the use of back propagated neural networks in the detection of diabetic features. Red free fundus photographs of the posterior pole of 200 diabetic patients with retinopathy and 101 normals were digitised to a 700×700 pixel square. Each image was divided into smaller 30×30 and 20×20 pixel elements. Detection rates for the recognition of vessels, exudates, and haemorrhages were 91.7%, 93.1% and 73.8% respectively. When compared to the performance of an ophthalmologist the network achieved a sensitivity of 88.4%, and a specificity of 83.5% for the detection of diabetic retinopathy. As Williamson and Keating point out (1998) treatments for diabetic retinopathy exist, however the infrastructure to detect

appropriate patients for treatment are not universally available. With the increasing advent of high resolution digital cameras, fundus images could be electronically sent to computers where advanced image interpretation (e.g. artificial neural networks) could reduce the number requiring expert examination by 70% (Gardner *et al*, 1996). This could reduce the 8% of the national health care budget devoted to diabetic patients. Our study aims to investigate morphometric changes of the conjunctival vascular network associated with diabetes which can be identified by image analysis. The ability to detect compromised vasculature, without operator intervention, may help reduce the needless amount of blind registrations due to diabetic retinopathy.

1.5 Summary

In this chapter we have discussed the importance of studying conjunctival vasculature. In the context of conjunctival vascular diabetic angiopathy the morphometric and morphological changes in vessels are likely to be slight. Subjective assessments of conjunctival vascular are associated with a large intra and inter session 95% confidence limit of repeatability which is unlikely to find difference between normal and challenged vasculature. Also, these methods probably lack the detailed information needed to find changes in vessels of the conjunctiva associated with diabetes and are tedious and time consuming. Images of the conjunctiva are plagued with imaging artefacts which can cause luminosity gradients across images. Hence, thresholding techniques, although offering an automated approach of vessel detection, will be sensitive to global intensity variations. However, edge detectors locate local discontinuities in image luminance and will not be effected by global differences in image luminance. Steger's (1998) algorithm to delineate curve linear structures offers a fully automated, robust method of segmenting vessels from their scleral surround. Its performance and use in finding differences between normal and diabetic conjunctival vasculature forms the subject of this thesis.

CHAPTER 2

2. Rationale for research

This research was instigated by the need to examine bulbar conjunctival vasculature. Conjunctival vessels form a complex network which cannot be adequately described by a human observer. Despite this subjective scaling of conjunctival vascularity has become common place. Clinically, in relation to judging the ocular performance of contact lenses, scaling methods were thought to be adequate but far from ideal. However, such measures are thought to be inadequate at discerning subtle conjunctival angiopathies. With the rapid developments of computer vision, the conjunctival bed offers an interesting structure for image segmentation and analysis, thus allowing more detailed information to be gleaned from this peripheral vascular bed.

There are many factors which affect conjunctival vessels, including systemic and ocular disease and environmental challenge. The objective of this work was to establish the angiopathic effects of diabetes on conjunctival vessels. As indicated in chapter 1 there is an abundance of literature concerning the effects of diabetes on retinal vasculature whilst the literature on conjunctival vessels is scarce, largely anecdotal and inadequate. Detailed morphometric analysis of retinal vasculature is confounded by the magnification effects of the cornea, lens and axial length of the eye. Superficial conjunctival vasculature is readily observed through its transparent mucus membrane without the complication of magnifying artefacts.

Previous attempts have been made to quantify vascular structures using computerised techniques. However, these are often computationally expensive, and require considerable manual input. Any method of vascular assessment which is labour intensive in application does not lend itself to large cohort studies. Any method advocating automation must be fully quantified in terms of what is actually being measured. It is not within the scope of this thesis to linger on the complexities of computer vision but to investigate what is actually being measured and establish if diseased vascular beds can be differentiated from the normal.

2.1 Aims

The aim of this work was to establish a fully automated system for quantifying images of conjunctival vasculature. This involved the automated extraction of vascular structures from the scleral surround and the derivation of indices to adequately describe the morphology and morphimetry of the vascular pattern. A healthy normal population, recruited from the academic, undergraduate, and postgraduate populations of City University, and from relatives of patients attending a hospital eye clinic, was studied to evaluate normal variations in the indices derived. The effect of smoking, age, blood pressure, time of measurement, and gender on the indices was then assessed. Comparisons between indices were then made between a normal and diabetic population. These indices were also assessed within the diabetic population to see if there was any association between the duration of diabetes, smoking, age, and the presence of diabetic retinopathy.

2.2 Plan for experimental work

At the commencement of this research, it became clear that the following procedures needed to be investigated and consolidated into the main project in order to answer the experimental aims.

- To simplify the task of image processing of conjunctival vessels the original image capture stage can be optimised by use of colour filtration. Image processing cannot extract vascular structures from images of poor quality. By considering the optical characteristics of each component of the experimental set-up and calculating the exposure densities of the target areas (blood and conjunctiva), filters can be introduced into the system to maximise image contrast between areas of interest. This forms the subject of chapter 3, where the concepts of exposure density are discussed and the performance of film and a CCD detector are compared, and the optimal method of imaging conjunctival vasculature was obtained.
- Many methods exist to quantify vessel width and are discussed in chapter 1 and 4. These methods often result in different interpretations of width. In the absence of a 'gold standard' of width determination, different approaches were assessed on an experimental model and 101 vessel locations. Each method was compared for inter session and inter method repeatabilities. This included the performance of a fully automated approach of segmenting vessels from their scleral surround, where σ selection was shown to alter the determination of width. Automated image segmentation of vascular structures has numerous advantages. The optimal method of running an automated vessel algorithm on images of the conjunctiva was established (chapter 4).
- Successful implementation of an automated method of measuring a vascular bed results in a large amount of quantitative data. This data must be processed in a useful manner. Establishing pertinent units of measure forms the subject of chapter 4. Tortuosity of a vessel, for example, is often expressed in terms of the ratio of chord length to actual length, however this may not be the best method of describing vessel tortuosity. Chapter 4 derives an experimental model to investigate the usefulness of different methods of quantifying vessel tortuosity. Chapter 4 derives a series of pertinent vascular indices to be calculated from the vessel algorithms output.
- Chapter 5 investigates the application of these indices to a population of 31 normotensives. The effects of age, gender, smoking, time of measurement, and blood pressure on these indices was established. Also the intra and inter session repeatabilities of each of these indices was measured. Knowledge of the variability in each index in a normotensive group is of paramount importance before conclusions about the effects of pathological disorders on the conjunctival bed can be established.
- The effects of both TI and TII diabetes on conjunctival vessels and further examinations of variations within a normal population were established (chapter 6). For this part of the study 60 'normal' patients, 17 TI and 36 TII diabetics were recruited. Images of the conjunctiva underwent image segmentation and vascular indices calculated for each patient. Comparisons between groups of patients were made using accepted statistical concepts.

It was hoped that this study would establish the usefulness of using fully automated computerised techniques to segment vessels from their conjunctival surround. By applying this methodology to the vascular bed of diabetics it was hoped that the usefulness of this technique would be demonstrated, and the effects of diabetes on a peripheral vascular bed be ascertained. It is noteworthy that the methods outlined are equally applicable to other vascular structures, such as the retina.

CHAPTER 3

3. Optimal imaging of ocular vasculature

3.1 Aim

The purpose of this chapter was to investigate the best filter to be used to obtain images of the bulbar conjunctiva using both film and CCD detectors from first principles and substantiate these calculations with experimental proof.

3.2 Introduction

Vogt first described red-free ophthalmoscopic examination of retinal vasculature in 1925 (cited from Delori *et al*, 1977) and demonstrated the clinical usefulness of spectral illumination. Since then red-free (green) illumination for the observation of retinal vasculature has become common place. Delori *et al* (1977) ventured this a step further by observing retinal vasculature and recording images to photographic film (Kodak X, black and white film) using numerous narrow band interference filters. They concluded that 'the predominant change that results from increasing the wavelength of illumination is a sharp increase in apparent light penetration of the fundus'. These findings led to development of the scanning laser ophthalmoscope, where infrared wavelengths of 670nm have been used to observe retinal vasculature and wavelengths of 830nm allowed visualisation of deeper choroidal vascular structures and retinal pigment epithelium (Manivannan *et al*, 1994). Delori *et al* (1977) subjectively found that retinal vasculature was optimally observed with illumination between 540 to 580nm, where a wavelength of 570nm was subjectively determined as the best, above 580nm retinal vessels were said to lose definition. Optimal photographic definition of retinal vessels was achieved with wavelengths between 560 to 575nm. These findings have greatly influenced subsequent studies needing optimal imaging of conjunctival or retinal vessels. Bracher *et al* (1979) photographed the fundus under green filtered illumination using high contrast black and white film. However the authors comment that this resulted in misleading interpretation of a vessels edge due to the 'steep gradation (high gamma)' of the mediums characteristic curve. Standardisation of exposure was thought to be impossible, due to inter and intra patient variations in fundus reflectance, differences in retinal pigment epithelium and blood volume in the choriocapillaris. Apparent blood vessel width is dependant on focusing (where optimal focus is difficult to achieve), resolution of optics, exposure and development of the film used. Ducrey *et al* (1979) concluded that 'restriction of the spectral content of illumination to an appropriate narrow spectral band or the use of monochromatic light improves both contrast and optical quality over that obtained with white light and results in enhanced visualisation of {vascular} structures'. Optimal visibility of retinal blood vessels and pathological structures allied to blood was obtained with yellow-green illumination of 570nm (as shown by Delori *et al*, 1977). The high absorption of light by blood at this wavelength produced an 'excellent demonstration of the vascular pattern'. Grunwald *et al* (1986) used monochromatic light centred at 570nm to obtain photographic images of retinal vasculature (using Kodak Plus X panochromatic black and white film). Calliper measurements of vessel width from projected negative images were

used to study the effects of diabetes (Grunwald *et al*, 1986), and a spontaneous rise in IOP (Grunwald *et al* 1988), on retinal vessel width. In conjunction with laser Doppler imaging blood flow was also determined (Riva *et al*, 1985). Nielsen (1988) used fluorescein angiography and red-free photography to enhance vessel contrast and showed that retinal microaneurysms were present in a 'normal' population. Fenton (1980) utilised green filtered illumination (using a Wratten 58 filter) to photograph conjunctival vasculature. A simple grid overlay enabled vessel area to be estimated from projected black and white negatives. Inferior limbal vessels photographed on Kodachrome 64 colour film under red-free illumination with a Nikon photo-slit lamp enabled McMonnies and Chapman-Davies (1982) to judge the response of conjunctival-limbal vasculature to contact lens wear. The increase in vessel contrast allowed the clinical effects of chronic vessel dilation associated with SCL wear to be observed.

For nearly 15 years red-free photographs have been electronically recorded to a digital format, using slide scanners and frame grabbers, allowing computerised assessment of vascular networks. It should be noted that this does not solve the many problems inherent with photographic imaging, and merely offers a further step in image acquisition which may present additional errors. However, the digital format can be used for image processing to allow better visualisation of vascular structures or computerised image segmentation. Recent years have seen an increase in the pixel resolution that an image can be scanned to. Hill and Crabtree (1984) took red-free photographs (Ilford Pan F film) and recorded them 'electronically' to a 64 grey level image. Chen *et al* (1987) digitised black and white photographic negatives taken under Wratten 58 (green) filtered illumination of the temporal conjunctiva to 128×128 pixels. After correcting for luminosity gradients vessel width, inter capillary distance, and vessel bifurcations were recorded. Cardiac synchronised photographs (using Kodak Technical Pan film) taken under green filtered illumination (optimal transmission at 570nm in accordance with Delori *et al*, 1977) were digitised to 512×512 pixels. Densitometric half height determination of width showed; variations in retinal calibre with the cardiac cycle (Chen *et al*, 1988), a lack of retinal vessel autoregulation in diabetic pregnancy (Chen *et al*, 1994), and vein dilation in patients with diabetic retinopathy (Patel *et al*, 1992). George *et al* (1990) digitised black and white negatives (Kodak Tri-X-film) taken with a Zeiss fundus camera through a green filter. This filter had maximum transmission at 540nm, but the paper states that a filter with optimal transmission at 570nm would have been preferred but for the greater illumination needed to obtain an adequate image. The authors advocate a highly reproducible technique of determining densitometric half height width using the digitised images obtained. Gardner *et al* (1996) digitised 60° red-free fundus photographs of the posterior pole obtained with a Cannon fundus camera to 700×700 pixels. By the application of a back propagated neural network diabetic and normal fundi could be discerned with a sensitivity of 88.4% and specificity of 83.5% compared to an ophthalmologists 'gold standard'. A more recent paper by Formaz *et al* (1997) digitised black and white fundus photographs taken with a green filter (optimal transmission at 540nm) to a resolution of 3072×2048. Using a rectangular fitting model to depict vessel width, retinal vessel dilation was found in response to exposure to a flicker stimulus.

Although photographic or digitised photographs form the mainstay of image capture increasingly video analogue and digital cameras are being used. This allows direct exposure to a charged couple device (CCD) negating the need for subsequent image digitisation. However, analogue video systems have to convert a digital image into an analogue image to be viewed on a video output. A 'frame grabber' is often needed to convert the analogue back into a digital image. Jung *et al* (1983) describe slit lamp video microscopy of the bulbar conjunctiva recorded on U-matic film. Optimal contrast between vessels and the scleral surround was obtained by illuminating the conjunctiva with light of the 'soret' band wavelength (410nm), which was considered to be the absorption peak of haemoglobin. This allowed the authors to manually determine erythrocyte velocity. Zhou *et al* (1994) used a 'frame grabber' to convert high resolution red-free video images of retinal vasculature to a 16 bit digital image of 1024×1024 pixels. A Gaussian shaped matched filter was used to segment vessels and allow automated tortuosity and width measures to be ascertained. Suzuki (1995) used a 512 linear array to record images of the fundus under halogen light with a 570nm interference filter. The linear array was manually rotated to be perpendicular to vessel direction. This allowed densitometric half height width to be directly ascertained. Stevenson and Chawala (1993) reported difficulty in obtaining video images of vessels at the limbus to sufficient contrast. Hence, they recorded a broad band of illumination below 600nm with a CCD camera (peak sensitivity at 520nm) using a Zeiss 30SL slit lamp with a Halogen light source filtered with a 500 to 580nm band pass filter. This technique was initially described by Meyer (1989). Willingham *et al* (1995) recorded images of bulbar conjunctivae using a Nikon FS-2 photo slit lamp fitted with a CCD camera, which recorded 640×480 pixel images equivalent to an object space of 3.8cm². Vessel area was calculated from the image obtained from the green component of the CCD array to optimise vessel contrast.

3.3 Principles of exposure density

As indicated conjunctival vessels are often observed using a green filter, which absorbs most of the red light reflected from haemoglobin making it appear dark, it also transmits over the spectral range to which the eye is most sensitive and so luminance is not unduly attenuated. When imaging conjunctival vessels by video, CCD, or photographic techniques, the spectral sensitivities of the recording media differ from the spectral luminous efficiency curve of human photopic vision. A specific filtering system is needed that utilises the spectral sensitivity of the medium used to record the image. Hence *ad hoc* approaches using green filters (as outlined above) may not result in optimum contrast. The choice of filter is not straight forward especially where it is necessary to enhance contrast between similar colours. The inclusion of a colour filter into the optical path of a system will alter the spectral transfer function. By considering all spectral components of the imaging system the concept of exposure density can be applied. Exposure density is a measure of the detector response to a particular target with spectral reflectance ρ . The system includes the radiant intensity, J , of the illuminating light source, the spectral sensitivity, S , of the detector, and the spectral transmittances of the lens (l) and filter (f). The exposure density (Brewer *et al*, 1949), or system exposure response (*SER*) (Palmer and Jacobson, 1994), represents the response of the system to the target relative to a perfect white surround, and is given by the following equation in which all the terms are functions of wavelength.

$$SER = \log \left(\frac{\int J(\lambda)l(\lambda)f(\lambda)S(\lambda)d\lambda}{\int J(\lambda)l(\lambda)f(\lambda)\rho(\lambda)S(\lambda)d\lambda} \right)$$

For 2 targets with spectral reflectance ρ_1 and ρ_2 , recorded with the same system, the system exposure response difference (*SERD*) is given by the following equation.

$$SERD = \log \left(\frac{\int J(\lambda)l(\lambda)f(\lambda)\rho_1(\lambda)S(\lambda)d\lambda}{\int J(\lambda)l(\lambda)f(\lambda)\rho_2(\lambda)S(\lambda)d\lambda} \right)$$

The magnitude of the *SERD* value indicates the degree of contrast expected, while the sign indicates which of the target areas will be reproduced lighter. For a system where the measure of response is logarithmic with exposure, that response will be proportional to the *SERD* value. For a photographic system, where the response is determined by the optical density of the developed film, the exposure density difference will be proportional to the difference in optical density between the image corresponding to the 2 target areas, provided they are both recorded on the straight line portion of the characteristic curve. Differences in film development times will also effect the contrast between target areas and γ characteristic of the film. For this study a fixed development time was used and thus these effects were not investigated further. The response of a CCD to light is almost linear (Newsom *et al*, 1992) as opposed to film, hence, the difficulty of ensuring that the 2 target areas lie on the linear part of the characteristic curve does not apply. The application of exposure density to the problem of optimal imaging of conjunctival blood vessels enables responses to be modelled and calculated without the need for extensive trial and error experimentation.

3.4 Experimental set-up

3.4.1 Instrumentation

Images of right temporal bulbar conjunctivae were captured using a Nikon FS-2 photo slit-lamp. The Nikon FS-2 slit lamp is a Galilean type stereo microscope with a continuous zoom magnification. The objective lenses can be continuously altered between a magnification of $\times 0.8$ to $\times 2.4$, with an eyepiece magnification of $\times 20$, giving a combined magnification of $\times 16$ to $\times 48$ to the observer. When recording to a film or CCD sensor the image plane magnification needs to be determined, and will be given under the appropriate section. Note that the magnification at the image plane is unaffected by eyepiece magnification. Refractive correction of the observer can be achieved by adjusting the eyepiece to the appropriate prescription (between $\pm 5.00D$). However all images were recorded by an emmetrope. The working distance of the slit lamp for optimal focus is 92mm. At this distance images appeared sharply focused in the eyepiece, and were concurrently focused on the image plane of the sensor used. Observation of the conjunctiva was achieved through the eyepieces at the highest magnification using a full beam (10mm \varnothing) halogen lamp source (12V - 30W). A dim light source was used to enhance patient comfort. Patients were positioned using chin and forehead rests. Forty five degree nasal rotation of the right eye was achieved by use of a fixation target (cross) at a distance of ~ 3 metres from the subject. Light was

directed onto the target area via a movable turret. The angle between observation and illumination was 30° with the optical axis being approximately normal to the curved conjunctival surface. This was experimentally found to minimise specular reflections from the tear layer. The right hand extremity of the circular image observed in the right eyepiece was manually positioned at the most lateral point of the limbus to afford an optimal view of the bulbar conjunctiva, as the right hand side of the microscope is responsible for the imaging optics. In built filters were not used due to lack of knowledge of their exact transmission characteristics hence filters of known specification were introduced over the illumination turret. Directional xenon flash (500WS) was used for imaging. Directional flash suffers from the disadvantage of producing luminosity gradients across the image, which presents difficulty in image segmentation of vessels from their surround which will be discussed elsewhere. To perform exposure density calculations the spectral emission of the xenon flash, transmission of lens optics, and filters used were obtained. Calculations were restricted to the range 300 to 700nm since glass of the optical components of the illumination system will absorb most of the radiation below $\sim 350\text{nm}$. The relative spectral emission of the xenon light source was obtained from the Philips Lighting Catalogue (1994), as shown in figure 3.1.

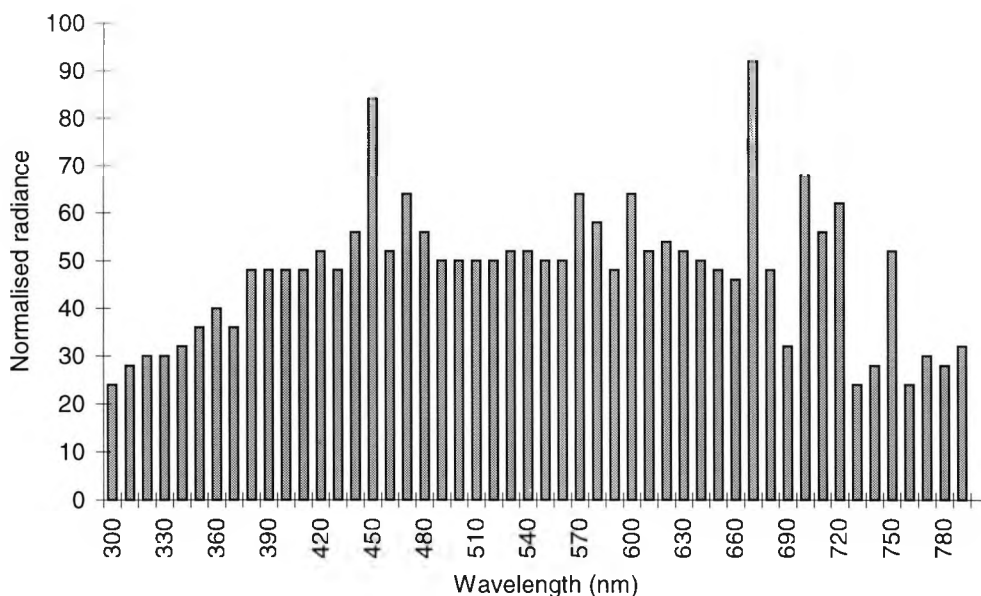


Figure 3.1 shows the relative spectral intensity distribution of low pressure xenon flash tube (from Philips Lighting catalogue, 1994).

Spectral transmittance of system optics, including illumination and imaging lenses was measured with a Perkin Elmer Lambda 2 UV/Vis spectrophotometer, and is shown in figure 3.2. A calibrated light source was shone through the system and simultaneously measured at the camera mounting.

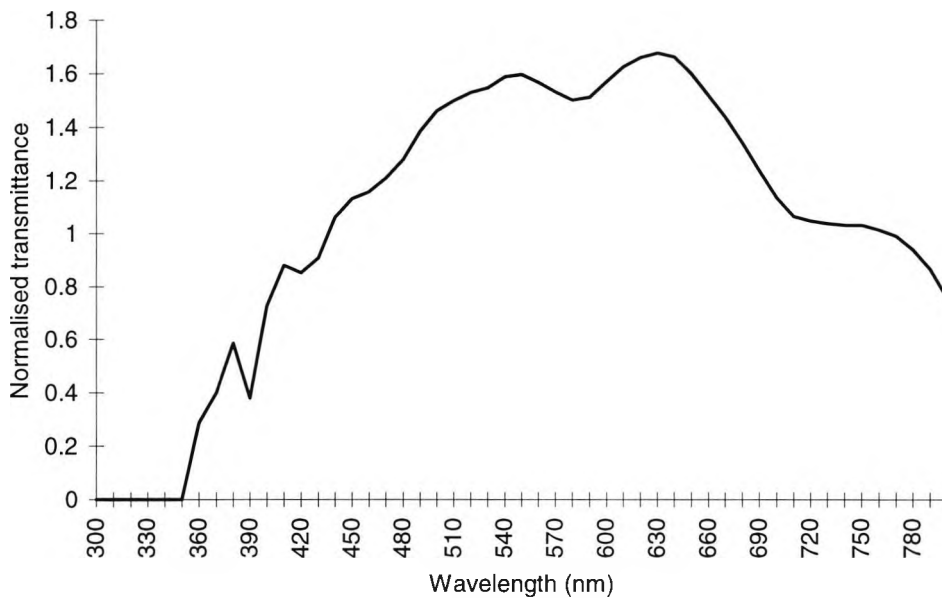


Figure 3.2 shows the spectral transmittance of system optics, including illumination and imaging lenses measured with a Perkin Elmer Lamda 2 UV/Vis spectrophotometer

The spectral transmission of ~ 80 Lee and Kodak Wratten filters were measured using a UV-2101 PC UV-Vis scanning spectrophotometer (Shimadzu). These included a Wratten 58 green filter which is typically used for colour separation and tricolour printing, but in our context is typically used for red-free imaging. The database included a variety of Wratten and Lee green filters for comparison.

3.4.2 Haemoglobin reflectance

The reflectance of a surface is defined as the ratio of the intensity of light incident on a surface to that reflected from the surface at a single wavelength or over a broad spectrum, and hence is often given as a percentage or as a decimal fraction of one. Measurement of haemoglobin reflectance is far from trivial and involves a complex optical process including refraction, scattering, absorption, diffraction and interference. Great efforts have been made to record light absorption and reflectance of blood because of its dependence on oxygen saturation (Mook *et al*, 1976), and hence permits an estimation of the rate of oxygen delivery to a particular tissue (Delori, 1988). *In vivo* measures of blood usually do not allow transmission data to be recorded as the detector and light source are usually on the same side of the tissue surface, hence this is often termed 'reflectance pulse oximetry' (Graaff *et al*, 1996). Reflectance oximetry has been used to measure cutaneous melanin and haemoglobin (Feather *et al*, 1988; Feather *et al*, 1989; Graaff *et al* 1996; Hajizadeh-Saffar *et al*, 1990; Landsman *et al*, 1978), and the haemoglobin content of the fundus (Delori *et al*, 1977; Delori, 1988; Delori and Pflibsen, 1989). Pulse oximetry studies of normal retinal vessels allowed Delori (1988) to calculate an oxygen saturation of $98 \pm 8\%$ for retinal arteries and $45 \pm 7\%$ for veins. A number of authors use the logarithm to the base 10 of reflectance which approximates to the sum of absorptances of a given tissue (Feather *et al*, 1988; Feather *et al*, 1989; Hajizadeh-Saffar *et al*, 1990). However, light reflection is affected by refractive index of plasma, plasma protein

concentration, pulsatile blood flow, erythrocyte; shape, aggregation, oxygenation, orientation and deformation (Delori, 1988; Graaff *et al*, 1996; Hajizadeh-Saffar *et al*, 1990; Landsman *et al*, 1978; Mook *et al*, 1968; Mook *et al*, 1976). Reflectance pulse oximetry will detect photons of different path length, with those of greater path length having a greater chance of absorption (see figure 3.3). This further complicates the measurement of reflectance.

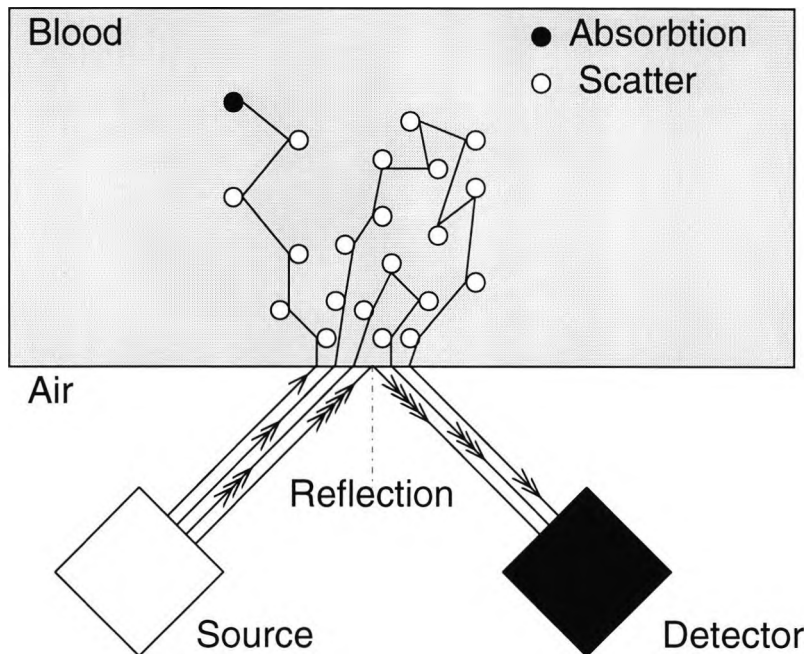


Figure 3.3 shows different paths of photons emitted by the source and emerging at the detector for the measurement of blood reflectance.

To accurately measure differences in oxygenated (arterial) and deoxygenated (venular) haemoglobin *in vitro* spectrophotometry has been used on specifically prepared blood samples (Mook *et al*, 1968; van Kampen *et al*, 1965; van Kampen and Zijlstra, 1983; Zijlstra *et al*; 1991). Although blood contains a number of differing haemoglobin products including carboxyhaemoglobin, haemoglobin, oxyhaemoglobin (HbO_2) and deoxyhaemoglobin (Hb) only the two latter principle components are considered. Zijlstra *et al* (1991) measured the absorptivity of prepared samples of HbO_2 and Hb at room temperature, between 450 and 700nm, which is shown in figure 3.4.

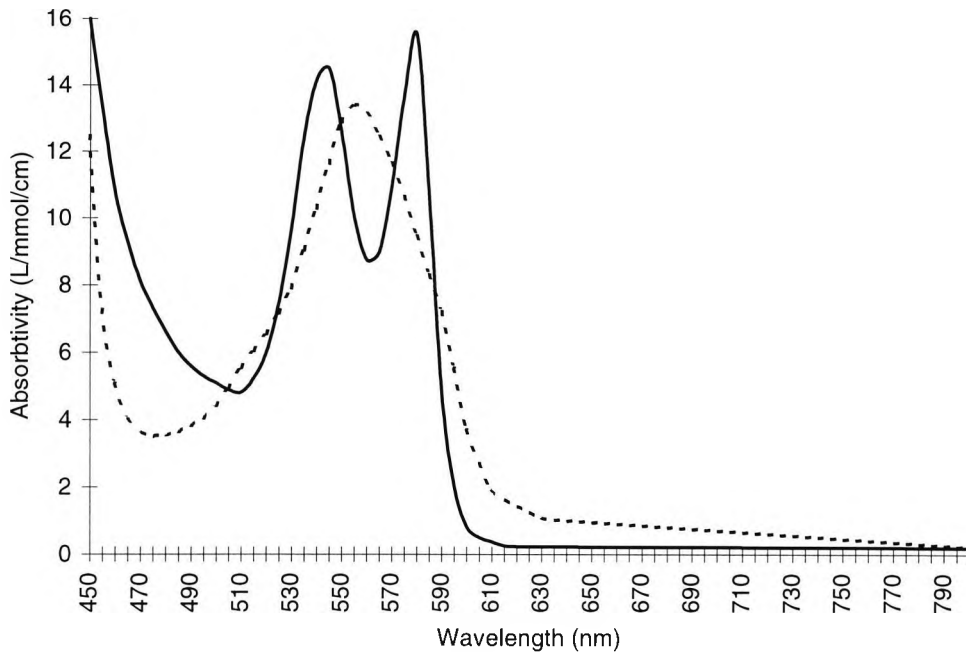


Figure 3.4 shows light absorption spectra of oxyhaemoglobin (solid line) and deoxyhaemoglobin (broken line) (from Zijlstra *et al*, 1991).

HbO₂ and Hb have characteristic maxima, minima and isobestic points which have been reported by a number of authors in a variety of contexts (Mook *et al*, 1968; Mook *et al*, 1976; van Kampen *et al*, 1965; van Kampen *et al*, 1983; Zijlstra *et al*, 1991) and are summarised in table 3.1. These characters allow the presence of haemoglobin to be observed within reflectance measurements of other tissue samples.

OXYHAEMOGLOBIN (HbO ₂)			DEOXYHAEMOGLOBIN (Hb)		
λ (nm)	ϵ^λ	Comment	λ (nm)	ϵ^λ	Comment
506.5	4.81	Isob Hb	431	140	Maximum
510	4.76	Minimum	478	3.31	Minimum
522	6.42	Isob Hb	506.5	4.81	Isob HbO ₂
542	14.37	Maximum	522	6.42	Isob HbO ₂
548.5	12.46	Isob Hb	548.5	12.46	Isob HbO ₂
560	8.47	Minimum	555	13.04	Maximum
569	11.27	Isob Hb	569	11.27	Isob HbO ₂
577	15.37	Maximum	586	7.23	Isob HbO ₂
690	0.07	Minimum	736	0.37	Minimum
815	0.22	Isob Hb	815	0.22	Isob HbO ₂

Table 3.1 shows characteristic points of Hb and HbO₂ where, ϵ^λ is absorptivity (litres mmol⁻¹ cm⁻¹), Isob Hb means isobestic with Hb, and Isob HbO₂ means isobestic with HbO₂ (from van Kampen *et al*, 1983).

Delori and Pflibsen (1989) measured the reflectance of the nasal fundus, perifovea, and fovea. Mean reflective data from 10 normal subjects are shown in figure 3.5, and reveal absorption characteristics of HbO₂. Distinct reflection minima or inflections are observed at ~540 and ~575nm which correspond to absorption maxima of HbO₂ and a pronounced increase in reflectance for wavelengths longer than ~575nm which

corresponds to a dramatic decrease in HbO₂ absorption. Note the similarity between fundus and conjunctival reflectivity shown in figure 3.7.

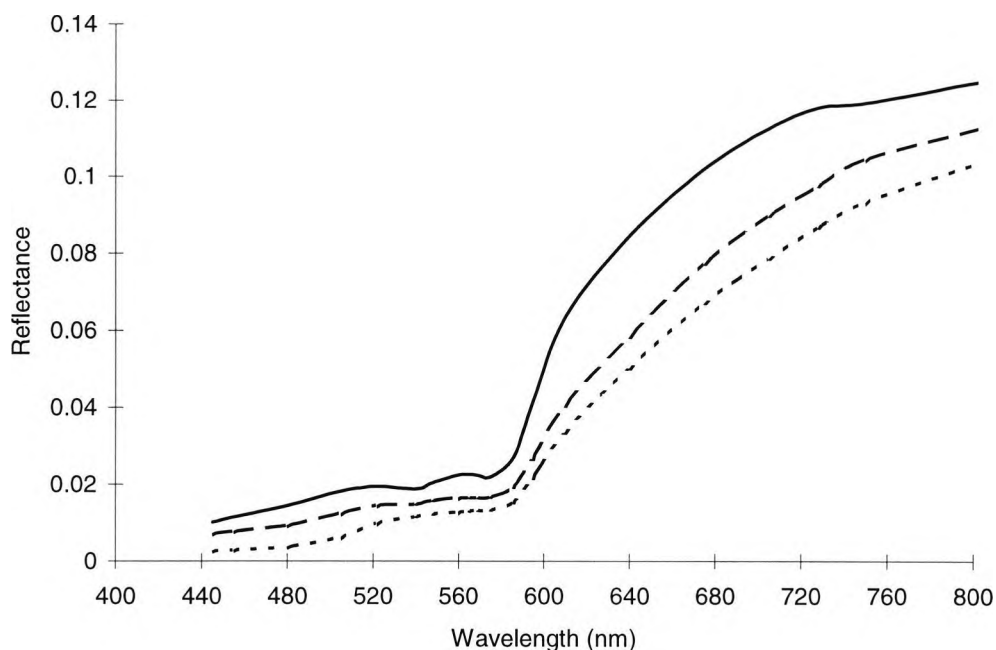


Figure 3.5 shows the mean reflectance ($n=10$) of nasal fundus (solid line), perifovea (long dashed line), and fovea (short dashed line) (from Delori and Pflibsen, 1989).

Delori and Pflibsen (1989) point out that the presence of melanin affects retinal reflectance often masking the presence of HbO₂ in heavily pigmented eyes.

Although a gross simplification, spectral reflectance of HbO₂ was measured from freshly obtained blood, extracted by venipuncture, using a Licor LI1800 telespectroradiometer. Since blood is partially transmitting, the imaging of the thin vasculature on the conjunctiva will include the effect of reflectances from the sclera behind the blood vessels. An attempt to account for this was made by measuring the reflectance of blood against a white background (see figure 3.6), thus including in the measurement the effects of partial transmittance / reflectance / absorbance. Although the precise values will be affected by the thickness of the sample and the effects of Hb, the approximation was considered sufficient for exposure density calculations.

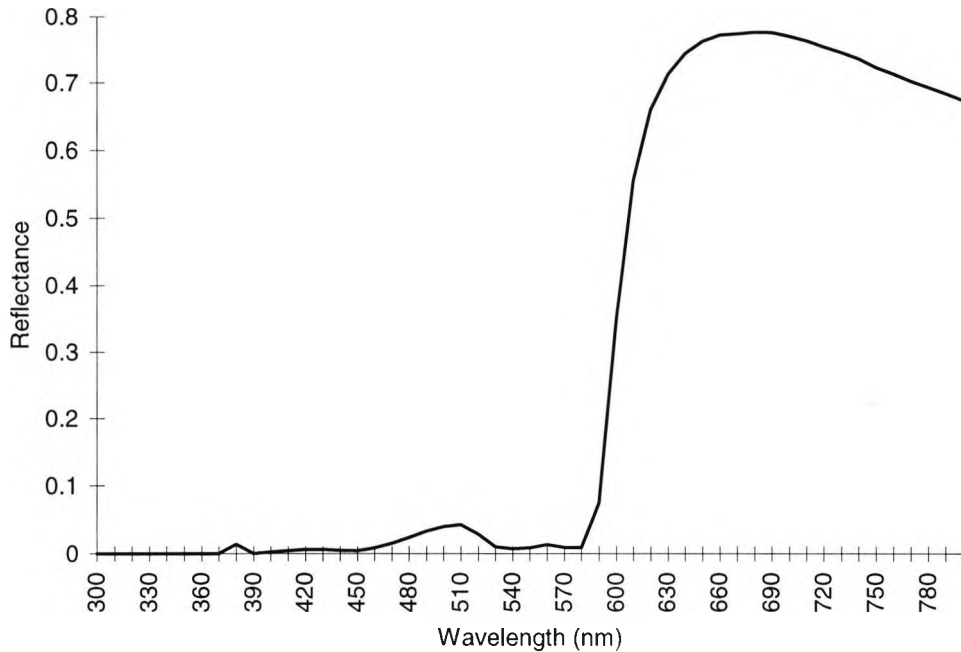


Figure 3.6 shows spectral reflectance of oxygenated haemoglobin freshly obtained by venipuncture measured on a white background of magnesium carbonate.

3.4.3 Conjunctival reflectance

According to Smith and Stein (cited from Delori and Pflibsen, 1989) the sclera is often considered as the most important reflector of the fundus. They measured scleral reflectance from enucleated eyes as 50-70% at 675nm. Delori and Pflibsen (1989) measured scleral reflectance in an aphakic subject with a coloboma as ~33% at 675nm. With an ocular transmission of 70-80% it was predicted that this would correspond to a scleral reflectance of 40-50%, which agreed with reflective measurements they took from the bulbar conjunctiva of one subject. They also noted that conjunctival reflectance decreased by a factor of 2.2 ± 0.6 between wavelengths of 500 to 800nm. When viewing the 'white' bulbar conjunctiva, lateral to the iris, there are a number of other refractive components which are viewed. Many of these structures appear translucent such as the tear film, conjunctival epithelium, conjunctival submucosa, and episclera. Structures visualised include 'white' sclera and overlying vasculature. Refractive components of the tear film include an oil layer, epithelium, aqueous phase and mucus layer. Conjunctival epithelium constituents include melanocytes (melanin less so in a Caucasian population), mucin and cell active components such as mitochondria, and endoplasmic reticulum. Conjunctival submucosa is rich in immunological components such as lymphocytes, neutrophils, mast cells and plasma cells. It is the conjunctival submucosa and episclera which are rich in vasculature containing both HbO_2 (arterial) and Hb (venular) blood. The 'white' appearance of sclera is due to dense collagenous tissue, where collagen forms 75% of the dry scleral weight (Williams *et al*, 1989). The sclera also contains elastic fibres, which are responsible for maintaining its viscoelastic nature for regulation of intraocular pressure. In addition the sclera contains fibroblasts, melanin, and tendons from the rectus muscles are sometimes observed. For the purposes of this thesis it was assumed that the lateral aspect of the bulbar conjunctiva is divided into the following refractive components in descending order of occurrence; water (at 35°C), collagen,

elastic fibres, mucus, oil, melanin, endoplasmic reticulum, mitochondria, lymphocytes, neutrophils, mast cells, plasma cells, with traces of tendon. Transmission and reflective characteristics of these components are necessary when attempting to calculate the spectral reflectivity of conjunctiva. The relative proportion of these components needs to be established so that they may be combined appropriately. However, such information is not readily available. Hence conjunctival reflectance was measured directly using a Licor LI1800 telespectroradiometer with a quartz microscope attachment (acceptance angle 1.8°), by comparison to a calibrated magnesium carbonate standard. Spectral reflectivity was measured normal to the curved conjunctival surface with an angle of $\sim 30^\circ$ between illumination and observation systems, in accordance with imaging geometry. Six subjects were measured with a range of ages (22 to 50 years) and racial origin (2 Asian, 4 Caucasian). The test area measured ~ 1 mm in diameter and was positioned on the conjunctiva to be free of obvious vasculature. It was acknowledged that the effects of haemoglobin would affect the results and this is evident by the absorption minima observed in figure 3.7, at ~ 542 nm and ~ 577 nm where HbO_2 has peak absorption, and absorption maxima at 510nm and 560nm where HbO_2 has minimum absorption. Inter subject differences in conjunctival reflectivity were small, hence, an average was used for exposure density calculations, as shown in figure 3.7.

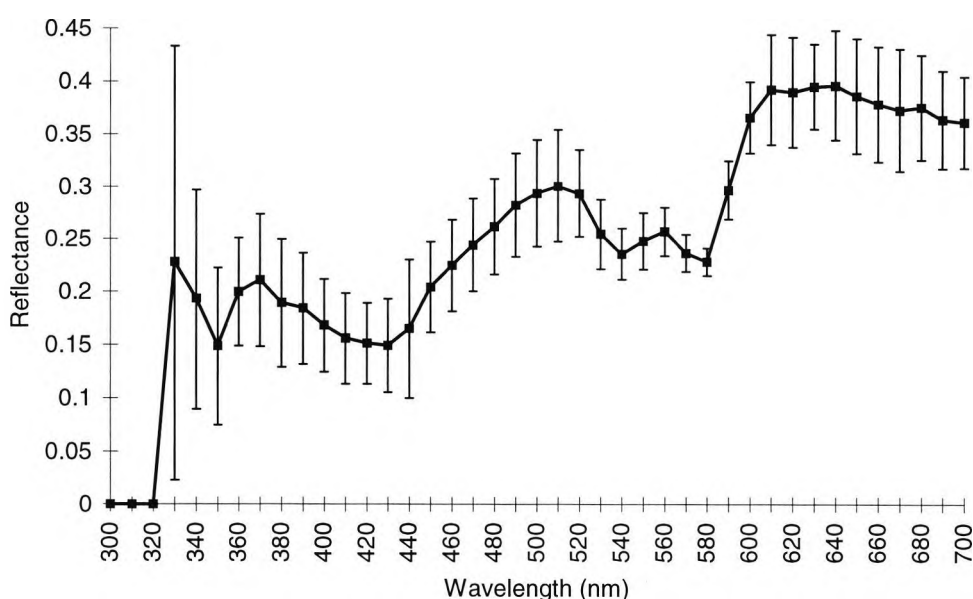


Figure 3.7 shows the average spectral reflectance of the bulbar conjunctiva for 6 subjects, where the error bars represent \pm standard deviations.

3.4.4 Film sensor

Images were captured to both film and CCD. Film images were recorded on monochrome Ilford HP5 plus film, developed in Kodak D-19 high contrast developer for 8 minutes with intermittent agitation. Spectral sensitivity of HP5 plus film was determined by means of a spectrosensitometer based on a Bentham M300L monochromator system (Bentham Instruments, Reading, Berkshire, England) after the method of Palmer and Jacobson (1994). A series of exposures were made at each selected wavelength from 300 to 800nm at 10nm intervals. The sensitivity was

determined as the reciprocal of exposure (in mJm^{-2}). The spectral response of HP5 plus is shown in figure 3.8 (data provided by Dr J R Palmer, Imaging Technology Group, University of Westminster, London, UK). Note the relative sensitivity beyond 650nm is negligible.

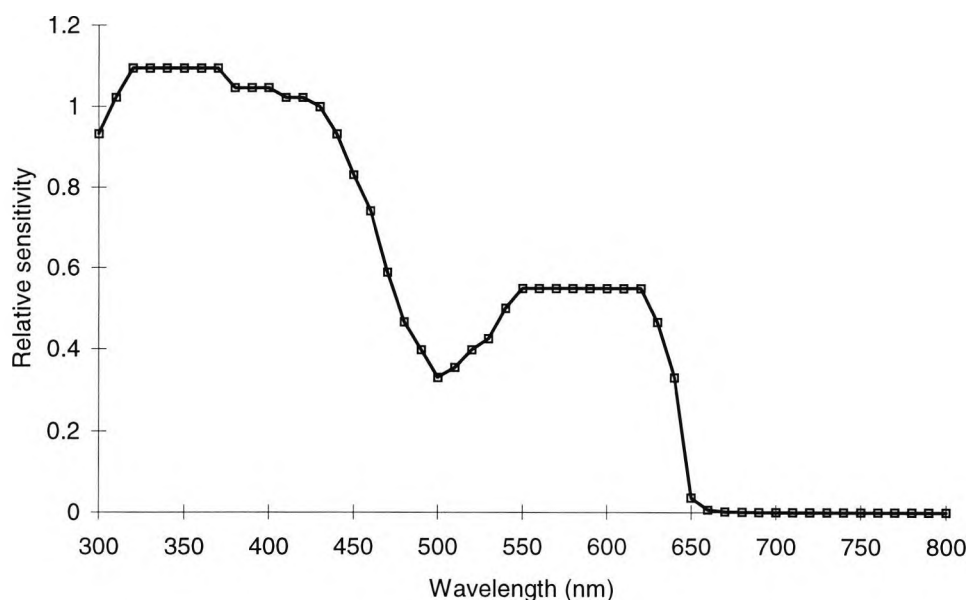


Figure 3.8 shows spectral sensitivity of HP5 plus film. Reciprocal of exposure required to produce constant density in negative.

3.4.5 Magnification at the film plane

Magnification at the film plane was calculated by photographing 4 millimetres of a vernier scale (Vickers, England) 10 times. Photographic images were projected on a slide viewer of calibrated magnification. Mean of 10 measures used, multiplied by known magnification of the projector system, divided by 4 to give a mean film magnification of $\times 3.101 \pm 0.005$ (\pm SD) on the film plane. Hence 1mm in object space measures 3.101mm on a film negative.

3.4.6 CCD sensor

CCD image capture was recorded using the Kodak DCS 100 digital camera. This camera was launched by Kodak in 1991, and has since been superseded by a vast array of digital cameras. The Kodak digital camera system (DCS) uses a familiar unmodified Nikon F3 camera body, but the back has a CCD array with 1.3 million pixels (1024×1280 pixels) which measures 16.4×20.5 mm, as against the 24×36 mm standard for 35mm gauge film. Hence a modified image area is seen through the view finder. Using a Nikon F3 camera body allows compatibility with the camera mounting on the Nikon FS-2 photo-slit lamp without modification, where images correctly focused in the eyepieces will be correctly focused on the CCD image plane. The DCS 100 is connected to a digital storage unit (DSU), by an umbilical cable, which is a 200 MB recorder which can store 150 uncompressed or 600 compressed images. A motor driven exposure release allows 2.5 images per second to be taken with a maximum burst length of 24 exposures. A built-in monochrome liquid crystal display (LCD) allows instantaneous viewing of an image taken, although to limited resolution,

allowing unwanted images to be deleted. However, the DSU has a video output facility which allowed monochrome images to be simultaneously viewed on an external video monitor. More recent digital cameras have done away with the cumbersome DSU, and incorporate storage facilities within the camera body, for example the DCS 200. However, this has the effect on increasing the size of the camera body and does not allow the unit to be fitted to the photo-slit lamp camera mounting due to size constraints.

Pixels on the CCD array are coloured red, green, and blue and the arrangement is shown in figure 3.9. This arrangement can easily be viewed by observing the CCD array under light microscopy. Green pixels amount to 75% of the total array, blue and red 12.5% respectively. Note that the pixel arrangement used on the DCS 100 has been superseded by a 'Bayer' pixel arrangement on newer Kodak digital cameras.

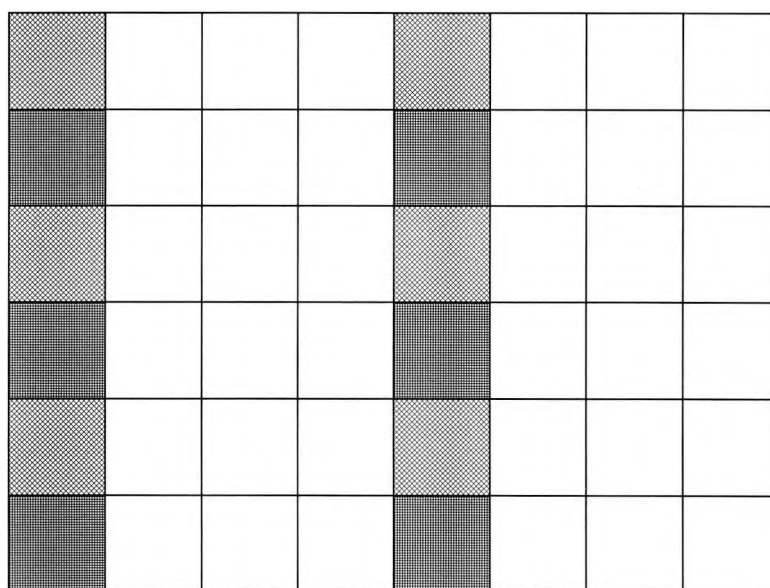


Figure 3.9 shows the pixel arrangement on the DCS 100 where green pixels are the unfilled squares (75%), red pixels (12.5%) diagonal chequered squares, and blue pixels (12.5%) horizontally chequered squares. Note that the entire CCD array is 1280 pixels wide and 1024 pixels tall.

Images are imported into a computer via a SCSI card, using Aldus PhotoStyler version 1.1 (Aldus Corporation, Seattle, USA) software. Each 24 bit colour image was ~4.1MB in size. Alternatively the image can be stored from each colour channel as an 8 bit ~1.38MB file. Clearly the signal from the red and blue pixels are considerably interpolated to give images of equivalent file sizes, whereas the green image requires less interpolation. This interpolation can be seen by the presence of vertical 'jaggies' in the image.

Although the spectral sensitivity of the CCD array could have been measured, the facilities were not at the authors disposal. Hence, spectral sensitivity data was provided by Kodak Eastman (Rochester, New York, USA) and is shown in figure

3.10. However, data was only provided to 700nm for the red, green and blue channels and to 800nm for the signals combined.

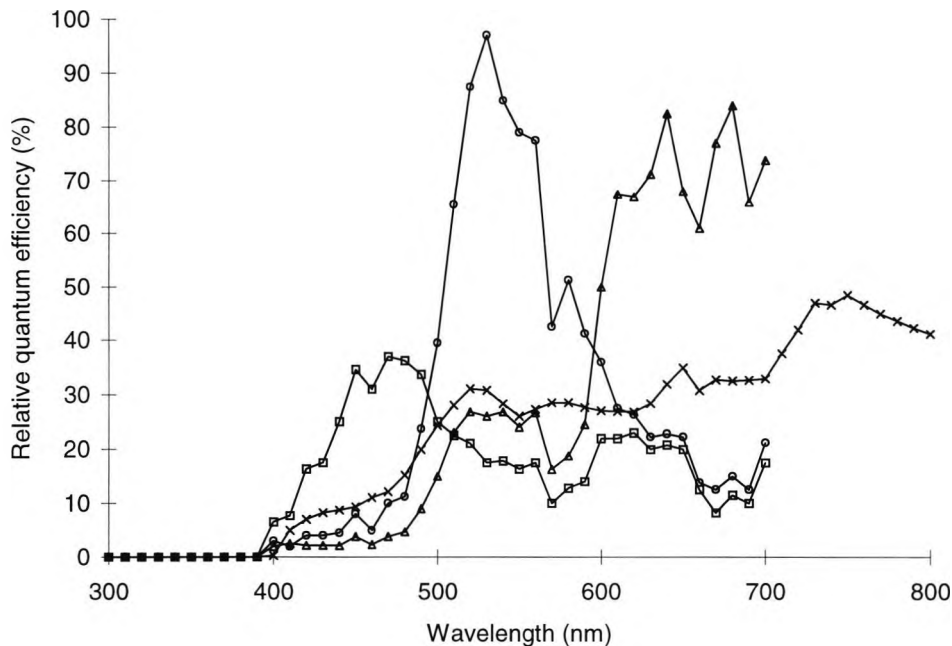


Figure 3.10 shows the spectral sensitivity of the DCS 100 CCD array, where open squares represents response of blue pixels, open circles green pixels, open triangles red pixels, and crosses the response of the combined colour channels (data courtesy of Kodak Eastman, Rochester, New York, USA).

Manufacturing data reveal that a CCD detector is more responsive than film to lower light levels (Kodak Eastman, Rochester, New York, USA), and that the response of a CCD to light is almost linear as opposed to film (Newsom *et al*, 1992). Note that images taken on the non linear 'S' shaped characteristic curve of photographic film will lead to intensity attenuations in the image. The spectral sensitivity curves of both film and CCD show that film has peak sensitivity below 400nm, where the CCD has minimal response. However, a CCD reacts to longer wavelengths, unlike the film used which does not respond to wavelengths longer than ~650nm. Hence, HP5 film can be regarded as responding to near UV wavelengths, and CCD IR.

3.4.7 Magnification on the CCD array

More care was taken establishing the magnification at the digital image plane, as the position of a scale graduation may fall at an inter-pixelated distance. Hence, 6.1 millimetres of a vernier scale containing graduations at 0.1mm intervals, were imaged 10 times. Each graduation was made by a darkly etched band. Densitometric profiles, approximately 1200 pixels in length, were taken along the scale using appropriate image software (acquired using Matlab for Windows © Version 4.2c1). Local minima in the densitometric profile equated to the etched 0.1mm marks, and are shown in figure 3.11. The pixel position of each inflection point was recorded and plotted against the vernier scale. The slope of the linear regression line through the data points revealed the magnification for each image. Note that all regression lines gave an R^2 value of 1.00. Mean (\pm SD) magnification for the 10 images was 188.494 ± 0.032 pixels per millimetre of object space. Alternatively, 1 pixel represents $5.305 \mu\text{m}$ in object space.

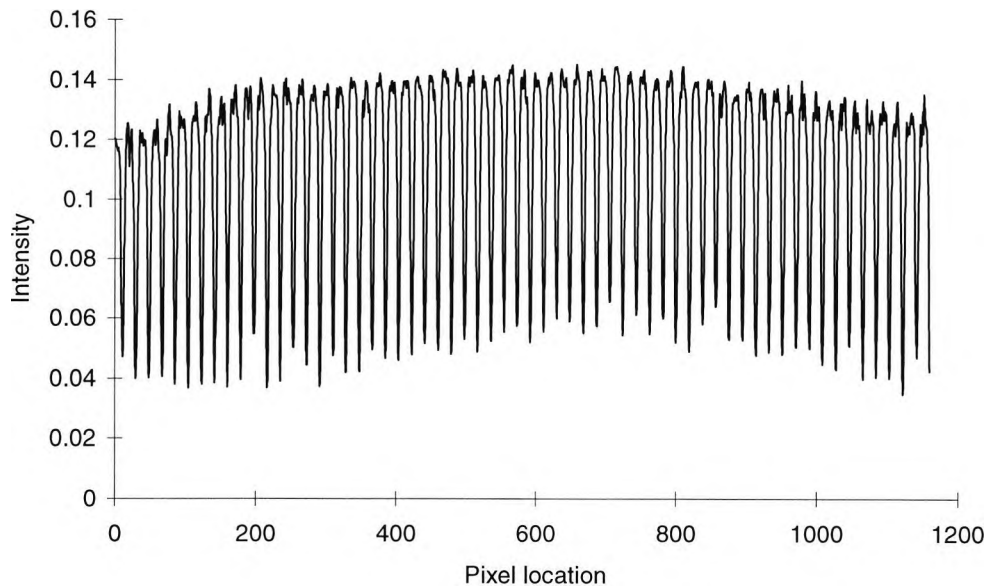


Figure 3.11 shows the densitometric profile obtained along an image of a vernier scale, local minima equate to 0.1mm graduations in the vernier scale.

3.4.8 Filter transmission characteristics

As indicated a database of ~80 Wratten (Kodak Eastman, Rochester, New York, USA) and Lee filters (Lee, Andover, UK) was introduced into the optical system over the illumination turret. Transmission characteristics were measured using a spectrophotometer (UV-2101PC UV-Vis Scanning Spectrophotometer, Shimadzu) and checked, where possible, against manufacturing literature. Transmission was measured at wavelengths between 300 and 800nm in 10nm steps. Transmission characteristics of a selected number of filters are shown in figure 3.12, for a Wratten 58 (green filter), Wratten 47B (blue filter), Wratten 99 (green filter) and Wratten 96 (neutral density filter 0.5). With knowledge of all the other spectral transmittances and reflectances of the optical system the database of filters can be altered to maximise the SERD equation, to give optimal contrast between blood vessels and the scleral surround.

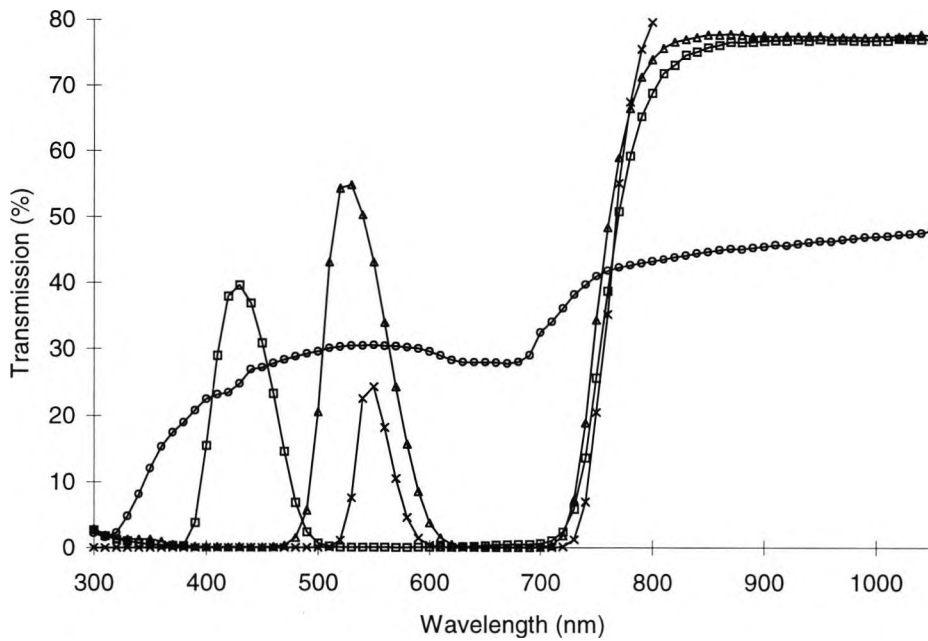


Figure 3.12 shows the transmission characteristics of a Wratten 47B - open square symbols, Wratten 58 open triangular symbols, Wratten 96 open circular symbols, and Wratten 99 crossed symbols.

3.5 Exposure density calculations for film

Calculations of the SERD were performed for the system as it stood and as modified by the inclusion of a filter from a database of ~80 coloured glass and interference filters. A selection of filters from the database are shown in table 3.2, in descending order of SERD value, and graphically in figure 3.13.

Filter	Comments	SER (conj)	SER (blood)	SERD
Wrat 18a	UV transmission	0.710	2.216	1.506
Wrat 35	Purple blue	0.781	2.205	1.424
Wrat 47b	Blue narrow cut	0.743	2.133	1.390
Wrat 99	Green	0.609	1.897	1.288
Wrat 74	Dark green	0.594	1.854	1.260
Lee 118	Green	0.662	1.792	1.130
Wrat 61	Deep green narrow cut	0.582	1.682	1.100
Wrat 58	Green	0.583	1.559	0.977
Wrat 11	Yellow green	0.562	1.079	0.517
None	None	0.595	0.901	0.306
Wrat 96	ND filter	0.587	0.885	0.299
Wrat 22	Deep orange	0.475	0.430	-0.045
Wrat 23a	Light red	0.452	0.353	-0.099
Lee ht019	Fire red	0.433	0.282	-0.151
Wrat 25	Red tricolour	0.417	0.235	-0.181

Table 3.2 shows a selection of results of SER for conjunctiva and blood and the calculated SERD for images captured on HP5 plus film.

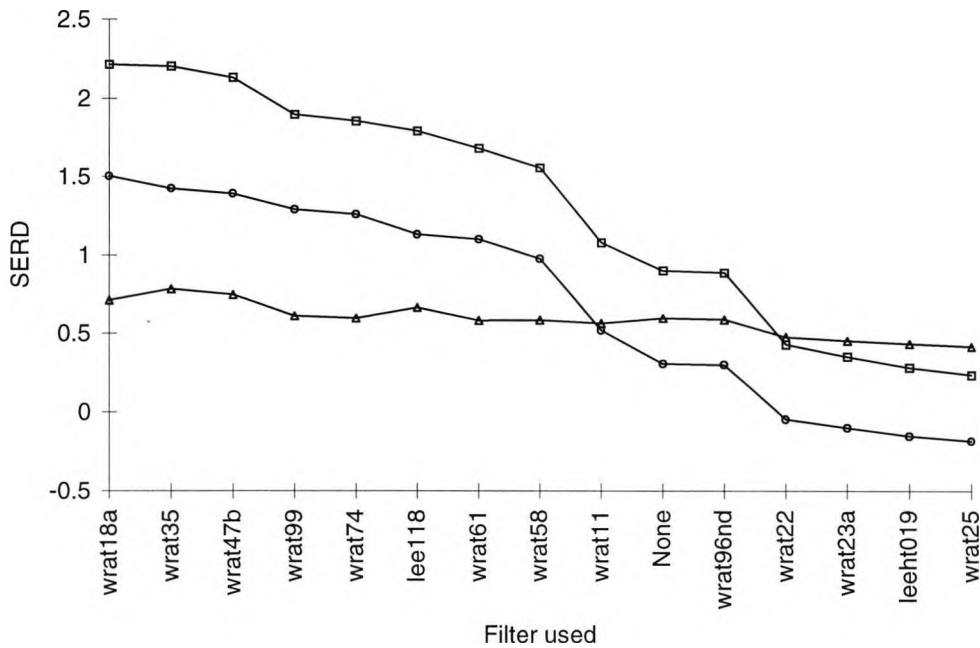


Figure 3.13 shows a selection of results of SER for conjunctiva (open triangular symbols) and blood (open square symbols) and the calculated SERD (open circular symbols) for images captured on HP5 plus film.

From table 3.2 it can be seen that the calculation of the SERD value with no filtration and a neutral density filter are similar (0.306 and 0.299 respectively). As shown in figure 3.12 neutral density filters (Wratten 96) reduce the intensity of visible light, providing a uniform attenuation throughout the visible spectrum (400 to 700nm). As the SERD calculations are restricted to wavelengths from 300 to 700nm similar values are obtained for a Wratten 96 and an optical system without filtration. Evidently filters which transmit UV radiation (Wratten 18a, 35) will increase vessel contrast seen on the film recording media. A Wratten 35 (purple filter) will increase the contrast over the standard system by approximately 4.5 times, assuming that the input-output characteristic remains constant. The SERD calculation predicts that a Wratten 22 (deep orange) and Wratten 23a (light red) filter will give ~ 0 contrast between haemoglobin and the conjunctival surround, as the SER of haemoglobin and conjunctiva are similar. The SERD calculation predicts negative values for Lee ht 019 (fire red) and Wratten 25 (red tricolour) filters implying that haemoglobin will appear brighter than the conjunctiva on the film image.

3.6 Experimental verification for film

Figure 3.14 shows the effect on the resultant image of using the Wratten 35 filter over the illumination turret exit window. Both figures were digitised from prints reproduced from consecutive exposures made on the same film. The inclusion of the filter necessitated an increase in the illumination power setting from 1 to 4 (on a scale of 1 to 5). It can be seen that there is greater contrast in the image with filtration, particularly in the rendition of smaller vessels. To test whether the visual impression of increased vessel contrast is correct, a microdensitometer was used to scan the negatives. Figure 3.15 shows microdensitometer traces of the same blood vessel in the 2 photographic negatives. The trace of the image made without filtering shows that the signal-to-noise ratio is much lower, making it more difficult to determine the

boundaries of the vessel. Note that the trace is of a large, clearly visible blood vessel, and many have much lower contrast than this one, although the increase in signal-to-noise ratio will occur with all blood vessels irrespective of their size, since the technique is based on the spectral reflectances. However, it is apparent that the absolute contrast has not increased by the predicted 4.5 times. This is because the exposures were made on the non-linear portion of the film's photographic characteristic curve. Inspection of the negatives showed that the image without filtration was slightly overexposed and the filtered one slightly underexposed. This underlies the importance of using the SER as a measure of useful contrast. Although the absolute contrast is little different, the great improvement in signal-to-noise ratio provides an image with increased information content, which can aid image processing.

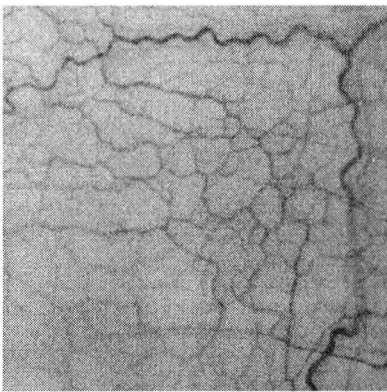


Figure 3.14a

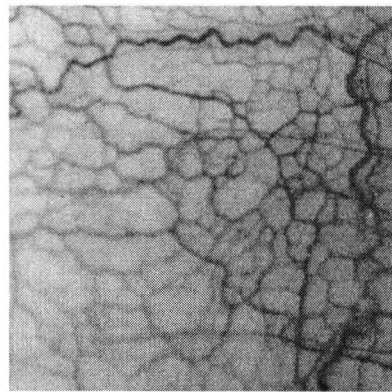


Figure 3.14b

Figure 3.14 shows images digitised from consecutive photographs of the bulbar conjunctiva taken (a) without filtering, power setting 1, and (b) with a Kodak Wratten 35 filter, power setting 4. The increased information content in terms of image contrast is visible. The square represents $\sim 3.4\text{mm}^2$ of conjunctiva.

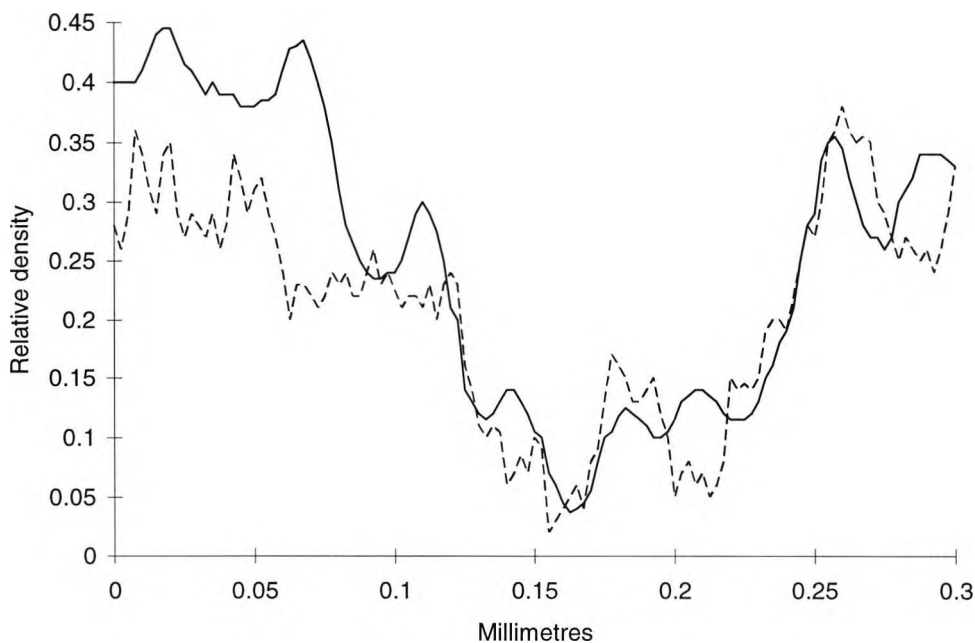


Figure 3.15 shows microdensitometer traces over the same blood vessel imaged without filtering (dashed line); and with a Wratten 35 filter over the light source (solid line).

3.7 Exposure density calculations for CCD

Calculations of the SERD value for the CCD can be made for differing sensors namely the red, green, blue, and colour channels combined. SERD values are shown in table 3.3 for each of the digital sensors and the sensors combined in descending order of the green CCD's response. Figure 3.16 shows the SERD values in graphical form which allows the relationship between differing sensors and their SERD values to be observed.

<i>Filter</i>	<i>Comments</i>	<i>SERD (CCD)</i>	<i>SERD (R-CCD)</i>	<i>SERD (G-CCD)</i>	<i>SERD (B-CCD)</i>
Wratt 99	Green	-0.180	1.222	1.343	1.271
Wratt 74	Dark green	-0.117	1.161	1.249	1.197
Wratt 61	Deep green narrow cut	0.041	1.029	1.127	1.035
Wratt 58	Green	0.041	0.830	1.081	0.930
Lee 118	Green	-0.041	0.307	0.878	0.889
Wratt 47b	Blue narrow cut	-0.262	0.032	0.681	1.112
Wratt 11	Yellowish green	-0.020	0.078	0.660	0.418
Wratt 96nd	ND filter	-0.144	-0.179	0.225	0.089
None	None	-0.129	-0.183	0.213	0.087
Wratt 22	Deep orange	-0.245	-0.244	-0.093	-0.188
Wratt 23a	Light red	-0.264	-0.253	-0.153	-0.210
Lee ht019	Fire red	-0.285	-0.265	-0.203	-0.231
Wratt 18a	UV transmission	-0.342	-0.309	-0.215	-0.159
Wratt 25	Red tricolour	-0.292	-0.269	-0.233	-0.244
Wratt 35	Purple blue	-0.333	-0.322	-0.299	-0.211

Table 3.3 shows a selection of results of SERD values for each sensor for a selection of filters, in descending order of value for the green CCD sensor.

SERD values using the sensors combined give a limited range of values from -0.333 to 0.041, with a value of -0.129 for the optical system without filtration. The red sensor gives an extended range of values from -0.299 to 1.22, with -0.183 for no filter. A similar range is obtained for the blue channel with values ranging from -0.244 to 1.271, with 0.087 for the system on its own. The green sensor was associated with the highest SERD values ranging from -0.299 to 1.343. Note the SERD value without the interference of filters gave 0.213, hence the inclusion of a Wratten 99 (green) filter is predicted to improve the contrast considerably. It is of interest to note that it is predicted that the inclusion of a Wratten 99, 74, 61 or 58 (green) filter recorded on the combined CCD array will give inferior contrast to images recorded on the green sensor alone. The inclusion of green filters into the imaging system and the recording of images onto the green sensor is predicted to result in a sizeable increase in vessel contrast on the recording media.

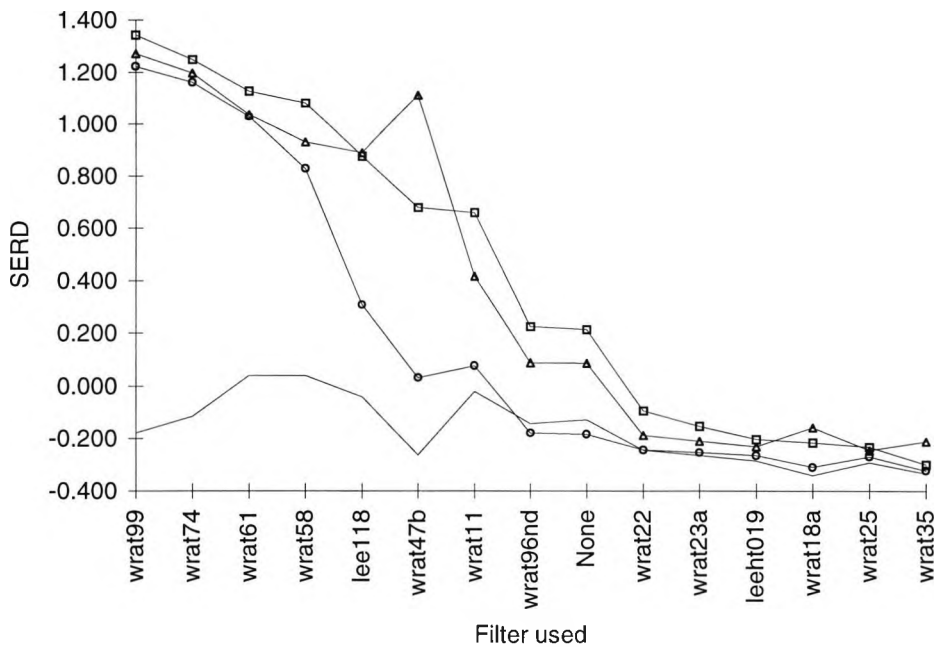


Figure 3.16 shows the SERD values for the CCD sensor combined (solid line with no symbols), red sensor (open circles), green sensor (open squares), and blue sensor (open triangles), for differing filters, in descending order of green sensor response.

3.8 Experimental verification for CCD

3.8.1 Introduction

Although the calculation of the SERD value is a useful prediction of vessel contrast it is prone to a number of experimental artefacts. As mentioned such artefacts are associated with the difficulties in measuring the reflectances of certain target areas (vessel and conjunctiva). The experimental derivation of conjunctival vessel contrast has not yet been considered. Anecdotal findings are usually used to govern the use of filters and detector types (Meyer, 1988; Stevenson and Chawala, 1994; Willingham *et al.*, 1995). This is also the case when deciding the best filter to be used for retinal imaging (Delori, 1977). From the SERD calculations it is predicted that images of conjunctival vessels are best taken using a green filter (Wratten 99) on the green CCD sensor. Less contrast is predicted for vessels recorded on the green sensor without filtration. Images recorded on the combined sensor through a green filter are only slightly superior to images recorded on the combined sensor without filtration, but both of these are predicted to be inferior to images recorded on the green CCD with green filtration. Deriving a model which best describes the entirety of a densitometric profile taken across conjunctival vessels acquired under differing optical configurations, allows the background to blood vessel intensity difference or contrast to be measured. Experimental models were derived to negate the need to predict vessel characteristics from noisy data which may lead to spurious findings. These models were tested using digital images of conjunctival vessels.

3.8.2 Gaussian model of densitometric profile

Digital images of the conjunctiva of one individual were obtained from the red, green, blue and combined CCD array, through various filters, and viewed using Matlab for

Windows © Version 4.2c1 software. All images were obtained within the same session. Densitometric profiles were manually orientated to be perpendicular to the vessels direction. Densitometric data was imported into a Microsoft Excel (version 5.0a) spreadsheet. In agreement with the findings of Chaudhuri *et al* (1989), and Zhou *et al* (1994), densitometric profiles resembled a Gaussian curve. The following equation of Gaussian curve was fitted by the least squares method, where A is the amplitude of the Gaussian curve, B is the midpoint of the curve, and C is the background intensity, as shown in figure 3.17. Using the solve function (in Microsoft Excel version 5.0a) a least squares fit was obtained by allowing parameters A , B , C , and σ to change.

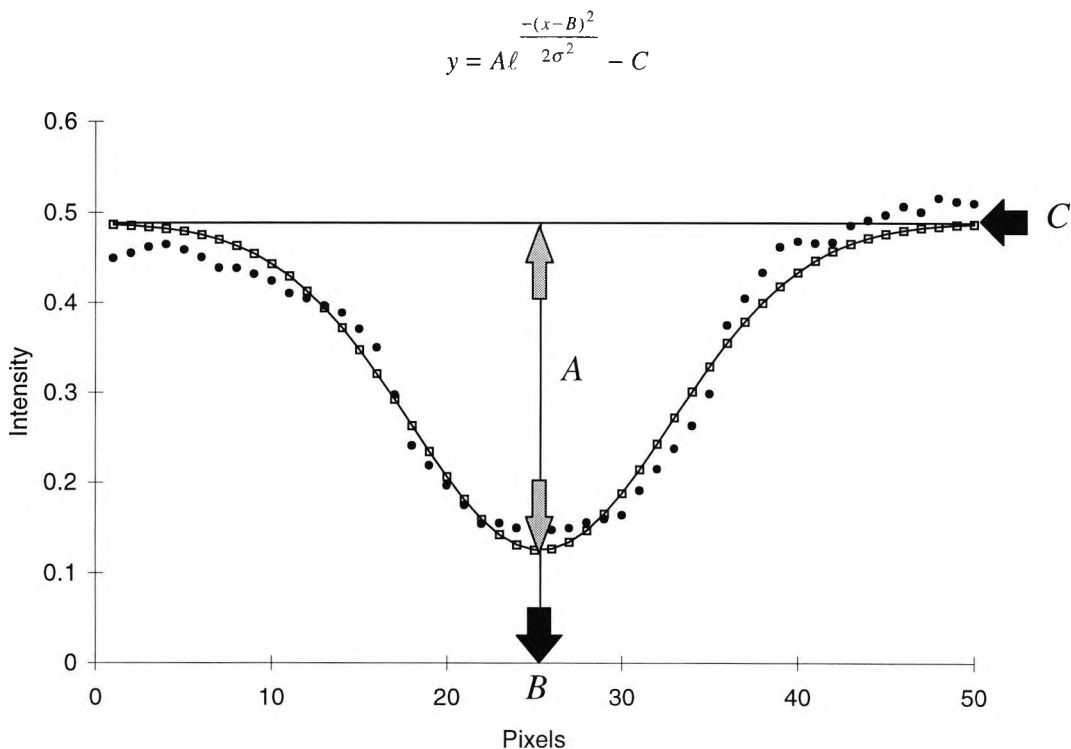


Figure 3.17 shows a densitometric profile taken across an arterial vessel of the conjunctiva (solid circles), and a least squares fitted Gaussian curve (open squares), where A is the amplitude of the Gaussian curve, B is the midpoint of the curve, and C is the background intensity. Note σ equals 7.53 pixels.

Evidently the Gaussian curve appears to overestimate the darkness of the vessels centre. To assess the agreement further regression analysis was performed. Figure 3.18 shows a plot of residuals against the least squares fitted Gaussian model for the raw data shown in figure 3.17. Over estimation of the data by the model is shown by the 6 positive residuals observed at model values between 0.12 and 0.14. The assumption of normality was assessed by a means of a normal plot of the residuals which appeared to be linear and evenly spread about the origin. The ability of the model to predict the raw data was made by regression analysis and is displayed as an analysis of variance table in table 3.4. To consider the goodness-of-fit of the model to the data we considered the proportion of the total variation explained by the model. This was done by considering the R^2 value which is the sum of the squares explained by the model as a percentage of the total sum of squares i.e. $R^2 = 0.830 / 0.857 = 0.968$.

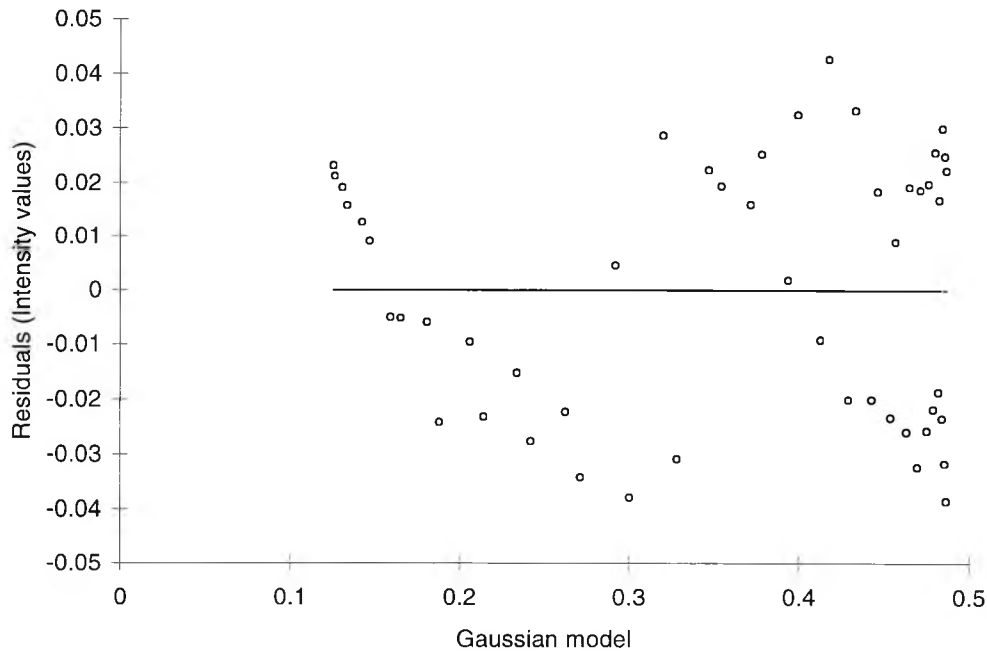


Figure 3.18 shows a plot of residuals against the least squares fitted Gaussian model for the raw data shown in figure 3.17.

Source of variation	Degrees of freedom	Sums of Squares	Mean squares	F	P
Regression	1	0.8303	0.8303	1474.7	$P < 0.0001$
Residual	48	0.02703	0.00056		
Total	49	0.85732			

Table 3.4 shows an analysis of variance table corresponding to the ability of the Gaussian model to predict the densitometric profile shown in figure 3.17. Note the R^2 value was 0.968.

Clearly the Gaussian curve, fitted by a method of least squares, offers of good overall prediction of the densitometric profile. However, the Gaussian model over predicts the amplitude of the profile at the vessels' centre. This was not the case for densitometric profiles taken across vessels deeper in the conjunctiva. Deeper vessels are subjected to greater image blurring and hence become more Gaussian in shape. To measure a vessels contrast exact quantification of the densitometric profile for both the vessel surround and centre was required. Hence this method was rejected in favour of a more appropriate model which might predict the vessels' central minima with greater accuracy.

Pappas and Lim (1988) modelled coronary arteries from their X-ray projections. Vessels were assumed to be generalised cylinders with elliptical cross sections. They assumed that the point spread function of the optical system was Gaussian. Hence, Gaussian blurred cylindrical profiles were fitted, by a least squares method, to densitometric profiles obtained perpendicular to the vessels direction. Miles and Nutall (1993) observed images of blood vessels in the cochlea filled with a contrast agent (fluorescein dye). They proposed that vessels were composed of contiguous circular cylinders. Hence, a densitometric profile across a vessel could be described by a blurred half-elliptical projection. Optical blurring was achieved by convolving the

half-elliptical profile with a Gaussian function. The sum of the absolute differences between the model and the manually specified intensity profile were minimised to achieve an optimal fit. A similar cylindrical model was derived by Shmueli *et al* (1983) to describe densitometric profiles obtained across vessels imaged during catheter arteriography. Gaussian blurred cylindrical models were fitted to densitometric profiles obtained across images of conjunctival vessels. However, before these cylindrical models could be applied the image distortion of the optical system needed to be ascertained.

3.8.3 Image blurring of optical system

Pappas and Lim (1988) proposed that the point spread function of an optical system could be described by a Gaussian curve. Hence any model must be convolved with an appropriate Gaussian function of a given σ before application to the raw densitometric data. To obtain the degree of Gaussian blurring an understanding of imaging geometry is needed. As indicated earlier in this chapter images of the dextro bulbar conjunctiva were taken on a Nikon FS-2 photo slit-lamp at a working distance of 92mm. At this distance images were sharply focused in the eyepiece, and were concurrently focused on the image plane of the CCD sensor. Observation of the conjunctiva was achieved through the eyepieces at the highest magnification. Note that the digital imaging optics correspond to the image perceived through the right eye piece only.

To measure Gaussian blurring images of a horizontal step edge were taken at optimal focus under dark field illumination. Ten images were obtained, on separate sessions, by conventional binocular focus of the step edge. Another 10 images were taken, on separate sessions, by viewing the step edge through the right eyepiece, with the observer's left eye, while the right eye fixated on a distant cross-hair target (in the hope of stabilising the observers accommodation). In addition the observation system was controlled by a micrometer screw gauge. Ten independent assessments of focus (achieved by the previous monocular method) were averaged and an image taken. This procedure was repeated 10 times to give the most accurate attempt at optimal focus. The above methods will be termed binocular, monocular, and exact monocular respectively. Note that conventional slit-lamp biomicroscopy is achieved by binocular focus.

Vertical densitometric slices were taken from each image ($n=30$) over the entire image plane (1024 pixels) using Matlab for Windows © Version 4.2c1 software, incorporating both the dark and bright areas of the step edge. The mean grey level for dark and light portions of the step edge were calculated from the last 50 pixels of the 1024 pixel slice. The image slice was then truncated to 25 pixels centred about the nearest pixel with grey level intensity half way between mean light and dark values. The truncated slice was then interpolated linearly with 10 gradations between each pixel. A theoretical step edge was derived with light and dark values equivalent to the mean values calculated above. The transition of the theoretical step edge from light to dark was manually positioned closest to the half way inter-pixel value on the raw data slice. The theoretical step edge was convolved with a Gaussian function, of differing sigma's, to give a least squares fit to the raw interpolated image slice. The Gaussian convolution of the interpolated theoretical step edge was performed over a ± 47 inter-pixel width (or ± 4.7 pixel width). The σ which produced the best fit to the

interpolated data was divided by 10 to give the σ value of the Gaussian function to convolve raw pixel data. Figure 3.19 shows a truncated linearly interpolated 25 pixel slice across a step edge, a theoretical step edge, and Gaussian blurring of the theoretical step edge to give a best least squares fit to the densitometric profile. For the example given, the theoretical step edge was convolved with a Gaussian curve of σ 1.04 to give a least squares fit to the interpolated densitometric data. A σ of 1.04 pixels is equivalent to a real size of $5.52\mu\text{m}$.

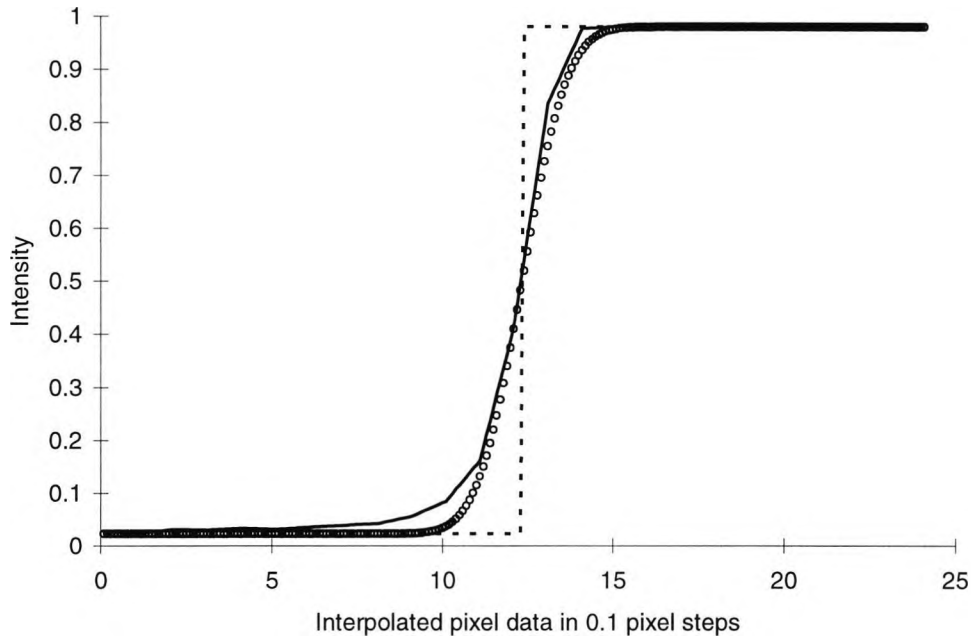


Figure 3.19 shows a truncated linearly interpolated 25 pixel slice across a step edge (solid line), a theoretical step edge (dotted line), and Gaussian blurring of the theoretical step edge to give a least squares fit to the densitometric profile (open circles).

The Gaussian curve appears to give a good estimate of the interpolated pixel data. However, the real data appears slightly skewed: this may be explained by diffractive effects at the step edge or difficulty in positioning the theoretical step edge. For the purposes of this investigation this effect was ignored. To assess the agreement further regression analysis was performed. Figure 3.20 shows a plot of residuals against the least squares fitted Gaussian blurred step edge model for the raw data shown in figure 3.19. There is a non-linear relationship between the model and the raw data shown by the curved association between the residuals and model values. However, a good fit was obtained at the minimum, maximum, and mid intensity values.

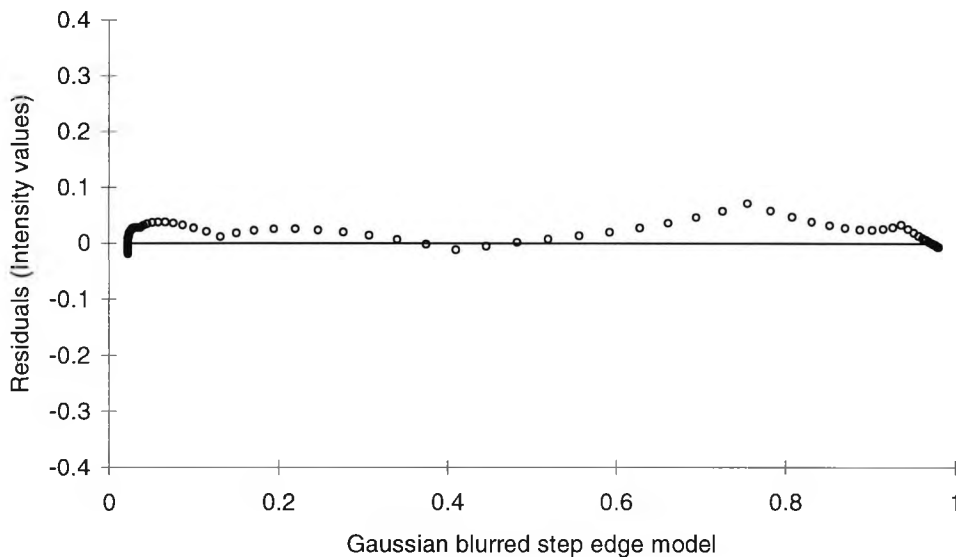


Figure 3.20 shows a plot of residuals against the least squares fitted Gaussian blurred step edge model for the raw data shown in figure 3.19

The assumption of normality was assessed by means of a normal plot of the residuals which showed the positive residual bias indicated in Figure 3.20. An analysis of variance table is shown in table 3.5. Goodness-to-fit of the model to the data was obtained by calculating the R^2 value, which in this case was 0.999. This near perfect R^2 value was due to the large amount of minima and maxima data.

Source of variation	Degrees of freedom	Sums of Squares	Mean squares	F	P
Regression	1	48.4958	48.4958	193286	$P < 0.0001$
Residual	239	0.05997	0.00025		
Total	240	48.5558			

Table 3.5 shows an analysis of variance table corresponding to the ability of the Gaussian model to predict the densitometric profile shown in figure 3.19. Note the R^2 value was 0.999.

For the purposes of measuring Gaussian blurring the method outlined above was considered satisfactory. However, it must be acknowledged that linear interpolation between pixels on the densitometric profile was not ideal. A quadratic or cubic interpolation may have been more appropriate, but the linear interpolation was considered satisfactory.

Table 3.6 shows the σ needed to Gaussian blur a theoretical step edge, to give a least squares fit to the densitometric profile of each of the 30 images. Note that the σ values are in pixels i.e. inter-pixelated σ value divided by 10. The binocular method was associated with a greater degree of defocus ($\sigma = 1.655 \pm 0.337$), than monocular focus ($\sigma = 1.156 \pm 0.223$), and exact monocular focus ($\sigma = 0.929 \pm 0.084$). Analysis of variance revealed significant differences between the σ values for each method ($P < 0.0001$). A multiple comparisons test using the Bonferroni correction method

revealed that the level of σ blurring for binocular focus was statistically higher than monocular and exact monocular methods ($P < 0.0001$, $P < 0.0001$ respectively). Although the exact monocular focus was associated with a 0.227 σ decrease in Gaussian blurring compared to monocular focus, the difference was not statistically significant ($P = 0.127$).

Image	Binocular	Monocular	Exact monocular
1	1.413	1.075	1.050
2	1.187	0.921	1.050
3	1.565	1.257	0.934
4	1.708	0.952	0.901
5	1.160	0.996	0.939
6	1.966	1.507	0.942
7	1.949	1.453	0.942
8	1.580	1.385	0.915
9	1.856	1.038	0.853
10	2.163	0.977	0.764
Average	1.655	1.156	0.929
Standard deviation	0.337	0.223	0.084

Table 3.6 shows the σ needed to Gaussian blur a theoretical step edge, to give a least squares fit to the densitometric profile of each of the 30 images.

To investigate the effects of defocus, optimal binocular focus of the step edge was achieved, and an image taken. By deliberately defocusing the observation system by use of a micrometer screw gauge images were obtained from 0 to 1mm towards the step edge (in 0.1mm intervals), from 1 to 1.6 mm towards the step edge (in 0.2mm intervals), from 0 to 1mm away from the step edge (in 0.1mm intervals), and from 1 to 1.4mm away from the step edge (in 0.2mm intervals). The σ blurring of the theoretical step edge, measured from each image, was calculated on 2 separate occasions and is graphically represented in figure 3.21.

Figure 3.21 shows that superior focus may be achieved by moving the observation optics ~ 0.1 mm towards the object of interest from the position of optimal binocular focus. This characteristic may be unique to each slit-lamp and may indicate that an image focused in the eyepiece will not exactly correspond to optimal focus at the image plane, and/or the observer may have a slight refractive error. However, this effect was not considered significant. The ability to return to the same point of focus of the step edge was estimated by measuring the distance of the observation optics from a referenced point with a micrometer screw gauge. The 95% confidence interval of repeatability for 10 attempts at focus was ± 0.0836 mm, indicating that the observer can find the same position of optimal focus within $\sim \pm 0.1$ mm. The mean and standard deviation of σ Gaussian blurring of the step edge (for session one and two shown in figure 3.21) at 0, 0.1, and -0.1 mm of defocus was 1.325 ± 0.413 . This value is within the range previously calculated for σ blurring of 1.655 ± 0.337 . Hence, the line spread function of our optical system was considered to be equivalent to a Gaussian curve with a $\sigma = 1.655 \pm 0.337$. Hence, any geometric model which is used to describe a feature in image space must be convolved with a Gaussian blurring function with a $\sigma = 1.655$.

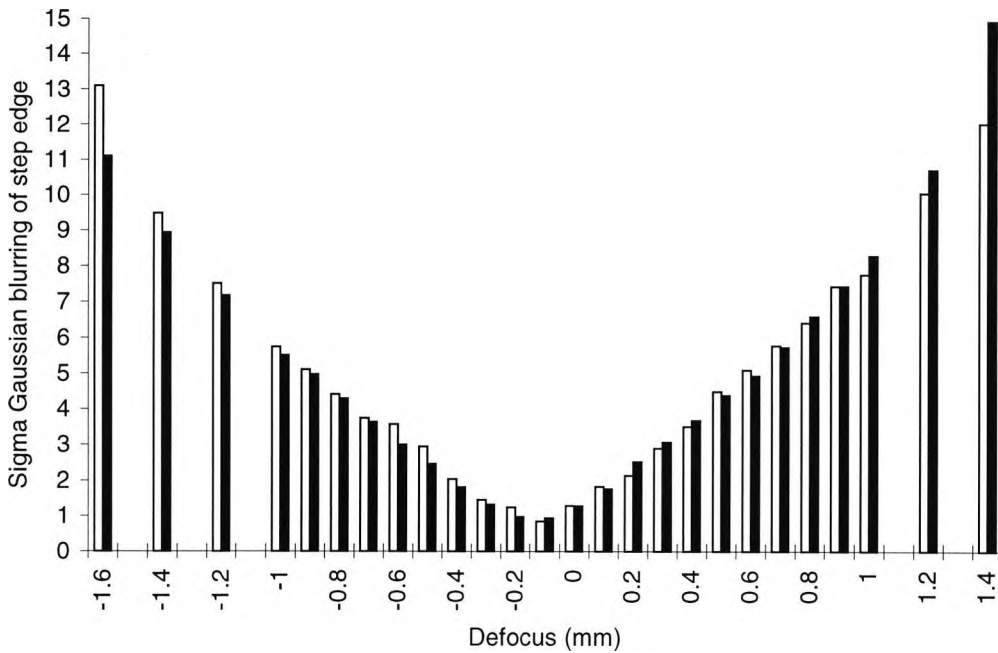


Figure 3.21 shows σ blurring of step edge with defocus of Nikon FS-2 photo slit-lamp observation optics where negative defocus represents movement towards the step edge and positive movement away from the step edge. Open bars represents session one, solid bars session 2.

3.8.4 Cylindrical model of densitometric profiles

In accordance with the methods of Shmueli *et al* (1983), Pappas and Lim (1988), Miles and Nutall (1993) densitometric profiles across conjunctival vessels can be described by Gaussian blurred cylindrical projections. The following equation of a Gaussian blurred cylindrical profile was fitted by a least squares method to densitometric profiles across conjunctival vessels, where B is the midpoint of the curve, κ is proportional to density of the blood column, C is the background intensity, r is the radius of the cylinder, and $\otimes G\sigma$ represents convolution with a Gaussian function of $\sigma = 1.655$. Using Microsoft Excel version 5.0a software a least squares fit was obtained allowing parameters B , κ , C and r to change. The application of this equation to a densitometric profile is shown in figure 3.22.

$$y = \left(C - \left(\kappa \times \sum_{B-r}^{B+r} \sqrt{r^2 - (x-B)^2} \right) \right) \otimes G\sigma$$

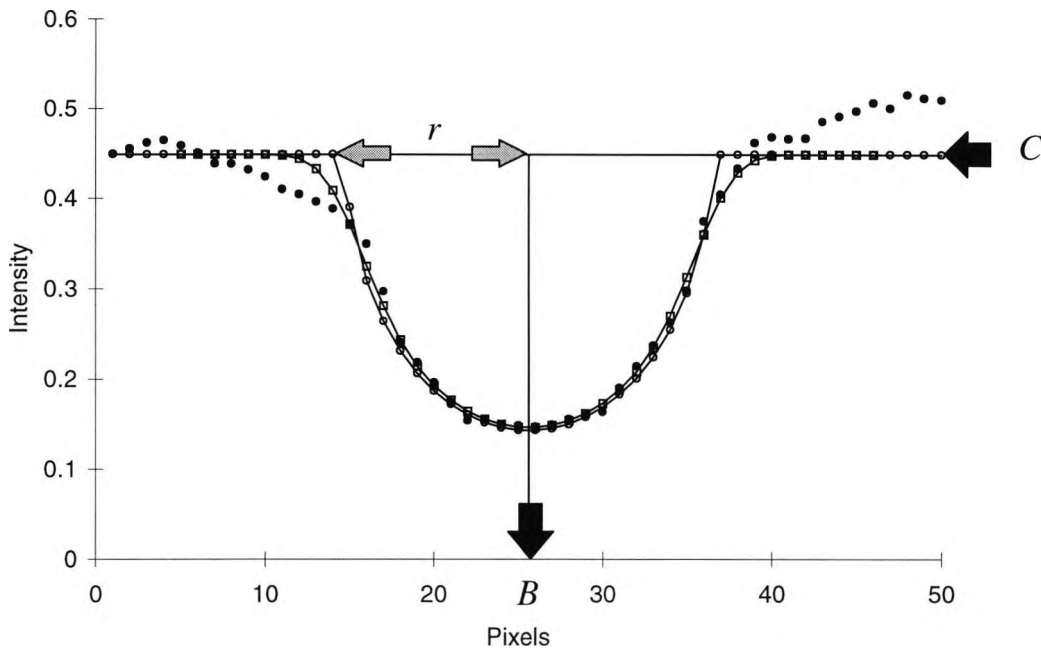


Figure 3.22 shows a densitometric profile across an arterial vessel of the conjunctiva (solid circles), cylindrical profile (open circles), and a blurred cylindrical profile convoluted with a Gaussian function with $\sigma = 1.655$ (open squares), where B is the midpoint of the curve, C is the background intensity, and r is the radius of the cylinder.

The Gaussian blurred cylindrical model gives a good estimate of the densitometric data, and appears to fit more closely to the central portion of the densitometric profile than the Gaussian curve model. Figure 3.23 shows a plot of residuals against the least squares fitted Gaussian model for the raw data shown in figure 3.22.

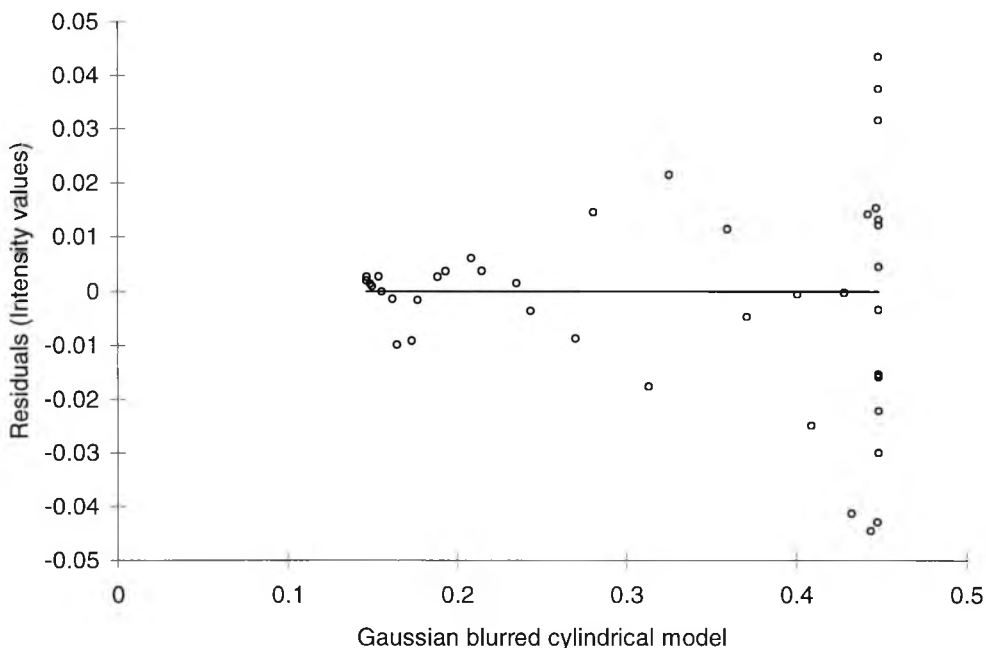


Figure 3.23 shows a plot of residuals against the least squares fitted Gaussian blurred cylindrical model for the raw data shown in figure 3.22.

Figure 3.23 indicates that the residuals have greater variability towards the peripheral part of the densitometric profile. However, the model gives a good description of the densitometric data for intensity values from ~ 0.14 to ~ 0.4 . The assumption of normality was assessed by a means of a normal plot of the residuals which appeared to be linear and evenly spread about the origin. An analysis of variance table is shown in table 3.7. As a measure of goodness-to-fit an R^2 value of 0.975 was obtained. Note that the degrees of freedom for Gaussian blurred models are less than those for the Gaussian curve model (see table 3.4). Gaussian blurring is performed with a one dimensional ± 4 pixel filter, hence the model profile is 8 pixels less than the raw densitometric profile. The Gaussian curve model is applied over the entirety of the densitometric data.

Source of variation	Degrees of freedom	Sums of Squares	Mean squares	F	P
Regression	1	0.66927	0.66927	1537.82	$P < 0.0001$
Residual	40	0.01741	0.00044		
Total	41	0.68667			

Table 3.7 shows an analysis of variance table corresponding to the ability of the Gaussian blurred cylindrical model to predict the densitometric profile shown in figure 3.22. Note the R^2 value was 0.975.

Although the Gaussian blurred cylindrical model appeared to offer a superior description of the densitometric data compared to the performance of the Gaussian model, it failed to adequately describe vessel edges. This can be observed in figure 3.22 by the gap between the densitometric data and Gaussian blurred cylindrical model at the vessels' edges. It was assumed that this may be due to the transmission characteristics of the vessels' wall. Hence an attempt was made to derive tubular models.

3.8.5 Tubular models of densitometric profiles

The mathematical model described by Rassam *et al* (1994) depicted a densitometric profile across a retinal vessel by two concentric circles, the inner circle representing the blood column and the outer circle representing the vessel wall. The thickness of an arterial wall was one sixth that of the blood column width, and the venous wall one tenth of its blood column. Rassam *et al* (1994) proposed the presence of 'kick points' which demarcate the transmission profile of the blood filled vessel lumen from the profile of the vessels wall. However, these inflections were identified manually from the densitometric profile, and no attempt was made to model this transition.

To investigate the relationship between vessel wall to lumen size ratio, a transverse section of human bulbar conjunctiva ($n=1$, aged 14 years) was observed under light microscopy ($\times 80$). A microscopic graticule eyepiece (Vickers, England) was used to measure lumen, and vessel wall thickness. Only those arteries and veins that were near circular in section were measured. Where vessels showed elliptical cross sections the lumen and wall size were determined along the smaller dimension. Vessels that had been deformed during histological preparation were ignored. The outer wall diameter of a vessel was measured from one external surface of the tunica adventitia to the other along a direction governed to be the centre of the vessel. The diameter of a vessel lumen was measured between the internal surface of the tunica intima

(endothelial layer) in the same direction as the vessel wall measurement. In addition the depth of the vessel was measured from the superficial mucus layer to the most anterior point on the vessel. To prevent repetition of measuring the same vessel only one histological preparation of the series of sections was used. The histological transverse section was taken 7mm from the limbus. Seven arterioles and eight veins were measured. A mean of 4 measures of each vessel, taken on separate sessions, were averaged, to give a mean vessel depth, outer and internal diameter. Table 3.8 summarises the results for the vessel measured.

Bulbar conjunctival	N	Internal diameter	External diameter	Depth	Wall size / Lumen size
Arteriole	7	19.6±5.18µm	41.0±7.00µm	111.8±18.4µm	0.590±0.216
Vein	8	45.5±19.8µm	54.3±20.7µm	127.2±33.6µm	0.120±0.062

Table 3.8 lists the mean ± standard deviation, depth, internal and external diameter of the 7 arterioles and 8 veins measured. The calculated ratio of wall size to lumen size is shown in the final column.

The ratio of wall size to lumen size for the veins (0.120±0.062) was similar to the figure of 0.1 used by Rassam *et al* (1994) and quoted by Williams *et al* (1988). Arterioles had a ratio of 0.590±0.216 indicating that wall sizes of bulbar conjunctival arterioles are half the thickness of the lumen dimension. This figure is considerably higher than the ratio of 0.166 used by Rassam *et al* (1994) and quoted by Williams *et al* (1988). However, our figure has a large standard deviation indicating a sizeable variation in the dimensional characteristics of conjunctival arterioles. The vessels measured lie in excess of 100µm from the conjunctival surface. However, as indicated by the large standard deviations vessel depth can vary enormously giving rise to the characteristic appearance of buried and superficial vessel on the conjunctival surface. For the purposes of our model we will use the ratios quoted by Rassam *et al* (1994) and Williams *et al* (1988) of 0.1 for veins and 0.166 for arteries. However, we acknowledge, from the measurements taken, that the arterial ratio may not best describe conjunctival arterioles.

The following equation of a Gaussian blurred tubular arterial profile was fitted by a least squares method to densitometric profiles across conjunctival vessels, where B is the midpoint of the curve, κ_1 is proportional to density of the blood column, κ_2 is proportional to density of the vessels wall, C is the background intensity, r is the radius of the cylinder, and $\otimes G\sigma$ represents convolution with a Gaussian function of $\sigma = 1.655$. Using Microsoft Excel version 5.0a software a least squares fit was obtained (using the solving function) allowing parameters B , κ_1 , κ_2 , C and r to change. The application of this equation to a densitometric profile is shown in figure 3.24.

$$y = \left(C - \left(\left(\kappa_1 \times \sum_{B-r}^{B+r} \sqrt{r^2 - (x-B)^2} \right) + \kappa_2 \times \left(\left(\sum_{B-4/3r}^{B+4/3r} \sqrt{(4/3)^2 r^2 - (x-B)^2} \right) - \left(\sum_{B-r}^{B+r} \sqrt{r^2 - (x-B)^2} \right) \right) \right) \right) \otimes G\sigma$$

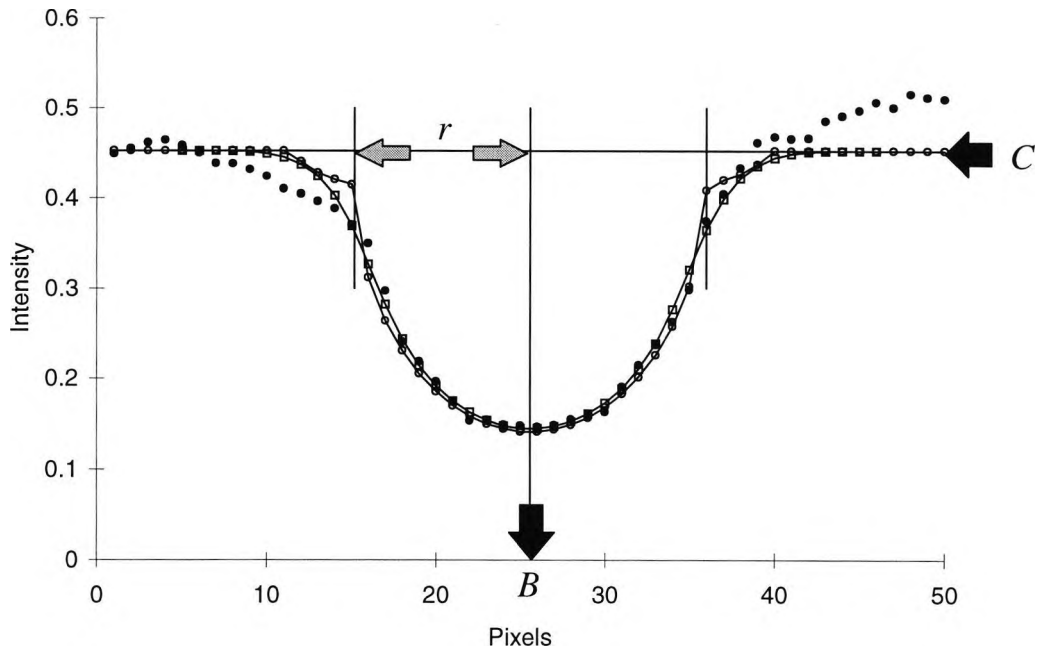


Figure 3.24 shows a densitometric profile across an arterial vessel of the conjunctiva (solid circles), tubular profile, with wall size one sixth lumen diameter (open circles), and a blurred tubular profile convoluted with a Gaussian function with $\sigma = 1.655$ (open squares), where B is the midpoint of the curve, C is the background intensity, and r is the predicted radius of the lumen.

The Gaussian blurred tubular arterial model gives a good estimate of the densitometric data. Figure 3.25 shows a plot of residuals against the least squares fitted Gaussian blurred tubular model for the raw data shown in figure 3.24.

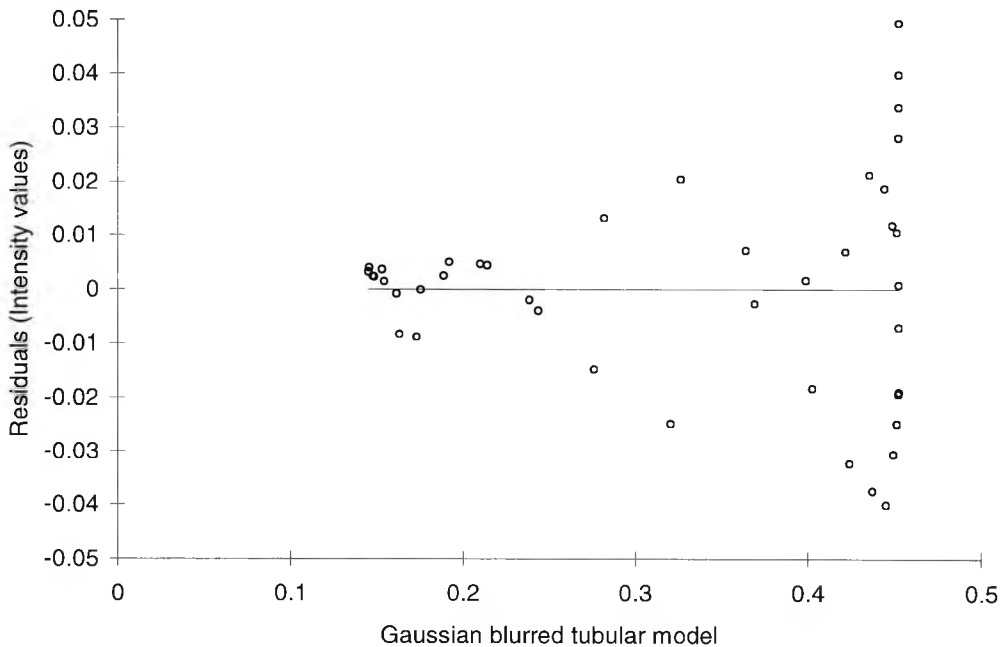


Figure 3.25 shows a plot of residuals against the least squares fitted Gaussian blurred tubular model for the raw data shown in figure 3.24.

As with the cylindrical model figure 3.25 indicates that the residuals have greater variability towards the peripheral part of the densitometric profile. However, the model gives a good description of the densitometric data for intensity values from ~0.14 to ~0.4. The assumption of normality was assessed by a means of a normal plot of the residuals which appeared to be linear and evenly spread about the origin. An analysis of variance table is shown in table 3.9. As a measure of goodness-to-fit an R^2 value of 0.977 was obtained.

Source of variation	Degrees of freedom	Sums of Squares	Mean squares	F	P
Regression	1	0.67112	0.67112	1726.23	P<0.0001
Residual	40	0.01555	0.00039		
Total	41	0.68667			

Table 3.9 shows an analysis of variance table corresponding to the ability of the Gaussian blurred tubular model to predict the densitometric profile shown in figure 3.24. Note the R^2 value was 0.977.

In addition to this arterial model a venular model was derived based on a vessel wall thickness one tenth of the lumen size. The equation is similar to the previous tubular model, the only difference being that the radius of the outer vessel wall is $\times 6/5 r$, instead of $\times 4/3 r$ for the arterial model.

$$y = \left(C - \left(\left(\kappa_1 \times \sum_{B-r}^{B+r} \sqrt{r^2 - (x-B)^2} \right) + \kappa_2 \times \left(\left(\sum_{B-6/5r}^{B+6/5r} \sqrt{(6/5)^2 r^2 - (x-B)^2} \right) - \left(\sum_{B-r}^{B+r} \sqrt{r^2 - (x-B)^2} \right) \right) \right) \right) \otimes G\sigma$$

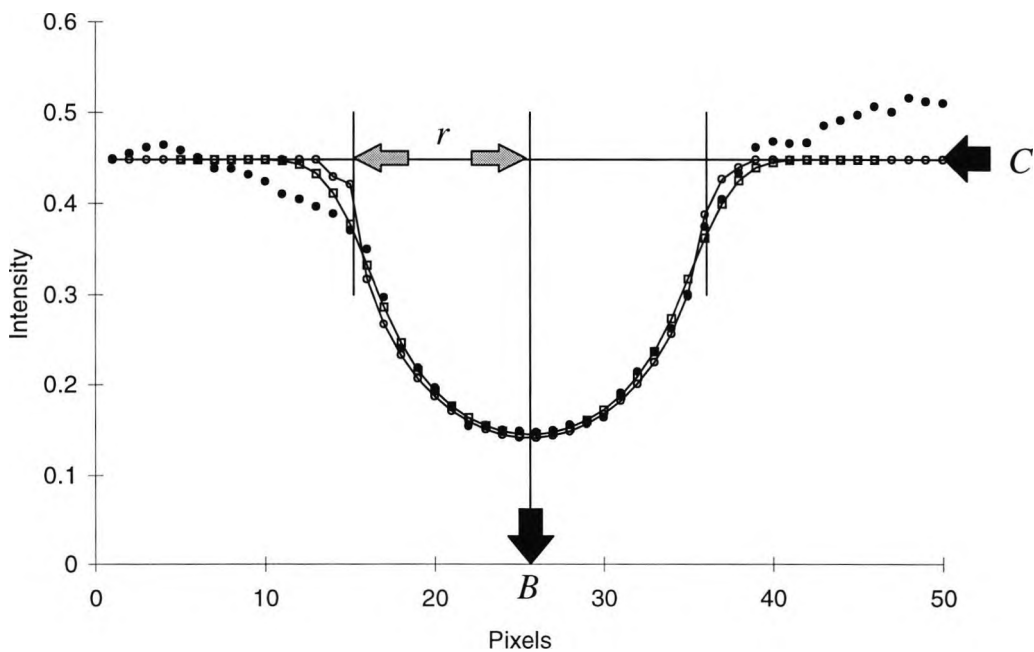


Figure 3.26 shows a densitometric profile across an arterial vessel of the conjunctiva (solid circles), tubular profile, (with wall size one tenth lumen diameter (open circles), and a blurred tubular profile convoluted with a Gaussian function with $\sigma = 1.655$

(open squares), where B is the midpoint of the curve, C is the background intensity, and r is the predicted radius of the lumen.

The Gaussian blurred tubular venular model gives a good estimate of the densitometric data. Figure 3.27 shows a plot of residuals against the least squares fitted Gaussian model for the raw data shown in figure 3.26.

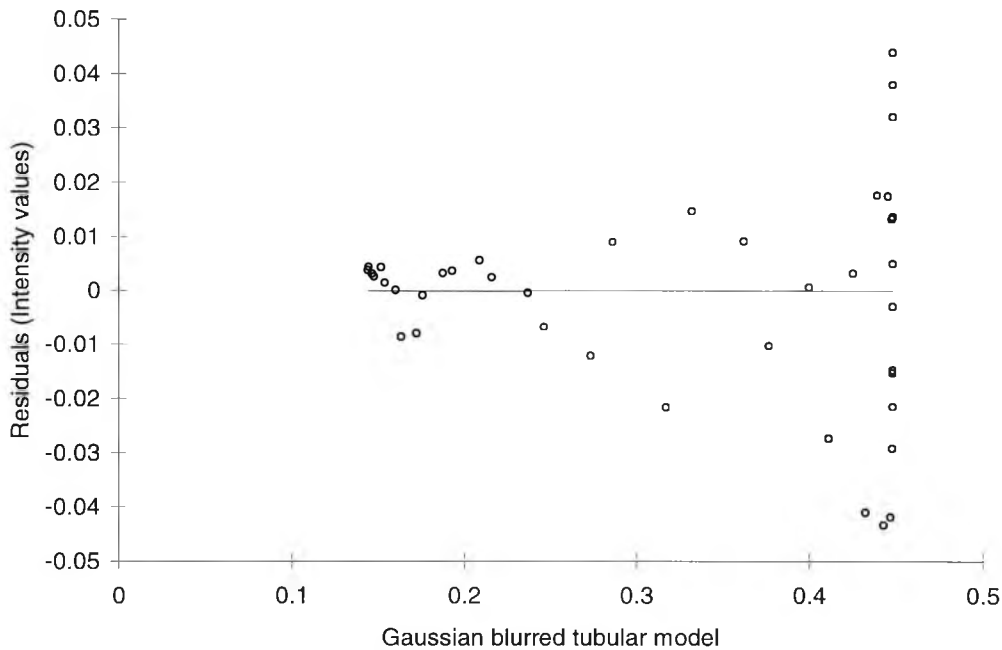


Figure 3.27 shows a plot of residuals against the least squares fitted Gaussian blurred tubular model for the raw data shown in figure 3.26.

As with the previous tubular and cylindrical model figure 3.27 indicates that the residuals have greater variability towards the peripheral part of the densitometric profile. However, the model gives a good description of the densitometric data for intensity values from -0.14 to -0.4 . The assumption of normality was assessed by a means of a normal plot of the residuals which appeared to be linear and evenly spread about the origin. An analysis of variance table is shown in table 3.10. As a measure of goodness-to-fit an R^2 value of 0.974 was obtained. This was slightly less the R^2 value obtained for the arterial model (0.977), and similar to the R^2 value for the cylindrical model (0.975).

Source of variation	Degrees of freedom	Sums of Squares	Mean squares	F	P
Regression	1	0.66911	0.66911	1523.68	$P < 0.0001$
Residual	40	0.01757	0.00044		
Total	41	0.68667			

Table 3.10 shows an analysis of variance table corresponding to the ability of the Gaussian blurred tubular model to predict the densitometric profile shown in figure 3.24. Note the R^2 value was 0.974.

The R^2 values for the cylindrical, and both tubular models were higher than the figure for the Gaussian curve model (0.968). This may indicate that shape modelling may be a superior method of describing densitometric data. However, the R^2 figures quoted

are for one densitometric profile and are not indicative of the variety of vessels observed on the conjunctiva. To investigate the goodness-to-fit of the differing models 108 images slices (acquired using Matlab for Windows © Version 4.2c1) were manually taken from 12 images of 12 individuals from vessels of differing width and depth (7 to 11 slices per image). The R^2 value was calculated for the Gaussian curve, Gaussian blurred cylinder, Gaussian blurred arterial, and Gaussian blurred venular models. Figure 3.28 shows the R^2 values for the Gaussian curve model plotted against Gaussian half height width for the 108 vessels measured. The fitted linear regression line indicates a near constant ability of the Gaussian curve model to predict densitometric data across vessels of different widths. Figure 3.29 shows the R^2 values for the Gaussian blurred tubular model for veins against blood column width for 108 vessels measured. Note that this figure is similar to the plots obtained for the blurred cylindrical, and arterial tubular model. Unlike the Gaussian curve model, the linear regression line indicates an improvement in the ability of the tubular model to predict densitometric data across wider vessels.

Table 3.11 shows the mean R^2 and standard deviation of each model for the 108 densitometric profiles measured. Despite the fact that the venular and arterial models appeared to perform the best, an analysis of variance did not reveal a significant difference between the R^2 values ($P=0.655$).

It is noteworthy, that the x -axis in figures 3.28 and 3.29 represent width measurements from the same 108 densitometric slices. The different horizontal spread of data indicates that the Gaussian half height width measures differently to tubular width. This forms the subject of chapter 4 which compares a variety of manual, semi-automated, and automated methods of measuring vessel width. However, for the purposes of this chapter the Gaussian blurred tubular model was used to measure the amplitude of densitometric profiles. This was chosen for its ability to adequately describe the central portion of the densitometric profile referring to the vessels' apex, and its superior, although not significant, R^2 performance at modelling 108 vessel profiles. Arterial and venular models performed equally, hence the venular model was randomly chosen as the method of choice.

Model	N	Mean \pm SD R^2 value
Gaussian curve model	108	0.938 \pm 0.054
Gaussian blurred cylindrical model	108	0.943 \pm 0.060
Gaussian blurred tubular model (venular)	108	0.944 \pm 0.060
Gaussian blurred tubular model (arterial)	108	0.944 \pm 0.057

Table 3.11 shows the mean R^2 and standard deviation of each model for the 108 densitometric profiles measured. Note that the differences between R^2 values was not significant.

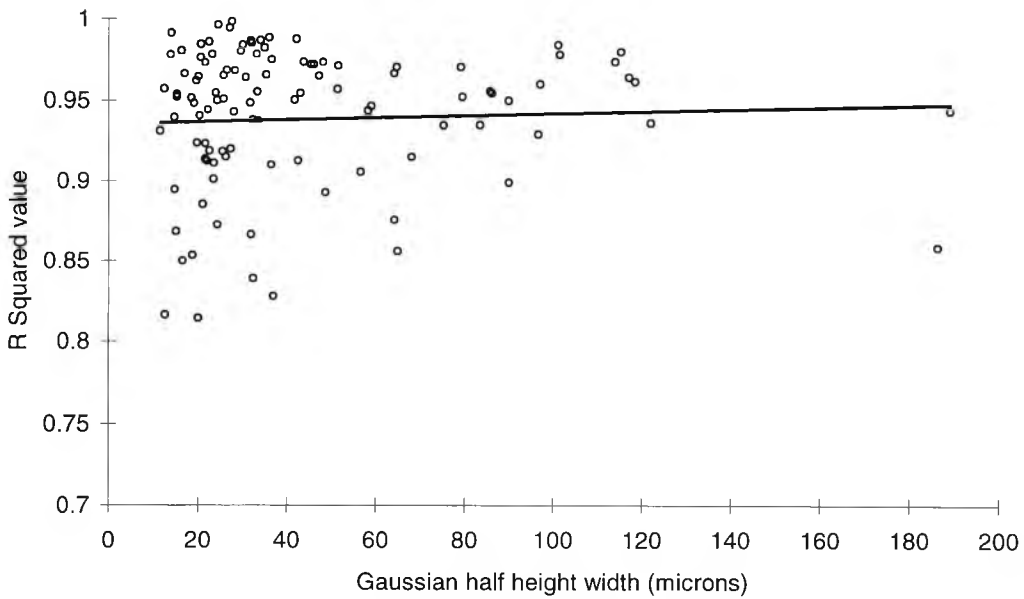


Figure 3.28 shows the R^2 values for the Gaussian curve model plotted against Gaussian half height width for the 108 vessels measured. The fitted linear regression line indicates a near constant ability of the Gaussian curve model to predict densitometric data across vessels of different widths.

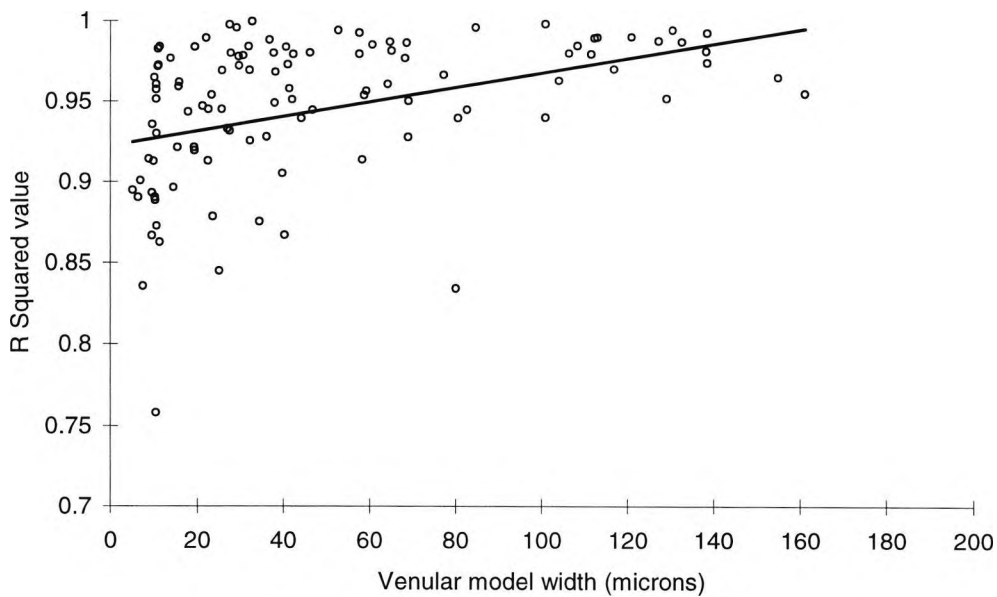


Figure 3.29 shows the R^2 values for the Gaussian blurred tubular model for veins against blood column width for the 108 vessels measured. The linear regression line indicates an improvement in the model to predict densitometric data across larger vessels.

3.8.6 Method of verifying the optimal optical system for the CCD

A single conjunctival vascular bed was digitally imaged repetitively, within the same session, using the Nikon FS-2 photo slit-lamp under a variety of optical configurations. Digital images from the combined CCD were viewed simultaneously on the DSU's monochrome liquid crystal display and an external video monitor. Neutral density filters of differing densities were placed over the illumination turret to produce images which were perceived to give the correct exposure. Images were then imported into a computer via a SCSI card, using Aldus PhotoStyler version 1.1 (Aldus Corporation, Seattle, USA) software. The 24 bit colour image (~4.1MB file size) was separated into its green (G-CCD) and blue CCD (B-CCD) components and saved as separate monochrome 8 bit images (~1.38MB file size). An 8 bit monochrome equivalent of the combined colour image (C-CCD) was also stored (~1.38MB file size). Note that the response from the red CCD was largely ignored due to its poor quality as predicted by the exposure density calculations in table 3.3. Densitometric profiles were manually acquired using Matlab for Windows © Version 4.2c1 software across 3 vessels. The location of the densitometric profiles were chosen to represent a large anterior vessel (anterior ciliary artery), a medium sized anterior vessel (anterior ciliary artery), and a small buried vessel. Vessel locations are shown in figure 3.30.

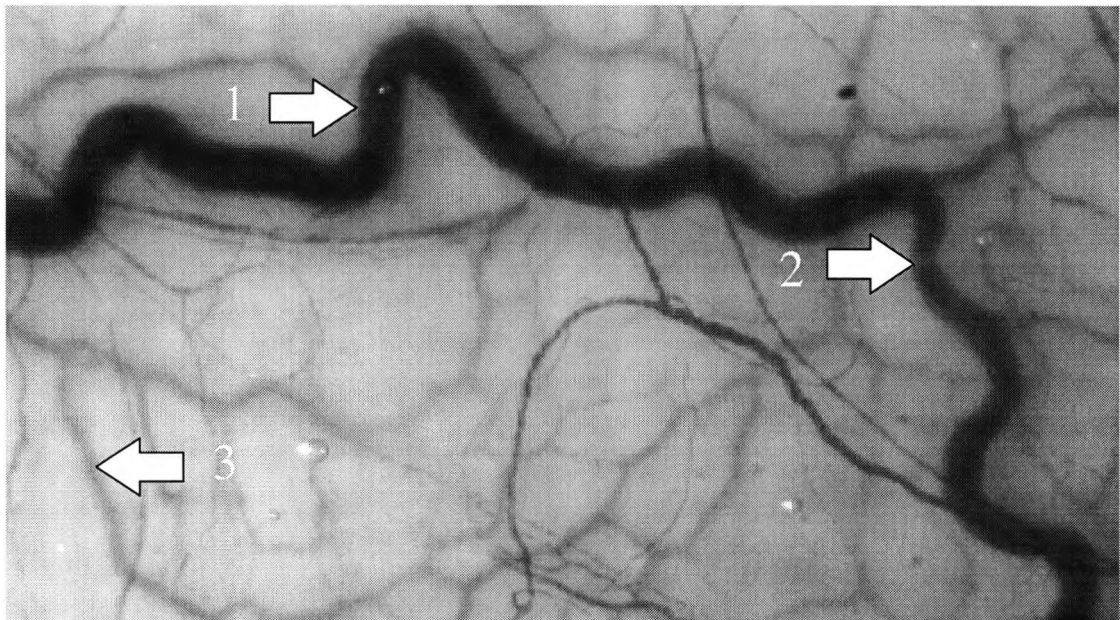


Figure 3.30 shows the location where 3 densitometric profiles were measured for each image taken under differing optical configurations. The dimensions of the image shown is 250×450 pixels, equivalent to 1.33×2.39mm in object space.

A Gaussian blurred tubular model with wall width one tenth larger than the lumen (venular model shown in figure 3.26) was fitted by a least squares method to each densitometric profile. The amplitude and width of the vessel was recorded.

3.8.6.1 Statistical analysis

Measurements of amplitude and width at each location were compared to measurements taken with different optical configurations. For the purposes of this investigation 4 optical configurations were considered and are discussed below. Statistically significant differences in amplitude and width were analysed using an

analysis of variance. When significant differences were found ($P < 0.05$) multiple comparisons between groups were performed using the Bonferroni correction method.

3.8.6.2 E3.1 Effect of recording images on the B-CCD, G-CCD, and C-CCD

Digital images of the conjunctival bed shown in figure 3.30 were taken without filtration. Images appeared over-exposed when taken with the xenon flash on the minimum intensity (power setting 1). Hence, a 0.4 log unit neutral density filter (Wratten 96) was placed over the illumination turret to give images which were perceived as having optimal contrast. The best of 5 images was viewed using Aldus PhotoStyler version 1.1 (Aldus Corporation, Seattle, USA) software. The image from the G-CCD, B-CCD, and C-CCD were then saved. Ten densitometric profiles were measured using Matlab for Windows © Version 4.2c1 across the 3 vessel locations shown in figure 3.30. A venular model was fitted to each densitometric profile and ten measures of vessel amplitude and width were recorded for each vessel location. Making a total of 30 width and 30 amplitude measurements per image. These parameters for each of the 3 images, at each vessel location, were statistically compared. An analysis of variance was used to find overall differences in the data. Multiple comparisons between groups were made using the Bonferroni correction method.

3.8.6.3 E3.2 Effect of recording on the B-CCD, G-CCD, and C-CCD with green filters

Fifty digital images of the conjunctival bed were taken with the xenon flash unit on the minimum setting, through a green (Wratten 99) and neutral density filter (Wratten 96, 0.2 log units) to achieve optimum vessel contrast. Each image was separated into its G-CCD, B-CCD and C-CCD components. One densitometric profile was measured across the 3 vessel locations. The venular model was used to record the amplitude and width of each vessel location, for each image. Hence, 50 measures of width and amplitude, for each vessel location, for each of the 3 types of image, were recorded. These parameters for each vessel location were statistically compared. An analysis of variance was used to find overall differences in the data. Multiple comparisons between groups were made using the Bonferroni correction method.

3.8.6.4 E3.3 Effect of recording on the G-CCD with different green filters

Images taken from the G-CCD were visually assessed as having superior vessel contrast. However, exposure density calculations (table 3.3) predicted that further improvement could be made by introducing green filters over the xenon flash source. To investigate this further 5 green filters, which gave the best predicted vessel contrast from exposure density calculations, were selected and introduced over the illumination optics. Even with the xenon flash source set at its minimum intensity the red-free images viewed on the video output were notably over exposed. Hence, neutral density filters (Wratten 96) of differing densities (0.1 to 1.0 log units, in 0.1 steps) were placed over the illumination optics to give the correct exposure. The five green filters and neutral density filters are listed in table 3.12.

Five images were taken through each filter, and the best of the five chosen. Ten densitometric profiles were taken at each of the 3 vessel locations, taken from the G-CCD image. A venular model was fitted to each densitometric profile and ten measures of vessel amplitude and width were recorded for each vessel location.

Making a total of 30 width and 30 amplitude measurements per image. These parameters for each of the 5 images, taken with each of the green filters listed in table 3.12, at each vessel location, were statistically compared. An analysis of variance was used to find overall differences in the data. Multiple comparisons between groups were made using the Bonferroni correction method.

Green filter used	Neutral density filter used
Wratten 56	0.8 log units
Wratten 57	0.9 log units
Wratten 61	0.6 log units
Wratten 74	0.2 log units
Wratten 99	0.2 log units

Table 3.12 shows the five green filters used and the neutral density filter needed to achieve optimal perceived contrast.

3.8.6.5 E3.4 Effect of recording on G-CCD and C-CCD with and without a Wratten 99 filter

The best of 5 images obtained from the G-CCD without filtration, G-CCD filtered with a Wratten 99 green filter, C-CCD without filtration, and C-CCD filtered with a Wratten 99 green filter were compared. Ten densitometric slices were taken at the 3 vessel locations from each of the 4 images taken with different optical set-ups. A venular model was fitted to each densitometric profile and ten measures of vessel amplitude and width were recorded for each vessel location. A total of 30 width and 30 amplitude measurements were made on each image. These parameters for each of the 4 images, taken with each optical configurations listed above, at each vessel location, were statistically compared. An analysis of variance was used to find overall differences in the data. Multiple comparisons between groups were made using the Bonferroni correction method.

3.8.7 Results using different optical configurations

The results section is divided into 4 parts in accordance with the methodology section. This includes amplitude and width measures of the 3 vessel locations for images recorded on the B-CCD, G-CCD and C-CCD. Amplitude and width measures from images recorded on the B-CCD, G-CCD and C-CCD taken with a green filter. Measurements were taken from images from the G-CCD through different green filters. Also measurements taken on the G-CCD and C-CCD with and without a Wratten 99 (green) filter. Results are presented under their respective headings

3.8.7.1 E3.1 Results of recording images on the B-CCD, G-CCD and C-CCD

Mean amplitude and width measures calculated from the 10 densitometric profiles taken from the 3 vessel locations are presented in table 3.13.

An analysis of variance of the data for position 1 revealed that differences between amplitudes were statistically significant ($P < 0.0001$). Multiple comparisons between groups using the Bonferroni correction method revealed that the difference between the amplitude recorded on the G-CCD was significantly higher than the amplitudes measured on the B-CCD and C-CCD ($P < 0.0001$, $P < 0.0001$ respectively). The difference in amplitudes between the B-CCD and C-CCD was less dramatic but did

reach significance ($P=0.036$). An analysis of variance of the widths also revealed statistically significant differences between imaging methods ($P=0.0005$). Multiple comparisons between groups using the Bonferroni correction method showed that the widths calculated from images taken on the G-CCD were smaller than those from the C-CCD ($P<0.0001$), otherwise the differences were not significant.

An analysis of variance of the data for position 2 revealed that differences between amplitudes were statistically significant ($P<0.0001$). Multiple comparisons between groups using the Bonferroni correction method revealed that the difference between the amplitude recorded on the G-CCD was significantly higher than the amplitudes measured on the B-CCD and C-CCD ($P<0.0001$, $P<0.0001$ respectively). The difference in amplitudes between the B-CCD and C-CCD was small and did not reach significance ($P=0.427$). An analysis of variance of the widths revealed statistically significant differences between imaging methods ($P=0.0333$). Multiple comparisons between groups using the Bonferroni correction method showed that the widths calculated from images taken on the C-CCD were smaller than those from the B-CCD ($P=0.034$), otherwise the differences were not significant.

POSITION 1 (LARGE VESSEL)			
Image sensor	N	μ amplitude \pm SD (I)	μ width \pm SD (μm)
B-CCD	10	0.193 \pm 0.007	97.4 \pm 2.49
G-CCD	10	0.276 \pm 0.004	94.7 \pm 2.65
C-CCD	10	0.199 \pm 0.005	100.5 \pm 3.37
POSITION 2 (MEDIUM VESSEL)			
Image sensor	N	μ amplitude \pm SD (I)	μ width \pm SD (μm)
B-CCD	10	0.138 \pm 0.050	64.5 \pm 0.770
G-CCD	10	0.187 \pm 0.007	60.4 \pm 4.64
C-CCD	10	0.142 \pm 0.005	58.6 \pm 7.03
POSITION 3 (SMALL VESSEL)			
Image sensor	N	μ amplitude \pm SD (I)	μ width \pm SD (μm)
B-CCD	10	0.176 \pm 0.004	21.5 \pm 10.23
G-CCD	10	0.203 \pm 0.014	20.9 \pm 3.85
C-CCD	10	0.159 \pm 0.009	15.0 \pm 5.05

Table 3.13 lists the mean and standard deviations of the 10 estimates of vessel amplitude and width for the 3 vessel locations measured.

An analysis of variance of the data for the smallest vessel (position 3) revealed that differences between amplitudes were statistically significant ($P<0.0001$). Multiple comparisons between groups using the Bonferroni correction method revealed that the difference between the amplitude recorded on the G-CCD was significantly larger than the amplitudes measured on the B-CCD and C-CCD ($P<0.0001$, $P<0.0001$ respectively). The difference in amplitudes between the B-CCD and C-CCD was less dramatic (0.017) but did reach significance ($P=0.001$). An analysis of variance of the widths did not reveal statistically significant differences between imaging methods ($P=0.0879$).

3.8.7.2 Conclusions of experiment E3.1

Evidently the vessel amplitudes calculated from images recorded on the G-CCD are larger than those from the B-CCD or C-CCD for all three vessel locations. Hence, vessel imaged on the G-CCD are of superior contrast.

3.8.7.3 E3.2 Results of recording on B-CCD, G-CCD and C-CCD with green filters

Mean amplitude and width measures calculated from the 50 densitometric profiles taken from the 3 vessel locations are presented in table 3.14. Note that the images were recorded using the same sensors but with the introduction of a green filter (Wratten 99) over the illumination optics.

An analysis of variance of the data for position 1 revealed that differences between amplitudes were statistically significant ($P < 0.0001$). Multiple comparisons between groups using the Bonferroni correction method revealed that the difference between the amplitude recorded on the G-CCD was significantly higher than the amplitudes measured on the B-CCD and C-CCD ($P < 0.0001$, $P < 0.0001$ respectively). The difference in amplitudes between the B-CCD and C-CCD were less dramatic (0.028) but did reach significance ($P < 0.0001$). An analysis of variance of the widths also revealed statistically significant differences between imaging methods ($P < 0.0001$). Multiple comparisons between groups using the Bonferroni correction method showed that the widths calculated from images taken on the G-CCD were larger than those from the C-CCD ($P < 0.0001$), and B-CCD ($P < 0.0001$). The difference between widths measured on the B-CCD and C-CCD was not significant ($P = 0.183$).

POSITION 1 (LARGE VESSEL)			
Image sensor	N	μ amplitude \pm SD (I)	μ width \pm SD (μm)
G-CCD+Wratten 99	50	0.301 \pm 0.016	102 \pm 4.74
B-CCD+Wratten 99	50	0.178 \pm 0.010	95.5 \pm 5.41
C-CCD+Wratten 99	50	0.207 \pm 0.012	97.5 \pm 6.01
POSITION 2 (MEDIUM VESSEL)			
Image sensor	N	μ amplitude \pm SD (I)	μ width \pm SD (μm)
G-CCD+Wratten 99	50	0.198 \pm 0.014	66.0 \pm 5.62
B-CCD+Wratten 99	50	0.120 \pm 0.008	60.6 \pm 9.89
C-CCD+Wratten 99	50	0.140 \pm 0.008	60.9 \pm 7.03
POSITION 3 (SMALL VESSEL)			
Image sensor	N	μ amplitude \pm SD (I)	μ width \pm SD (μm)
G-CCD+Wratten 99	50	0.204 \pm 0.038	27.5 \pm 4.56
B-CCD+Wratten 99	50	0.148 \pm 0.023	20.2 \pm 4.59
C-CCD+Wratten 99	50	0.162 \pm 0.037	19.7 \pm 8.44

Table 3.14 lists the mean and standard deviations of the 50 estimates of vessel amplitude and width for the 3 vessel locations measured.

An analysis of variance of the data for position 2 revealed that differences between amplitudes were statistically significant ($P < 0.0001$). Multiple comparisons between groups using the Bonferroni correction method revealed that the difference between the amplitude recorded on the G-CCD was significantly higher than the amplitudes measured on the B-CCD and C-CCD ($P < 0.0001$, $P < 0.0001$ respectively). The difference in amplitudes between the B-CCD and C-CCD was less marked but did

reach significance ($P < 0.0001$). An analysis of variance of the widths revealed statistically significant differences between imaging methods ($P = 0.0007$). Multiple comparisons between groups using the Bonferroni correction method showed that the widths calculated from images taken on the G-CCD were larger than those from the B-CCD ($P = 0.002$), and C-CCD ($P = 0.004$). The smaller difference between widths measured on the B-CCD and C-CCD ($0.300\mu\text{m}$) was not significant ($P = 1.000$).

An analysis of variance of the data for the smallest vessel (position 3) revealed that differences between amplitudes were statistically significant ($P < 0.0001$). Multiple comparisons between groups using the Bonferroni correction method revealed that the difference between the amplitude recorded on the G-CCD was significantly higher than the amplitudes measured on the B-CCD and C-CCD ($P < 0.0001$, $P < 0.0001$ respectively). The difference in amplitudes between the B-CCD and C-CCD was less dramatic (0.014) and did not reach significance ($P = 0.122$). An analysis of variance of the widths revealed statistically significant differences between imaging methods ($P < 0.0001$). Multiple comparisons between groups using the Bonferroni correction method showed that the widths calculated from images taken on the G-CCD were larger than those from the B-CCD ($P < 0.0001$), and C-CCD ($P < 0.0001$). The smaller difference between widths measured on the B-CCD and C-CCD ($0.532\mu\text{m}$) was not significant ($P = 1.000$).

3.8.7.4 Conclusions of experiment E3.2

Vessel amplitudes calculated from images recorded on the G-CCD are higher than those from the B-CCD or C-CCD for all three vessel locations. It also appears that the amplitudes recorded from images taken through a Wratten 99 filter in table 3.14 are superior to those taken without (see table 3.13). However, direct comparisons are misleading due to the different number of images used. The performance of images taken with and without green filtration are statistically compared in the final section.

3.8.7.5 E3.3 Results of recording on the G-CCD with different green filters

Images recorded on the G-CCD showed better vessel contrast than those recorded on the B-CCD or C-CCD. Also the use of a green filter over the illumination optics would appear to enhance vessel contrast further. To see how green filtration alters vessel contrast, images were taken through 5 different green filters. Mean amplitude and width measures calculated from the 10 densitometric profiles taken from the 3 vessel locations, for each filter used, are presented in table 3.15

An analysis of variance of the data for position 1 revealed that differences between amplitudes were statistically significant ($P < 0.0001$). Multiple comparisons between groups using the Bonferroni correction method revealed that the difference between the amplitude recorded from images through the Wratten 74 and 99, and the Wratten 57 and 61 were statistically similar ($P = 0.358$, $P = 0.156$ respectively). However, all other differences in amplitude were statistically significant ($P < 0.0001$ in all cases). Hence, the filter associated with the best contrast for large vessels was the Wratten 56. An analysis of variance of the widths also revealed statistically significant differences between imaging methods ($P = 0.001$).

An analysis of variance of the data for position 2 revealed that differences between amplitudes were statistically significant ($P < 0.0001$). Multiple comparisons between

groups using the Bonferroni correction method revealed that the difference between the amplitude recorded from images through the Wratten 56 and 99, Wratten 74 and 99, and Wratten 57 and 61 were statistically similar ($P=0.115$, $P=1.000$, $P=1.000$ respectively). However, all other differences in amplitude were statistically significant ($P<0.0001$ in all cases except between the Wratten 56 and 74 where $P=0.003$). Hence, the filters associated with the best contrast for medium sized vessels were the Wratten 56 and 99. An analysis of variance of the widths also revealed statistically significant differences between imaging methods ($P<0.001$).

POSITION 1 (LARGE VESSEL)			
Image sensor	N	μ amplitude \pm SD (I)	μ width \pm SD (μm)
G-CCD+Wratten 56	10	0.324 \pm 0.004	104 \pm 2.92
G-CCD+Wratten 57	10	0.288 \pm 0.008	105 \pm 1.82
G-CCD+Wratten 61	10	0.281 \pm 0.003	97.8 \pm 3.64
G-CCD+Wratten 74	10	0.302 \pm 0.006	100 \pm 7.22
G-CCD+Wratten 99	10	0.308 \pm 0.007	103 \pm 2.16
POSITION 2 (MEDIUM VESSEL)			
Image sensor	N	μ amplitude \pm SD (I)	μ width \pm SD (μm)
G-CCD+Wratten 56	10	0.213 \pm 0.007	71.4 \pm 2.64
G-CCD+Wratten 57	10	0.182 \pm 0.005	56.7 \pm 4.42
G-CCD+Wratten 61	10	0.183 \pm 0.003	67.2 \pm 1.50
G-CCD+Wratten 74	10	0.205 \pm 0.003	68.2 \pm 1.18
G-CCD+Wratten 99	10	0.207 \pm 0.003	66.5 \pm 2.28
POSITION 3 (SMALL VESSEL)			
Image sensor	N	μ amplitude \pm SD (I)	μ width \pm SD (μm)
G-CCD+Wratten 56	10	0.231 \pm 0.017	22.7 \pm 4.20
G-CCD+Wratten 57	10	0.168 \pm 0.014	30.3 \pm 1.84
G-CCD+Wratten 61	10	0.185 \pm 0.007	30.7 \pm 3.50
G-CCD+Wratten 74	10	0.175 \pm 0.008	26.4 \pm 4.74
G-CCD+Wratten 99	10	0.261 \pm 0.009	27.4 \pm 3.07

Table 3.15 lists the mean and standard deviations of the 10 estimates of vessel amplitude and width for the 3 vessel locations measured through each filter used.

An analysis of variance of the data for the smallest vessel revealed that differences between amplitudes were statistically significant ($P<0.0001$). Multiple comparisons between groups using the Bonferroni correction method revealed that the difference between the amplitude recorded from images through the Wratten 57 and 74, Wratten 61 and 74 were statistically similar ($P=1.000$, $P=0.583$, respectively). However, all other differences in amplitude were statistically significant ($P<0.0001$ in all cases except between the Wratten 57 and 61 where $P=0.022$). Hence, the filter associated with the best contrast for small vessels was the Wratten 99. An analysis of variance of the widths also revealed statistically significant differences between imaging methods ($P<0.0001$).

3.8.7.6 Conclusions of experiment E3.3

Filtering the light source with a Wratten 56 optimises the contrast recorded from large anterior vessels. A Wratten 56 or 99 optimises the contrast of medium sized vessels

and a Wratten 99 optimises the contrast of smaller vessels. Note that the smaller vessel is buried in the conjunctiva which might alter the spectral transmission characteristics of the vessel making it more suited to imaging using the Wratten 99 filter as opposed to the 56. The amplitudes calculated using the Wratten 56 and 99 over the illumination optics are larger than those obtained in table 3.13 without filtration. A direct comparison of imaging with and without green filtration is presented in the following section. The green filter of choice was the Wratten 99 due to its ability to optimise vessel contrast of smaller and medium sized vessels.

3.8.7.7 E3.4 Results of recording on G-CCD and C-CCD with and without a Wratten 99

The results indicate that images recorded on the G-CCD are superior to those imaged using the C-CCD or B-CCD. Also, the use of green filter can further enhance vessel contrast. To directly compare their performance images were recorded on the G-CCD and C-CCD both with and without a Wratten 99 green filter. Mean amplitude and width measures calculated from the 10 densitometric profiles taken from the 3 vessel locations, from the best of five images using each optical configuration are listed in table 3.16.

POSITION 1 (LARGE VESSEL)			
Image sensor	N	μ amplitude \pm SD (I)	μ width \pm SD (μm)
G-CCD	10	0.276 \pm 0.004	94.7 \pm 2.65
C-CCD	10	0.199 \pm 0.005	100 \pm 3.37
G-CCD+Wratten 99	10	0.308 \pm 0.007	103 \pm 2.16
C-CCD+Wratten 99	10	0.208 \pm 0.009	99.5 \pm 1.56
POSITION 2 (MEDIUM VESSEL)			
Image sensor	N	μ amplitude \pm SD (I)	μ width \pm SD (μm)
G-CCD	10	0.187 \pm 0.007	60.4 \pm 4.64
C-CCD	10	0.142 \pm 0.005	58.6 \pm 7.03
G-CCD+Wratten 99	10	0.208 \pm 0.003	66.5 \pm 2.28
C-CCD+Wratten 99	10	0.149 \pm 0.002	68.6 \pm 3.03
POSITION 3 (SMALL VESSEL)			
Image sensor	N	μ amplitude \pm SD (I)	μ width \pm SD (μm)
G-CCD	10	0.203 \pm 0.014	20.9 \pm 3.85
C-CCD	10	0.158 \pm 0.009	15.0 \pm 5.05
G-CCD+Wratten 99	10	0.261 \pm 0.009	27.4 \pm 3.07
C-CCD+Wratten 99	10	0.216 \pm 0.019	20.5 \pm 6.25

Table 3.16 lists the mean and standard deviations of the 10 estimates of vessel amplitude and width for the 3 vessel locations measured on the G-CCD and C-CCD with and without Wratten 99 filtration.

An analysis of variance of the data for position 1 revealed that differences between amplitudes were statistically significant ($P < 0.0001$). Multiple comparisons between groups using the Bonferroni correction method revealed that the difference between the amplitude recorded from images were all statistically significant ($P < 0.0001$ in all cases, except between the amplitudes recorded from the C-CCD image and the C-CCD image taken with a Wratten 99 filter where $P = 0.031$). Hence, images recorded with the G-CCD with a Wratten 99 result in the greatest contrast (largest amplitude)

for vessels of large calibre ($\sim 100\mu\text{m}$). These images are of superior vessel contrast to those imaged on the G-CCD without filtration and markedly better than those imaged on the C-CCD either with or without green filtration. An analysis of variance of the widths also revealed statistically significant differences between imaging methods ($P < 0.0001$).

An analysis of variance of the data for position 2 revealed that differences between amplitudes were statistically significant ($P < 0.0001$). Multiple comparisons between groups using the Bonferroni correction method revealed that the difference between the amplitude recorded from images were all statistically significant ($P < 0.0001$ in all cases, except between the amplitudes recorded from the C-CCD image and the C-CCD image taken with a Wratten 99 filter where $P = 0.006$). Hence, images recorded with the G-CCD with a Wratten 99 result in the highest contrast (largest amplitude) for vessels of medium calibre ($\sim 60\mu\text{m}$). An analysis of variance of the widths also revealed statistically significant differences between imaging methods ($P < 0.0001$).

3.8.7.8 Conclusions of experiment E3.4

A similar analysis of variance was performed on the data from the smallest vessels. The differences between amplitudes were statistically significant ($P < 0.0001$). However, a multiple comparisons between groups using the Bonferroni correction method revealed that the difference between the amplitude recorded from images taken on the G-CCD and the C-CCD with a Wratten 99 green filter was not significant ($P = 0.253$). All other amplitudes were significantly different ($P < 0.0001$ in all cases) indicating that images of small vessels ($\sim 20\mu\text{m}$) have optimal contrast when recorded on the G-CCD with a Wratten 99 over the incident flash source. As indicated by table 3.16 the improvement in small vessel amplitude was $\sim 21\%$ compared to images recorded on the C-CCD with green filtration, $\sim 30\%$ compared to images recorded on the G-CCD alone, and $\sim 65\%$ compared to images recorded on the C-CCD.

3.8.8 General discussion

The methodology outlined to determine vessel contrast was detailed and complex. It required the laborious collection of numerous densitometric profiles, knowledge of the blurring characteristics of the systems optics, and the application of the most appropriate model to describe vessel attributes. For our purposes a Gaussian blurred tubular model was found to give the best estimate of the vessels' amplitude and hence a measure of contrast. A plot of the residuals showed that the model gave a good fit over the vessel portion of the densitometric profile. However, the model was less good at predicting the vessels' background. Variabilities in width measurement between optical configurations may be explained by the inadequacy of the model to predict the vessels' profile at its edges. The comparative performance of differing models to predict vessel width forms the subject of the next chapter. The variabilities in width prediction may also be explained by slight differences in exposure. Note that obtaining the best exposure is judged by the response of the combined CCD output on the monochrome display. Once imported into the computer the C-CCD appeared to have optimal exposure, the R-CCD was grossly under exposed, G-CCD was slightly over exposed, and the B-CCD appeared to be slightly under exposed.

Previous methods of predicting the best optical set-up have relied on subjective interpretation of the best photographic (Delori *et al*, 1977; Bracher *et al*, 1979; Grunwald *et al*, 1986; Fenton, 1980; McMonnies and Chapman-Davies, 1982) or digital image (Stevenson and Chawala, 1993; Meyer, 1989; Willingham *et al*, 1995). The inadequacies of visual interpretation of image quality became apparent when observing G-CCD images taken through different green filters. Visually these images appeared of similar quality, however, as the results section indicates the use of a Wratten 56 or 99 showed a distinct improvement in contrast for the three vessel locations measured.

Some authors (Meyer, 1989; Stevenson and Chawala, 1993) recorded images of limbal vasculature using a broad band of illumination below 600nm with a CCD camera (peak sensitivity at 520nm) using a Zeiss 30SL slit lamp with a Halogen light source filtered with a 500 to 580nm band pass filter. However, the results section shows that further improvement may be obtained by using the image recorded by the G-CCD as opposed to the CCD combined. Willingham *et al* (1995) recorded images of the bulbar conjunctiva vasculature using a CCD camera but only used the response of the G-CCD. However, green filtration of the light source may have caused further improvement in vessel contrast. Note that the experimental set-up of recording images on the G-CCD with the xenon light source filtered with a Wratten 99, is unique. If any component of the system were to change e.g. a different CCD camera, the best optical configuration would have to be re-established. As indicated in figure 3.9 75% of the pixels on the CCD array of the DCS 100 digital camera are green. Hence, an image taken from the G-CCD is not unduly interpolated, unlike those obtained from the B-CCD or R-CCD.

We conclude that to acquire images of the conjunctiva using the Nikon FS-2 photo slit-lamp and DCS 100 digital camera, the xenon light source must be filtered with both a Wratten 99 and Wratten 96 (0.2 log units) and set to the minimum power setting (power 1). The images obtained from the G-CCD of the DCS 100 digital camera's CCD array exhibited optimal vessel contrast. Images taken in this way, for the 3 locations measured, exhibit from 11 to 29% superior contrast than vessels measured on the G-CCD alone, between 46 to 65% improvement than those measured on the C-CCD alone, and between 21 to 48% improvement from those recorded on the C-CCD with a Wratten 99 over the illumination optics. To our knowledge our findings are the first to advocate using images from the green component of a digital camera in conjunction with green filtration.

3.9 Optimal imaging of conjunctival vasculature

The purpose of this chapter was to investigate the optimum filter to be used to obtain images of the bulbar conjunctiva using both film and CCD detectors from first principles and substantiate these calculations with experimental proof. Also to consider the comparative performance of the two recording mediums.

Any photographic medium has a non-linear response to light, where the characteristic curve is typically 'S' shaped. Bracher *et al* (1979) found (using high contrast monochrome film) that this resulted in misleading interpretations of retinal vessel edges, especially when the exposure lies on the non-linear part of the mediums

characteristic curve. In contrast, the response to light of a CCD is almost linear (Newsom *et al*, 1992) and hence does not suffer from the same difficulties.

Manufacturing data reveals that a CCD detector is more responsive than film to lower light levels (Kodak Eastman, Rochester, New York, USA). Therefore, lower light levels can be used to digitally image ocular structures, improving patient comfort.

The spectral sensitivity curves of HP5 film and the DCS 100 digital camera are very different. HP5 film has peak sensitivity below 400nm, whereas the DCS 100 has a minimal response. Conversely, the DCS 100 has its maximum response to higher wavelengths, unlike film which does not respond to wavelengths greater than ~650nm. Hence, HP5 film can be regarded as responding to near UV wavelengths, and the digital camera to IR. Filters of different spectral transmissions are needed to optimise conjunctival vessel contrast. We have shown that film requires a filter which transmits in the UV region of the spectrum (a purple Wratten 35 filter) and the DCS a green filter which has a small window of transmission centred at 550nm and responds to wavelengths above 750nm (a Wratten 99). The introduction of colour filtration over the xenon light source was associated with a marked improvement in vessel contrast.

A big disadvantage of film is the need for development. Indeed the author has lost many photographic images due to experimental artefacts. Arnold *et al* (1994) have also found dramatic variations in the apparent width of the same vessel depending on the film used, developer used, the duration of development and exposure time. This was particularly true of high contrast films. Conversely, digital images can be viewed instantaneously and if not of sufficient quality can be instantly retaken.

For nearly 15 years red-free photographs have been electronically recorded to a digital format, using slide scanners and frame grabbers, allowing computerised assessment of vascular networks. It should be noted that this does not solve the many problems inherent with photographic imaging, and merely offers a further step in image acquisition which may present additional errors. Spencer *et al* (1992) believe that 'images should be acquired directly to avoid the numerous non-linearities inherent with photography which can diminish the quality of the measurement', and advocated the use of digital cameras. Both video analogue and digital cameras allow direct exposure to a charged couple device (CCD) negating the need for subsequent image digitisation. However, video analogue systems have to convert a digital image into an analogue image to be viewed on a video output. A 'frame grabber' is then needed to convert the analogue back into a digital image. Digital cameras do not suffer from this drawback and provide images, of high resolution, ready for image analysis. Hence, the use of the DCS 100 digital camera, in association with green filtration, was the method of choice for vascular imaging of the conjunctiva.

CHAPTER 4

4. Method of conjunctival vascular image analysis

4.1.1 Aim

The aim of this chapter was to explore different methods of describing vessel width, in order to obtain a 'gold standard' of measure. The 'gold standard' was then compared with a fully automated approach of segmenting vessels from their surround, where σ selection was shown to alter the description of width. The implementation of a vessel algorithm to the conjunctival bed results in a vast amount of quantitative data which must be interpreted in a useful manner. Vascular indices calculated from the vessel algorithms output were derived and investigated. In the case of tortuosity, an index based on the squared angular change between successive points on a vessel was used in favour of conventional vessel length to chord length ratios.

4.1.2 Introduction

There are a variety of methods for establishing vessel width. It was implied in chapter 3 that Gaussian half height interpretation of width was different from tubular assessment of width. This section aims to compare different methods of establishing vessel width. However, comparisons are difficult when the true vessel width dimension is unknown. Hence, the shape models discussed in chapter 3 were applied to capillary models of blood vessels using glass capillary tubes of known diameter. Five shape models were used including, a Gaussian model, cylindrical model, tubular model with wall size one sixth (arterial model), and one tenth that of the lumen (venular model), and a tubular model with a lumen to wall size ratio governed by the known dimensions of the glass capillary tube. After applying these models to simulated vessel cross-sections, manual, semi-automated, and automated models were applied to conjunctival vessels and their performance compared.

4.2 Capillary tube width determination

Rassam *et al* (1994) derived experimental models of blood vessels using 2 plastic tubes. These tubes were filled with human blood and EDTA added to prevent clotting. The true calibre of the tubes were measured using a travelling microscope as 987.5 μm and 735 μm and compared to densitometric half height and 'kick point' widths. We adopted this method to determine whether shape models were accurate in determining the real width of a hypothetical blood column. An experimental model was designed using glass capillary tubes. Glass capillary tubes were chosen as they were of known dimension, and were of smaller diameter than plastic equivalents.

4.2.1 Method

The 2 smallest capillary tubes which could be found had a volumetric capacity of 5 μl and 20 μl and were manufactured to known specifications (Sigma, England). The manufacturer claimed that the internal diameter of the smallest tube was 0.340mm with an external diameter of 1.0922mm. The larger tube had an internal diameter of 0.578mm and an external diameter of 1.3462mm. Tubes were orientated vertically, filled with blood (treated with potassium EDTA to prevent clotting), and viewed

through the Nikon FS-2 photo slit-lamp at the highest magnification under direct illumination. Images were taken on the DCS 100 digital camera, and the response of the green CCD array was extracted and stored. Horizontal densitometric slices 340 (for the smaller capillary tube) to 380 (for the larger capillary tube) pixels in length were measured across the hypothetical vessel using Matlab for Windows © Version 4.2c1 software. A graphical output of the densitometric data was then viewed. It became apparent that the highly reflective nature of the air to glass interface produced interference which nearly obliterated the densitometric profile of the blood filled column. Movement of the direct light source in numerous directions, immersion of the capillary tube in oil and water did not eradicate this problem. Hence, images were obtained by dark field illumination which appeared to dampen the occurrence of bright reflections. However, dark field illumination made the blood columns opaque, leading to a square wave densitometric profile. As indicated from previous densitometric profiles across retinal and conjunctival blood vessels, blood is both reflective, absorptive, and transmissive and not opaque. The width of the blood column in the capillary tubes (340 μm and 578 μm) was well in excess of the width of conjunctival blood vessels (<100 μm) adding to the absorption which occurs. For these reasons the capillary tubes were filled with a 0.05% toluidine blue (tolonium chloride) ink solution which gave densitometric profiles resembling those found across conjunctival vessels. However, the data obtained did contain a poor signal-to-noise ratio due to the low light levels used to obtain images of the correct exposure. Hence, a one dimensional averaging filter (± 10 pixels in length) was used to smooth the data as shown in figures 4.1 and 4.2.

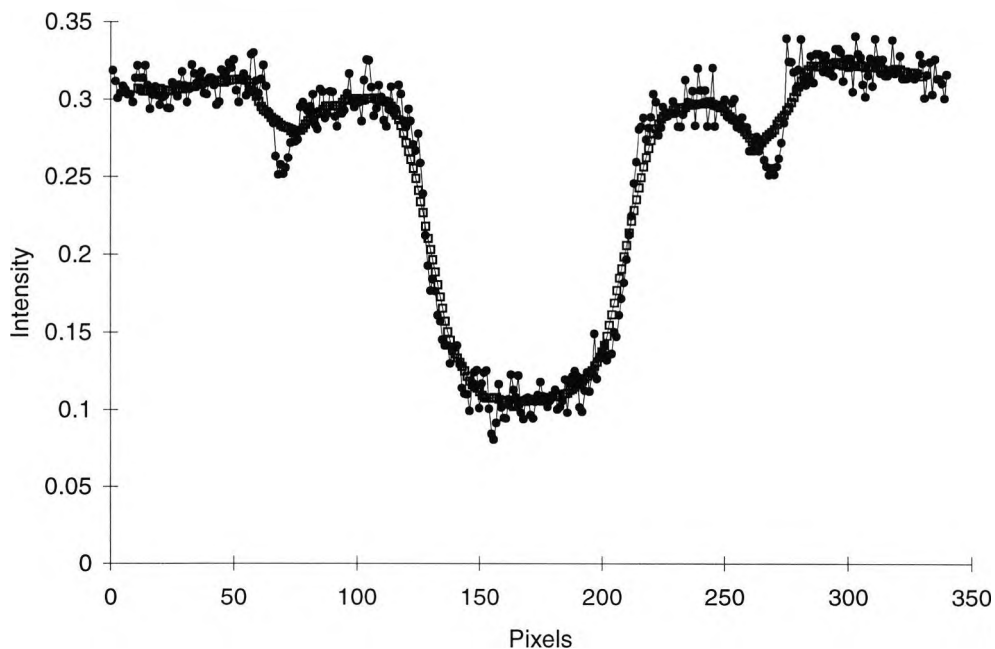


Figure 4.1 shows a densitometric profile taken across a glass capillary tube with internal diameter 0.340mm (~64 pixels in width) and external diameter 1.092mm (~206 pixels in width). Raw densitometric profile shown by closed circles, and averaged data open squares.

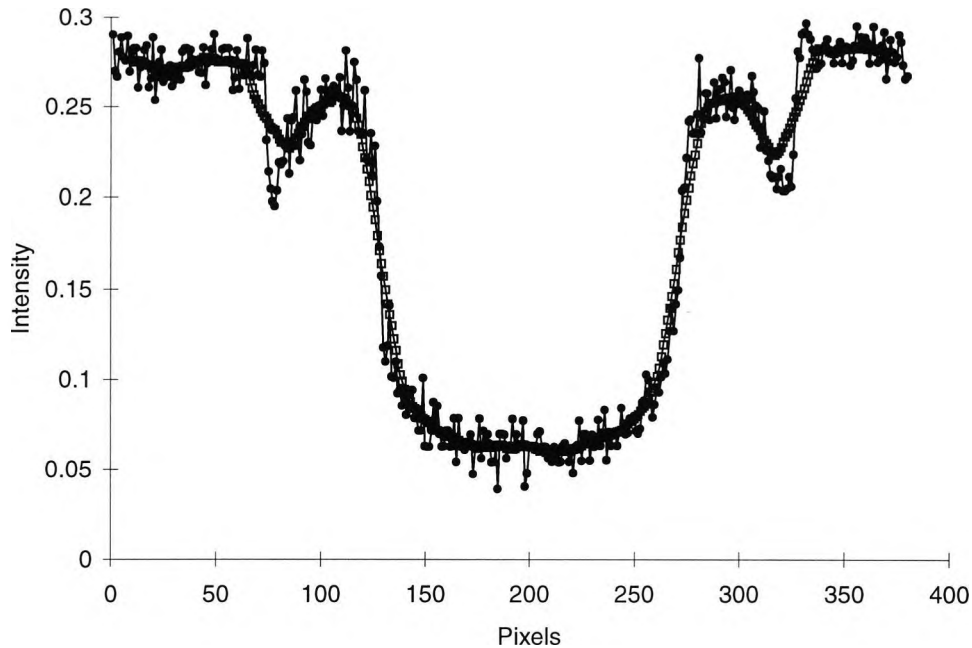


Figure 4.2 shows a densitometric profile taken across a glass capillary tube with internal diameter 0.578mm (~109 pixels in width) and external diameter 1.346mm (~254 pixels in width). Raw densitometric profile shown by closed circles, and averaged data open squares.

Note how the densitometric profile in figure 4.2 is more rectangular than figure 4.1. This is because more light is absorbed as it travels through a greater thickness of toluidine blue. Both figures 4.1 and 4.2 show greater reflectance at the capillary wall edges which was an experimental artefact of the illumination method used. However, this artefact was minor in comparison to the huge reflections obtained by direct illumination.

Ten images of each vertically orientated capillary model were taken. One horizontal densitometric slice was taken across each image. Five shape models were optimally fitted to each densitometric profile. Models included a Gaussian model (to give half height and maximum gradient measures of width), cylindrical model, tubular model with wall size one sixth (arterial model), and one tenth that of the lumen (venular model), and a tubular model with a lumen to wall size ratio governed by the known dimensions of the glass capillary tube. The equations of the first 4 models were given in chapter 3.

The following gives the equations of the two Gaussian blurred tubular profiles fitted by a least squares method to the densitometric profiles obtained across the large and small capillary tubes, where B is the midpoint of the curve, κ_1 is proportional to density of the toluidine blue filled column, κ_2 is proportional to density of the glass wall, C is the background intensity, r is the radius of the internal calibre width, and $\otimes G\sigma$ represents convolving the data with a Gaussian function of $\sigma = 1.655$. Using Microsoft Excel version 5.0a software a least squares fit was obtained (using the solving function) allowing parameters B , κ_1 , κ_2 , C and r to change. Note that the outer wall width is $\times 3.21$ the internal calibre width for the smaller capillary tube

(=1.0922 / 0.340) and $\times 2.33$ (=1.3462 / 0.578) the internal calibre for the larger capillary tube.

$$y = \left(C - \left(\left(\kappa 1 \times \sum_{B-r}^{B+r} \sqrt{r^2 - (x-B)^2} \right) + \kappa 2 \times \left(\left(\sum_{B-3.21r}^{B+3.21r} \sqrt{(3.21)^2 r^2 - (x-B)^2} \right) - \left(\sum_{B-r}^{B+r} \sqrt{r^2 - (x-B)^2} \right) \right) \right) \right) \otimes G\sigma$$

$$y = \left(C - \left(\left(\kappa 1 \times \sum_{B-r}^{B+r} \sqrt{r^2 - (x-B)^2} \right) + \kappa 2 \times \left(\left(\sum_{B-2.33r}^{B+2.33r} \sqrt{(2.33)^2 r^2 - (x-B)^2} \right) - \left(\sum_{B-r}^{B+r} \sqrt{r^2 - (x-B)^2} \right) \right) \right) \right) \otimes G\sigma$$

Widths obtained from each slice were averaged and compared to the known calibre of the capillary tube.

4.2.2 Results

The 12 column widths obtained from the 2 capillary tubes using each of the 5 shape model are listed in ascending order of percentage error from the true width in table 4.1. Note that the mean and standard deviation of 10 densitometric slices are quoted. To consider the goodness-of-fit of the model to the data an R^2 value was calculated.

Model used	Actual width	Model width	% error	R^2 value
Gaussian max gradient	64.1	61.6±0.583	-3.89%	0.952
Gaussian max gradient	109.0	113.0±0.787	3.67%	0.932
Gaussian ½ height	64.1	72.5±0.687	13.2%	0.952
Venular tubular model	109.0	131.2±0.188	20.5%	0.975
Gaussian ½ height	109.0	133.0±0.927	22.1%	0.932
Venular tubular model	64.1	88.0±0.368	37.4%	0.977
Arterial tubular model	64.1	88.6±2.769	38.2%	0.977
Arterial tubular model	109.0	159.5±0.614	46.4%	0.975
Glass tubular model	64.1	94.5±0.745	47.4%	0.977
Glass tubular model	109.0	160.7±0.598	47.5%	0.978
Cylindrical model	109.0	161.5±0.520	48.3%	0.974
Cylindrical model	64.1	96.2±0.469	50.1%	0.973

Table 4.1 lists the 12 column widths obtained from the 2 capillary tubes using each of the 5 shape models. Note that widths are given in pixels where 188.494 pixels equals 1mm.

The model which most accurately predicted vessel width was the fitted Gaussian curve. Widths measured between the points of maximum gradient on this curve gave the best estimate of model width with a percentage error of -3.89% and 3.67% for the smaller and larger capillary tubes respectively. Widths measured at the fitted Gaussian curves half height were 13.2 and 22.1% larger than the true width.

Although the optimally fitted Gaussian blurred tubular models produced superior fits to the densitometric data than the optimally fitted Gaussian curves, they grossly overestimated column width. Tubular models of width based on a venular relationship between wall to lumen size overestimated the true vessel width by 20.5 and 37.4%. Other tubular models with different ratios of wall to lumen size overestimated the true width by greater amounts (see table 4.1). Optimally fitted Gaussian blurred cylindrical

models measured widths some 50% larger than the true width (50.1 and 48.3% for the smaller and larger capillary tubes respectively). Evidently the models used lead to very different estimates of the same widths.

4.2.3 Discussion

Closer analysis of the maximum gradient width and half height width on the fitted Gaussian curve revealed a linear relationship. The Gaussian half height width and maximum gradient width can be derived from the σ of the fitted Gaussian curve. Let the equation of a Gaussian curve be $f(x)$ as shown below, where A is the amplitude of the Gaussian curve, B is the midpoint of the curve, and C is the background intensity.

$$f(x) \Rightarrow y = A \ell \frac{(x-B)^2}{2\sigma^2} - C$$

To simplify the equation let $B=0$ and $C=0$, so the equation becomes $g(x)$. Also consider the first differential $g(x)'$ and the second differential $g(x)''$.

$$g(x) \Rightarrow y = A \ell \frac{x^2}{2\sigma^2}$$

$$g(x)' \Rightarrow \frac{dy}{dx} = \frac{-Ax}{\sigma^2} \ell \frac{x^2}{2\sigma^2}$$

$$g(x)'' \Rightarrow \frac{d^2y}{dx^2} = \frac{A(x^2 - \sigma^2)}{\sigma^4} \ell \frac{x^2}{2\sigma^2}$$

The half height width will occur when the y value equals half of the curve's amplitude (A) and is expressed by the following equation.

$$\frac{A}{2} = A \ell \frac{x^2}{2\sigma^2}$$

$$0.693 = \frac{x^2}{\sigma^2}$$

$$x^2 = 1.386 \times \sigma^2$$

$$x = 1.177 \times \sigma$$

Half height width is equivalent to twice the x value which equals $2.355 \times \sigma$. The maximum gradient on the Gaussian curve can be derived from the zero crossing point of the second differential $g(x)''$ of the Gaussian equation $g(x)$.

$$0 = \frac{A(x^2 - \sigma^2)}{\sigma^4} \ell \frac{x^2}{2\sigma^2}$$

This will occur when $x=\sigma$. Therefore, maximum gradient width is equivalent to twice the x value which equals $2 \times \sigma$. Hence, the width measured between the points of

maximum gradient on the Gaussian curve multiplied by 1.177 gives the width at the Gaussian curve's half height.

Table 4.1 shows that there was a large variation in the widths measured by the different methods. Gaussian curve models appear to give more accurate determination of width than tubular and cylindrical models. Also, shape models based on the maximum gradient would appear to give the best estimate of width. Caution must be exercised when interpreting this data as the densitometric profiles obtained across glass capillary tubes were very different to those obtained across blood vessels. Also, the homogenous structure of the model was dissimilar to the cellular and particulate structure of blood vessels. However, the application of shape models to these profiles shows that different approaches yield different widths. A comparative study of the performance of differing methods of establishing vessel width was needed and forms the subject of the remainder of this chapter.

4.3 Vessel width determination

This work compares manual, semi-automated, and automated methods of establishing conjunctival vessel widths. Manual methods include observer driven selection of the vessel edge whether by determination from Ektachrome® slides of the bulbar conjunctiva (BC) using electronic callipers, from digitally created Ektachrome® images (using a WinRascol Version 3.11, Lasergraphics, slide maker) of the BC using electronic callipers, or by mouse controlled determination directly from a pixelated digital image using a graphics package (Paint Shop Pro © Version Shareware 3.11). Semi-automated methods involved image profiling (shape modelling) of densitometric profiles across vessels of interest (manually acquired using Matlab for Windows © Version 4.2c1). These include optimally fitted Gaussian curves to the densitometric profile by a least squares method and measuring the width at the half height and maximum gradient. Also fitting an expandable cylindrical model, and tubular model with a wall width one sixth (arterial model) and one tenth (venular model) that of the lumen size. Cylindrical and tubular models are corrected for systemic optical distortions by convolving the model with an experimentally derived Gaussian filter ($\sigma = 1.655 \pm 0.337$ SD pixels) as shown in chapter 3. Magnifications of the photographic, digitally created photograph and digital images were experimentally derived and applied, so data sets could be compared directly in real size. Automated methods were based on Steger's algorithm for unbiased detection of curvilinear structures (Steger, 1996; 1998), set at different sigma's and thresholds in order to find optimal settings for the task of segmenting conjunctival vascular structures. Intra-session repeatabilities of each method, and inter-method comparisons were measured from the analysis of 101 vessel locations taken from 24 images (12 patients each with 2 images selected from 5 taken in each session) with 7-11 vessel locations selected per image. Although no gold standard of vessel width determination exists, the most reliable method was identified and compared with the automated approach.

4.3.1 Method

4.3.1.1 Image acquisition

Images of the dextro temporal BC of 12 patients were acquired using a Nikon FS-2 photo slit-lamp with a Nikon FS-2 camera. Five images were exposed to

Ektachrome® film (ASA 100). All photographic images were recorded to two 36 exposure films and processed concurrently to minimise developmental errors. The camera back was changed to a Kodak DCS 100 CCD camera, a Wratten 99 (green) filter introduced, and another 5 images acquired. Images were recorded within the same session to prevent the possibility of environmental or diurnal fluctuations in the vasculature. The best two slides/images from the data sets were used for the analysis for each of the 12 patients. In total 24 slides and 24 digital images were recorded. Slides were glass mounted to prevent distortion on projection, and digital images stored to CD. Note that only the signal from the green channel on the CCD array was recorded to obtain maximum vessel contrast as detailed in chapter 3. A random selection of 101 vessel locations were selected from 12 images and duplicated on the second image of the session. Each image had between 7-11 vessels selected. Locations were principally chosen at random but clear of interference with surrounding structures, so as to present a near uniform background. Vessels were chosen at differing depths to allow for the effects of buried vessels on determination of width. Digital images were viewed in a graphics package (Microsoft PowerPoint Version 4.0a) and vessel locations of interest identified with a cross cursor and numbered consecutively. Updated images were printed to Ektachrome® using a slide maker, and laser printed to A4 sized paper to provide a thumbnail copy. Methods of vessel width determination can be divided into manual, semi-automated, and automated. Manual methods included measurement directly from Ektachrome® slides using electronic callipers, measurement from digitally created Ektachrome® slides using electronic callipers, and by directly measuring from the pixelated image in a graphics package (Paint Shop Pro © Version Shareware 3.11) using a mouse to select the pixel closest to the vessel edge. Semi-automated methods were based on shape profiling of the densitometric profile across a specific vessel location. A Gaussian curve fitted on a least squares principal allowed the distance between Gaussian half height and maximum gradient to be measured. An optimally fitted cylindrical model and tubular model with wall width one sixth (arterial model) and one tenth (venular model) of the lumen size were also used. Cylindrical and tubular models were corrected for systemic optical distortions by convolving the model with an experimentally derived Gaussian filter ($\sigma 1.655 \pm 0.337$ SD pixels). Automated measurement of width used Steger's algorithm for unbiased detection of curvilinear structures. This algorithm can be run at different levels depending on the selection of σ and thresholds.

4.3.1.2 Manual methods

Manual methods involved observer driven selection of vessel width. Photographic slides were displayed using a slide projector. To determine magnification at the projected image plane, 5 consecutive images of an accurate millimetre scale (Vickers, England) were taken. Millimetre distances at the image plane were measured at half millimetre object distances from 0 to 6.5 mm. The gradient of the fitted linear regression line gave the magnification. This was measured on 5 occasions and a mean taken. Magnification at the image plane was $\times 154.76 \pm 0.0422$ SD. Note that there were no peripheral optical magnifications or minifications observed in the linear regression lines. A similar method was utilised for digitally created Ektachrome® images but with only 2 images of a millimetre scale giving a magnification of $\times 188.175 \pm 0.134$ SD at the image plane. Projected slides of each conjunctival vascular bed were measured at a location indicated by the thumbnail image using electronic

callipers. The observer was blind to all readings to avoid human bias. Widths were also determined directly from the digital image using a graphics package. Digital images were displayed on low magnification and marked with a single pixel line to denote the perpendicular of the vessel direction at each location to be measured. The digital image was then displayed at high magnification, corresponding to approximately $\times 430$ 'on screen' magnification from real size. The cursor was positioned using the mouse to visually represent the vessel edge, parallel to the direction line. The corresponding pixel on which the cursor laid was recorded for both sides. The pixelated Euclidean distance was converted to a real size and recorded as the width. Magnification of the digital image was calculated in chapter 3 as 188.494 ± 0.0621 SD pixels per millimetre.

4.3.1.3 Semi-automated methods

Semi-automated determination of vessel width refers to manual acquisition of the densitometric profile across a vessel, which must be judged to be perpendicular to vessel direction, however the decision of vessel width is determined by shape modelling. In total 4 shape models were used, a Gaussian model, cylindrical model, tubular model with wall size one sixth (arterial model), and one tenth that of the lumen (venular model). The cylindrical models were convolved with a Gaussian filter to correct for systemic optical distortion of the imaging set-up. This was experimentally derived to be equivalent to convolving with a Gaussian filter of $\sigma 1.655 \pm 0.337$ SD and has been explained in chapter 3. The pixelated distance was then converted to real size by applying the appropriate magnification factor.

4.3.1.4 Automated methods

Automated methods were based on the work of Steger (Steger, 1996; 1998) to delineate curved linear structures. Details of this algorithm can be found in chapter 1. The algorithm can be used with different sigma's and thresholds. The σ value can be thought of as a space-scale constant i.e. it is designed to be matched to the scale of the feature to be detected. Hence, sigma's were selected to match the approximate feature size of blood vessel widths in the image and were based on an incremental pixel scale from 1 to 5 in half pixel increments (except $\sigma 1.5$) which relates to a true size from $5.305 \mu\text{m}$ to $26.526 \mu\text{m}$ respectively. From Steger's paper (1998) the optimum value of σ for detecting a feature $2w$ wide can be derived from the equation below.

$$\sigma \geq \frac{w}{\sqrt{3}}$$

Hence, if the average width of a conjunctival vessel is assumed to be 8 pixels ($\approx 40\mu\text{m}$) then $w = 4$, and the optimal value for σ should be 2.3 pixels. Hence, the σ values chosen were designed to fall either side of this predicted optimal value.

Low detection thresholds were selected to ensure that all detail was detected, where the lower threshold equalled 0 pixels and the upper 0.5 pixels. When $\sigma = 1$, the low thresholds detected spurious noise; however all vessel locations were detected. In total 8 experiments were recorded with σ equal to 1.0, 2.0, 2.5, 3.0, 3.5, 4.0, 4.5, and 5.0.

4.3.1.5 Intra-session analysis

There were 3 manual determinations of width, 5 semi-automated, and 8 automated estimations of vessel width, for the 101 vessel locations, taken from 12 images of 12 patients for the first session of measurement and duplicated on the second image taken, for both the digital and photographic methods. Repeatabilities of each technique were assessed based on the differences between measurement on the same locations for the 2 sessions. The mean difference gave the estimated bias, the systemic difference between sessions, and the SD of the differences measured random fluctuations around the mean. The 95% limits of agreement, mean difference plus or minus 1.96 SDs told us how far apart measurements by this method are likely to be for the assessment of width. This method described by Bland and Altman (1986) is preferred to simply quoting the coefficient of variation. It was envisaged that the mean difference for the image set will be close to zero. The 95% coefficient of variation is indicative of the variability of the measurement and should ideally be small in relation to the values to be measured. Provided the difference within the 95% confidence interval is not clinically important one can say that the repeatability of the method used is good. A plot of the mean value for each location for the 2 sessions of measurement against the difference between sessions will indicate the accuracy of measurement over the range of values measured. The appearance of funnelling or sloping effects show inaccuracies within the method.

4.3.1.6 Inter-method analysis

Mean values from session one and two of each of the 16 methods used were statistically compared. The aim was to show whether two methods agreed sufficiently well for them to be used interchangeably. Analysis was based on the differences between measurements on the same vessel locations by paired methods. The mean difference gave the estimated bias, the systematic difference between methods, and the SD of the differences measured random fluctuations around this mean. The mean difference plus or minus 1.96 SDs tells us how far apart the measurements by the 2 methods are likely to be for measuring vessel widths (Bland and Altman 1986). It has been conclusively proved that plotting one method against another is both confusing and regression analysis misleading (Bland and Altman 1995). By comparing each of the automated methods against the best of the manual / semi-automated approaches gave the best σ for the Steger algorithm to be run at to measure vessel width.

4.3.2 Results

In total 5 images of the temporal BC of the right eye were taken using both the photographic and digital camera. Visually the best 2 images were selected and stored as session one and two. One hundred and one vessel locations were selected free of extreme background illumination differences and confusing underlying vascular structures. These 101 vessel locations were measured using each of the 16 outlined methodologies. This provided the data for analysis.

4.3.2.1 Intra-session repeatabilities

The mean difference, 95% confidence interval (CI) between session one and session two of measurement for each of the 16 methods is shown in table 4.2, in ascending order of coefficients of repeatability.

<i>Method</i>	<i>MDμm</i>	<i>+95% CI</i>	<i>-95% CI</i>	<i>C of R</i>	<i>Min μm</i>	<i>Max μm</i>
Auto $\sigma = 3$	0.469	9.414	8.475	17.889	23.444	90.547
Digital photo	0.414	10.122	9.294	19.416	14.401	140.029
Auto $\sigma = 4$	-0.016	10.561	10.545	21.122	6.666	115.731
Auto $\sigma = 2$	0.419	10.603	11.022	21.206	21.385	60.453
Auto $\sigma = 1$	0.095	10.793	10.602	21.395	6.403	29.932
Mouse driven	-0.131	11.201	11.463	22.664	10.610	123.452
Photographic	-0.993	10.522	12.508	23.029	15.328	133.241
Auto $\sigma = 2.5$	-0.379	11.521	12.280	23.800	21.605	75.429
Auto $\sigma = 4.5$	0.141	12.859	12.578	25.122	8.395	129.344
Auto $\sigma = 3.5$	-0.392	13.289	14.074	27.363	21.470	105.173
Gauss max G	0.327	17.471	16.817	34.288	11.048	134.912
Auto $\sigma = 5$	-0.058	18.843	18.785	37.685	8.400	129.431
Gauss $\frac{1}{2}$ H	0.385	20.570	19.800	40.371	13.008	158.847
Arterial tube	-0.492	20.826	21.809	42.635	7.541	144.999
Cyl width	-1.126	20.255	22.507	42.762	7.910	148.543
Venular tube	-0.577	21.088	22.243	43.331	4.600	144.962

Table 4.2 shows the MD, \pm 95% confidence limits of repeatability (± 1.96 SD), minimum and maximum values for each method used to measure vessel width on sessions 1 and 2, shown in ascending order of coefficient of repeatability (2×1.96 SD).

Automated estimation of vessel width using the Steger algorithm with $\sigma = 3$, and measurement with electronic callipers on the digitally created photographs gave coefficients of repeatability of less than 20 microns, with $+9.414\mu\text{m}$ to $-8.475\mu\text{m}$ and $+10.122\mu\text{m}$ to $-9.294\mu\text{m}$ respectively. Figures 4.3 and 4.4 show a plot of the differences between paired values for sessions 1 and 2 plotted against the mean for the automated method using $\sigma = 3$ and manual method from digitally created slides respectively. The data presented in figures 4.3 and 4.4 appears free from ‘funneling’ affects, but this was difficult to judge with the preponderance of data being at smaller vessel widths. However linear regression lines fitted to both data sets did not reveal sizeable gradients, indicating an insignificant measurement error. Note the difference in the range of mean differences for the 2 data sets with manual assessment measuring a greater range than the automated method, indicating that although the intra-session repeatabilities are similar the 2 methods measure differently to each other. The maximum and minimum average value of session 1 and 2 measured is shown in table 4.2. Differences in the spread of measurements are observed.

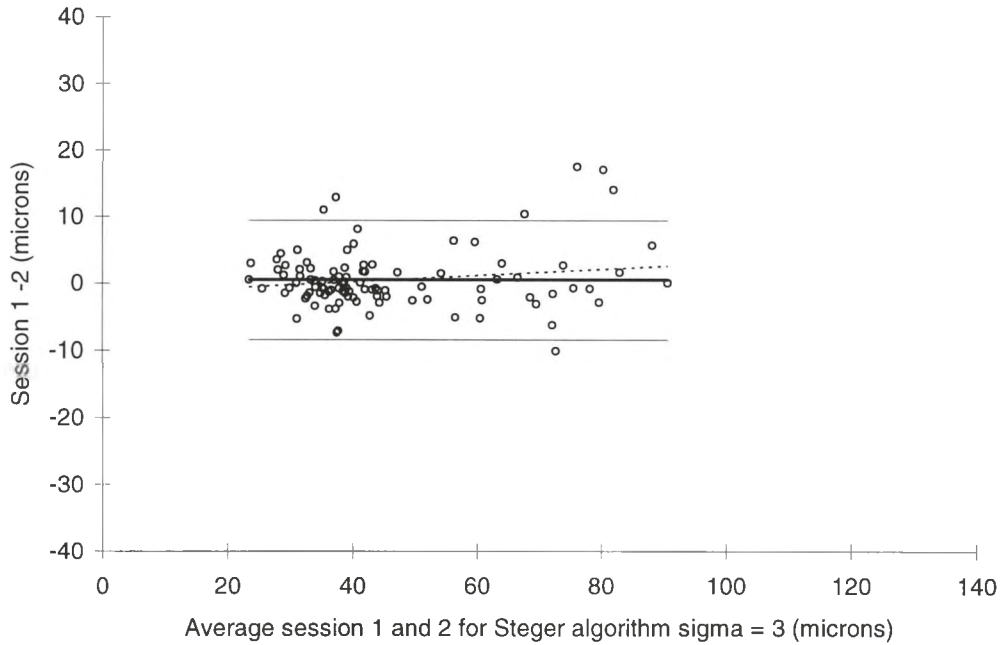


Figure 4.3 shows difference between paired values of vessel width for sessions 1 and 2 plotted against their mean ($n=101$) using the Steger's algorithm at $\sigma = 3$. Thick solid line represents mean difference, and thin lines $\pm 95\%$ CI. The dashed line with a slight positive gradient is a linear regression line of the data points showing insignificant measurement error.

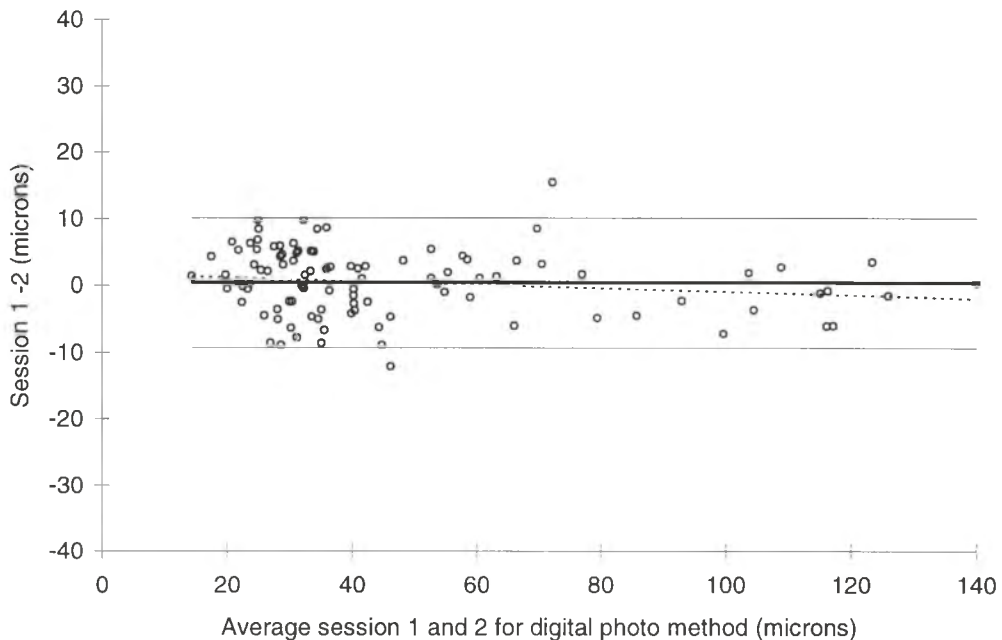


Figure 4.4 shows difference between paired values of vessel width for sessions 1 and 2 plotted against their mean ($n=101$) using manual measurement from digital slide images. Thick solid line represents mean difference, and the thin lines $\pm 95\%$ CI. The dashed line with a slight negative gradient is a linear regression line of the data points showing insignificant measurement error.

Manual methods, using electronic callipers, digital methods by mouse driven determination of vessel edge, and automated methods, using sigma's 1.0, 2.0, 2.5, 3.5, 4.0, and 4.5, gave coefficients of repeatabilities between 21.122 to 27.363 μm . Automated determination of vessel width using $\sigma = 5$ and all semi-automated methods gave poor intra-session repeatabilities between 34.288 to 43.331 μm . All mean differences were within 0.469 μm showing insignificant systematic error in measurement between sessions. The exceptions to this were the tubular and cylindrical semi-automated methods which appeared, on average, to read 0.492 to 1.126 μm higher on the second session of measurement, but with such a large 95% confidence interval it is difficult to draw any conclusions from this.

4.3.2.2 Inter-method repeatabilities compared to manual photographic method

To assess inter-method repeatabilities a method demonstrating good intra-session repeatability is needed. As it was the comparative performance of the automated method which was desired the manual method from digital photographs was chosen as the gold standard. Data for each method was taken as the average of the 2 readings taken on each session. Inter-method repeatabilities were measured for each method against the digitally created photographic method. The mean difference, 95% confidence interval between methods of measurement and the 'gold standard' is shown in table 4.3.

<i>Method</i>	<i>MD μm</i>	<i>+95% CI</i>	<i>-95% CI</i>	<i>Coeff of R</i>
Photographic calliper	0.462	10.958	10.033	20.992
Digital image mouse	5.161	17.679	7.358	25.037
Gaussian $\frac{1}{2}$ height	5.280	19.830	9.270	29.100
Gaussian maximum gradient	11.573	27.113	3.966	31.080
Artery tubular width	3.404	22.135	15.327	37.462
Venule tubular width	3.207	22.858	16.443	39.301
Automated $\sigma = 4.5$	-8.397	11.794	28.588	40.382
Automated $\sigma = 4$	-5.678	15.649	27.005	42.654
Cylinder width	1.267	23.391	20.856	44.247
Automated $\sigma = 5$	-9.653	14.998	34.303	49.301
Automated $\sigma = 3.5$	-2.524	24.216	29.264	53.479
Automated $\sigma = 3$	1.354	35.190	32.481	67.671
Automated $\sigma = 2.5$	5.196	44.243	33.851	78.094
Automated $\sigma = 2$	9.842	53.894	34.211	88.106
Automated $\sigma = 1$	21.966	79.171	35.239	114.410

Table 4.3 shows the MD and $\pm 95\%$ confidence limits of inter-method repeatability (± 1.96 SD) for each method used against measurement from digitally created photographs using electronic callipers, shown in ascending order of coefficient of repeatability (2×1.96 SD).

The method which gave the best agreement with vessel width determination from digitally created photographic slides, unsurprisingly were measurements taken directly from Ektachrome® slides, despite the difference in calculated magnification for each imaging system. Figure 4.5 shows a plot of the difference against the average of the manual calliper measurement from photographs and calliper measurements from

digitally created images. There are no apparent funnelling effects and the gradient of the fitted regression line to the data points has a negligible positive gradient.

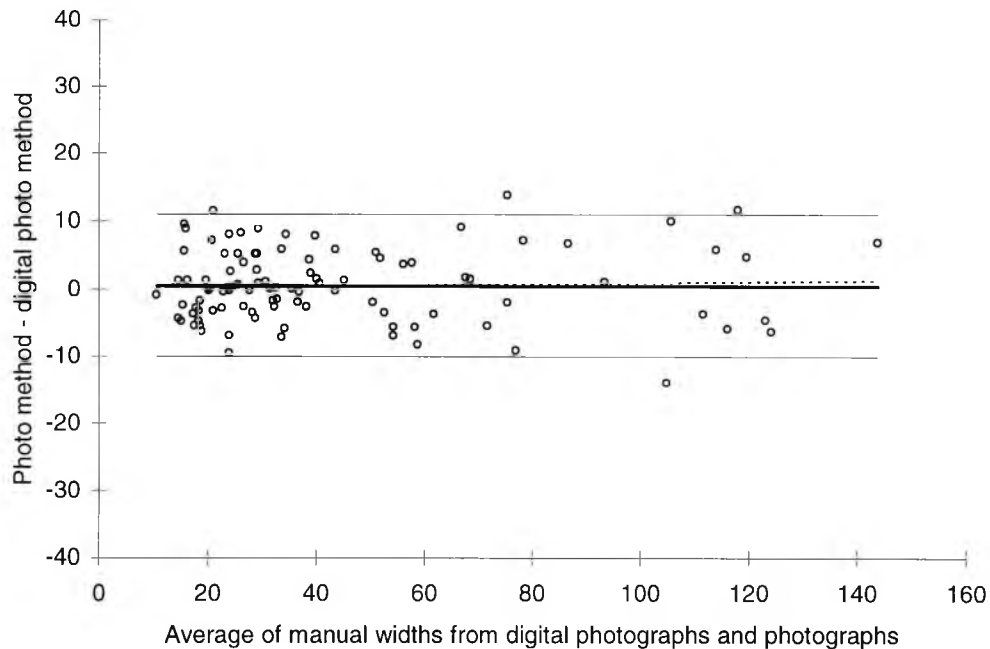


Figure 4.5 shows differences between paired values of vessel width for average measurements taken from photographs and digitally created photographs using callipers, plotted against their mean ($n=101$). Thick solid line represents the mean difference, thin lines $\pm 95\%$ CI. Dashed line with a very slight positive gradient is a linear regression line of the data points.

Interestingly vessel width determination from digital images using a mouse and semi-automated measurement using Gaussian half height gave similar mean differences and coefficients of repeatability when compared to electronic calliper assessment, with $5.161\mu\text{m} +17.679 -7.358\mu\text{m}$, and $5.280\mu\text{m} +19.830 -9.270\mu\text{m}$ respectively. As shown in figures 4.6 and 4.7 respectively. This may indicate a systematic error with photographic imaging where vessels are visually over estimated due to developmental changes. It may be that photographic film is more responsive to contrast levels at the vessel edge hence appearing darker than a digital image. It is known that the characteristic curve of a CCD camera is linear, whereas photographic film has a 'S' type responsiveness. The possibility of this relationship is investigated further where the out-put of the mouse driven method is used as the 'gold standard' to compare inter-method repeatabilities (see later).

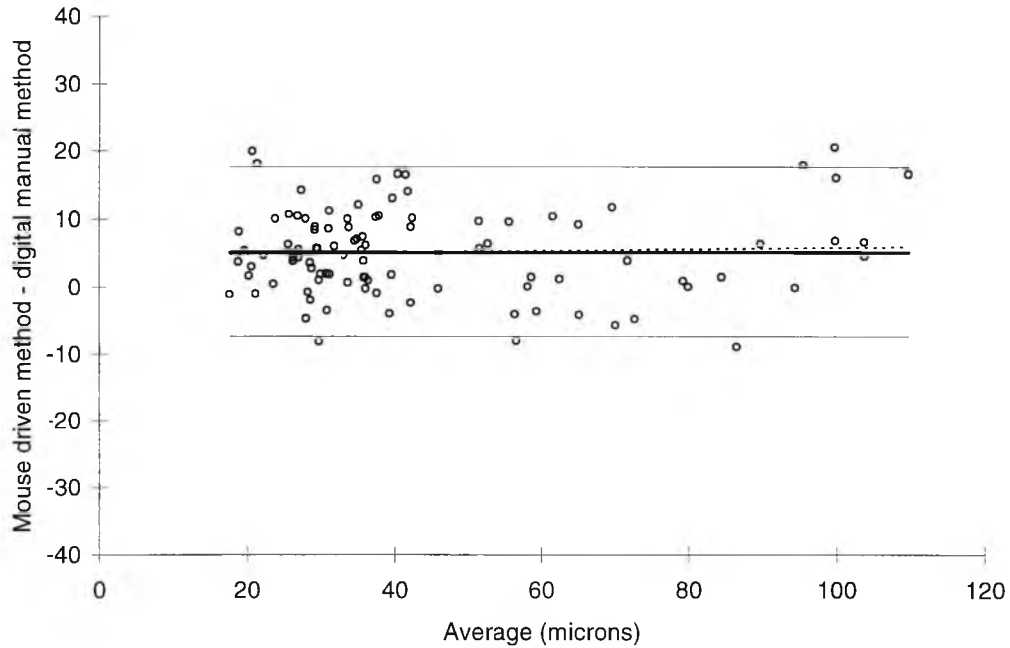


Figure 4.6 shows differences between paired values of vessel width for average measurements taken mouse driven methods and digitally created photographs using callipers, plotted against their mean ($n=101$). Thick solid line represents the mean difference, thin lines $\pm 95\%$ CI. Dashed line with a very slight positive gradient is a linear regression line of the data points.

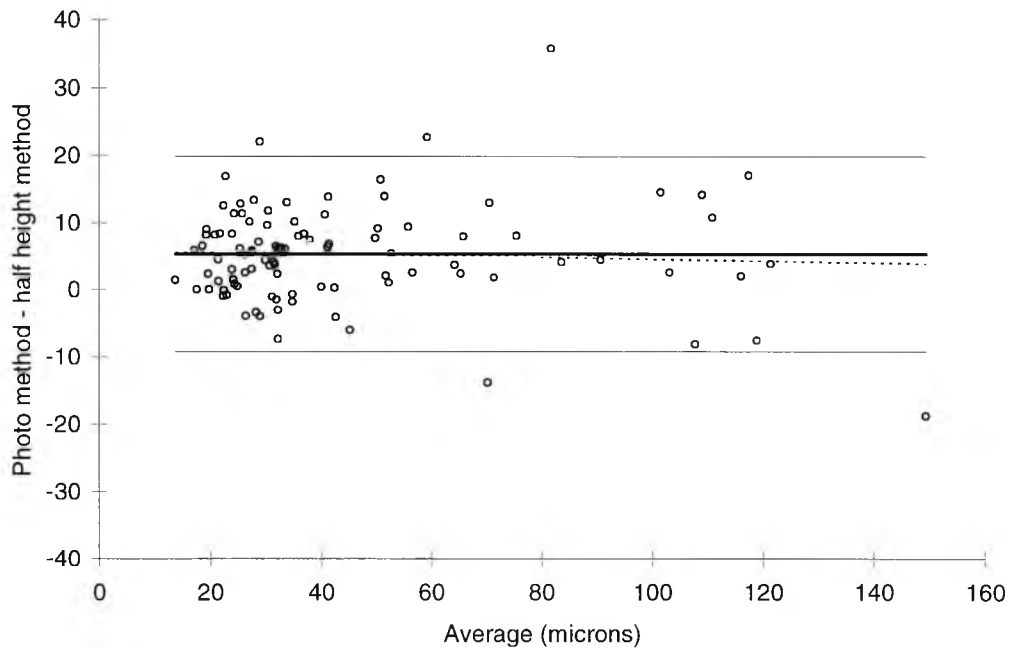


Figure 4.7 shows differences between paired values of vessel width for average measurements of Gaussian half height and digitally created photographs using callipers, plotted against their mean ($n=101$). Thick solid line represents the mean difference, thin lines $\pm 95\%$ CI. Dashed line with a very slight negative gradient is a linear regression line of the data points.

Cylindrical and tubular (arterial and venular) shape models gave a mean difference between 1.267 to 3.404 μm , with coefficients of repeatability between 37.462 and 44.247 μm , showing that these semi-automated methods slightly underestimate vessel width with respect to manual methods. However inter-method repeatability plots show that the relationship between the 2 types of vessel width determination are quite different. Figure 4.8 shows the difference between paired values for the cylinder model and electronic calliper width. Note that figure 4.8 is similar to plots obtained with both tubular models. The linear regression line of the data points shows that widths obtained using cylindrical or tubular shape modelling underestimate small vessel widths and overestimate large vessel widths, compared to electronic calliper measurements from digital photographs.

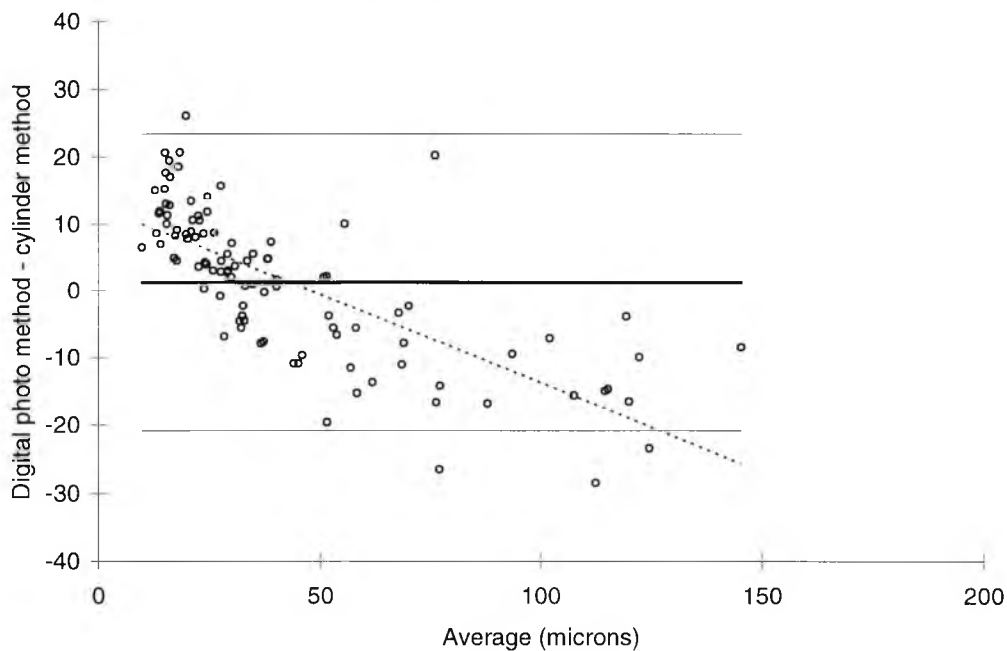


Figure 4.8 shows differences between paired values of vessel width for average measurements of cylinder model and digitally created photographs using callipers, plotted against their mean ($n=101$). Thick solid line represents the mean difference, thin lines $\pm 95\%$ CI. Dashed line with a steep negative gradient is a linear regression line of the data points.

Disappointingly automated methods did not agree well with manual calliper measurement. When the algorithm was set at $\sigma = 1$ vessels were comparatively underestimated by a mean difference of 21.966 μm , with a large coefficient of repeatability (114.410 μm). When the algorithm was set at $\sigma = 5$ vessel were overestimated by a mean difference of -9.653 μm , but with a lower coefficient of repeatability (49.301 μm). The best agreement was obtained with $\sigma = 3$ where a mean difference of 1.354 μm and a coefficient of repeatability of 67.671 μm were obtained. A plot of the inter-method repeatabilities for $\sigma = 3$ against manual calliper measurement from digital photographs is shown in figure 4.9. Although the regression line of the data points shows a positive trend, the data points are stepped, showing a region of good prediction followed by a sharp linear increase. Overall these results indicate that on average low sigma's tend to underestimate and high sigma's tend to overestimate vessel width in comparison to manual photographic methods.

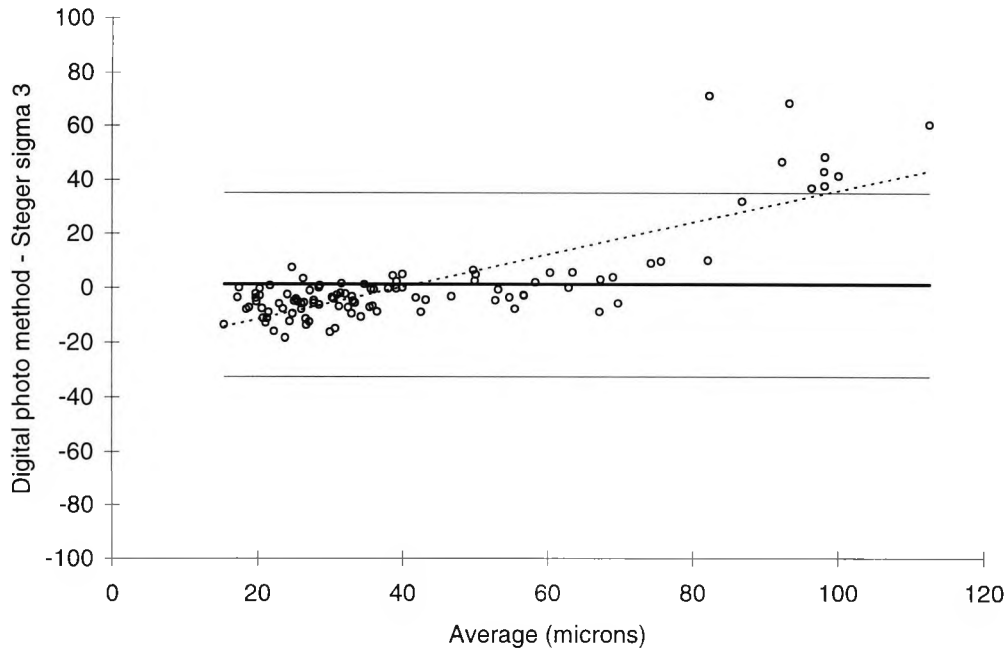


Figure 4.9 shows differences between paired values of vessel width for average measurements of automated width ($\sigma = 3$) and digitally created photographs using callipers, plotted against their mean ($n=101$). Thick solid line represents the mean difference, thin lines $\pm 95\%$ CI. Dashed line with a steep positive gradient is a linear regression line of the data points.

To investigate the relationship further the 101 vessel widths were analysed in groups of size. Figure 4.10 shows a 3 dimensional plane surface of the mean difference of the manual calliper method minus the automated method, for differing sigma's of Steger algorithm, plotted against differing vessel bins, varying in size from less than $20\mu\text{m}$ ($n=3$) to less than $110\mu\text{m}$ ($n=93$) in increments of $10\mu\text{m}$, as measured from digitally created photographic slides with electronic callipers. Conversely figure 4.11 shows a 3 dimensional plane surface of the mean difference of the manual calliper method minus the automated method, for differing sigma's of Steger algorithm, plotted against differing vessel bins varying in size from greater than $20\mu\text{m}$ ($n=98$) to greater than $110\mu\text{m}$ ($n=8$), in increments of $10\mu\text{m}$, as measured from digitally created photographic slides with electronic callipers. Note that the 95% confidence interval has been omitted to prevent confusion.

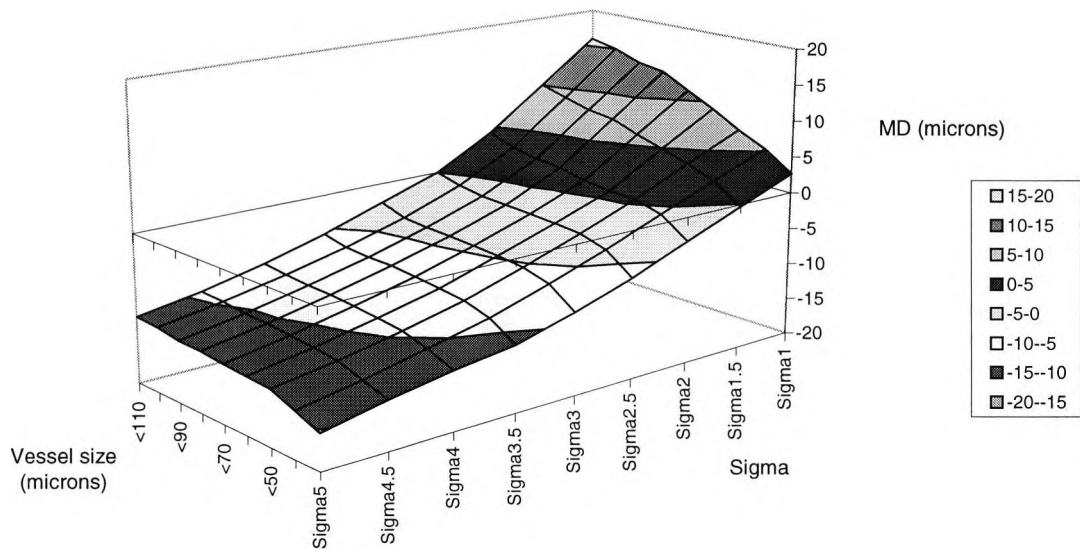


Figure 4.10 shows a 3 dimensional plane surface of the mean difference of the manual calliper method minus the automated method, for differing sigma's of Steger algorithm, plotted against differing vessel bins varying from less than $20\mu\text{m}$ ($n=3$) to less than $110\mu\text{m}$ ($n=93$) as measured from digitally created photographic slides with electronic callipers.

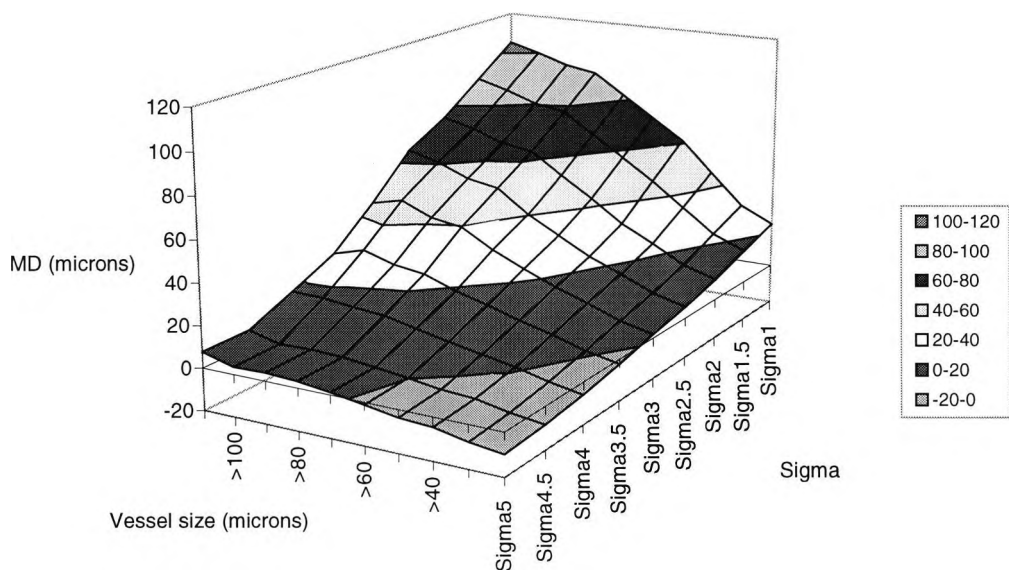


Figure 4.11 shows a 3 dimensional plane surface of the mean difference of the manual calliper method minus the automated method, for differing sigma's of Steger algorithm, plotted against differing vessel bins varying from greater than $20\mu\text{m}$ ($n=98$) to greater than $110\mu\text{m}$ ($n=8$) as measured from digitally created photographic slides with electronic callipers.

To interpret figures 4.10 and 4.11 observe the MD zero plane as it intersects the 3 dimensional surface. In figure 4.10 the zero plane indicates that for vessels manually measured less than $30\mu\text{m}$ in width, a $\sigma = 1.5$ is needed for automated measurement to give a MD of approximately zero. However if measuring widths of less than $110\mu\text{m}$ then a $\sigma = 2.5$ would be needed to give a mean difference of zero. For vessel widths $30\mu\text{m}$ or less, an automated measurement using a $\sigma = 5$ would grossly overestimate width with a mean difference of $-15.238\mu\text{m}$, and a $\sigma = 1$ would underestimate by a mean difference of $2.678\mu\text{m}$. As width increases in size from less than $20\mu\text{m}$ to less than $110\mu\text{m}$ so the σ needed to obtain a mean difference of zero increases from 1.5 to 2.5 in a near linear fashion. Figure 4.11 shows that for vessels greater than $20\mu\text{m}$ ($n=98$) to vessels greater than $110\mu\text{m}$ ($n=8$) differing sigma's are needed to obtain a MD of zero between manual and automated techniques. In figure 4.11 the zero plane indicates that for vessels greater than $30\mu\text{m}$ in width (measured manually) a σ between 3 and 3.5 would be needed to give a MD of zero. For measuring vessels greater than 60 microns then a $\sigma = 4.5$ would be needed to give a MD of zero. Note that for measuring vessels greater than $110\mu\text{m}$ in width (by manual techniques) a $\sigma = 1$ would underestimate the width by $104.220\mu\text{m}$. Higher sigma's tend to be less variable in their interpretation of width for the different bins, giving less of a slope from the MD zero plane, compared to the large slope observed with $\sigma = 1$. This interpretation of the data allows two more reliable sigma's to be selected for determining width based on size, where the mean difference is approximately zero. Note that the sigma's used for the Steger algorithm are in increments of 0.5 pixels from 1.0 to 5.0. These pixelated dimensions relate to real size. The nearest pixel increment to a MD of zero is quoted. However the 3 dimensional surface plotted in figures 4.10 and 4.11 appear to show a near linear relationship between data points so linear interpolation could be used to predict a MD of zero. However for the results presented in table 4.4 this was not deemed necessary. Values greater than 60 are not given as sigma's greater than 5 are needed to give a predicted MD of zero and interpolation beyond the data measured is of dubious validity.

<i>Vessel bin</i>	σ	<i>MD μm</i>	<i>+95% CI</i>	<i>-95% CI</i>	<i>C of R</i>
For vessels $< 20\mu\text{m}$	1.0	-2.16	2.97	7.28	10.25
For vessels $\geq 20\mu\text{m}$	3.0	1.73	35.81	32.35	68.15
For vessels $< 30\mu\text{m}$	1.0	2.68	9.43	4.07	13.51
For vessels $\geq 30\mu\text{m}$	3.5	1.09	29.32	27.15	56.47
For vessels $< 40\mu\text{m}$	2.0	-0.64	8.37	9.64	18.02
For vessels $\geq 40\mu\text{m}$	4.0	0.83	23.11	21.45	44.56
For vessels $< 50\mu\text{m}$	2.0	0.42	10.33	9.50	19.83
For vessels $\geq 50\mu\text{m}$	4.5	2.05	17.50	21.60	39.10
For vessels $< 60\mu\text{m}$	2.0	0.63	10.58	9.32	19.90
For vessels $\geq 60\mu\text{m}$	4.5	0.10	20.68	20.48	41.16

Table 4.4 shows the best σ to be used, in increments of 0.5 pixels, which gives the nearest MD of zero when compared to digital photographic measurement of width. MD \pm 95% confidence interval (CI) of inter-method repeatability, and coefficient of repeatability (C of R) are given, for differing vessel bin sizes.

Table 4.4 demonstrates the best σ to be used, for operation of the Steger algorithm, to most agree with widths measured from digitally created photographic slides. However it could be argued that the measurement from photographic slides may be open to a systematic measurement error as indicated by the similar inter method repeatabilities obtained for the Gaussian half height and mouse driven determination of width directly from digital images. Hence before these results are interpreted inter-method repeatabilities are also calculated using mouse driven methods as the gold standard.

4.3.2.3 Inter-method repeatabilities compared to mouse driven method

Intra-session repeatability of the mouse driven method gave a MD of $-0.131\mu\text{m}$ and 95% confidence interval of $+11.201$ to $-11.463\mu\text{m}$ (see table 4.2). This method gave a higher coefficient of variability than manual calliper measurement from digital photographic slides with $22.664\mu\text{m}$ and $19.416\mu\text{m}$ respectively. Note that this method is disadvantaged by a 0.5 pixel ($2.653\mu\text{m}$) systematic error because it does not have a continuous scale of measure. Widths can only be taken to the nearest pixel. Calliper measurements have a continuous scale, as with semi-automated, and automated measures which give interpolated pixel widths. However, because this may be a better estimation of width, the average of 2 sessions of measurement were taken as the 'gold standard' and compared to other methods. The mean difference, 95% confidence interval, and coefficient of repeatability between each method of measurement and the 'gold standard' are shown in table 4.5.

<i>Method</i>	<i>MD μm</i>	<i>+95% CI</i>	<i>-95% CI</i>	<i>Coeff of R</i>
Photographic calliper	-4.70	6.82	16.21	23.03
Digital photographs	-5.16	7.30	17.61	24.91
Gaussian $\frac{1}{2}$ height	0.12	16.34	16.09	32.43
Gaussian maximum gradient	6.42	23.06	10.23	33.28
Automated $\sigma = 4.5$	-13.27	6.09	32.63	38.73
Artery tubular width	-1.75	18.36	21.87	40.23
Venule tubular width	-1.95	18.32	22.22	40.55
Automated $\sigma = 4$	-10.69	10.56	31.94	42.50
Cylinder width	-3.89	19.07	26.85	45.92
Automated $\sigma = 5$	-14.71	9.44	38.86	48.29
Automated $\sigma = 3.5$	-7.68	18.97	34.34	53.31
Automated $\sigma = 3$	-3.80	29.03	36.64	65.67
Automated $\sigma = 2.5$	0.04	37.40	37.32	74.72
Automated $\sigma = 2$	4.68	47.02	37.65	84.67
Automated $\sigma = 1$	16.86	73.72	40.00	113.72

Table 4.5 shows the MD and $\pm 95\%$ confidence limits of inter-method repeatability (± 1.96 SD) for each method used against mouse driven measurement from digital images, shown in ascending order of coefficient of repeatability (2×1.96 SD).

Widths determined using manual callipers measured from photographic images created conventionally or digitally, gave the lowest coefficient of repeatability with $23.028\mu\text{m}$ and $24.911\mu\text{m}$ respectively. A plot of the inter-method repeatability of mouse driven methods and calliper measurement from digitally created photographs is shown in figure 4.6. As indicated previously, the 2 photographic calliper measurements overestimate width by $\approx 5\mu\text{m}$ compared to mouse driven methods.

Gaussian half height measurement using shape modelling agrees well with digital mouse driven determination of width, although the confidence interval is greater than photographic methods. Figure 4.12 shows a plot of the difference against the average of the mouse driven and shape modelled Gaussian half height. The mean difference was $0.122\mu\text{m}$, with $+16.338$ to -16.093 95% confidence interval, note that a regression line fitted to the data points reveals a negligible negative gradient, showing an insignificant measurement error. The relationship between these 2 methods of measurement may indicate that human selection of a vessel width corresponds to the half way point between darkness of a vessel and brightness of its surround. In photographic reproduction exaggeration of contrast may lead to further darkening of this transition, increasing the observer driven estimation of width.

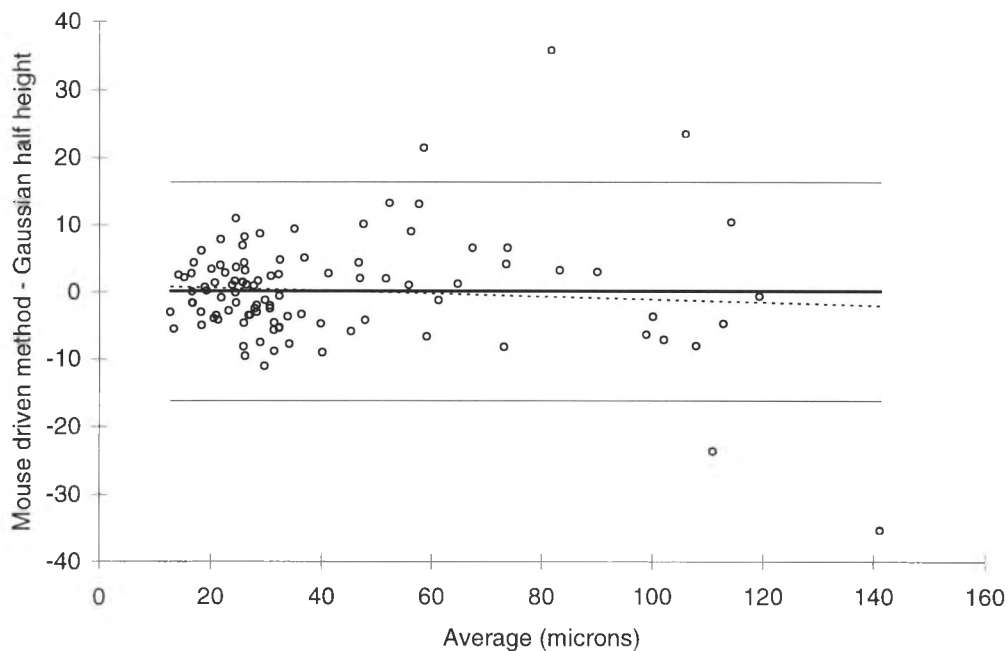


Figure 4.12 shows differences between paired values of vessel width for average measurements of the mouse driven and shape modelled Gaussian half height measures of width plotted against their mean ($n=101$). Thick solid line represents the mean difference, thin lines \pm 95% CI. Dashed line with a slight negative gradient is a linear regression line of the data points.

As with comparison with electronic calliper assessment of width, linear regression lines of data points showed that widths obtained using cylindrical or tubular shape modelling underestimate small vessel widths and over estimate large vessel widths, compared to mouse driven determination. As with calliper methods automated methods did not agree well with mouse driven determination of width. When the algorithm was set at $\sigma = 1$ vessels were comparatively underestimated by a mean difference of $16.860\mu\text{m}$, with a large coefficient of repeatability ($113.720\mu\text{m}$). When the algorithm was set at $\sigma = 5$ vessels were overestimated by a mean difference of $-14.709\mu\text{m}$, but with a lower coefficient of repeatability ($48.292\mu\text{m}$). The best agreement was obtained with $\sigma = 2.5$ where a mean difference of $0.038\mu\text{m}$ but with a high coefficient of repeatability of $74.718\mu\text{m}$. A plot of the inter-method repeatabilities for $\sigma = 2.5$ against manual calliper measurement from digital photographs is shown in figure 4.13. Although the regression line of the data points

shows a positive trend, the data points are stepped, showing a region of good prediction followed by a sharp linear increase. Results indicate that on average low sigma's tend to underestimate and high sigma's tend to overestimate vessel width in comparison to mouse driven methods.

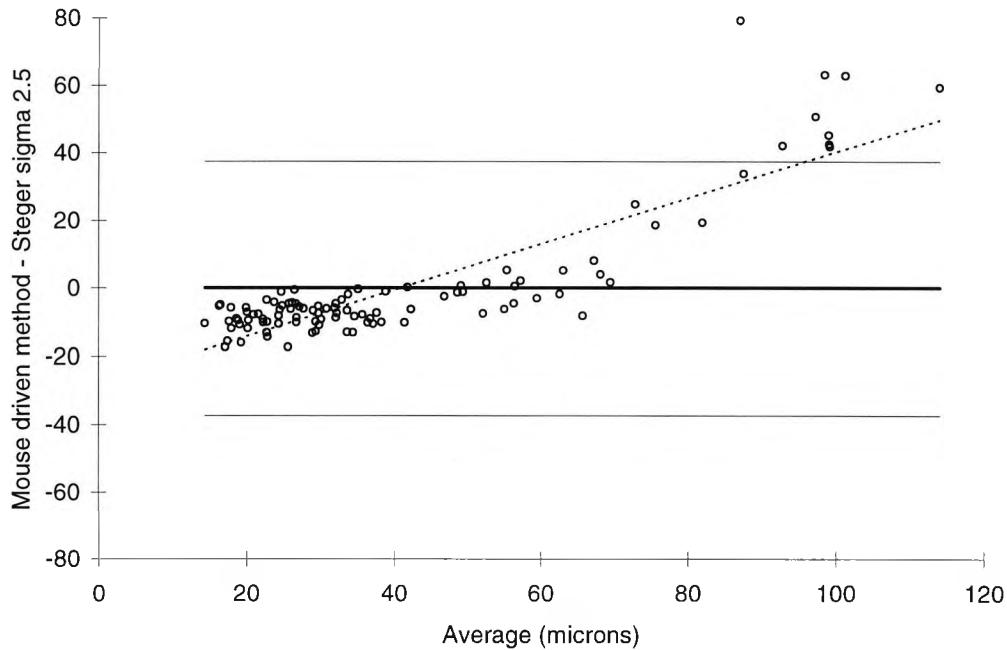


Figure 4.13 shows differences between paired values of vessel width for average measurements of automated width ($\sigma = 2.5$) and mouse driven determination, plotted against their mean ($n=101$). Thick solid line represents the mean difference, thin lines $\pm 95\%$ CI. Dashed line with a steep positive gradient is a linear regression line of the data points.

As with the previous 'gold standard' figure 4.14 shows a 3 dimensional plane surface of the mean difference of the mouse driven method minus the automated method, for differing sigma's of Steger's algorithm, plotted against differing vessel bins, varying in size from less than $20\mu\text{m}$ ($n=16$) to less than $110\mu\text{m}$ ($n=96$) in increments of $10\mu\text{m}$, as measured by mouse driven methods. In contrast figure 4.15 shows a 3 dimensional plane surface of the mean difference of the mouse driven method minus the automated method, for differing sigma's of Steger's algorithm, plotted against differing vessel bins, varying in size from greater than $20\mu\text{m}$ ($n=85$) to greater than $110\mu\text{m}$ ($n=5$) in increments of $10\mu\text{m}$, as measured by mouse driven methods. As with figures 4.10 and 4.11 the 95% confidence interval has been omitted to prevent confusion.

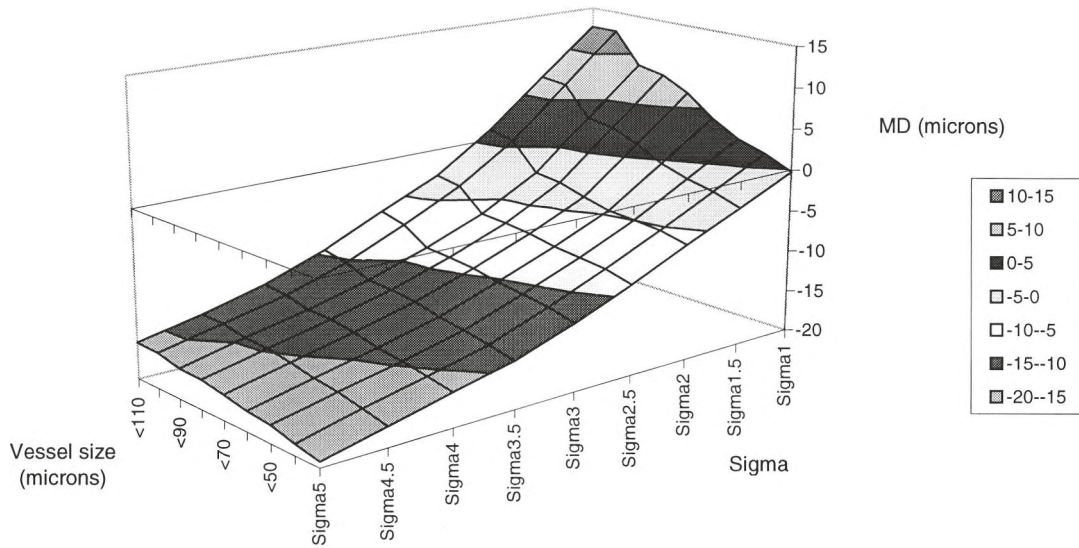


Figure 4.14 shows a 3 dimensional plane surface of the mean difference of the mouse driven method minus the automated method, for differing sigma's of Steger algorithm, plotted against differing vessel bins varying from less than 20 μm ($n=16$) to less than 110 μm ($n=96$) as measured from digitally created photographic slides with electronic callipers.

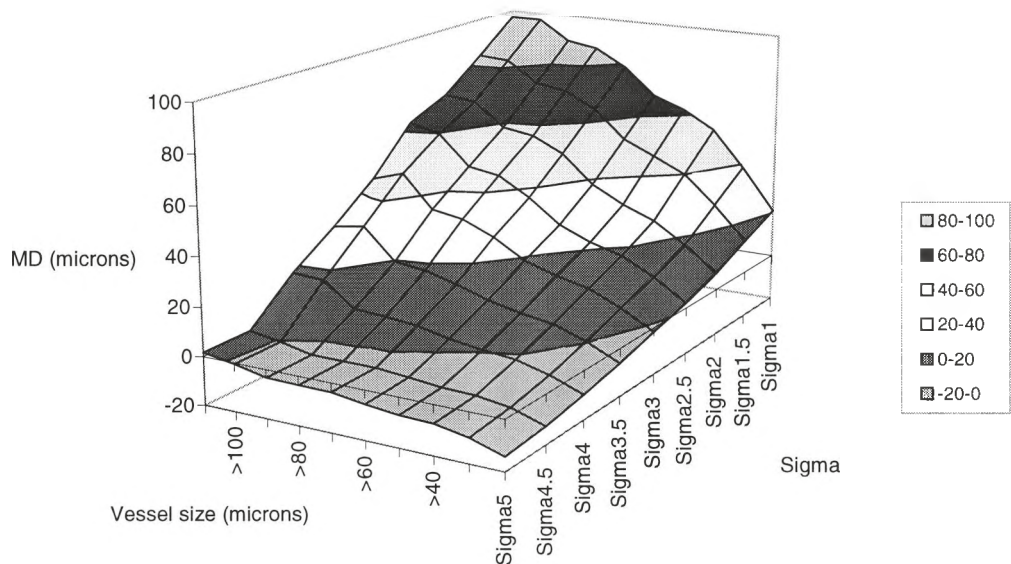


Figure 4.15 shows a 3 dimensional plane surface of the mean difference of the mouse driven method minus the automated method, for differing sigma's of Steger algorithm, plotted against differing vessel bins varying from greater than 20 μm ($n=85$) to greater than 110 μm ($n=5$) as measured from digitally created photographic slides with electronic callipers.

Interpretation of figures 4.14 and 4.15 gives table 4.6 which shows the optimum σ to be used to detect vessels to agree with mouse driven determination of width, for differing vessel sizes.

<i>Vessel bin</i>	σ	<i>MD μm</i>	<i>+95% CI</i>	<i>-95% CI</i>	<i>C of R</i>
For vessels < 20 μm	1.0	-2.852	0.866	6.571	7.437
For vessels \geq 20 μm	3.0	-1.945	32.461	36.350	68.811
For vessels <30 μm	1.0	-0.231	5.151	5.612	10.764
For vessels \geq 30 μm	3.5	0.329	32.021	31.362	63.384
For vessels <40 μm	1.0	1.171	9.334	6.993	16.327
For vessels \geq 40 μm	4.0	-0.794	21.406	22.996	44.402
For vessels <50 μm	1.0	2.212	13.308	8.883	22.191
For vessels \geq 50 μm	4.0	0.382	23.414	22.650	46.065
For vessels <60 μm	1.0	4.010	22.871	14.852	37.724
For vessels \geq 60 μm	4.0	2.382	26.141	21.376	47.517

Table 4.6 shows the best σ to be used, in increments of 0.5 pixels, which gives the nearest MD of zero when compared to mouse driven determination of width. MD \pm 95% confidence interval (CI) of inter-method repeatability, and coefficient of repeatability (C of R) are given, for differing vessel bin sizes.

4.3.3 Discussion

4.3.3.1 Sigma selection

Selection of the best σ to correctly predict vessel width is far from trivial. Current image segmentation techniques, to delineate vascular structures, fail to substantiate or investigate what is being measured. However, in the absence of a true 'gold standard' it is difficult to comment. This work has used electronic calliper measurement from digitally created slides, and mouse driven determination from digital images as the gold standards, as these represent methods of good intra-session repeatability, and give a good range of measurement, visually indicative of the structure being measured. When replacing manual with automated measurement the ability to know the best estimate of vessel width, i.e. the 'gold standard' is no longer available. Hence modifications of the automated approach must be made from an initial automated output. These modifications are based on their comparison with the 'gold standard' used, and are based on the findings listed in table 4.4 and 4.6. However, the range of measurement of each automated approach must be considered (see table 4.2), for example when using Steger's algorithm at $\sigma = 2$ all vessels are measured between 21.385 μm and 60.453 μm , whereas at $\sigma = 4$ the same vessels are measured between 6.666 μm and 115.731 μm . Therefore vessels which are large in size (>100 μm) are wrongly measured as \approx 60 μm or less. Experimentally we have found that incorrectly measured vessels usually correspond to approximately the top fifth of the range. Hence when selecting the appropriate sigma's a cut off well below the maximum of the range must be used. To explain this further an example is given using calliper measurements from digital photographs as the 'gold standard'. From table 4.4 to best agree with the 'calliper gold standard' vessels less than 60 μm in size would have to be measured using $\sigma = 2$, whilst those greater than or equal to 60 μm would have to be

measured using $\sigma = 4.5$. However, as stated $\sigma = 2$ measures all vessels between 21 and $60\mu\text{m}$ which encompasses larger vessels which should have been measured with $\sigma = 4.5$. Hence an arbitrary cut off of $40\mu\text{m}$ width would allow all small vessels ($<40\mu\text{m}$) to be correctly measured according to the 'calliper gold standard', and larger vessels measured as greater than $40\mu\text{m}$, using $\sigma = 2$, would then be re-measured using $\sigma = 4$, to give a mean difference of $0.831\mu\text{m}$ compared with the 'calliper gold standard'. In other words applying $\sigma = 2$ and re-measuring widths greater than or equal to $40\mu\text{m}$ is used to filter out wrongly measured widths. The same scenario using mouse driven determination of vessel width as the 'gold standard' produces different results. From table 4.6 to best agree with the 'mouse gold standard' vessels less than $60\mu\text{m}$ in size would have to be measured using $\sigma = 1$, whilst those greater than or equal to $60\mu\text{m}$ would have to be measured using $\sigma = 4$. However, $\sigma = 1$ measures all vessels between 6.3403 and $\approx 30\mu\text{m}$ which encompasses larger vessels which should have been measured with $\sigma = 4$. Hence a far lower cut off would have to be used to filter out incorrectly measured widths. The difficulty in using the algorithm with $\sigma = 1$ to measure vessels less than $60\mu\text{m}$ in size is in the detection of spurious noise, which is not evident when using higher sigma's ($\sigma > 1$). To eradicate noise the algorithm is set at higher thresholds at the cost of losing detail. Hence although it is acknowledged that using electronic calliper measurement from digitally created photographic images may overestimate vessel width by $\approx 5\mu\text{m}$ its performance is more reliable and less affected by noise.

Automated detection of conjunctival vessels is best achieved using $\sigma = 2$, run at low thresholds (lower threshold 0 pixels, higher threshold 0.5 pixels). Vessel strings with mean widths greater than or equal to $40\mu\text{m}$ are then re-measured using Steger's algorithm run at $\sigma = 4$, at similar thresholds, allowing correct identification of larger vessels incorrectly measured at the lower σ . The combined output represents the best morphometric equivalent to manual calliper measurement from digitally created photographic images. However, if a single σ were to be chosen to measure all vessels it would have a value of 3.

4.3.3.2 Intra-session repeatabilities for large ($\geq 40\mu\text{m}$) and small vessels ($< 40\mu\text{m}$)

Tables 4.7 and 4.8 show the intra-session repeatabilities for vessels less than $40\mu\text{m}$ in size, and vessels greater than $40\mu\text{m}$, respectively, as determined by Steger's algorithm run at $\sigma = 2$. Note how the maximum and minimum measures differ for each method. Our recommended methodology of measuring vessels shows a 95% confidence interval of $+5.493\mu\text{m}$ to $-6.235\mu\text{m}$ for vessel widths $< 40\mu\text{m}$ in diameter (using $\sigma = 2$), and $+12.554\mu\text{m}$ to $-12.825\mu\text{m}$ for vessels $\geq 40\mu\text{m}$ in diameter (using $\sigma = 4$), which is shown in figures 4.16 and 4.17 respectively. Note that the 2 outliers shown in figure 4.17 have a large effect on the confidence range due to the smaller sample size ($n=34$). A reduced confidence range could be achieved by using $\sigma = 3, 3.5$ or 5 with 95% confidence intervals of $+13.920$ to $-11.029\mu\text{m}$, $+7.347$ to $-6.315\mu\text{m}$, and $+6.425$ to $-7.538\mu\text{m}$ respectively. However, it has been shown that this does not give the best inter-method repeatability with calliper width. Tables 4.7 and 4.8 also show that the intra-session repeatability is superior for small vessels rather than large. Ideally changeable sigma's should be used for differing widths of vessels. However, further division of the data would only increase the chance of spurious findings due to

decreased sample sizes, which is demonstrated by the increased confidence range due to the presence of 2 outliers for vessels $\geq 40\mu\text{m}$ in size.

Method	MD μm	+95% CI	-95% CI	C of R	Min μm	Max μm
Auto $\sigma = 2$	-0.371	5.493	6.235	11.728	21.385	38.866
Auto $\sigma = 2.5$	-0.374	5.877	6.626	12.503	21.605	42.041
Auto $\sigma = 3$	-0.026	6.343	6.396	12.739	23.444	45.232
Auto $\sigma = 3.5$	-0.019	6.892	6.929	13.822	21.470	48.882
Auto $\sigma = 1$	-0.603	7.111	8.318	15.429	15.738	29.871
Gauss max G	0.016	9.199	9.166	18.365	11.048	32.357
Auto $\sigma = 4$	0.045	9.430	9.340	18.770	6.666	52.352
Digital photo	0.534	10.647	9.580	20.227	14.401	48.253
Mouse driven	-0.827	9.525	11.180	20.705	10.610	39.846
Gauss $\frac{1}{2}$ H	0.019	10.831	10.792	21.623	13.008	38.097
Photographic	-0.687	10.678	12.052	22.730	15.328	46.837
Auto $\sigma = 4.5$	0.426	15.329	14.477	29.807	8.395	56.607
Arterial tube	-1.268	19.813	22.348	42.161	7.541	42.735
Venular tube	-1.011	20.745	22.767	43.512	4.600	42.460
Cyl width	-1.609	21.026	24.243	45.269	7.910	44.246
Auto $\sigma = 5$	0.221	23.227	22.786	46.014	8.400	62.270

Table 4.7 shows the MD, $\pm 95\%$ confidence limits of repeatability (± 1.96 SD), minimum and maximum values for each method used to measure vessel width on sessions 1 and 2, for values less than $40\mu\text{m}$ in width as measured with $\sigma = 2$ ($n=67/101$ profiles), shown in ascending order of coefficient of repeatability (2×1.96 SD).

Method	MD μm	+95% CI	-95% CI	C of R	Min μm	Max μm
Auto $\sigma = 3.5$	0.519	7.347	6.315	13.662	25.165	91.905
Auto $\sigma = 5$	-0.556	6.425	-7.538	13.963	41.007	129.431
Digital photo	0.178	9.162	8.806	17.968	40.281	140.029
Photographic	-1.596	10.289	13.482	23.771	34.774	133.241
Auto $\sigma = 3$	1.446	13.920	11.029	24.948	35.357	90.547
Auto $\sigma = 4$	-0.135	12.554	12.825	25.379	44.585	115.731
Mouse driven	1.242	14.030	11.547	25.577	35.671	123.452
Auto $\sigma = 1$	1.605	16.633	13.422	30.055	6.403	29.932
Auto $\sigma = 4.5$	-0.073	15.562	15.707	31.269	40.193	103.256
Auto $\sigma = 2$	1.976	18.021	14.068	32.089	40.781	60.453
Auto $\sigma = 2.5$	-0.390	18.344	19.124	37.468	38.452	75.429
Cyl width	-0.174	18.673	19.022	37.695	51.206	148.543
Venular tube	0.277	21.989	21.434	43.422	47.619	144.962
Arterial tube	1.038	22.817	20.741	43.558	47.189	144.999
Gauss max G	0.939	27.768	25.890	53.657	33.890	134.912
Gauss $\frac{1}{2}$ H	1.106	32.694	30.483	63.176	39.903	158.847

Table 4.8 shows the MD, $\pm 95\%$ confidence limits of repeatability (± 1.96 SD), minimum and maximum values for each method used to measure vessel width on sessions 1 and 2, for values $\geq 40\mu\text{m}$ in width as measured with $\sigma = 2$ ($n=34/101$ profiles), shown in ascending order of coefficient of repeatability (2×1.96 SD).

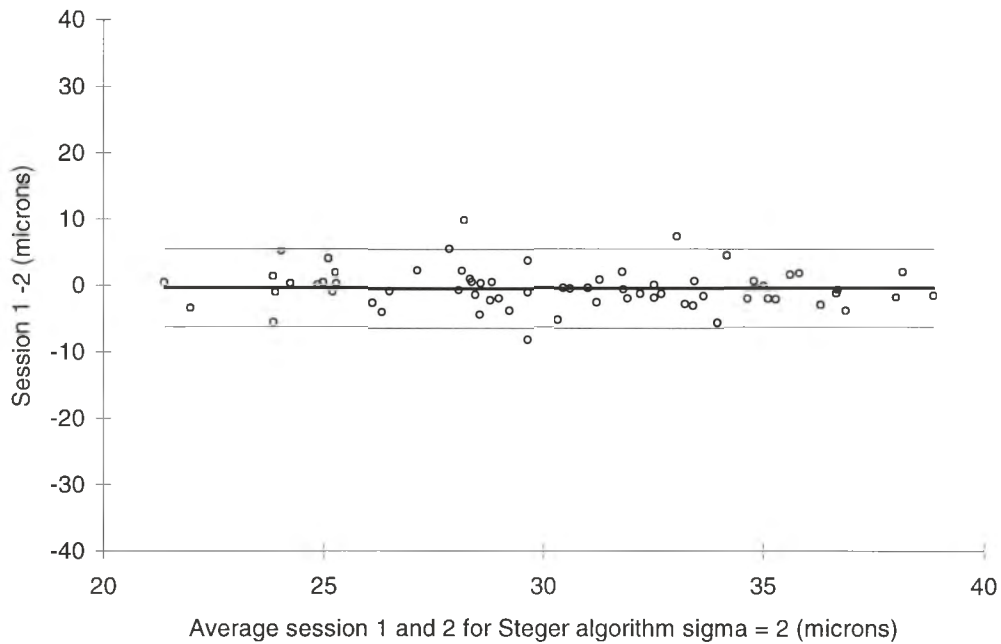


Figure 4.16 shows difference between paired values of vessel width for sessions 1 and 2 plotted against their mean ($n=67/101$) using Steger's algorithm at $\sigma = 2$ for vessels $<40\mu\text{m}$. Thick solid line represents mean difference, and thin lines $\pm 95\%$ CI. The solid line also indicates a linear regression line of the data points showing insignificant measurement error.

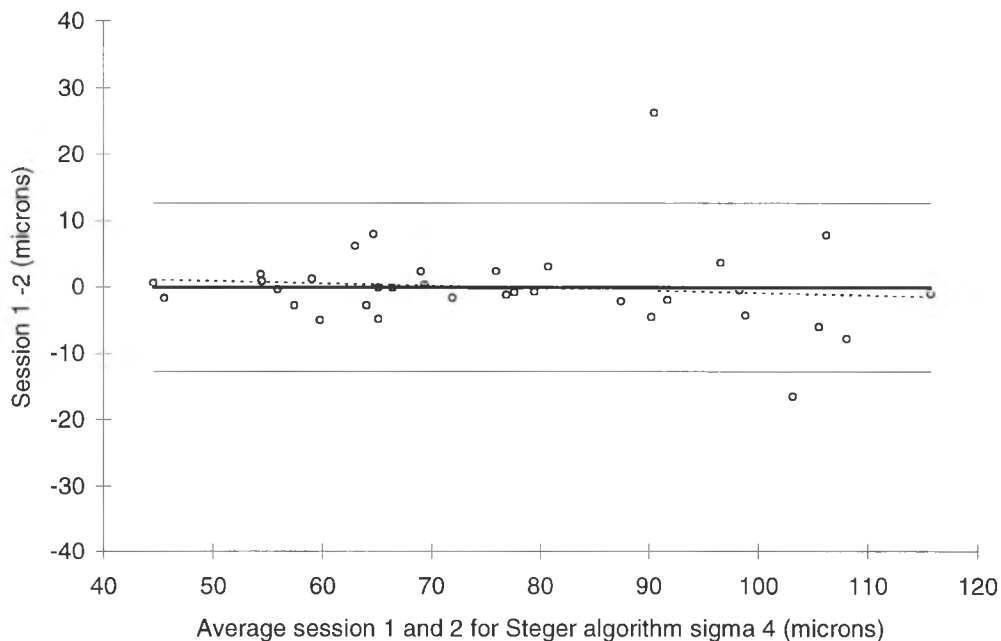


Figure 4.17 shows difference between paired values of vessel width for sessions 1 and 2 plotted against their mean ($n=34/101$) using Steger's algorithm at $\sigma = 4$ for vessels $<40\mu\text{m}$ (as measured by $\sigma = 2$). Thick solid line represents mean difference, and thin lines $\pm 95\%$ CI. The dashed line with a slight negative gradient is a linear regression line of the data points showing insignificant measurement error.

4.4 Vascular tortuosity measurement

4.4.1 Introduction

Retinal vessel tortuosity is often used as a measure of diagnostic value for conditions such as hypertension, atherosclerosis, and diabetes. Subjective scaling of tortuosity, at best using graded values (usually from 0 non-tortuous to 5 severe tortuosity), form the mainstay of assessment. Lotmar *et al* (1979) claim that measurement of tortuosity is more accurate than vessel diameter. Diametric measurement is plagued by variations in photographic processing or image quality where tortuosity is not so readily affected. Kylstra *et al* (1986) investigated the relationship between tortuosity and width in a latex tube model. Tortuosity did not increase until a 'critical pressure' was reached below which width was a more sensitive measure of transmural pressure. However above this 'critical pressure' tortuosity was superior, but extrapolations to retinal findings are difficult. Objective means of tortuosity assessment principally involve a ratio of vessel to chord length. A variety of methods have been used to obtain an approximation of vessel length including direct measurement or from assumptions made from specific measured vessel dimensions. Lotmar *et al* (1979) projected photographs of tortuous vessels onto a graticuled plate, and subdivided them into a series of arcs, allowing chord and sagittal lengths to be measured. An approximate mathematical formula was derived to give vessel length from these values, however this equation is less accurate the more tortuous the vessel and 'vessels tend to be sinusoidal (in shape) rather than a sequence of circles'. The method outlined was considered as a more accurate means of obtaining a ratio of vessel to chord length than manual measurement. Another method (Strömmland *et al*, 1995) using fundus photographs (35mm) digitised to 480×700 pixels with a region of interest 385×512 centred on the optic disc were displayed on a VDU. Mouse driven determination of the vessel axis allowed the vessel to chord length ratio to be computationally measured, between 2 reference circles (centred on the optic disc). Children (n=6) with foetal alcohol syndrome who exhibit hypoplastic optic discs and tortuous branching retinal vessels were compared to age matched normals (n=6). Affected children showed more tortuous arteries (P=0.002) and veins (P=0.0001) compared to normals by this method. However the method proved time consuming and tedious. Retinopathy of prematurity is typified by dilated tortuous vessels at the posterior pole. Capowski *et al* (1995) studied 14 eyes from 7 infants with this condition. Digitised fundus photographs (2000×2000 pixels) were viewed and vessels traced using a mouse. Tortuosity was measured by comparing vessel to chord length. Vessels suffering from retinopathy of prematurity were found to have a distinctive dimension to their tortuosity with a mean distance across the mouth of a vessel 'wobble' of 292µm (± 87µm SD) and length of 992µm (± 212µm SD). An algorithm designed to detect this feature was said to distinguish between those requiring and those not requiring treatment. However the statistical verification of this statement was incomplete. Kylstra *et al* (1995) believe that computer assisted measurement of vessel tortuosity, using conventional vessel to chord length, from digitised fundus photographs, provides an index to diagnose retinopathy of prematurity. Mean tortuosity for 7 individuals with retinopathy of prematurity gave a value of 1.23 ± 0.65 compared to 1.09 ± 0.07 for 7 normal patients (P<0.001). With a cut-off of 1.18 being indicative of retinopathy of prematurity, sensitivity was 85% and specificity 91%. Although these papers appear to show the usefulness of vessel to chord length

tortuosity measures they have rarely been applied to blood vessels in the conjunctiva. Here, the density and size of vessels is widely variable, and the vessel measurement more problematic, with substantial bifurcation / crossing of the vascular complex. With computerised automated detection of a vessels edge and axis tortuosity can be easily calculated. However curve to chord length may not be the best measure of tortuosity, hence, we have investigated the specificity of curve energy and local curvature estimates using an experimental sinusoidal model.

4.4.2 Method

Most objective methods which investigate tortuosity rely on analysing data from actual vessels. However comparisons of sophisticated methods have to be made with subjective clinical measurement, which is open to a large variation in interpretation. A more controlled method is to create a simulated vessel where the degree of tortuosity can be varied.

4.4.2.1 Vessel tortuosity model

A model was designed to be indicative of a vessel found on the conjunctiva, which could be representative of vessels found elsewhere. A vessel 360 units long was created using the sinusoidal model as shown by the equation below, where A was the amplitude of wave form and given a value of 5 units, C the sinusoidal wave cycles in a 360 unit length.

$$y = A \sin\left(C \times \frac{\pi \cdot x}{2}\right)$$

Figure 4.19 shows 20 sinusoidal waveforms. Cycles vary from 0 at the top (a non-tortuous straight vessel) to 20 cycles at the bottom (extremely tortuous). Differing methods of quantifying tortuosity were used including a conventional ratio between vessel length and chord length, local curvature estimates based on the mean of incremental estimates of curvature, curve energy based on the mean square of incremental radian angle deviations. The method of calculating each index is given below.

Mean vessel to chord length ratio

The horizontal chord length of the sinusoidal waveform was known to be 360 units. This curve was divided into horizontal increments of one unit and the curve length calculated as the linear distance from a co-ordinate (x_n, y_n) to (x_{n+1}, y_{n+1}) on the waveform. Hence vessel (curve) length can be determined from the following equations.

$$\text{vessel length} = \sum_{n=360}^{n=0} \sqrt{\left((y_{n+1} - y_n)^2 + (x_{n+1} - x_n)^2\right)}$$

$$\text{chord length} = 360 \quad x_{n+1} - x_n = 1$$

$$\frac{\text{vessel length}}{\text{chord length}} = \frac{\sum_{n=360}^{n=0} \sqrt{\left((y_{n+1} - y_n)^2 + 1\right)}}{360}$$

Vessel length was measured using the linear distance between each increment, totalling 360 lengths, and divided by a chord length of 360 units (the total horizontal distance of the model). This gave a vessel to chord length ratio.

Local curvature estimates were calculated by fitting a circular model to each sinusoidal half cycle. The circular model was fitted to a chord distance of half a cycle ($=180/C$) and the amplitude ($A=5$ units), the radius calculated gave the mean curvature estimate. Figure 4.18 shows a 20 unit portion of a sinusoidal wave form 360 units in length and the circular model fitted to the amplitude and chord length.

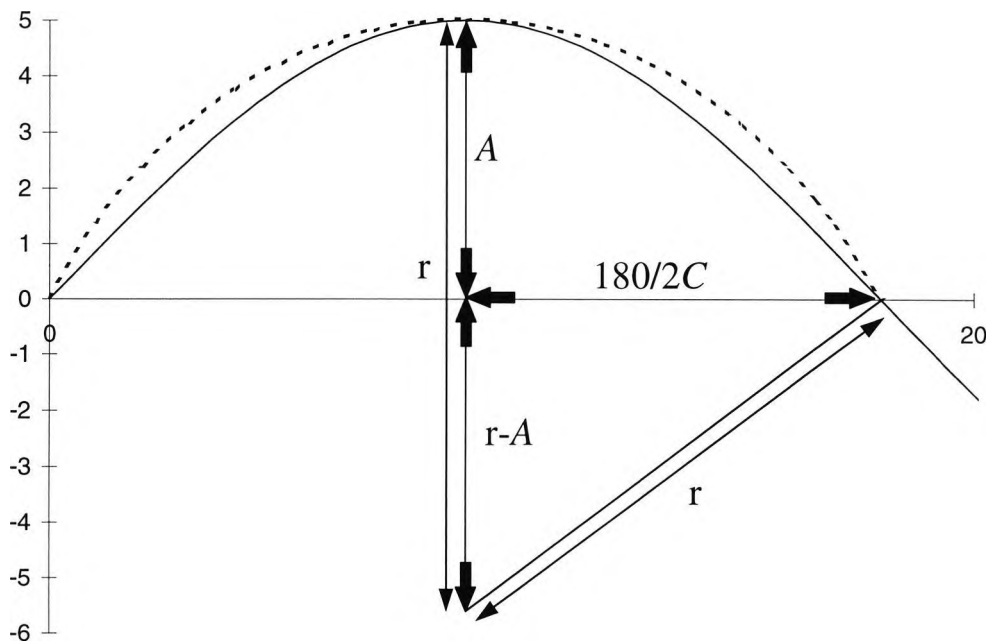


Figure 4.18 shows a 20 unit portion of a sinusoidal wave form 360 units in length and the circular model fitted to the amplitude and chord length, where $A =$ amplitude (5 units) and chord length $= 180/2C$.

From figure 4.18 the radius of the circular model fitted to each half sinusoidal waveform can be calculated from the following equations.

$$r^2 = (r - A)^2 + \left(\frac{180}{2C}\right)^2$$

$$r = \frac{5}{2} + \frac{810}{C^2}$$

Curve energy was calculated as the mean of the squared angular change between each increment. In total 360 radian angular changes were squared and the mean calculated to give a positive angular change between each increment (without squaring the positive angular changes would be equalled by the negative changes giving a zero value). The mean of these squared values gave curve energy and is given by the following equation.

$$\text{Curve energy} = \frac{\sum_{n=360}^{n=0} \left(\text{Inv sin} \left(\frac{y_{n+1} - y_n}{\sqrt{(y_{n+1} - y_n)^2 + 1}} \right) \right)^2}{360}$$

A graph for each tortuosity measurement against cycles was plotted and modelled using powered or polynomial trendlines. The decision as to the best tortuosity measure was based on the method giving the most increment of change with increasing tortuosity.

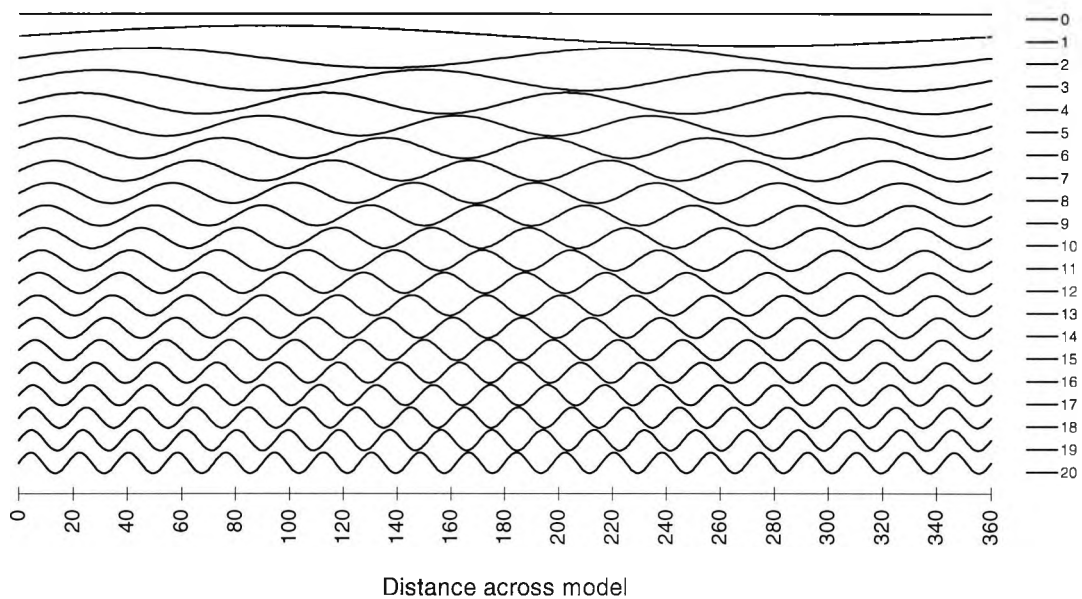


Figure 4.19 shows 20 sinusoidal waveforms with varying cycles (0 to 20 cycles per 360 unit of length), with amplitude of 5 units.

4.4.3 Results

Figures 4.20 to 4.22 shows the relationship between differing tortuosity measures and cycles per 360 unit model length, for vessel to chord length ratio, mean local curvature estimates, and curve energy respectively. Each data point refers to the waveforms shown in figure 4.19 in ascending order of tortuosity.

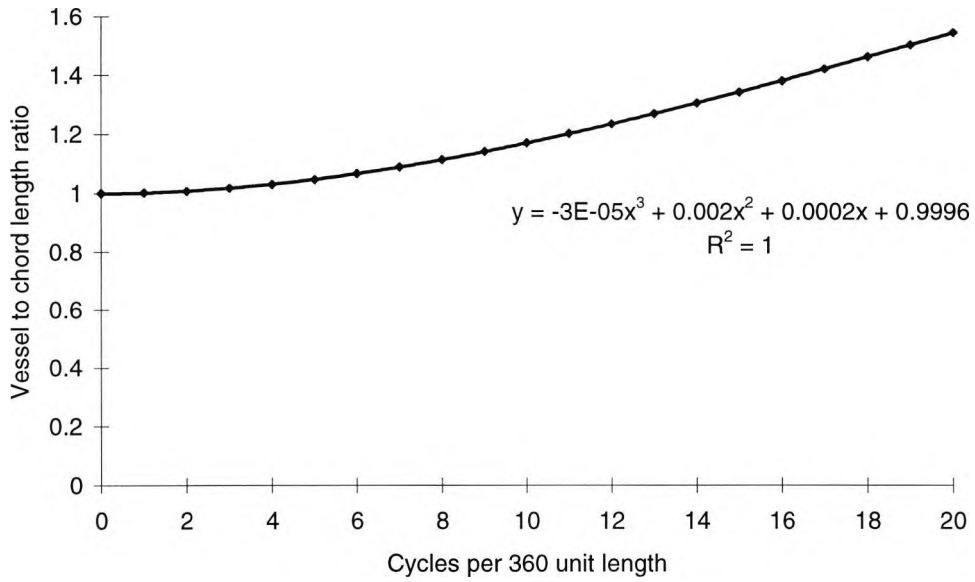


Figure 4.20 shows the relationship between vessel to chord length ratio and cycles per 360 unit length. A third order polynomial trendline is shown with equation of the line and regression value.

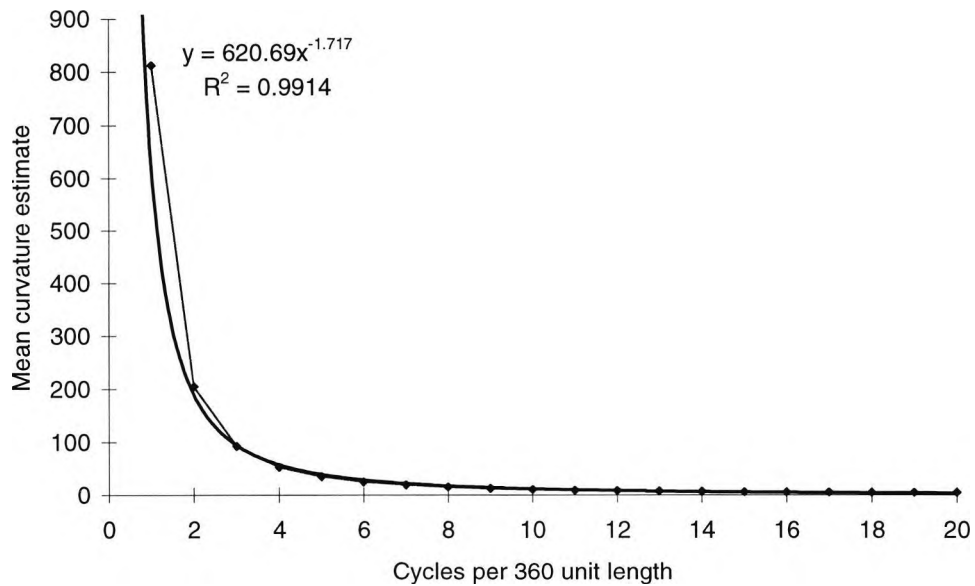


Figure 4.21 shows the relationship between mean curvature estimates and cycles per 360 unit length. A powered trendline is shown with equation of the line and regression value.

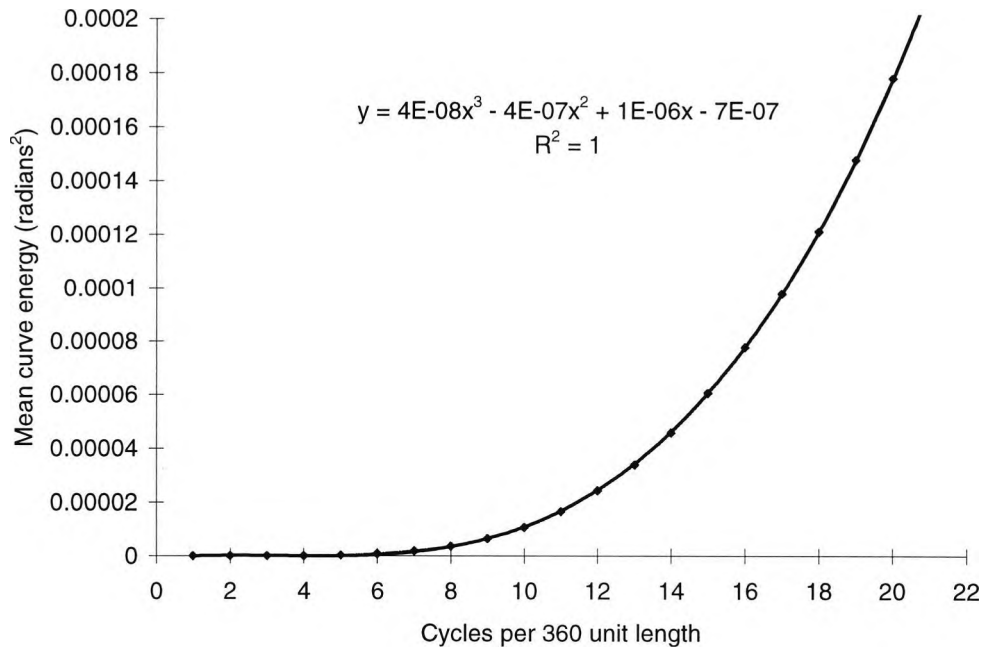


Figure 4.22 shows the relationship between mean curve energy (based on the square of the radian change between wave increments) and cycles per 360 unit length. A third order polynomial trendline is shown with equation of the line and regression value.

4.4.4 Discussion of vessel tortuosity measures

Although the vessel to chord length ratio gives a third order polynomial relationship it does not escalate to large values over the range of tortuosity measured (0 to 20 cycles per 360 unit length) (see figure 4.20). However if the cycles were increased a sharp escalation would be seen, typified by a third order polynomial graph. However the examples measured are indicative of vessels found on the conjunctiva and are not likely to be drastically more tortuous. Vessel to chord length ratios suffer from a major drawback which is demonstrated in figure 4.23, where a long arcing length between 2 data points will give the same value as a tortuous waveform. Reducing chord length will only reduce the ratio, to a point where chord length becomes the increment of vessel length and the tortuosity value will equal one. Table 4.9 lists the tortuosity values obtained for the non tortuous and tortuous waveforms shown in figure 4.23 and the percentage difference between them. Evidently, curve energy shows the greatest degree of change between the 2 waveforms shown.

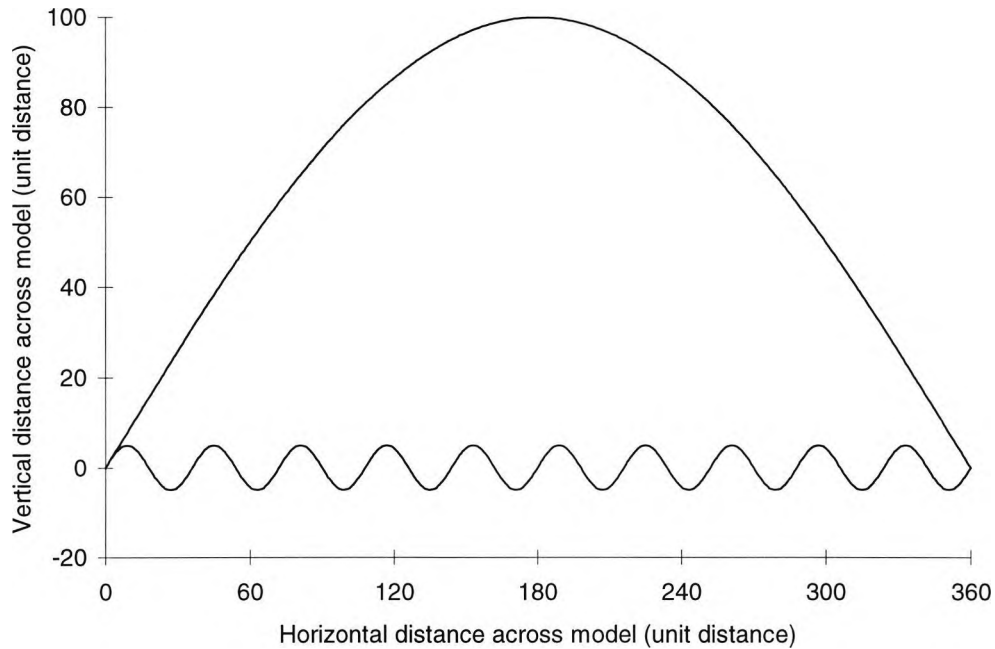


Figure 4.23 shows two sinusoidal waveforms which would give the same vessel to chord length ratio, but are clearly dissimilar in tortuosity.

TORTUOSITY MEASURE	NON TORTUOUS	TORTUOUS	% Δ
Vessel / Chord Length	1.17	1.17	0 %
Mean curvature estimate	213	10.6	-95.0 %
Curve energy (radians ²)	0.000022	0.0087	39450 %

Table 4.9 lists vessel /chord length ratio, mean curvature estimate, and curve energy values for the non tortuous and tortuous waveforms in figure 4.23.

Local curvature estimates have an inverse relationship with sinusoidal cycle increase, and show less change with higher levels of tortuosity. They are sensitive to minor changes in vessel meandering although such minor changes are unlikely to be indicative of a challenged vascular system. The method best suited to tortuosity changes is that of mean curve energy. Although showing minor increase with sinusoidal waveforms less than 7 cycles per 360 unit length, they increase dramatically above this. From figure 4.19 wavelengths below 7 cycles per 360 unit length do not appear to be clinically tortuous, however above this tortuosity becomes clinically significant. Any measurement has an associated error but a method which shows a large increment of change with increasing clinical effect improves the ability to observe true differences. This sinusoidal model exemplifies the use of curve energy as a measure of tortuosity over conventional methods of vessel to chord length ratios, and hence will be used here.

4.5 Measurement of vascular indices

4.5.1 Introduction

As detailed previously in this chapter considerable lengths have been made to verify the use of Steger's algorithm (1996; 1998) in detecting conjunctival vessels. It has allowed us an understanding of the performance of the algorithm in describing vessel widths. However, the output of Steger's program, which results in some 20,000 to

50,000 measurements per image, must be used to give useful morphological and morphometric information about the vessel organisation on the conjunctiva. Vascular indices must be designed to detect environmentally and / or pathologically challenged conjunctivae. This section details the use of Steger's algorithm and generates vascular indices to be used.

4.5.2 Method

To measure vessel tortuosity on conjunctival vessels reliable image segmentation of a vascular axis is needed. We used Steger's algorithm (1996; 1998) for this task. Details of the algorithm are described elsewhere. Suffice to say that the algorithm returns the precise sub-pixel axis position, and the width of the vessel for each axis point with sub pixel accuracy and is able to detect 'strings' of vessels. Previous work using this algorithm suggests that automated detection of vessel width was best described using a $\sigma = 2$ for vessels less than $40\mu\text{m}$ in size. Those greater than $40\mu\text{m}$ should then be re-measured with $\sigma = 4$ to give a more appropriate estimation of vessel size. Previous work has shown a 95% confidence interval of intra-session repeatability of $+5.493\mu\text{m}$ to $-6.235\mu\text{m}$ for vessel widths $<40\mu\text{m}$ in diameter (using $\sigma = 2$), and $+12.554\mu\text{m}$ to $-12.825\mu\text{m}$ for vessels $>40\mu\text{m}$ in diameter (using $\sigma = 4$). These figures are shown in tables 4.7 and 4.8 respectively.

We proposed 4 arbitrary bins of width measure. Vessels less than $25\mu\text{m}$ using $\sigma = 2$, 25 to $<40\mu\text{m}$ using $\sigma = 2$, 40 to $<80\mu\text{m}$ using $\sigma = 4$, and $\geq 80\mu\text{m}$ using $\sigma = 4$. A vessel bin size $<25\mu\text{m}$ in diameter represents capillaries ($9-10\mu\text{m}$), and post capillary venules ($10-30\mu\text{m}$). Vessels between 25 and $<40\mu\text{m}$ relate to collecting venules ($30-50\mu\text{m}$). Arteriole vasculature tends to manifest at dimensions above $40-50\mu\text{m}$ hence vessels between 40 to $<80\mu\text{m}$ are likely to contain venules ($>50\mu\text{m}$), and arterioles ($>40\mu\text{m}$). Vessels $\geq 80\mu\text{m}$ will predominantly contain muscular arterioles, veins, and major arterioles such as the anterior ciliary artery. It is important to realise what the differing vessel bins represent, because certain bin sizes may show greater or lesser change in the event of vascular disease or challenge. Although there are a number of morphological indicators to visually help classify a vessel as an artery or vein, these are not readily available when using an algorithm to detect vessels, unless a specific algorithm is developed. It was not within the bounds of this thesis to develop such a program. Hence vessels were classified diametrically only.

The digital images (1024×1280 pixels) acquired correspond to an area of $5.433 \times 6.791\text{mm}$ of the conjunctiva (36.894mm^2), where 1 millimetre equals 188.494 pixels. Images were acquired using a Xenon flash source through a Wratten 99 filter (green) and recorded to an 8 bit, 256 grey level image from the green channel of the CCD array (as detailed in chapter 3). Each image was saved in a portable grey map format and archived on a writable compact disc.

Images containing tear layer reflections of the flash source correspond to grey levels in excess of 249 (this value was experimentally derived), hence values greater than this were ignored from analysis. Images then underwent Steger's algorithm (Steger 1996; 1998) for detection of curve linear structures using a $\sigma = 2$ and repeated for $\sigma = 4$. Note the lower threshold for both sigma's was set at 0.0 pixels and the upper 0.5 pixels to ensure all detail was found. The raw output of Steger's algorithm gave a

series of detected vessel strings of a given pixel length. String lengths less than 10 pixels in length ($53.1\mu\text{m}$) were ignored to prevent the detection of spurious noise. Each string consisted of a series of sub-pixel x,y co-ordinates which refers to one of n axis points along a vessel string. In addition a left and right hand pixel distance from the centre point to the vessels edge for each x,y value was given. The sum of the left and right hand widths divided by 0.188494 gave the real width in microns. The average width along a vessel string was calculated using the $\sigma = 2$ data file. If the average pixel width of a string was less than $40\mu\text{m}$ it was considered correct. However, if the average was greater than or equal to $40\mu\text{m}$ the data was replaced with the pixel string detected from the $\sigma = 4$ data file. Retrieved data must be within close proximity to the string co-ordinates detected using $\sigma = 2$. Hence, a Euclidean pixel tolerance of search was decided upon, where the corresponding pixel string for the $\sigma = 4$ output was within $\sqrt{2}$ pixels of the $\sigma = 2$ co-ordinates. The combined output gave the true vessel widths and vessel axis positions (in terms of x,y co-ordinates) for the image measured. Curve energy measurements were then calculated as the square of radian angular change between each x,y co-ordinate. The data was described by five indices, which are considered to give the most pertinent characters indicative of pathology. The mean width ($\mu_{1w}, \mu_{2w}, \mu_{3w}, \dots, \mu_{kw}$) and variance ($\sigma_{1w}^2, \sigma_{2w}^2, \sigma_{3w}^2, \dots, \sigma_{kw}^2$) of each string was calculated and multiplied by vessel string length ($n_1, n_2, n_3, \dots, n_k$), summed across all strings and divided by the combined string length ($n_1+n_2+n_3+\dots+n_k$). The mean width (W) calculated was identical to taking the entire number of widths, over all vessels, and dividing by the total number of measures. However, this was not the case for variance (WV), where the weighted calculation of mean variance allowed a more indicative measure of intra vessel width variation, as opposed to summing all variances for different calibres of vessels. It was accepted that unlike the W index, WV was not the best statistical representation of the data. Vessels within the same subject are dependent on each other. The measurement of variance surmises that the data is independent. Hence, it could be argued that multivariate or hierarchical modelling would be a more appropriate method of treating the data. However, for the purposes of this thesis the simpler measurement of weighted variance was considered satisfactory. It is noteworthy that W is expressed in microns, and WV in microns squared.

$$W = \frac{(\mu_{1w} \times n_1) + (\mu_{2w} \times n_2) + (\mu_{3w} \times n_3) + \dots + (\mu_{k.w} \times n_k)}{n_1 + n_2 + n_3 + \dots + n_k}$$

$$WV = \frac{(\sigma_{1w}^2 \times n_1) + (\sigma_{2w}^2 \times n_2) + (\sigma_{3w}^2 \times n_3) + \dots + (\sigma_{k.w}^2 \times n_k)}{n_1 + n_2 + n_3 + \dots + n_k}$$

The mean tortuosity was calculated in a similar fashion, where mean tortuosity ($\mu_{1t}, \mu_{2t}, \mu_{3t}, \dots, \mu_{kt}$) and variance ($\sigma_{1t}^2, \sigma_{2t}^2, \sigma_{3t}^2, \dots, \sigma_{kt}^2$) of each string was calculated and multiplied by vessel string length ($n_1, n_2, n_3, \dots, n_k$), summed across all strings and divided by the combined string length ($n_1+n_2+n_3+\dots+n_k$). As with the calculation of mean width (W), mean tortuosity (T) was identical to taking each separate calculation of tortuosity, over all vessels, and dividing by the total number of measures. This was not the case for variance (TV), where the weighted calculation of mean variance allowed a superior measure of intra vessel tortuosity variation, as opposed to summing

all variances for different calibres of vessels, which would give an unduly elevated measure of tortuosity variance. However, the same statistical arguments for *WV* apply to *TV*. Note that *T* was measured in units of curve energy and *TV* in units of curve energy squared.

$$T = \frac{(\mu_{1t} \times n_1) + (\mu_{2t} \times n_2) + (\mu_{3t} \times n_3) + \dots + (\mu_{k,t} \times n_k)}{n_1 + n_2 + n_3 + \dots + n_k}$$

$$TV = \frac{(\sigma_{1t}^2 \times n_1) + (\sigma_{2t}^2 \times n_2) + (\sigma_{3t}^2 \times n_3) + \dots + (\sigma_{k,t}^2 \times n_k)}{n_1 + n_2 + n_3 + \dots + n_k}$$

In addition to the above a total vascular density was calculated. As stated previously areas within the image having grey levels in excess of 249/256 were experimentally found to represent reflections of the flash source in the anterior tear layer causing gross overexposure obscuring underlying vasculature. Hence total area of conjunctiva equalled $5.433 \times 6.791 \text{ mm}$ (1024×1280 pixels) minus any area of reflection. The total vascular area was calculated from the combined vessel string area divided by the total area of conjunctiva to give vascular density in mm^2 of vessel per mm^2 of conjunctiva, hence this index could be considered as a proportion of vasculature.

Data was then divided into bins where vessel widths $<25\mu\text{m}$ represent capillaries, 25 to $<40\mu\text{m}$ venules, 40 to $<80\mu\text{m}$ arterioles and venules, $\geq 80\mu\text{m}$ arterioles and veins. Within each bin size, mean vessel width (*W*) and string variance (*WV*), mean tortuosity (*T*) and string variance (*TV*), and vascular density were calculated. Hence a total of 25 indices.

The computation of maximum capillary perfusion distance (i.e. the largest distance between a vessel and the surround) may have been of use but was omitted due to programmable difficulties.

The above indices were measured on 2 very different vascular beds and their performance visually compared. A cropped portion of the images of patient 1 and 2 used are shown in figure 4.24 and 4.25 respectively. It is noteworthy that the two vascular beds are very different, hence, the vascular indices were compared in order to gauge the performance of the algorithm.

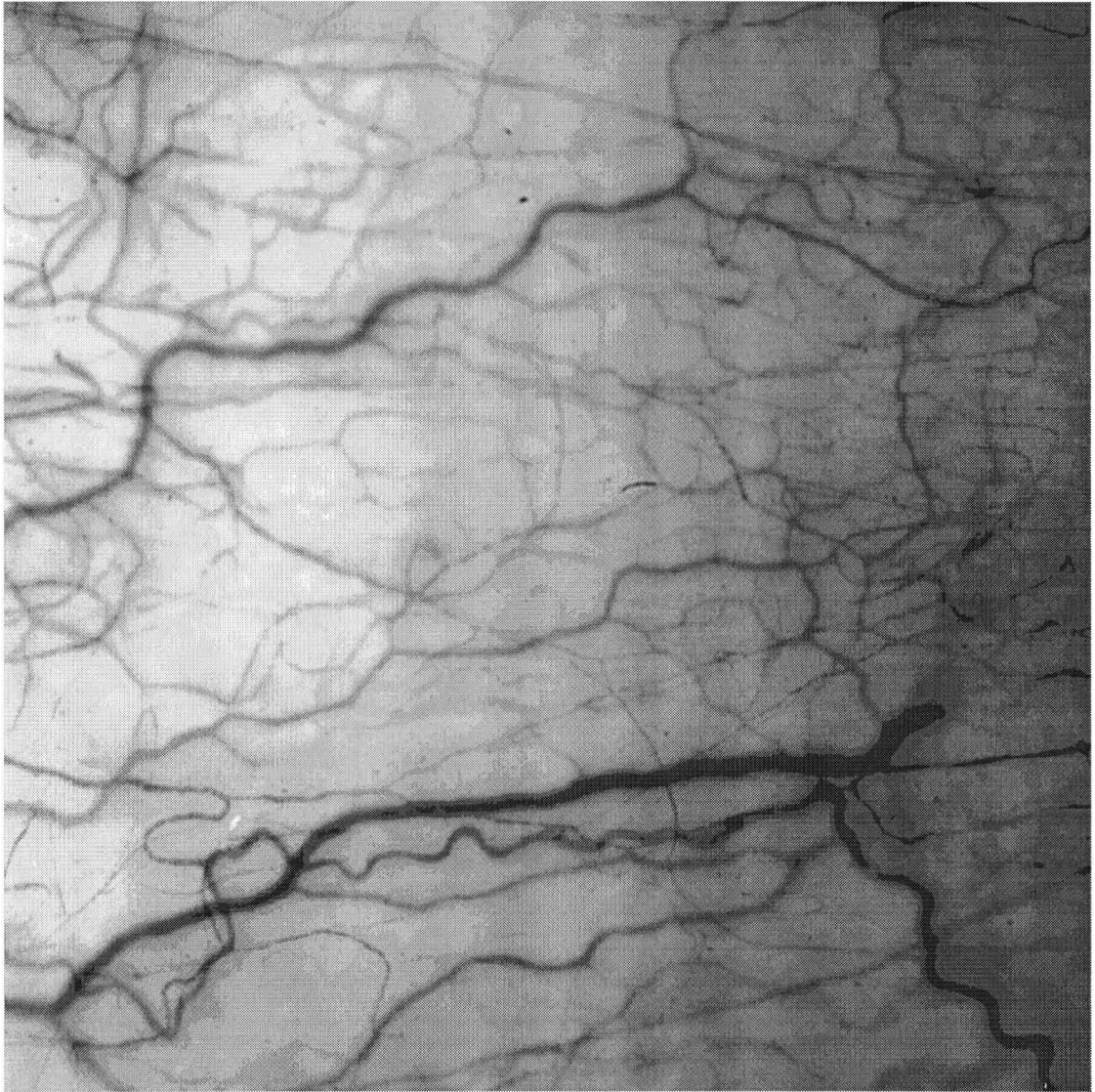


Figure 4.24 shows a 900×900 pixel portion of the 1024×1280 pixel image of patient 1.

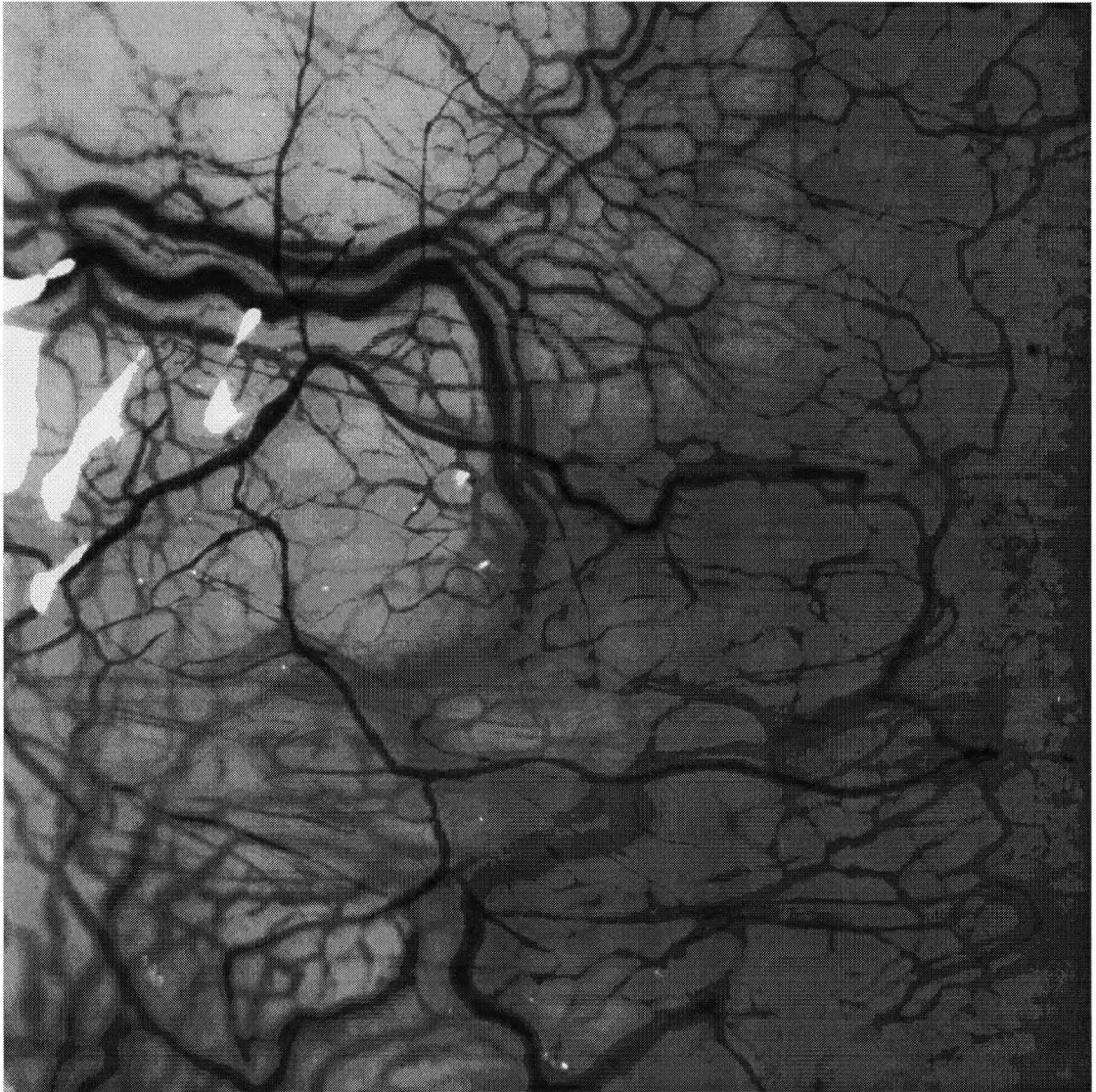


Figure 4.25 shows a 900×900 pixel portion of the 1024×1280 pixel image of patient 2.

4.5.3 Results and discussion

Figures 4.26 and 4.27 shows the image of patient 1 with the output of Steger's algorithm, used at $\sigma = 2$, and 4 respectively, with the vessel boundary and axis points overlaid. Figure 4.28 and 4.29 shows the same algorithms overlaid on an image of patient 2. Note that the algorithm was run at low thresholds in all cases to ensure all detail was detected (lower threshold 0.0 pixels, upper threshold 0.5 pixels).

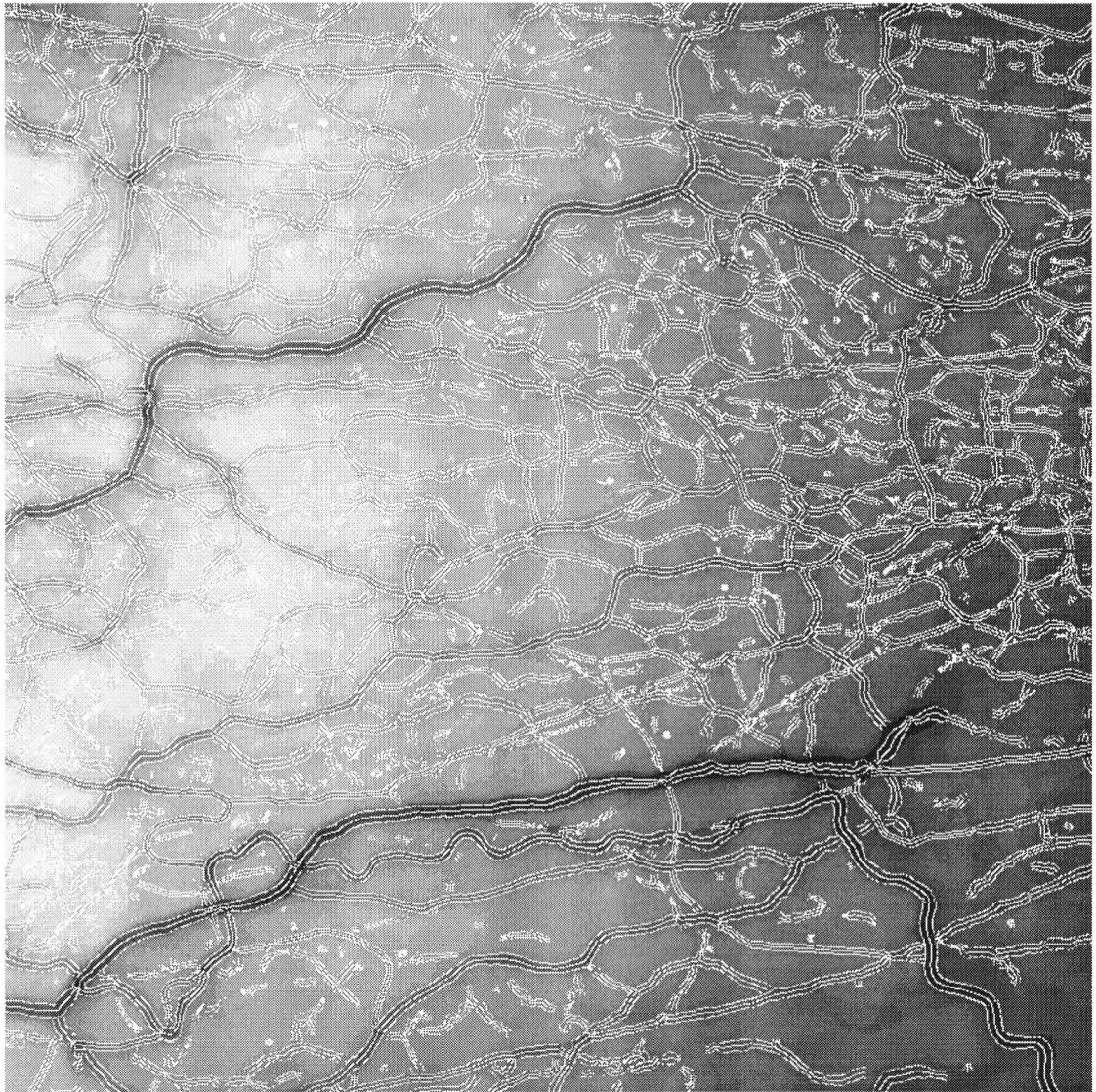


Figure 4.26 shows the output of Steger's algorithm, used with $\sigma = 2$, with the vessel boundary and axis points overlaid on the image of patient 1.

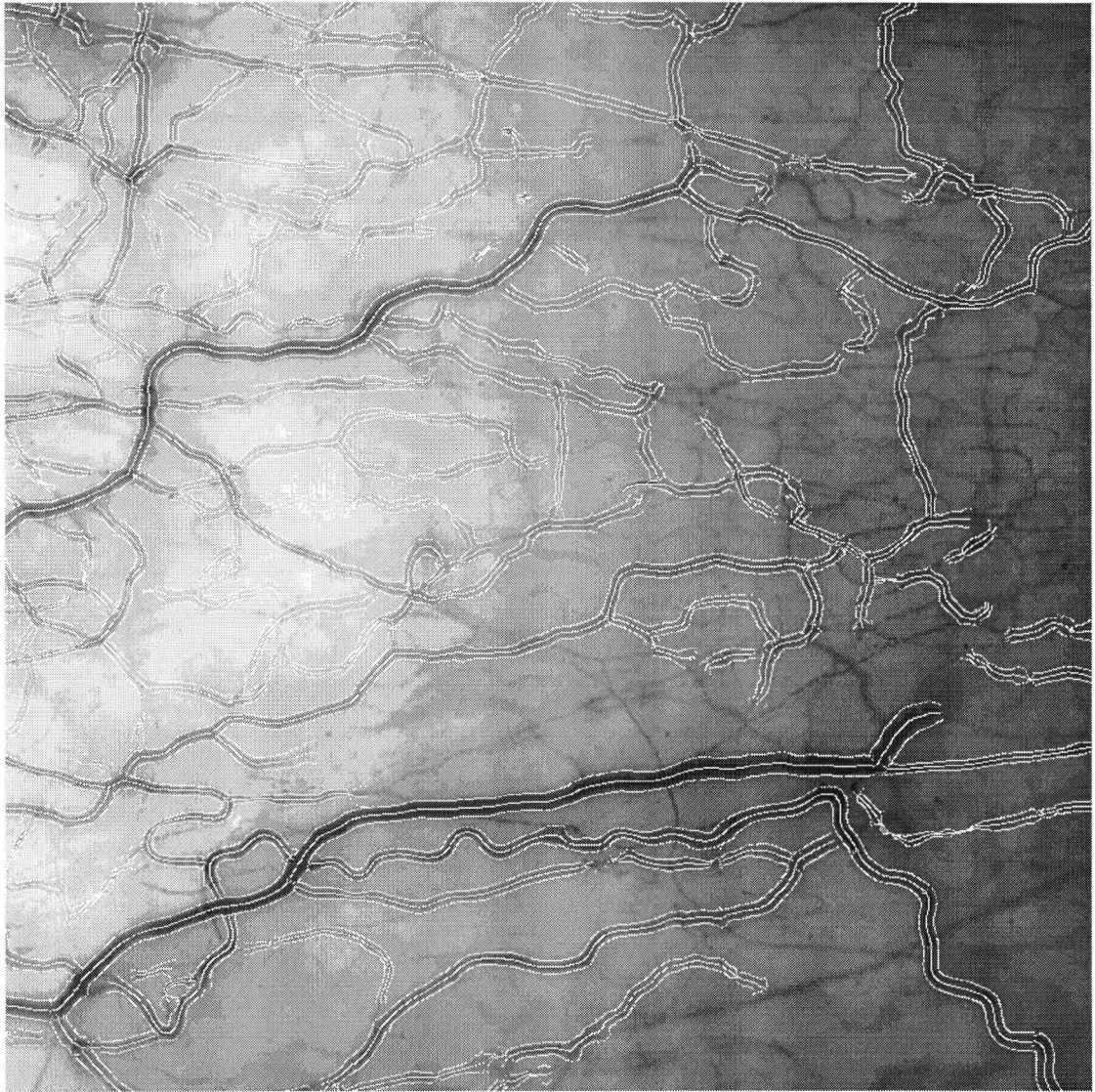


Figure 4.27 shows the output of Steger's algorithm, used with $\sigma = 4$, with the vessel boundary and axis points overlaid on the image of patient 1.

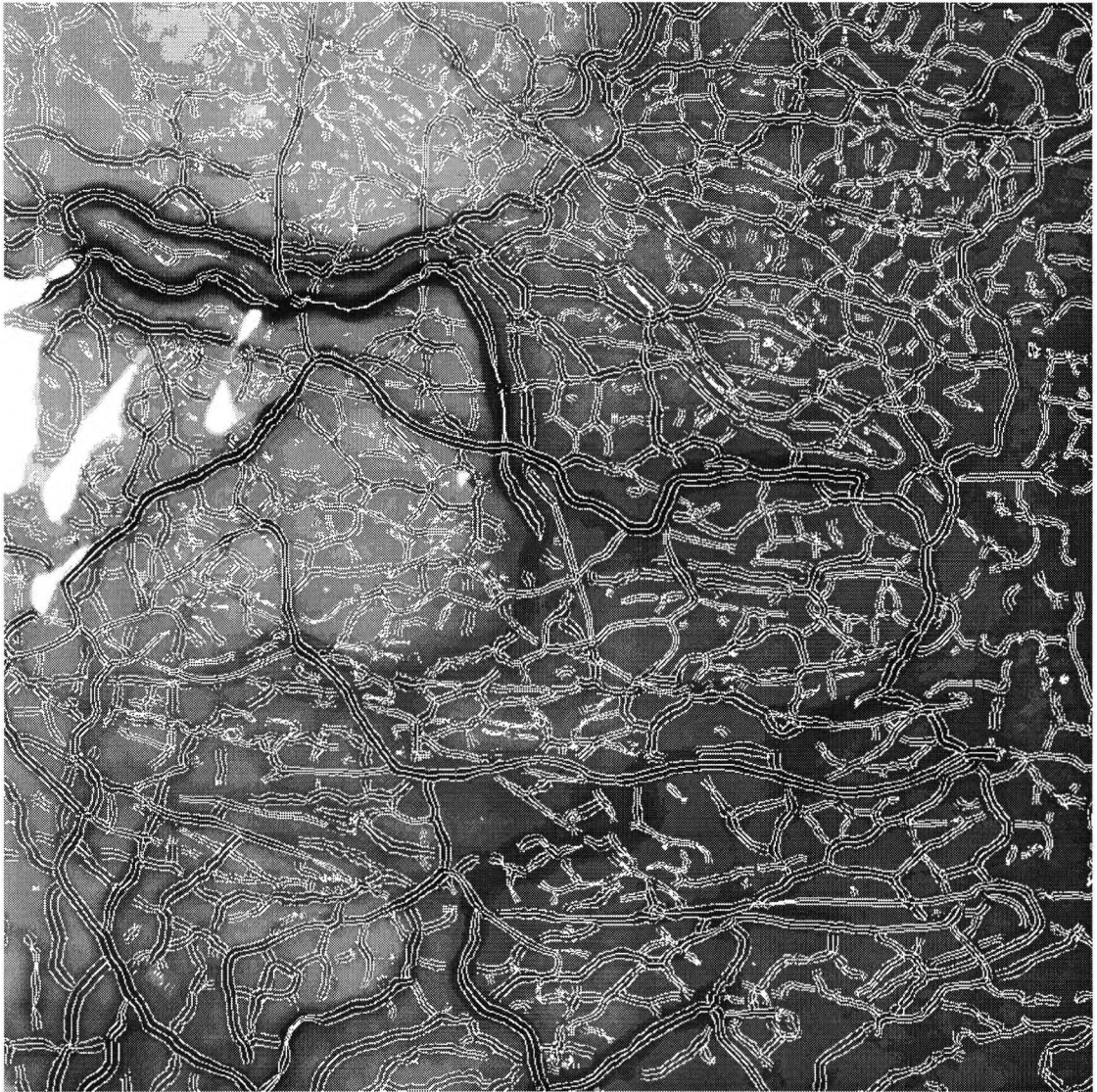


Figure 4.28 shows the output of Steger's algorithm, used with $\sigma = 2$, with the vessel boundary and axis points overlaid on the image of patient 2.

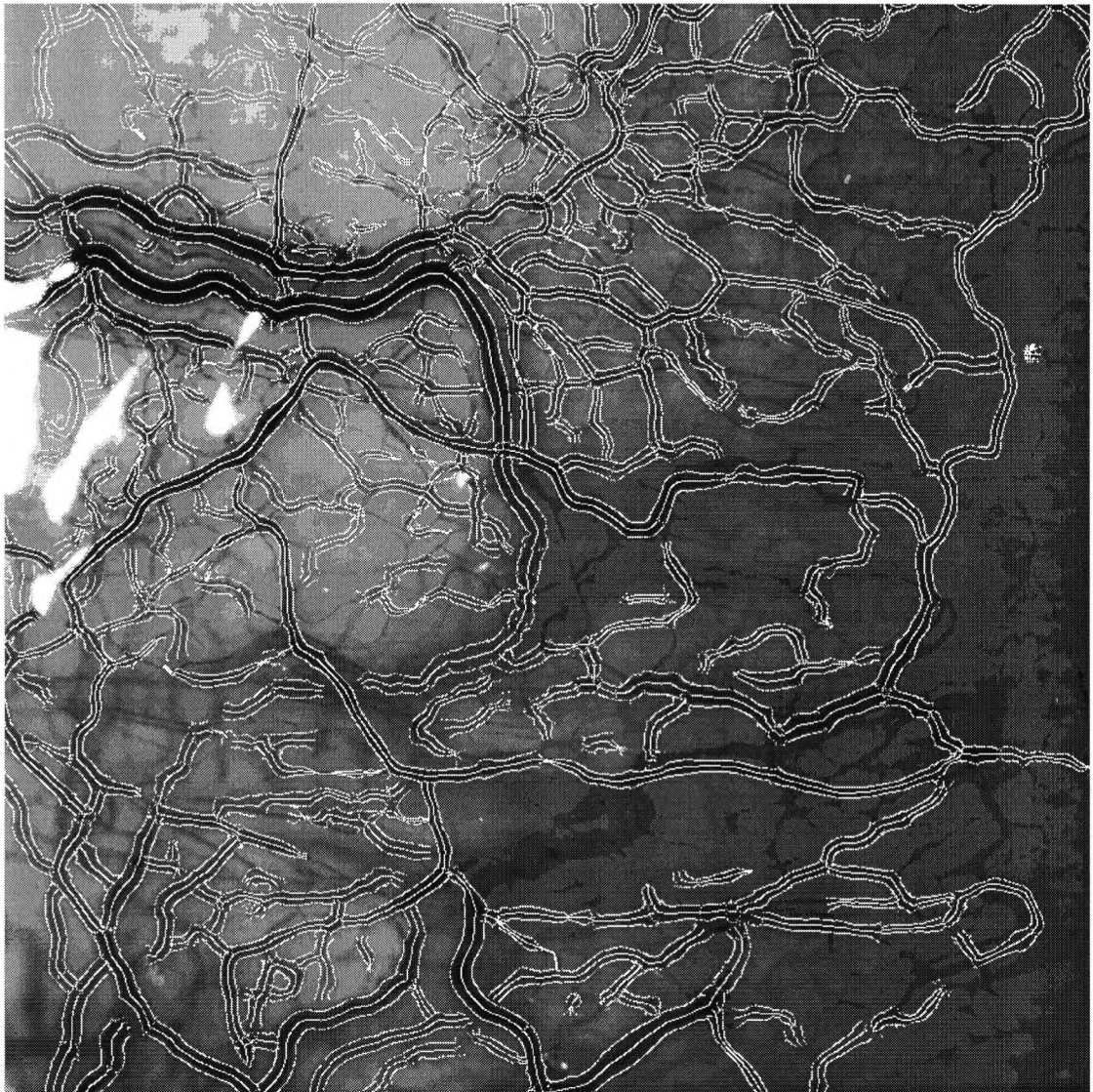


Figure 4.29 shows the output of Steger's algorithm, used with $\sigma = 4$, with the vessel boundary and axis points overlaid on the image of patient 2.

As indicated in section 4.3.2.2 low sigma's ($\sigma = 1$ or 2) tend to underestimate large vessels and correctly detect small vessels and that large sigma's ($\sigma = 4$) correctly estimate large vessels and overestimate smaller vessels. The evidence for this can be observed from figures 4.26 to 4.29. To further visualise this a 230×230 pixel extract from figure 2.25 was repetitively imaged using the algorithm at $\sigma = 2, 3$, and 4 and are shown in negative format in figure 4.30. As shown the output of $\sigma = 2$ grossly underestimates the width of the anterior ciliary artery, $\sigma = 3$ appears to slightly underestimate the width, while $\sigma = 4$ appears to give a good visual estimate of the vessels edge. However, as σ is increased so the total area of vessels detected decreases as shown by the vascular network contained in the vascular arch of the anterior ciliary artery. The detected width of the capillary network is overestimated by the algorithm at $\sigma = 4$, but appears to give a good indication of the vessels edge at $\sigma = 2$. These findings support the view that different sigma's should be used to detect vessels of different widths. As indicated previously optimal detection of vessels less than $40\mu\text{m}$ in width should be carried out with $\sigma = 2$, and those greater than or equal to $40\mu\text{m}$ with $\sigma = 4$.

It was not envisaged that there would be difficulty in retrieving vessel strings with W values greater than or equal to $40\mu\text{m}$, as measured by Steger's algorithm with $\sigma = 2$, from the data measured with $\sigma = 4$. However, in practice, this proved to be computationally complex. An entire vessel segment measured with $\sigma = 2$ would not necessarily be entirely measured with $\sigma = 4$ and vice-versa. Also, when using low sigma's, the algorithm tends to break up vessels into shorter lengths. Hence, vessel segments measured using $\sigma = 2$ could not always be interchanged with the data measured on the same vessel string using $\sigma = 4$. Attempts were made to connect vessel strings into similar lengths but this proved computationally expensive. Also a vessel string with a W of slightly greater than $40\mu\text{m}$ may have widths well above and below this value, hence those below would be correctly measured with $\sigma = 2$ and be incorrectly measured with $\sigma = 4$. Despite these difficulties an algorithm was derived which measured using both sigma's.

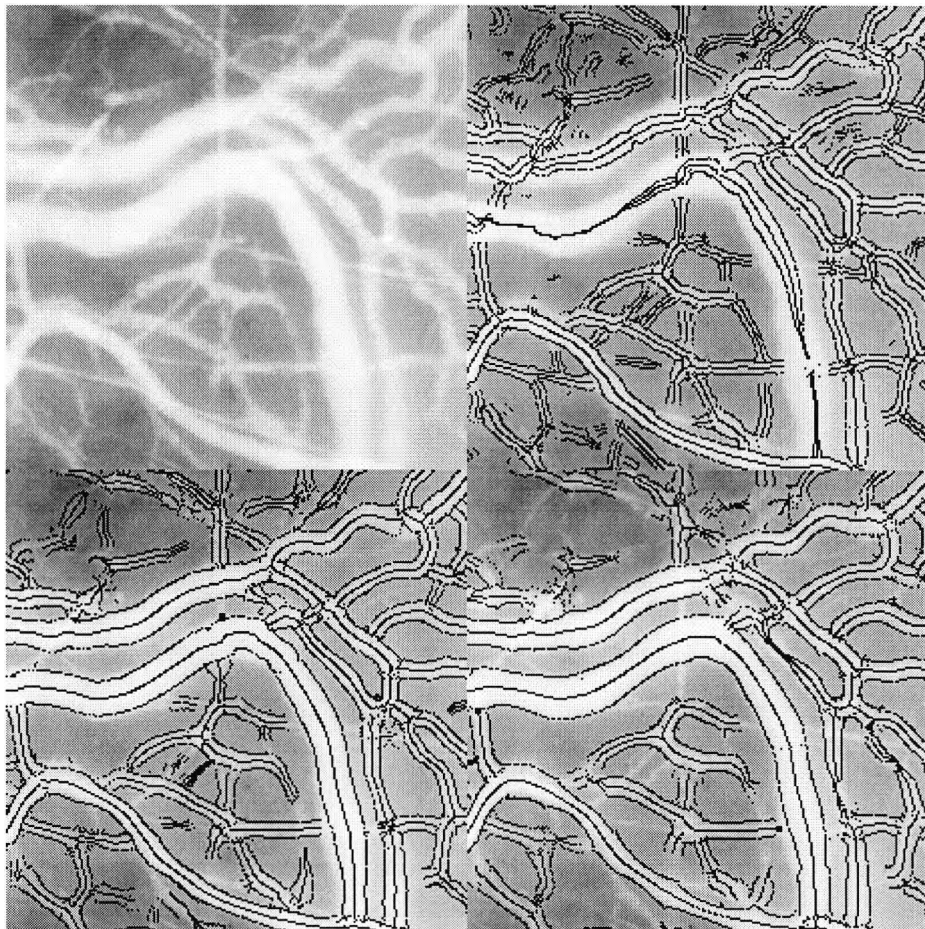
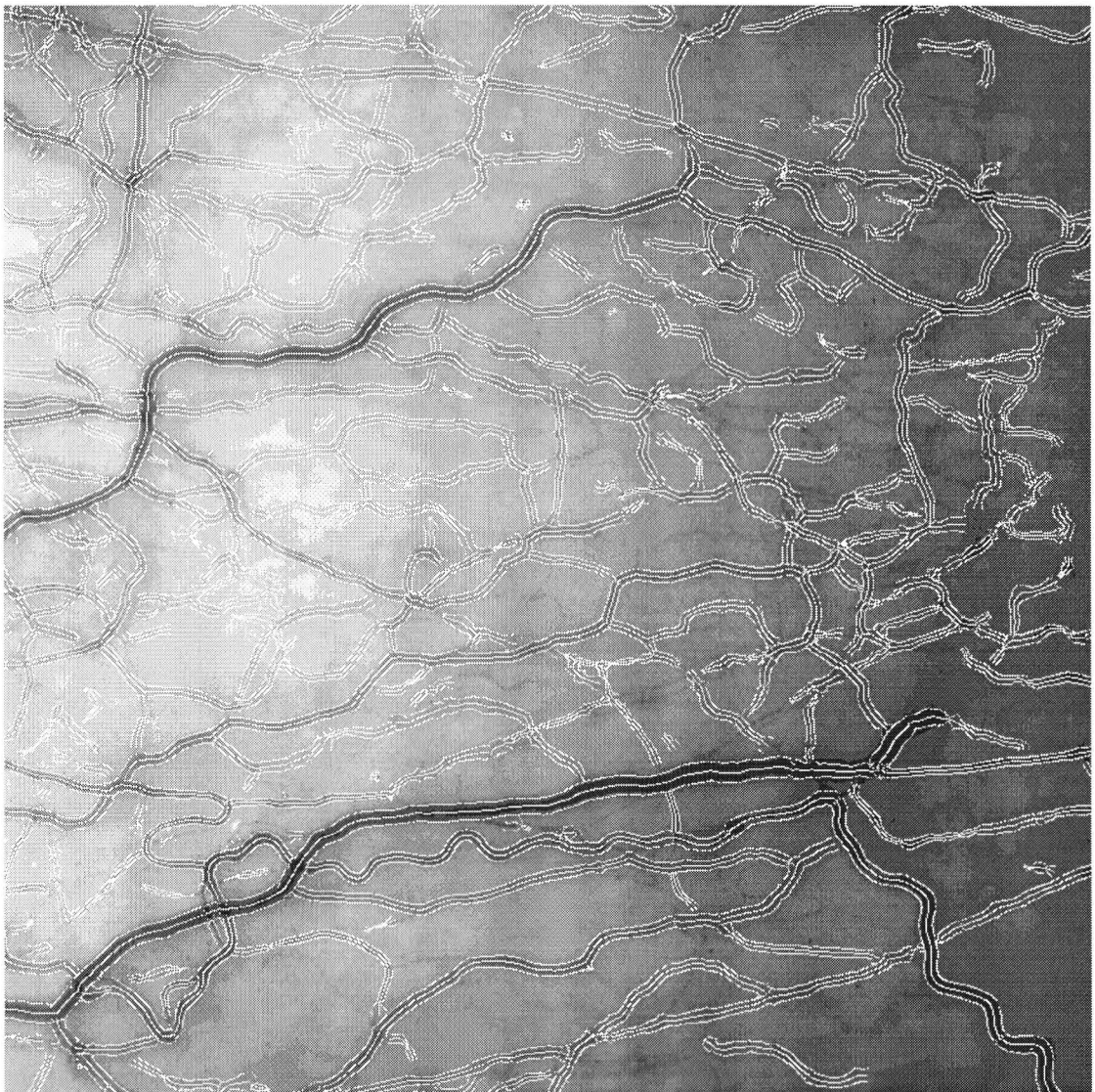


Figure 4.30 shows a 230×230 pixel portion of figure 4.25 of an anterior ciliary artery and underlying vascular network. All images are shown in negative to help visualisation. The raw image is shown top left, the raw image with the output of the algorithm run at $\sigma = 2$ top right, $\sigma = 3$ bottom left, and $\sigma = 4$ bottom right.

As an alternative images were also measured using Steger's algorithm with a robust setting of $\sigma = 3$, negating the need for 2 separate σ values to be used for vessels of different width. This proved to be a much simpler way of analysing vascular images.

Figure 4.30 shows that the use of the algorithm at $\sigma = 3$ offers a good compromise between the disadvantages of using sigma's 2 and 4 alone.

As indicated in table 4.2 that the intra-session repeatability of Steger's algorithm, set at $\sigma = 3$, for repetitively measuring 101 vessel widths had a mean difference of $0.469\mu\text{m}$ with a 95% confidence interval of $+9.414\mu\text{m}$ to $-8.475\mu\text{m}$, and a range of width measures from $23.444\mu\text{m}$ to $90.547\mu\text{m}$. Further analysis revealed that the intra-session repeatability for vessels less than $40\mu\text{m}$ in width using $\sigma = 3$ had a mean difference of $-0.026\mu\text{m}$ and a 95% confidence interval of $+6.343$ to $-6.396\mu\text{m}$ (see table 4.7), and a mean difference of $1.446\mu\text{m}$ and a 95% confidence limit of $+13.920\mu\text{m}$ to $-11.029\mu\text{m}$ for vessels larger than or equal to $40\mu\text{m}$ (see table 4.8). From table 4.3 it was also shown that automated determination of vessel width using $\sigma = 3$ best agreed with manual measurement of width from digitally created photographs (see table 4.3). Figures 4.31 and 4.32 shows the output of Steger's algorithm, used with a $\sigma = 3$, with the vessel boundary and axis points overlaid on the original images.



Figures 4.31 shows the output of Steger's algorithm, used with a $\sigma = 3$, with the vessel boundary and axis points overlaid on the image of patient 1.

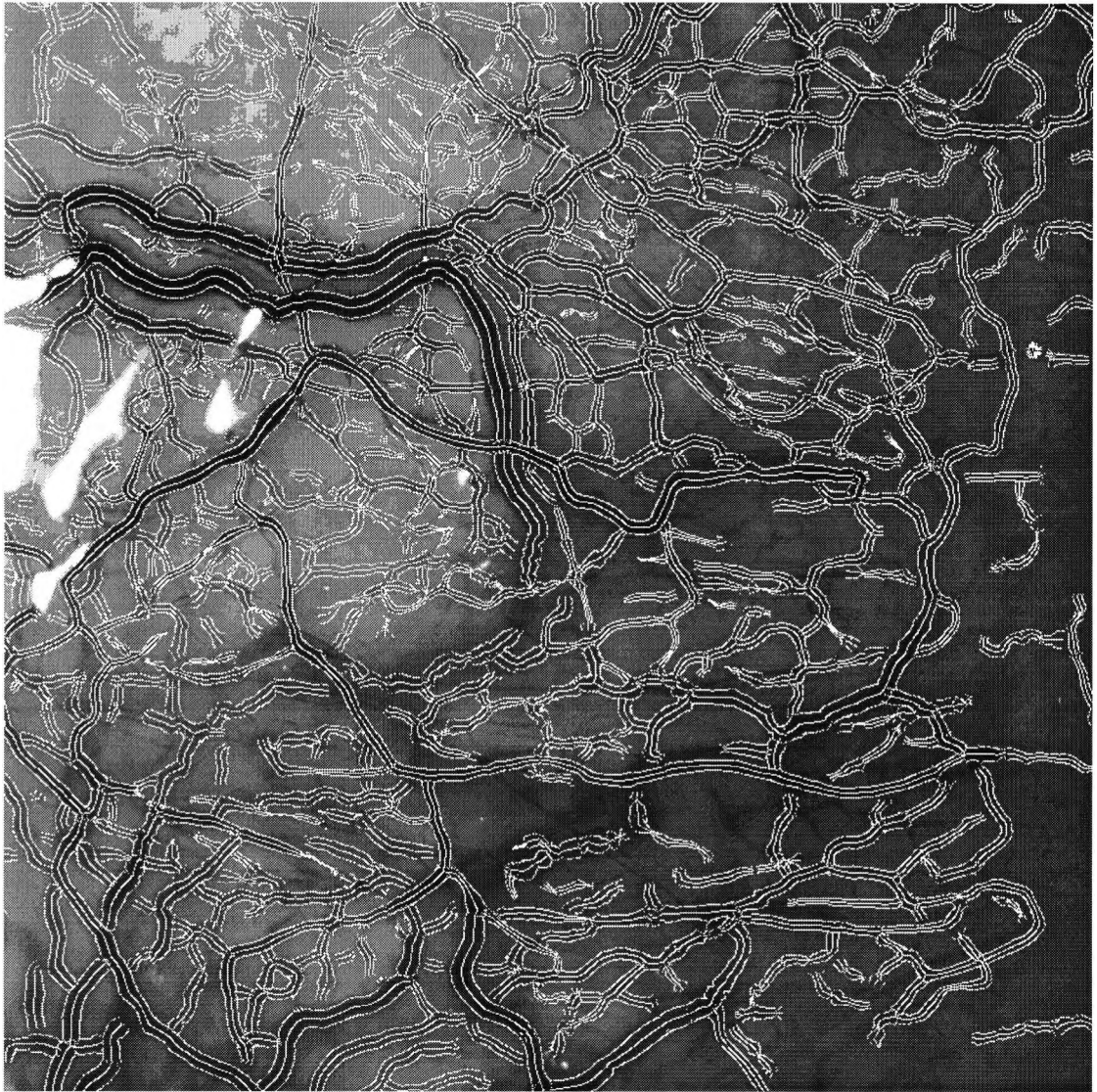


Figure 4.32 shows the output of Steger's algorithm, used with a $\sigma = 3$, with the vessel boundary and axis points overlaid on the image of patient 2.

Evidently the output shown in figure 4.31 and 4.32 shows that the selection of $\sigma = 3$ offers a robust way of segmenting vascular structures from their surround.

To investigate the relationship between the different types of measure further, vascular indices for the 2 patients, measured with sigma's 2 / 4 and 3, are listed in table 4.10. For comparison the percentage change in indices between the 2 patients using $\sigma = 2 / 4$ and 3 are listed. These results are discussed in turn under their respective width categories.

Vessels less than 25 μ m in diameter (capillaries)

Indices measured from vessels detected using the algorithm with a combined $\sigma = 2$ and 4 showed little difference in W , T , TV , or *Density*. However, a sizeable increase was found in WV in patient 2 compared to patient 1, indicating that patient 2 has a greater diversity of vessel sizes within its capillary group. However, indices calculated from the output of $\sigma = 3$ showed that T and TV were sizeably greater in

patient 2 than patient 1 with a 22% and 100% increase respectively. This would agree with the visual interpretation of the vascular bed of increased tortuosity. Interestingly, capillary density appeared less in patient 2 compared to patient 1 which, at first glance, appears contrary to the visual impression of the vascular network.

Vessels 25 μ m to <40 μ m in diameter (venules)

Indices calculated from the output of the combined σ algorithm showed little difference in W , and T . However, indices in patient 2 appeared to have greater WV (47%) and TV (19%) than patient 1, indicating that there was a greater diversity of widths in this vessel group and that these vessel were more angular for patient 2. A surprising finding was that patient 2 had less vascular density than patient 1 (-19%) which would appear contrary to the visual interpretation of the vascular bed. The indices calculated from the output of $\sigma = 3$ also showed an increase in WV (25%) and TV (47%) in patient 2 compared to patient 1, and showed little difference between vascular beds in W and T . However, unlike the *Density* index calculated from the combined output there was no appreciable difference in *Density* which agrees with the observed findings.

σ VALUE		$\sigma = 2$ AND 4			$\sigma = 3$		
Index	VW bin	Patient 1	Patient 2	% Δ	Patient 1	Patient 2	% Δ
W	vw < 25 μ m	21.934	21.332	-2.744	19.194	19.013	-0.942
WV	vw < 25 μ m	55.056	84.116	52.783	134.680	141.099	4.766
T	vw < 25 μ m	0.018	0.0160	-9.064	0.011	0.014	22.395
TV	vw < 25 μ m	0.004	0.003	-11.928	0.001	0.003	100.710
<i>Density</i>	vw < 25 μ m	0.013	0.013	-1.115	0.002	0.002	-11.334
W	25 to < 40 μ m	32.499	32.868	1.134	35.557	34.450	-3.113
WV	25 to < 40 μ m	49.485	72.962	47.442	114.963	143.347	24.690
T	25 to < 40 μ m	0.014	0.014	6.100	0.010	0.011	11.708
TV	25 to < 40 μ m	0.003	0.003	19.023	0.001	0.002	47.438
<i>Density</i>	25 to < 40 μ m	0.140	0.114	-18.735	0.049	0.052	5.053
W	40 to < 80 μ m	60.447	62.836	3.952	48.252	56.126	16.320
WV	40 to < 80 μ m	142.513	262.164	83.958	91.238	141.014	54.555
T	40 to < 80 μ m	0.006	0.008	33.620	0.008	0.009	13.331
TV	40 to < 80 μ m	0.0004	0.001	162.690	0.001	0.001	52.244
<i>Density</i>	40 to < 80 μ m	0.075	0.141	88.881	0.146	0.167	14.390
W	vw \geq 80 μ m	83.168	87.906	5.696	0	84.157	NA
WV	vw \geq 80 μ m	189.486	304.935	60.927	0	77.124	NA
T	vw \geq 80 μ m	0.004	0.006	59.277	0	0.006	NA
TV	vw \geq 80 μ m	0.0001	0.0004	233.582	0	0.0005	NA
<i>Density</i>	vw \geq 80 μ m	0.083	0.068	-18.335	0	0.010	NA
W	All vessels	43.320	47.352	9.307	43.623	49.056	12.454
WV	All vessels	85.086	159.150	87.046	99.608	140.242	40.793
T	All vessels	0.011	0.012	3.549	0.009	0.010	12.217
TV	All vessels	0.002	0.002	10.761	0.001	0.002	50.346
<i>Density</i>	All vessels	0.311	0.336	7.981	0.198	0.231	16.751

Table 4.10 lists vascular indices for the 2 patients, measured with sigma's 2/4 and 3, where W is measured in μ m, WV in μ m², T in units of curve energy (CE), TV in units of CE², and *Density* in mm² of vessel per mm² of conjunctiva. The % Δ represent the percentage difference between patient 1 and 2.

Vessels 40 μ m to <80 μ m in diameter (venules and arterioles)

Indices calculated from the algorithm measuring with the two different sigma's showed an increase in *WV* (84%), *T* (34%), and *TV* (163%) for patient 2 compared to patient 1. Also, the index *Density* was 88% higher in patient 2 than patient 1, which agrees with the visual interpretation of the vascular bed. The output of the algorithm run at $\sigma = 3$ found similar difference between the 2 images but were less dramatic, especially for *Density* where the difference between patient 1 and 2 was 14%.

Vessels greater than 80 μ m in diameter (arterioles)

It was here that the output of the combined σ algorithm contradicted the visual interpretation of the images. From figures 4.24 and 4.25 it is evident that the preponderance of large vessels is greater in patient 2 than patient 1. However, the vascular *Density* index for this vessel group was greater in patient 1 than 2. Although the indices indicated an increase in *WV* (61%), *T* (59%), and *TV* (234%) in patient 2 compared to patient 1, the *Density* index was clearly at fault. However, the output of the algorithm using $\sigma = 3$ did not record any vessels of this calibre in patient 1.

All vessels

Indices calculated from the output of the combined σ algorithm showed an increase in all indices for patient 2 compared to patient 1, with an increase in *W* of 9%, *WV* of 87%, in *T* of 4%, and in *TV* of 11%. Disappointingly, *Density* only showed a 8% increase in patient 2 from patient 1. However, the *Density* index calculated using the output of the $\sigma = 3$ algorithm showed a 17% increase in vascular *Density* for patient 2 compared with the value for patient 1, with values of 0.231mm² of vessel per mm² of conjunctiva and 0.198mm² respectively. Other indices calculated from the output of the $\sigma = 3$ algorithm all showed greater values in patient 2 as shown in table 4.10. At first glance the 17% increase in vascular density between the two images does not appear enough. However, on observing the *Density* indices further it is apparent that the greatest difference in *Density* was in larger vessels (> 40 μ m in diameter) and that the density of capillaries (<25 μ m in diameter) was in fact greater in patient 1 than 2. Hence, visual interpretation of a vascular bed may be heavily influenced by the presence of larger vessels, making those images with macrovessels appear more hyperaemic than those without, and that smaller vessels are essentially ignored when interpreting the vascularity of a vessel bed. Such an argument might be levied as a disadvantage of subjective grading of conjunctival vascularity. Hence the need for an objective means of describing the conjunctival vascular network.

4.5.4 Summary

The $\sigma = 3$ algorithm did not falsely identify large vessels (greater than 80 μ m in diameter) in figure 4.24 and showed a greater difference in vascular density between the 2 images, in agreement with the visual interpretation of the images. Also the computation of this algorithm was far less complex than the computation of the combined $\sigma = 2$ and 4 algorithm. For these reasons $\sigma = 3$ was the vessel algorithm of choice and has been used for the remainder of this thesis in conjunction with the vascular indices outlined. Further investigation of the performance of the vascular indices outlined was carried out in chapter 5.

CHAPTER 5

5. Normal conjunctival vasculature

5.1 Aim

The purpose of this chapter was to quantify the performance of the indices discussed in the previous chapter on a normal population. The intra and inter session repeatability of each index was determined for a normal population.

5.2 Introduction

The assessment of conjunctival vascularity using photographic scales was popularised by McMonnies and Chapman-Davis (1987a, 1987b). A reference scale with 6 grades of hyperaemia was used. As stated in chapter 1, using the preferred method of Bland and Altman (1986), inter observer agreement gave a mean difference +0.056 between grades with a 95% confidence interval of +1.113 to -1.001, and intra observer agreement gave a mean difference of -0.222 with a 95% confidence interval of +0.616 to -1.061. Other subjective methods include pointwise counting techniques using a dotted or lined pattern overlay on conjunctival images (Fenton, 1980; Worthen *et al*, 1981; Villumsen and Alm, 1989), which were not assessed for their repeatability and were time consuming and tedious in application. Automated approaches using thresholding techniques have also been used to assess conjunctival vascularity (Chen *et al*, 1986; Owen *et al*, 1996). Inter session agreement of vascularity assessment gave a mean difference of +2.32% with a 95% confidence interval of +8.58% (+1.46mm²) to -3.95% (-0.67mm²) for the 17mm² area of conjunctiva assessed (Owen *et al*, 1996). Other methods of determining conjunctival vascularity involving colour image analysis have been used with some success (Willingham *et al*, 1995; Wilkins *et al*, 1996). However, the repeatabilities of these techniques were not published. Unlike general assessment of conjunctival vascularity, Guillon and Shah (1996) attempted to manually determine vessel width at referenced locations from the limbus using a computer mouse to mark vessel edges. A 95% confidence interval from 8.9 to 12.6µm was quoted. However, they did not use the preferred method of establishing inter session agreement (Bland and Altman, 1986).

The above methods give limited information about the morphometric and morphological nature of a conjunctival vascular bed. The indices proposed in the previous chapter offer conjunctival density (*Density*), mean width (*W*), width variance (*WV*), mean tortuosity (*T*), and tortuosity variance (*TV*) measures, for the vessels as a whole and for populations of vessels classified on the basis of width. The purpose of this chapter was to give the intra and inter session repeatabilities for these indices in a normal population. Also, to observe diurnal variations in the measurements and whether factors such as age, sex, MAP, and smoking exerted any effect. Without fully substantiating the limitations of a measurement on a normal population it is difficult to comment on changes which may be found in a diseased or challenged conjunctival vascular bed.

5.3 Method

Images of the right bulbar conjunctiva of 31 normal individuals were captured using the Nikon FS-2 photo slit-lamp, with a xenon flash power setting of one, together with a Wratten 99 and Wratten 96 neutral density filter (0.2 log units) over the illumination turret window (in agreement with the findings of chapter 3). Forty five degrees of nasal ocular rotation was achieved by use of a fixation target, to ensure maximal view of the conjunctiva without the need for manual lid retraction. Images were recorded to the DCS 100 digital camera, and were imported into a computer via a SCSI card. The image from the green channel of the CCD was extracted using Aldus PhotoStyler version 1.1 (Aldus Corporation, Seattle, USA) software, and archived to a writable CD as an 8 bit, monochrome, 1.38MB portable grey map file. Five images were taken within the same session, at five sessions throughout the day. The time delay between sessions was 2 hours, hence, images were obtained at approximately 0900, 1100, 1300, 1500, and 1700 hours. Therefore, a total of 25 images were taken per patient. In addition, a systemic and ocular history were taken including whether the patient smoked. If a patient was an RGP or SCL wearer they were advised not to wear their lenses on the day of measurement. Any significant systemic or ocular history barred entry into the study. This included the presence of hypertension, diabetes, previous ocular surgery, ocular allergy, or an episode of conjunctivitis within the last 6 months. On each examination systolic and diastolic blood pressures were recorded objectively using an auto-sphygmomanometer (Auto-sphygmomanometer UA-251, Copal, USA), as well as the time of examination, ambient room temperature, and relative humidity. MAP is the average pressure during a given cardiac cycle that exists in the aorta and its major branches. It can be approximated satisfactorily from the measured values of systolic (P_S) and diastolic (P_D) pressures to give a single value, by means of the equation below.

$$MAP = P_D + \frac{1}{3}(P_S - P_D)$$

Patients were recruited on a volunteer basis from the academic staff, post graduates and undergraduates at City University. All patients were told to keep within the confines of the building for the duration of the measurement to prevent the outdoor winter conditions exerting an effect on the conjunctival bed. Patients were advised not to purposely itch, rub, or scratch or interfere with their eyes and abstain from alcohol consumption. On the first session of the day a thumbnail drawing was made of the vessels on the conjunctiva and a distinctive branch, kink, crossing isolated in the centre of the field for the cross hairs in the observation optics to be tallied with on each subsequent image session.

Images obtained underwent Steger's algorithm (1996, 1998) for the detection of curve linear structures using a $\sigma = 3$, as detailed in the previous chapter. Mean vessel width (W) and string variance (WV), mean tortuosity (T) and string variance (TV), and vascular density were calculated for all vessels measured. Data was then divided into bins where vessel widths $<25\mu\text{m}$ represented capillaries, 25 to $<40\mu\text{m}$ venules, 40 to $<80\mu\text{m}$ arterioles and venules, $\geq 80\mu\text{m}$ arterioles and veins. The above indices (W , WV , T , TV and $Density$) were re-calculated for each vessel bin size giving a total of 25 indices.

5.4 Statistical analysis

5.4.1 Intra session repeatability

Intra session repeatability was calculated for each index in accordance with the method of Bland and Altman (1986) by comparing the first 2 images of the first session of the day of measurement. A mean difference and the 95% confidence interval were calculated for each index within each vessel bin, and for all vessels. A plot of the differences in each index measured on the first and second image were plotted against their mean allowing the accuracy of the measurement to be gauged over the range of measures. The plot of the differences against the mean should show an even scatter at all x values.

5.4.2 Inter session repeatability

Inter session repeatability was calculated for each index in accordance with the method of Bland and Altman (1995) using the mean measurement from the five taken on session one and the mean of the five taken on session three. Session three was chosen at random to assess the repeatability but the mean of session 2, 4 or 5, could equally have been chosen. Mean difference and the 95% confidence interval were calculated for each index, for each vessel category, and for the vessels as a whole. A plot of the differences for each index, for the 2 sessions of measurement, against their mean value indicated the accuracy of measurement over the range of values measured. The appearance of funnelling or sloping effects would show inaccuracies within the method. It was expected that the calculated inter session coefficient of repeatability might be less than that calculated for the intra session repeatability because inter session values were the mean of five measures, as opposed to the single value taken for the intra session measurements.

5.4.3 Variability in measurement

Many factors could affect the indices measured including the time of day of measurement, MAP, sex, age, and whether the patient smoked. Most standard statistical techniques, for example, the unpaired t-test, linear regression, Chi square test, and ANOVA, assume that observations in the data set are independent of each other. Unfortunately, this assumption is inappropriate when repeated observations are taken on the same subject because the observations will tend to be correlated, and are not independent. In other words, two observations taken at random from the same individual are more likely to be similar than two random observations taken from two different individuals. This means that each repeated observation in an individual may provide less information than a new observation on a new individual.

To examine the variability of the indices over time was not straight forward because; (a) measurements were repeated five times on the same individual and are therefore not independent, (b) and repeated measurements on the same individual are correlated with each other. It is important that these two factors are taken into consideration at the analysis stage. Recent advances in statistical theory and in software development have allowed studies based on such designs to be analysed more easily. The method adopted here is one discussed in detail by Burton *et al* (1998). A statistical package (Intercooled Stata 5.0 for Windows, USA) was used which allowed analysis by *generalised estimating equations* (GEE), which fits a statistical model that allows for

repeated measures on the same individual. The theory behind this approach was beyond the scope of this thesis but is comprehensively discussed by Zeger *et al* (1988). GEE were used to examine any association between vessel indices and the time of the measurement to evaluate the presence of any diurnal variation. The same technique was used to examine whether vessel indices were related to age, sex, MAP, smoking, RH, or temperature. This was carried out for the indices calculated from each vessel width band and for vessels as a whole.

A GEE can be thought of as an extension of linear regression or ANOVA. Consider the following equation of linear regression, where y is the outcome of interest i.e. a vessel index, x is one of the explanatory variables e.g. age, or sex, m is the effect per unit increase in x , and c is the intercept term, the value for y when x is zero.

$$y = mx + c$$

Explanatory variables were recorded as grouping and / or continuous variables in the following manner.

Grouping / categorical variables

- Sex was recorded as a 0 for male, 1 for female
- Time was recorded in 5 separate groups corresponding to the 5 sessions of measurement throughout the day. This allows for differences between sessions to be examined without assuming a linear increase (or decrease) of y with time, which would be the case if time was treated as a continuous variable.

Continuous variables

- Age recorded in years
- MAP was recorded in mmHg
- Temperature in degrees Celsius (°C)
- Relative humidity was expressed as a percentage

Clearly using the equation above for the continuous variables assumes a linear relationship between y (the vessel index) and x . This is a strong assumption, but the validity of this assumption can be evaluated by examining plots of the data against these continuous variables. A useful check is to convert each continuous variable into a categorical variable e.g. divide age into tertiles or quartiles (according to an individual's age) thereby giving 3 or 4 separate groups. It is then possible to analyse the data with the variable as a grouping variable (factor), simulating an ANOVA, or a score, and if both models fit the data equally well (evaluated by the F-test), then the linear assumption is not invalidated. This approach represents accepted statistical theory. However, with only 31 subjects, division into quartiles or tertiles results in very few subjects (7 to 10) per group and may not be an ideal way of treating the data. Hence, this approach was limited to those variables where the possibility of non-linearity was evident from graphical inspection of the data.

For a GEE the equation above needs to allow for repeated measurements on an individual and hence becomes the following equation. Where y is the outcome variable for person i on visit j , x is one of the explanatory variables for person i at visit j e.g. y is the value for MAP, for i th person at j th visit, m is the effect of a unit increase in x , and c is the intercept term as before.

$$y_{ij} = mx_{ij} + c$$

By using this approach a more statistically valid interpretation of any effect can be ascertained. The same approach was used to examine any diurnal variation in MAP, relative humidity and temperature

5.5 Results

In total 31 individuals were recruited who met the inclusion criteria. Table 5.1 shows their demographic details. It can be seen that more females participated who were on average younger than the male volunteers.

GENDER	NUMBER	MEAN AGE (YRS)	SD AGE (YEARS)	SMOKERS
Male	14	43.07	12.26	1
Female	17	34.14	11.74	1
TOTAL	31	37.52	12.54	2

Table 5.1 lists the demographic details of the sample.

Table 5.2 lists the mean data, standard deviation, maximum and minimum values for all indices measured for each session of measurement. Note that there were 31 observations taken at each session of measurement and that no measurements were missed. All patients were examined within 30 minutes of their scheduled examination time. As only 2 people smoked the effect of smoking could not be examined with any accuracy and therefore was excluded from further analysis.

BASELINE MEASUREMENTS					
Index	Vessel width bin (vw)	Mean	SD	Minimum	Maximum
<i>W</i>	vw < 25µm	20.73	0.306	19.91	21.27
<i>WV</i>	vw < 25µm	158.0	16.96	121.8	192.2
<i>T</i>	vw < 25µm	0.0109	0.0014	0.0083	0.0140
<i>TV</i>	vw < 25µm	0.0017	0.0003	0.0011	0.0024
<i>Density</i>	vw < 25µm	0.0041	0.0019	0.0019	0.0093
<i>W</i>	25µm ≤ vw < 40µm	33.96	0.589	32.98	35.21
<i>WV</i>	25µm ≤ vw < 40µm	116.3	8.426	93.55	130.6
<i>T</i>	25µm ≤ vw < 40µm	0.0099	0.0007	0.0080	0.0114
<i>TV</i>	25µm ≤ vw < 40µm	0.0014	0.0002	0.0010	0.0018
<i>Density</i>	25µm ≤ vw < 40µm	0.0591	0.0125	0.0391	0.0924
<i>W</i>	40µm ≤ vw < 80µm	50.73	2.092	47.01	54.61
<i>WV</i>	40µm ≤ vw < 80µm	114.34	14.08	81.25	155.8
<i>T</i>	40µm ≤ vw < 80µm	0.0084	0.0006	0.0069	0.0096
<i>TV</i>	40µm ≤ vw < 80µm	0.0010	0.0002	0.0007	0.0014
<i>Density</i>	40µm ≤ vw < 80µm	0.0889	0.0206	0.0580	0.1437
<i>W</i>	vw ≥ 80µm	23.24	23.79	0.000	83.21
<i>WV</i>	vw ≥ 80µm	24.97	26.13	0.000	95.10
<i>T</i>	vw ≥ 80µm	0.0016	0.0018	0.000	0.0085
<i>TV</i>	vw ≥ 80µm	0.0001	0.0003	0.000	0.0011
<i>Density</i>	vw ≥ 80µm	0.0013	0.0025	0.000	0.0119
<i>W</i>	All vessels	41.43	2.076	32.29	46.03
<i>WV</i>	All vessels	116.3	7.579	103.7	136.6
<i>T</i>	All vessels	0.0092	0.0006	0.0079	0.0103
<i>TV</i>	All vessels	0.0012	0.0002	0.0010	0.0016
<i>Density</i>	All vessels	0.1533	0.0207	0.1111	0.1858

MEASUREMENTS AFTER 2 HOURS					
<i>Index</i>	Vessel width bin (vw)	Mean	SD	Minimum	Maximum
<i>W</i>	vw < 25 μ m	20.63	0.460	19.76	21.23
<i>WV</i>	vw < 25 μ m	157.5	16.08	122.6	189.5
<i>T</i>	vw < 25 μ m	0.0112	0.0012	0.0085	0.0136
<i>TV</i>	vw < 25 μ m	0.0017	0.0003	0.0011	0.0021
<i>Density</i>	vw < 25 μ m	0.0041	0.0015	0.0014	0.0076
<i>W</i>	25 μ m \leq vw < 40 μ m	33.89	0.525	32.76	34.69
<i>WV</i>	25 μ m \leq vw < 40 μ m	117.0	9.826	93.10	135.7
<i>T</i>	25 μ m \leq vw < 40 μ m	0.0100	0.0007	0.0082	0.0111
<i>TV</i>	25 μ m \leq vw < 40 μ m	0.0014	0.0002	0.0011	0.0017
<i>Density</i>	25 μ m \leq vw < 40 μ m	0.0594	0.0142	0.0298	0.0876
<i>W</i>	40 μ m \leq vw < 80 μ m	50.62	2.190	47.19	56.70
<i>WV</i>	40 μ m \leq vw < 80 μ m	118.8	15.70	85.06	177.7
<i>T</i>	40 μ m \leq vw < 80 μ m	0.0083	0.0006	0.0069	0.0100
<i>TV</i>	40 μ m \leq vw < 80 μ m	0.0010	0.0001	0.0007	0.0014
<i>Density</i>	40 μ m \leq vw < 80 μ m	0.0861	0.0220	0.0507	0.1585
<i>W</i>	vw \geq 80 μ m	20.90	25.93	0.000	84.30
<i>WV</i>	vw \geq 80 μ m	21.71	31.10	0.000	111.2
<i>T</i>	vw \geq 80 μ m	0.0014	0.0017	0.000	0.0067
<i>TV</i>	vw \geq 80 μ m	0.0001	0.0001	0.000	0.0005
<i>Density</i>	vw \geq 80 μ m	0.0012	0.0028	0.000	0.0141
<i>W</i>	All vessels	41.18	2.314	37.98	47.85
<i>WV</i>	All vessels	119.3	10.07	101.1	147.4
<i>T</i>	All vessels	0.0093	0.0006	0.0081	0.0106
<i>TV</i>	All vessels	0.0012	0.0002	0.0009	0.0015
<i>Density</i>	All vessels	0.1509	0.0251	0.0852	0.2056

MEASUREMENTS AFTER 4 HOURS					
<i>Index</i>	Vessel width bin (vw)	Mean	SD	Minimum	Maximum
<i>W</i>	vw < 25 μ m	20.60	0.388	19.86	21.58
<i>WV</i>	vw < 25 μ m	156.7	13.93	134.0	195.2
<i>T</i>	vw < 25 μ m	0.0108	0.0012	0.0067	0.0124
<i>TV</i>	vw < 25 μ m	0.0016	0.0003	0.0009	0.0021
<i>Density</i>	vw < 25 μ m	0.0038	0.0013	0.0021	0.0068
<i>W</i>	25 μ m \leq vw < 40 μ m	33.96	0.362	33.18	34.66
<i>WV</i>	25 μ m \leq vw < 40 μ m	116.9	8.153	99.91	131.4
<i>T</i>	25 μ m \leq vw < 40 μ m	0.0100	0.0006	0.0086	0.0113
<i>TV</i>	25 μ m \leq vw < 40 μ m	0.0014	0.0002	0.0011	0.0019
<i>Density</i>	25 μ m \leq vw < 40 μ m	0.0584	0.0154	0.0317	0.0975
<i>W</i>	40 μ m \leq vw < 80 μ m	50.06	1.643	47.33	56.70
<i>WV</i>	40 μ m \leq vw < 80 μ m	116.1	15.20	96.60	161.5
<i>T</i>	40 μ m \leq vw < 80 μ m	0.0085	0.0005	0.0076	0.0094
<i>TV</i>	40 μ m \leq vw < 80 μ m	0.0011	0.0002	0.0008	0.0014
<i>Density</i>	40 μ m \leq vw < 80 μ m	0.0879	0.0230	0.0519	0.1537
<i>W</i>	vw \geq 80 μ m	20.83	20.14	0.000	51.52
<i>WV</i>	vw \geq 80 μ m	20.63	26.64	0.000	94.11
<i>T</i>	vw \geq 80 μ m	0.0014	0.0015	0.000	0.0049
<i>TV</i>	vw \geq 80 μ m	0.0002	0.0005	0.000	0.0025
<i>Density</i>	vw \geq 80 μ m	0.0010	0.0017	0.000	0.0073
<i>W</i>	All vessels	41.19	2.162	37.15	47.08
<i>WV</i>	All vessels	117.6	8.255	105.5	141.4
<i>T</i>	All vessels	0.0093	0.0006	0.0082	0.0105
<i>TV</i>	All vessels	0.0012	0.0002	0.0010	0.0017
<i>Density</i>	All vessels	0.1511	0.0247	0.1094	0.2008

MEASUREMENTS AFTER 6 HOURS					
<i>Index</i>	Vessel width bin (vw)	Mean	SD	Minimum	Maximum
<i>W</i>	vw < 25µm	20.64	0.386	19.79	21.43
<i>WV</i>	vw < 25µm	149.1	13.88	123.04	179.7
<i>T</i>	vw < 25µm	0.0111	0.0013	0.0085	0.0143
<i>TV</i>	vw < 25µm	0.0017	0.0003	0.0011	0.0023
<i>Density</i>	vw < 25µm	0.0040	0.0014	0.0007	0.0080
<i>W</i>	25µm ≤ vw < 40µm	33.92	0.504	32.99	35.24
<i>WV</i>	25µm ≤ vw < 40µm	118.33	7.294	105.9	132.6
<i>T</i>	25µm ≤ vw < 40µm	0.0101	0.0006	0.0085	0.0117
<i>TV</i>	25µm ≤ vw < 40µm	0.0014	0.0002	0.0011	0.0020
<i>Density</i>	25µm ≤ vw < 40µm	0.0589	0.0150	0.0294	0.1080
<i>W</i>	40µm ≤ vw < 80µm	50.43	2.154	45.65	54.89
<i>WV</i>	40µm ≤ vw < 80µm	118.3	15.55	96.33	171.69
<i>T</i>	40µm ≤ vw < 80µm	0.0086	0.0006	0.0071	0.0098
<i>TV</i>	40µm ≤ vw < 80µm	0.0011	0.0002	0.0008	0.0014
<i>Density</i>	40µm ≤ vw < 80µm	0.0864	0.0150	0.0294	0.1080
<i>W</i>	vw ≥ 80µm	18.05	20.09	0.000	66.64
<i>WV</i>	vw ≥ 80µm	16.51	22.31	0.000	75.44
<i>T</i>	vw ≥ 80µm	0.0013	0.0016	0.000	0.0052
<i>TV</i>	vw ≥ 80µm	0.0002	0.0004	0.000	0.0021
<i>Density</i>	vw ≥ 80µm	0.0009	0.0016	0.000	0.0052
<i>W</i>	All vessels	41.16	2.043	36.70	46.25
<i>WV</i>	All vessels	119.4	8.138	104.4	143.4
<i>T</i>	All vessels	0.0094	0.0006	0.0083	0.0106
<i>TV</i>	All vessels	0.0013	0.0002	0.0010	0.0017
<i>Density</i>	All vessels	0.1502	0.0251	0.1029	0.1934

MEASUREMENTS AFTER 8 HOURS					
<i>Index</i>	Vessel width bin (vw)	Mean	SD	Minimum	Maximum
<i>W</i>	vw < 25µm	20.59	0.460	19.45	21.51
<i>WV</i>	vw < 25µm	159.6	15.58	130.61	34.80
<i>T</i>	vw < 25µm	0.0111	0.0013	0.0084	0.0137
<i>TV</i>	vw < 25µm	0.0017	0.0003	0.0010	0.0023
<i>Density</i>	vw < 25µm	0.0037	0.0017	0.0016	0.0089
<i>W</i>	25µm ≤ vw < 40µm	33.89	0.409	33.09	34.80
<i>WV</i>	25µm ≤ vw < 40µm	117.7	10.28	99.31	143.6
<i>T</i>	25µm ≤ vw < 40µm	0.0101	0.0007	0.0082	0.0117
<i>TV</i>	25µm ≤ vw < 40µm	0.0014	0.0002	0.0010	0.0021
<i>Density</i>	25µm ≤ vw < 40µm	0.0554	0.0155	0.0324	0.1083
<i>W</i>	40µm ≤ vw < 80µm	50.73	1.885	46.80	55.09
<i>WV</i>	40µm ≤ vw < 80µm	118.0	15.91	91.76	173.4
<i>T</i>	40µm ≤ vw < 80µm	0.0085	0.0006	0.0072	0.0099
<i>TV</i>	40µm ≤ vw < 80µm	0.0011	0.00017	0.0008	0.0015
<i>Density</i>	40µm ≤ vw < 80µm	0.0872	0.0251	0.0474	0.1492
<i>W</i>	vw ≥ 80µm	14.84	19.21	0.000	65.81
<i>WV</i>	vw ≥ 80µm	13.55	18.22	0.000	63.70
<i>T</i>	vw ≥ 80µm	0.0011	0.0020	0.000	0.0102
<i>TV</i>	vw ≥ 80µm	0.00014	0.0004	0.000	0.0019
<i>Density</i>	vw ≥ 80µm	0.0007	0.0012	0.000	0.0054
<i>W</i>	All vessels	41.56	2.424	36.19	48.10
<i>WV</i>	All vessels	118.7	9.662	100.0	150.9
<i>T</i>	All vessels	0.0093	0.0007	0.0080	0.0107
<i>TV</i>	All vessels	0.0013	0.0002	0.0009	0.0018
<i>Density</i>	All vessels	0.1469	0.0268	0.0941	0.1945

Table 5.2 shows the sample mean, SD, maximum and minimum values for all indices, for each session of measurement, where W and WV are measured in μm and μm^2 respectively, T and TV in units of curve energy and curve energy². Density was measured in mm^2 of vessel per mm^2 of conjunctiva and hence can be regarded as a proportion

At this stage it is worth examining table 5.2 in a little more detail to describe the values observed for each index in relation to each vessel bin and overall.

There was large variability in measuring vessels larger than $80\mu\text{m}$. From table 5.2 the mean vessel width given at baseline in this vessel group is only $23.24\mu\text{m}$, with a range from 0.00 to 83.21 . Clearly this mean value is not within the width constraints of this vessel group. However, this can be explained quite simply. Firstly there were, in general, few vessels of this calibre in an individual eye. Secondly, $80\mu\text{m}$ was at the limit of measurement of the system. It is possible that one image will detect vessels greater than $80\mu\text{m}$ in width, but a sequential image of the same eye may detect the vessel as being $80\mu\text{m}$ or less. Thus, for the latter image no index would be calculated in the above $80\mu\text{m}$ vessel bin and the index would be given a value of zero. The observation of low vessel widths in this vessel bin was an artefact of using an arbitrary cut-off of $80\mu\text{m}$.

5.5.1.1 Vessel width

The average vessel width at baseline including all blood vessels was $41.43\mu\text{m}$. Mean vessel width measures at each subsequent session gave minimal difference from this baseline value, with all values being approximately $41\mu\text{m}$. It is noteworthy the SD of this measurement was fairly consistent throughout the day with values ranging from 2.043 (for hour 6) to $2.424\mu\text{m}$ (for hour 8).

Mean vessel widths for vessels $<25\mu\text{m}$, $\geq 25\mu\text{m}$ to $<40\mu\text{m}$, and $\geq 40\mu\text{m}$ to $<80\mu\text{m}$ also showed consistent values for each session of measurement and again the SDs were similar. However, the SD associated with the $>80\mu\text{m}$ vessel bin was considerably larger than the SD for the other vessel bins. As indicated above, larger vessels may not present in all individuals, and may be found on one session and be absent on a sequential session. Hence this measure is associated with a large SD in excess of that found for other vessel bins.

5.5.1.2 Vessel width variance

WV is a novel index, lacking any normal values for comparison. For all vessels WV was approximately $118\mu\text{m}^2$. Mean values for WV were $156\mu\text{m}^2$ in the smallest vessel category ($>25\mu\text{m}$), $117\mu\text{m}^2$ in the $\geq 25\mu\text{m}$ to $<40\mu\text{m}$ group, $117\mu\text{m}^2$ in the $\geq 40\mu\text{m}$ to $<80\mu\text{m}$ group and $19\mu\text{m}^2$ in the above $80\mu\text{m}$ group. It would appear that the smallest vessels show the largest values for WV and this decreases in larger vessels, with the largest population ($>80\mu\text{m}$) of vessels showing the lowest value for WV . This observation could be explained by the diversity of vessel sizes found in smaller vessels, or that smaller vessels show greater diametric change along their length than larger vessels. Note that a small diametric change in a small vessel will have a greater impact on the measurement of WV than the same magnitude of diametric change on a larger population of vessels. Also, the calculation of WV involves squaring the

standard deviation of widths measured along a vessel string and hence will elevate small differences. However, it is hoped that this would further emphasise differences between normal and compromised vasculature.

5.5.1.3 Curve energy

A typical value for this index for all vessels is approximately 0.01 units of curve energy (CE) and a similar average value exists for all other vessel groups except for vessels greater than 80 μm in diameter where the average value was approximately 0.001CE. Hence, it would appear that all vessels less than 80 μm in diameter have similar levels of tortuosity. These vessels represent capillaries, post capillary venules, and collecting venules. Vessels in excess of 80 μm in diameter appear less tortuous and refer to muscular arteries, veins and major arterioles such as the anterior ciliary artery. Although T values were similar for most vessel groups within this normal population it was envisaged that this parameter would show change in diseased vessels.

5.5.1.4 Curve energy variance

Mean values for TV were quite stable across most vessel groups with a mean value of 0.002CE^2 in the smallest vessel category ($>25\mu\text{m}$), 0.001CE^2 in the $\geq 25\mu\text{m}$ to $<40\mu\text{m}$ group, 0.001CE^2 in the $\geq 40\mu\text{m}$ to $<80\mu\text{m}$ group and 0.0001CE^2 in the above 80 μm group. Again it was envisaged that TV would show change when vessels are diseased.

5.5.1.5 Density

The percentage of conjunctiva which is covered by vessels from different categories was on average approximately, 0.4% for vessels $<25\mu\text{m}$ in diameter, 6% for vessels $25\mu\text{m}$ to $>40\mu\text{m}$ in diameter, 9% vessels $40\mu\text{m}$ to $>80\mu\text{m}$ in diameter, and for vessels $>80\mu\text{m}$ in diameter (which were few in number) only 0.1%. Using data from all vessels, approximately 15% of conjunctival area was vessel with a range between 8.5% to 21%. This may be regarded as quite low, but this sample is from a normal group of subjects and it is likely that very different values would be obtained from compromised or diseased conjunctivae.

In general, throughout the day all indices appeared to be reasonably consistent for this sample. This is examined in more detail in section 5.5.4.

5.5.2 Intra session repeatability

Intra session repeatabilities were calculated for each index in accordance with the method of Bland and Altman (1986) using the measurements taken from the first 2 images of the first session of the day and are listed in Table 5.3.

To help interpret these values the mean difference and 95% confidence interval are quoted in both units of the index and as a percentage of the mean value. As shown by the shaded areas in table 5.3 the W index measured on vessels with diameters, less than 25 μm in diameter, 25 to less than 40 μm , 40 to less than 80 μm , and all vessels showed acceptable levels of repeatability ($\sim\pm 10\%$). In addition the T index showed acceptable levels of repeatability when measured on all vessels. Repeatabilities within $\sim\pm 10$ to 20% were also considered as being satisfactory. Note that the repeatabilities of indices measured on vessels greater than 80 μm in diameter were very large. This

was because a vessel recorded in one image as having vessels in excess of 80 μm did not always show similar vessels on the second image analysed. Hence, interpretation of the results from vessels of this size must be treated cautiously. Although some of the 95% confidence intervals seem unduly large the relevance and significance of this must be seen in the context of the magnitude of the measurement. This point will be considered further in the following section.

Index	VW bin	MD	95%CI		%MD	%CI	
W	vw < 25 μm	0.00054	2.280	-2.279	-0.017	10.920	10.955
WV	vw < 25 μm	5.793	72.502	-60.916	3.905	45.093	37.283
T	vw < 25 μm	-0.0002	0.003	-0.003	-1.775	22.418	25.968
TV	vw < 25 μm	0.0001	0.001	-0.001	3.604	59.290	52.082
Density	vw < 25 μm	-0.0001	0.003	-0.003	-1.178	79.742	82.097
W	25 to < 40 μm	0.0427	1.638	-1.553	0.136	4.8449	4.574
WV	25 to < 40 μm	-0.327	21.982	-22.636	0.0929	19.831	19.645
T	25 to < 40 μm	0.00002	0.001	-0.001	0.268	12.228	11.692
TV	25 to < 40 μm	0.00001	0.0005	-0.0004	0.787	33.534	31.959
Density	25 to < 40 μm	0.001	0.024	-0.022	1.199	39.907	37.509
W	40 to < 80 μm	-0.048	3.769	-3.865	-0.088	7.380	7.556
WV	40 to < 80 μm	1.729	24.609	-21.151	1.415	20.837	18.007
T	40 to < 80 μm	0.00007	0.0013	-0.0012	0.773	15.932	14.386
TV	40 to < 80 μm	-0.0001	0.0004	-0.0004	-1.326	37.579	40.231
Density	40 to < 80 μm	-0.0034	0.0332	-0.040	-2.445	36.727	41.617
W	vw \geq 80 μm	-4.733	97.261	-106.73	-28.015	344.291	400.32
WV	vw \geq 80 μm	-15.015	131.406	-161.44	-30.506	341.124	402.14
T	vw \geq 80 μm	-0.001	0.009	-0.012	-28.786	343.754	401.33
TV	vw \geq 80 μm	-0.0002	0.001	-0.002	-27.715	345.609	401.04
Density	vw \geq 80 μm	0.0002	0.008	-0.008	-26.277	347.561	400.11
W	All vessels	-0.13	3.417	-3.677	-0.275	8.047	8.598
WV	All vessels	0.795	14.690	-13.100	0.706	12.810	11.399
T	All vessels	0.00003	0.0008	-0.0008	0.295	9.298	8.708
TV	All vessels	.000004	0.0003	-0.0003	0.207	23.413	22.999
Density	All vessels	-0.002	0.031	-0.036	-0.874	20.422	22.170

Table 5.3 lists the intra session repeatabilities of the 25 indices measured. The MD, 95% CI columns show mean difference, and 95% confidence interval in μm for W and μm^2 for WV, units of curve energy for T and curve energy squared for TV, and mm^2 of vessel per mm^2 of conjunctiva for Density. Columns % MD, and % CI, give repeatabilities as a percentage of the mean measurement. Shaded areas show those indices with an acceptable repeatability value ($\sim\pm 10\%$).

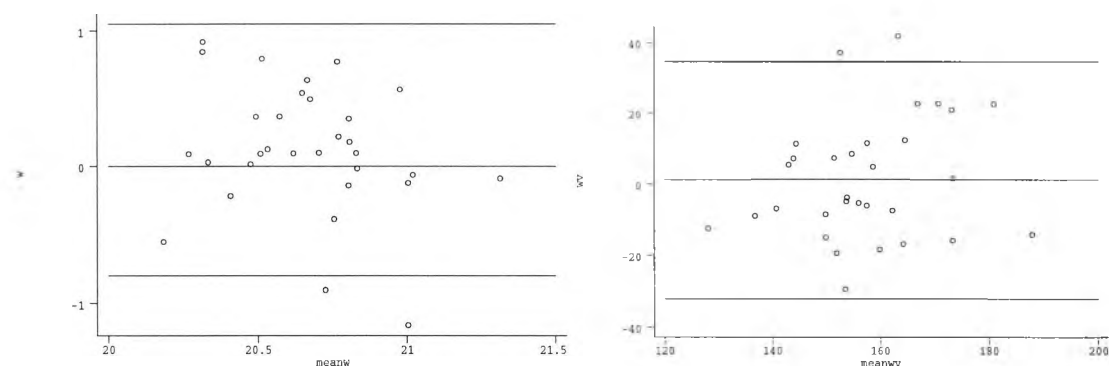
5.5.3 Inter session repeatability

Inter session repeatabilities were calculated for each index in accordance with the method of Bland and Altman (1986, 1995) using the mean measurement from the five images taken at session one and the mean of the five images taken at session three. The inter session repeatabilities are listed in table 5.4. Shaded areas show those indices with an acceptable repeatability value ($\sim\pm 10\%$). Evidently there are more indices with acceptable levels of repeatability than those found for the intra session repeatabilities (see table 5.3). In most cases the 95% CI of repeatability were smaller for the inter than intra session measurement.

Index	VW bin	MD	95%CI		%MD	% CI	
<i>W</i>	vw < 25 μ m	0.128	1.059	-0.803	0.626	5.132	-3.880
<i>WV</i>	vw < 25 μ m	1.257	34.725	-32.211	0.608	21.654	-20.299
<i>T</i>	vw < 25 μ m	0.0002	0.0027	-0.0024	1.505	26.966	-23.955
<i>TV</i>	vw < 25 μ m	0.00005	0.0008	-0.0006	2.522	46.848	-41.803
<i>Density</i>	vw < 25 μ m	0.0003	0.0024	-0.0018	2.643	54.312	-49.026
<i>W</i>	25 to < 40 μ m	0.006	0.895	-0.783	0.009	2.624	-2.343
<i>WV</i>	25 to < 40 μ m	-0.658	10.286	-11.602	-0.588	9.160	10.337
<i>T</i>	25 to < 40 μ m	-0.00007	0.0005	-0.0006	-0.771	5.279	-6.820
<i>TV</i>	25 to < 40 μ m	-0.00001	0.0002	-0.0002	-1.392	12.459	-15.243
<i>Density</i>	25 to < 40 μ m	0.0007	0.018	-0.027	1.190	38.732	-36.351
<i>W</i>	40 to < 80 μ m	0.303	3.157	-2.552	0.605	6.265	-5.055
<i>WV</i>	40 to < 80 μ m	-1.806	15.129	-18.742	-1.515	13.654	-16.675
<i>T</i>	40 to < 80 μ m	-0.0001	0.0005	-0.0007	-1.278	7.044	-9.601
<i>TV</i>	40 to < 80 μ m	-0.00002	0.0002	0.0002	-2.487	19.266	-24.242
<i>Density</i>	40 to < 80 μ m	0.001	0.030	-0.028	1.802	35.533	-31.930
<i>W</i>	vw \geq 80 μ m	5.192	53.882	-43.499	77.862	244.323	-88.599
<i>WV</i>	vw \geq 80 μ m	8.459	64.464	-47.546	89.193	264.744	-86.358
<i>T</i>	vw \geq 80 μ m	0.0002	0.004	-0.004	63.674	252.335	-124.99
<i>TV</i>	vw \geq 80 μ m	-0.00002	0.001	-0.001	-54.909	165.182	274.993
<i>Density</i>	vw \geq 80 μ m	0.0003	0.005	-0.004	84.132	261.485	-93.220
<i>W</i>	All vessels	0.271	3.239	-2.697	0.653	7.755	-6.449
<i>WV</i>	All vessels	-1.280	9.699	-14.260	-1.067	8.351	-10.485
<i>T</i>	All vessels	-0.00007	0.0004	-0.0005	-0.777	4.749	-6.303
<i>TV</i>	All vessels	-0.00002	0.0001	-0.0001	-3.818	7.816	-15.452
<i>Density</i>	All vessels	0.002	0.035	-0.031	1.891	24.651	-20.869

Table 5.4 lists the inter session repeatabilities of the 25 indices measured. The MD, 95% CI columns show mean difference, and 95% confidence interval in μ m for *W* and μ m² for *WV*, units of curve energy for *T* and curve energy squared for *TV*, and mm² of vessel per mm² of conjunctiva for *Density*. Columns %MD, and % CI, give repeatabilities as a percentage of the mean measurement. Shaded areas show those indices with an acceptable repeatability value ($\sim \pm 10\%$).

Figure 5.1 shows plots of the differences between session one and three for *W*, *WV*, *T*, *TV* and *Density* against their mean, for vessels less than 25 μ m in diameter. The 95% CI of repeatabilities are indicated by the 2 outer horizontal lines. It is reassuring that 95% of the observations lie within these limits and the differences show a reasonably random scatter across all *x*-values.



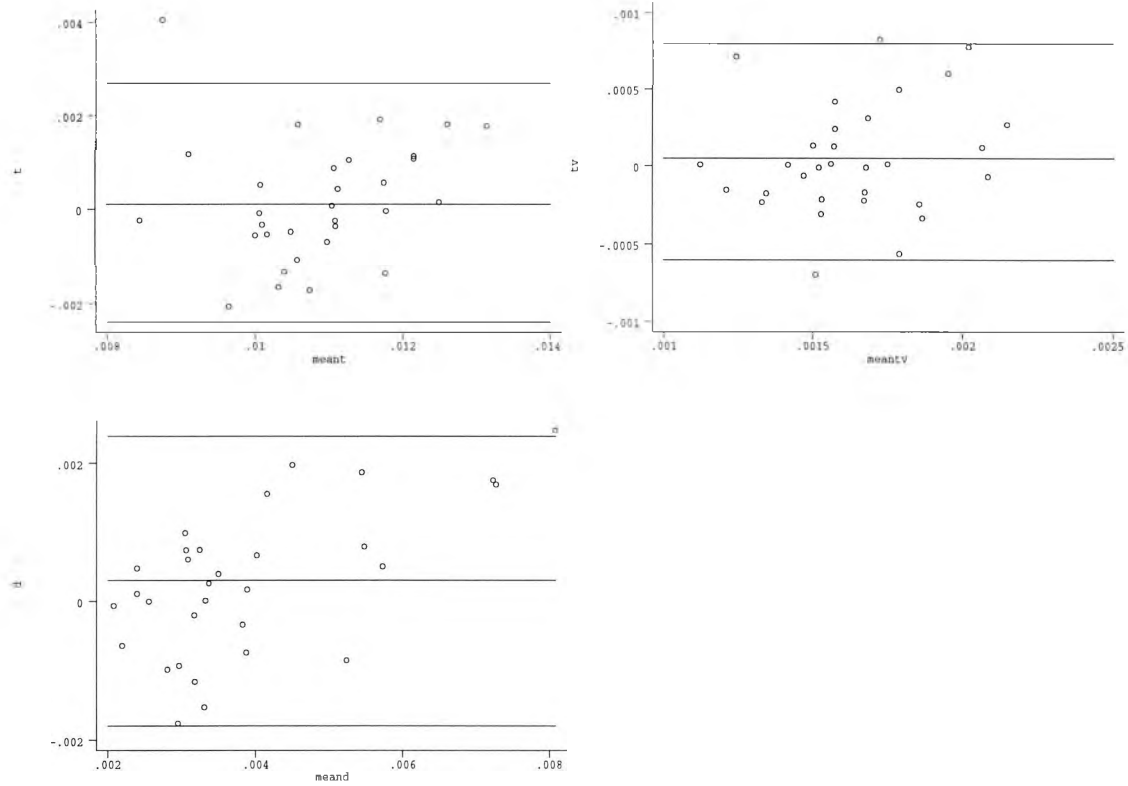
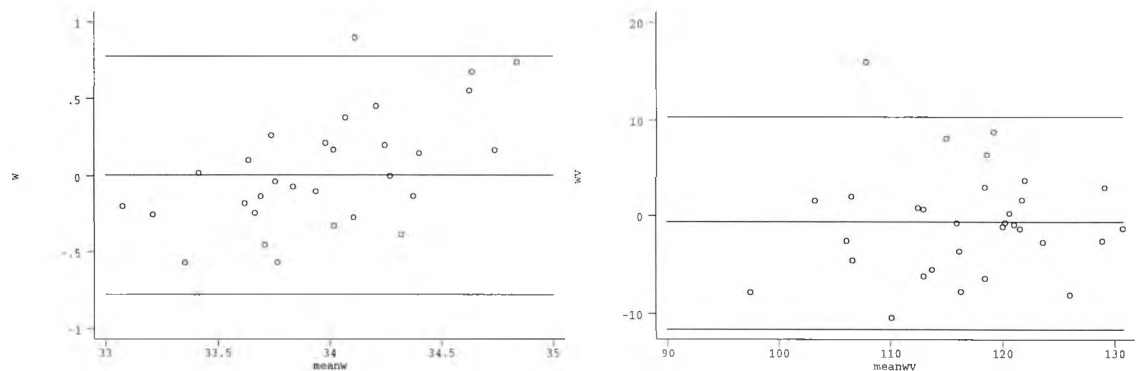


Figure 5.1 shows the differences between session 1 and session 3 for W, WV, T, TV and Density against their mean, for vessels <25µm in diameter. Horizontal lines represent the mean and the 95% CI of inter session repeatability.

Figure 5.2 shows plots of the differences between session one and three for W, WV, T, TV and Density against their mean, for vessels 25µm to less than 40µm in diameter. The 95% CI of repeatabilities are indicated by the 2 outer horizontal lines. Note that the coefficients of repeatability are wider for vessels less than 25µm in size than for vessels 25 to <40µm in diameter. Once again 95% of the observations lie within these limits and there are no apparent funnelling or sloping effects. Similar plots were obtained for all vessels and vessels 40 to less than 80µm in size, however, plots for vessel greater than 80µm in size showed wider 95% CI.



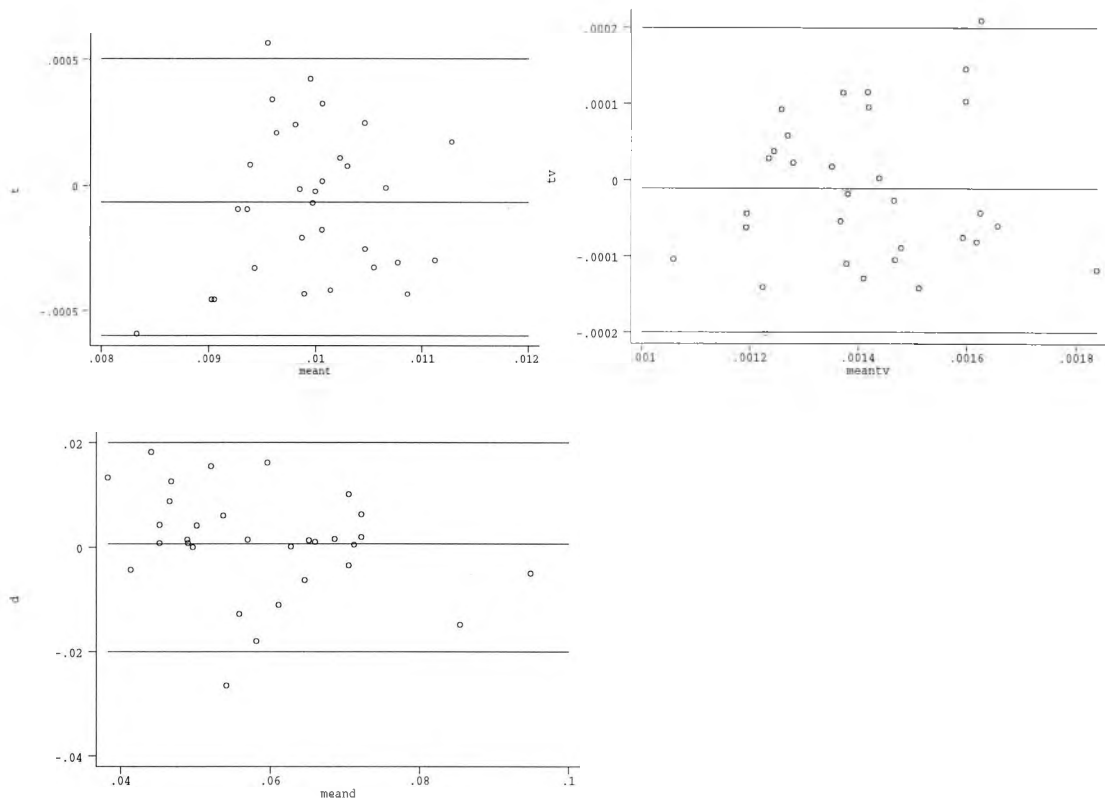


Figure 5.2 shows the differences between session 1 and session 3 for *W*, *WV*, *T*, *TV* and *Density* against their mean, for vessels 25 to $<40\mu\text{m}$ in diameter. Horizontal lines represent the mean and the 95% CI of inter session repeatability.

All *W* indices gave an acceptable level of repeatability except those where vessels were measured in excess of $80\mu\text{m}$. This phenomenon has been addressed above. *WV* measured from vessels with widths from 25 to less than $40\mu\text{m}$, and from all vessels, and *T* measured from vessel 25 to less than $40\mu\text{m}$ in diameter, 40 to less than $80\mu\text{m}$ in diameter, and all vessels gave an acceptable level of repeatability. In addition, *TV* indices measured from vessels 25 to less than $40\mu\text{m}$ in size and all vessels were associated with an acceptable level of repeatability. Note that repeatabilities measured from all vessels and vessels from 25 to less than $40\mu\text{m}$ were associated with the best levels of repeatability.

Density measures are associated with a larger 95% confidence limit for repeatability. However, these limits are not as disappointing as they appear at first glance. For example the percentage CI associated with the measure of total vascular density initially appears large (+24.651% to -20.869%). However, in the context of the actual measurement this will only make a small difference in the measured value, as shown in table 5.5. Unlike other methods of conjunctival vascularity assessment this technique also allows numerous populations of vessel to be interpreted, classified on the basis of size. Thus the repeatability of the density measure, were in reality, very good.

From a clinical view point the levels of repeatability for density are acceptable and certainly superior to any previous reported methods already discussed in the earlier chapters.

VW bin	Mean density (%)	%CI	Density range
vw < 25 μ m	0.4%	+54.3 to -49.0%	0.6 to 0.2%
25 to < 40 μ m	6%	+38.7 to -36.4%	8.3 to 3.8%
40 to < 80 μ m	9%	+35.5 to 31.9%	12.2 to 6.1%
vw \geq 80 μ m	0.1%	+261 to -93.2%	0.4 to 0.007%
All vessels	15%	+24.7 to -20.9%	18.7 to 11.9%

Table 5.5 the effect size of the 95% CI of repeatability on the actual measurement of vascular density.

The same reasoning can be applied to other indices where the repeatabilities appear to be unduly large e.g. *TV* and *WV*. The performance of these two indices are summarised in tables 5.6 and 5.7.

VW bin	Mean <i>WV</i>	%CI	<i>WV</i> range
vw < 25 μ m	156 μ m ²	+21.7 to -20.3%	190 to 124 μ m ²
25 to < 40 μ m	117 μ m ²	+9.16 to -10.3%	128 to 105 μ m ²
40 to < 80 μ m	117 μ m ²	+13.7 to -16.7%	133 to 97.5 μ m ²
vw \geq 80 μ m	19 μ m ²	+264 to -88.6%	69.2 to 2.17 μ m ²
All vessels	118 μ m ²	+8.35 to -10.5%	128 to 106 μ m ²

Table 5.6 the effect size of the 95% CI of repeatability on the actual measurement of *WV*.

VW bin	Mean <i>TV</i>	%CI	<i>TV</i> range
vw < 25 μ m	0.002CE ²	+46.8 to -41.8%	0.0029 to 0.0012CE ²
25 to < 40 μ m	0.001CE ²	+12.5 to -15.2%	0.0011 to 0.0008CE ²
40 to < 80 μ m	0.001CE ²	+19.3 to -24.2%	0.0012 to 0.0008CE ²
vw \geq 80 μ m	0.0001CE ²	+165 to -275%	0.0003 to -0.0002CE ²
All vessels	0.001CE ²	+7.82 to -15.5%	0.0011 to 0.00085CE ²

Table 5.7 the effect size of the 95% CI of repeatability on the actual measurement of *TV*.

The effect of large 95% confidence limits of repeatability for *WV* and *TV* has a small effect when the actual sizes are small. It is envisaged that the effect of pathological conditions on conjunctival vasculature, such as carotid cavernous sinus fistula, would have such a dramatic effect that it would more than exceed the CI quoted. However, it is difficult to draw conclusions such as these before a diseased vasculature is investigated. In accordance with the method of Bland and Altman (1986) none of the inter session differences were significantly different from zero, indicating the absence of systematic error between measurements. Note that the inter session repeatabilities are most pertinent when considering the performance of the method because future measurements were recorded as the mean of 5 taken from the one session.

5.5.4 Diurnal variation and association with other variables

In all cases the validity of the linearity assumption between vessel indices and variables was evaluated as outlined in the methods section. No instance occurred where the linearity assumption was shown to be invalid.

5.5.4.1 Pooled data from all vessels

As indicated in table 5.3, indices measured on the pooled data showed little difference over the 8 hours of measurement. A graphical representation of the index W measured on all vessels for each session is given in figure 5.3. Evidently, there is little difference in this index over time, which is true of the other indices measured on the pooled data. Therefore pooling the vessel data may mask smaller effects on individual populations of vessels. Hence, in addition each vessel width bin was examined.

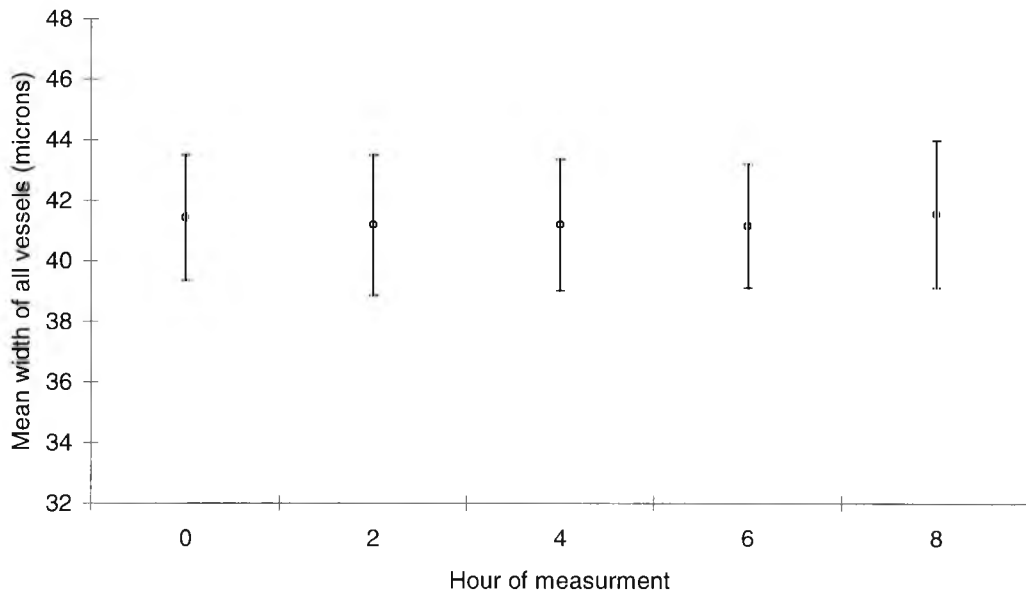


Figure 5.3 shows mean W index for all vessels at each 2 hour interval of measurement, error bars represent $\pm SD$.

The pooled data for each vessel index was observed to be approximately log-normally distributed hence, a log transformation for all indices was performed. The log transformation appeared to give a more acceptable Gaussian distribution thus allowing GEE to be fitted.

Vessel indices W , WV , T , and TV showed no statistically significant association with age, MAP, relative humidity or temperature, nor any difference between the sexes (in all cases $P > 0.1$). Also there was no statistically significant diurnal variation in the W index.

There was some evidence of an increase in WV in the second, sixth and eighth hour readings compared to baseline. The associated change in WV from baseline and 95% CI, expressed as a percentage, for all time bands are shown in table 5.8. Percentage differences from baseline are quoted to help visualise the magnitude of any change.

Although there was a small statistically significant percentage increase in WV at 2, 6, and 8 hours compared to baseline the effects were small. Especially when the 95% CI of inter session repeatability for this measurement was from +8.35% to -10.49% (see table 5.4). Clinically this effect can be regarded as insignificant. To check the goodness-to-fit of the GEE model to the data plots of the residuals were examined. The residuals plotted against WV did not show an even scatter when plotted against

WV. Hence, these results need to be treated cautiously as this model may not be the best for this type of data. Figure 5.4 shows the data for each individual from which it is evident that there was not a consistent pattern for WV over time, highlighting the inter subject variability.

HOUR	% CHANGE FROM BASELINE	95% CI	P VALUE
2	2.45%	+0.52 to +4.41%	0.012
4	1.07%	-0.83 to +3.00%	0.270
6	2.61%	+0.69 to +4.60%	0.008
8	1.92%	+0.0089 to +3.87	0.049

Table 5.8 lists the diurnal variation in pooled values of WV expressed as a percentage change from baseline measurement. P values and 95% CI are also given.

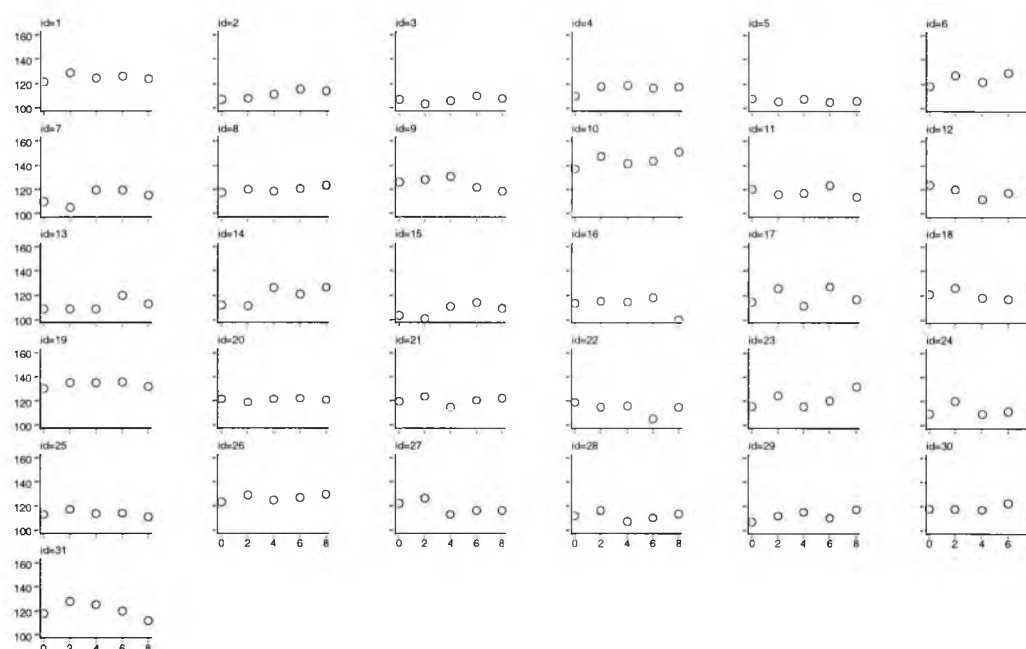


Figure 5.4 shows separate graphs of WV plotted against the hour of measurement for each of the 31 subjects

There was some evidence of an increase in T in the sixth and eighth hour readings compared to baseline. The associated change in T from baseline and 95% CI, expressed as a percentage, for all time bands are shown in table 5.9.

HOUR	% CHANGE FROM BASELINE	95% CI	P VALUE
2	0.68%	-0.45 to +1.81%	0.232
4	0.78%	-0.35 to +1.92%	0.175
6	2.08%	+0.94 to +3.24%	<0.001
8	1.25%	+0.12 to +2.40%	0.030

Table 5.9 lists the diurnal variation in pooled values of T expressed as a percentage change from baseline measurement. P values and 95% CI are also given.

As with the WV findings, the small statistically significant increase in T measured on

the sixth and eighth hour must be treated conservatively, especially when the 95% confidence interval of inter session repeatability was +4.03% to -8.16%. This small effect may be treated as being clinically insignificant.

There was some evidence of an increase in *TV* in the sixth hour reading compared to baseline. The change in *TV* from baseline and 95% CI, expressed as a percentage, for all time bands are shown in table 5.10. As with the other findings, the small increase in *TV* at the sixth hour was considered to be clinically insignificant.

HOUR	% CHANGE FROM BASELINE	95% CI	P VALUE
2	0.27%	-2.09 to +2.69%	0.824
4	1.55%	-0.84 to +4.00%	0.206
6	3.90%	+1.45 to +6.40%	0.002
8	2.19%	-0.21 to +4.66%	0.074

Table 5.10 lists the diurnal variation in pooled values of *TV* expressed as a percentage change from baseline measurement. *P* values and 95% CI are also given.

Vessel density (*Density*) showed no statistically significant association with age, relative humidity or temperature, nor between the sexes (in all cases $P > 0.1$). There was no statistically significant diurnal variation in vascular density. However, there appeared to be a statistically significant association between MAP and vessel density ($P = 0.047$). A 0.27% increase in density was found, with a 95% CI from +0.00405 to +0.54%, per 1 mmHg increase in MAP. A 10mmHg increase in MAP would increase vascular density by, on average 2.7% (95% CI between +0.04 to +5.4%). A scatter plot of vascular density against MAP, along with the fitted regression line is shown in figure 5.5.

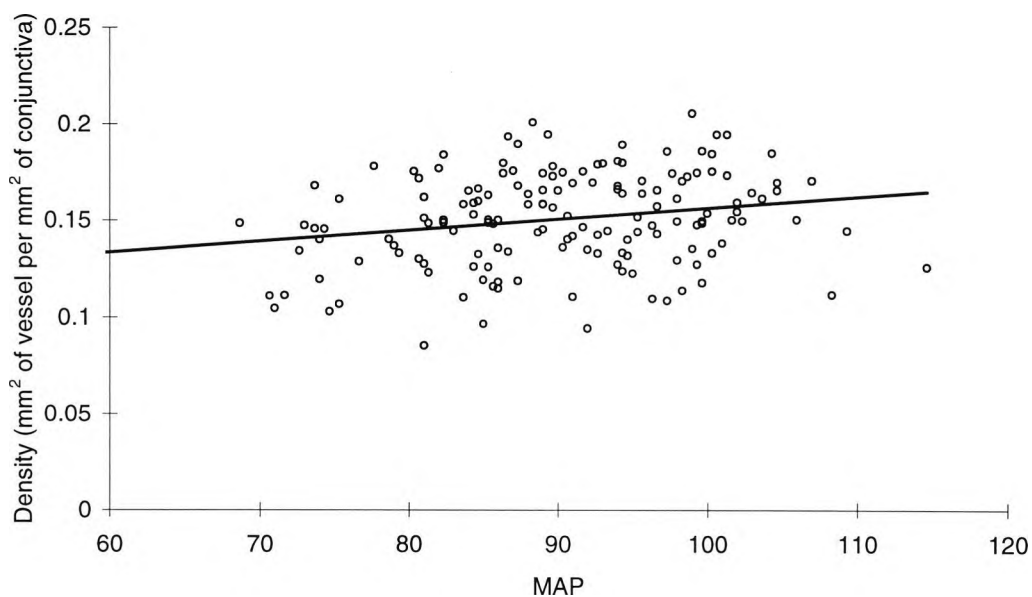


Figure 5.5 shows a scatter plot of MAP against total vascular density and a linear trend line which shows a slight positive gradient.

As shown in figure 5.5 the association between MAP and vessel density is weak. Unlike a traditional linear regression an R^2 value cannot be calculated, however, borderline significance was found ($P=0.047$). To check the goodness-to-fit of the GEE model to this data, plots of the residuals were examined. However, there was some departure from normality and this observation needs to be treated cautiously.

5.5.4.2 Data from vessels less than $25\mu\text{m}$ in diameter

None of the indices demonstrated a significant variation throughout the day. WV , T , and $Density$ showed no statistically significant association with age, MAP, relative humidity or temperature, nor any difference between the sexes (in all cases $P>0.1$). A univariate analysis of W appeared to show a statistically significant association with age ($P=0.01$), MAP ($P=0.03$), and sex ($P<0.001$). However, a multivariate model including all three of these parameters showed that the only statistically significant association was with sex. The effect of gender on W was very small constituting approximately a 1% increase (95% CI $+0.2$ to $+1.6\%$) in W in females compared to males. From a clinical point of view the size of the effect associated with sex was not considered to be important, especially when the 95% CI of inter session repeatability for the measurement of W was $+4.5$ to -3.6% (see table 5.4). The reason for the apparent association between W with age, and W and MAP in the univariate analysis is because of a significant correlation between age and sex ($R=0.41$, $P=0.02$), once the effect of sex is taken in to account age and MAP do not exert any independent effect on W . As shown in table 5.1 on average the sample contained more females, who were on average younger than the males.

TV was found to have a borderline association with MAP ($P=0.040$) from which a linear assumption is not unreasonable. Figure 5.6 shows a scatter plot of MAP against TV for vessels less than $25\mu\text{m}$ in width. A linear trendline shows a slight positive gradient.

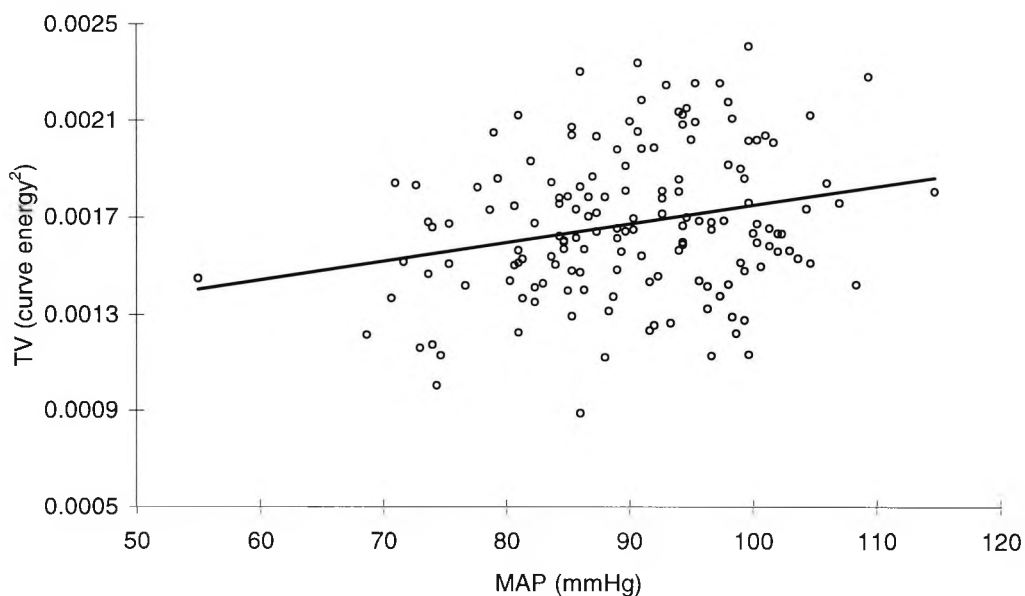


Figure 5.6 shows a scatter plot of MAP against TV for vessels less than $25\mu\text{m}$ in width and a linear trendline showing a slight positive gradient.

The equation of the regression line using GEE is given below.

$$TV=5.81\times 10^{-6}\times MAP+0.00115$$

The gradient (5.81×10^{-6}) is the effect for a 1mmHg increase in MAP

The average MAP of the sample was approximately 90mmHg (89.98mmHg), using the equation above TV is found to be 0.00167 units of curve energy squared (CE^2). Hypertensives may have systolic and diastolic pressures in excess of 140 and 90mmHg respectively. This gives a MAP of 107mmHg (106.7mmHg) which equates to a TV value of 0.00177 CE^2 . Hence a 17 mmHg rise in MAP was associated with a 0.0001 CE^2 increase in TV or an increase of 10mmHg in MAP is associated with a 0.00006 CE^2 increase in TV . This increase in TV may appear to be negligible, but the sample studied is from a normal population and is unlikely to have large values for curve energy as summarised in table 5.4. However, considering that the mean TV value was approximately 0.0017 CE^2 for each session, this equates to an increase of 3.42% (95% CI from +0.15 to +6.41%).

5.5.4.3 Data from vessels $\geq 25\mu m$ and $< 40\mu m$ in diameter

None of the indices showed any statistically significant association with age, MAP, relative humidity or temperature, nor between the sexes (in all cases $P>0.1$). Also there was no statistically significant diurnal variation in any index.

5.5.4.4 Data from vessels $\geq 40\mu m$ and $< 80\mu m$ in diameter

All indices showed no statistically significant association with age, MAP, relative humidity or temperature, nor between the sexes (in all cases $P>0.1$). Neither was there any diurnal variation in these indices.

5.5.4.5 Data from vessels $\geq 80\mu m$ in diameter

As indicated previously the 95% CI of inter session repeatability of all indices measured on this vessel group were very wide and hence examination of these values for this particular vessel group was of little use. Not surprisingly no association was found between any index in this group and any of the other variables, nor any significant variation throughout the day. Figure 5.7 illustrates the variability in measurement for this subgroup. In some instances an individual may record a reading at one session, and at the next no reading was obtained. Indeed for some individuals no diurnal readings were made.

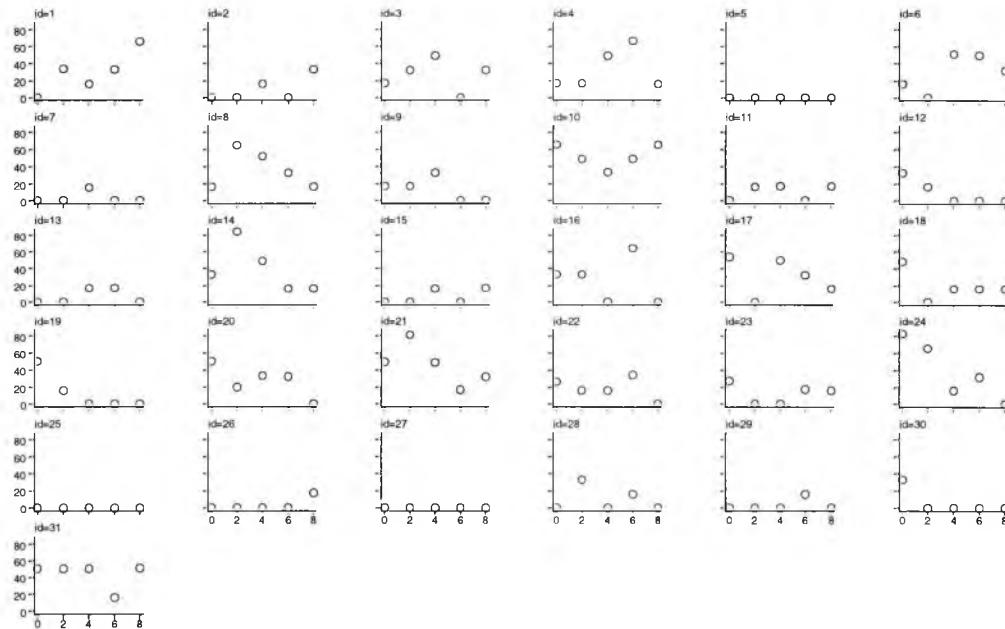


Figure 5.7 shows mean vessel widths for the above $80\mu\text{m}$ category plotted against hour for each subject separately.

A graphical representation for all indices against age and MAP for each visit separately is given in appendix A.1 for age and A.2 for MAP, from which no obvious trends can be seen.

5.5.4.6 Diurnal variation in MAP

A normal value for MAP is approximately 100mmHg. However, it is well known that this figure is not constant and is related to an individuals physical and mental status (Bell *et al*, 1980). Many attempts have been made to define normal values for MAP but all such efforts have been unsatisfactory. MAP is heavily influenced by a patients age, heredity, and environment. In this study, of 31 normotensives, a diurnal variation in MAP was found. A univariate analysis showed that MAP was highest in the morning and decreased throughout the day. MAP at baseline was 92.6mmHg with a SD of 10.8mmHg. Variations from this baseline level are summarised in table 5.11.

HOUR	% CHANGE FROM BASELINE	95% CI	P VALUE
2	-1.11%	-3.84 to 1.62%	0.427
4	-3.43%	-6.16 to -0.70%	0.014
6	-4.87%	-7.60 to -2.14%	0.000
8	-3.71%	-6.44 to -0.98%	0.008

Table 5.11 lists the diurnal variation in MAP expressed as a percentage change from baseline measurement. P values and 95% CI are also given.

Individuals recruited to the study often presented for their first examination of the day directly from their mode of transport in getting to the University. Hence, this might explain the elevation in MAP associated with the first measurement of the day.

5.5.4.7 *Relative humidity and temperature*

No diurnal variation in room temperature or relative humidity was recorded. Mean room temperature for the duration of the experiment was $22.7 \pm 1.22^\circ\text{C}$, and $64.9 \pm 7.69\%$ for relative humidity.

5.6 *Discussion*

This study represents the first detailed morphometric and morphological analysis of diurnal variations in conjunctival vessels in a sample of 31 normal subjects. This study was designed to achieve normotensive values for the indices outlined, and tolerances of measurement, so the technique could be performed on patients with pathologically or environmentally challenged vasculature.

As indicated in table 5.4 many indices show good inter session repeatabilities. Although, some indices appear to have unacceptably high levels of repeatability (in excess of $\pm 20\%$) this must be seen within the context of the measurement itself. As indicated by tables 5.5 to 5.7 where wider levels of inter session repeatabilities were seen, these made little difference to the actual measurement. The exception to this was the measurement of vessels in excess of $80\mu\text{m}$, where the inter session repeatabilities were considerably greater. Vessels of this calibre are at the limit of the algorithms detection and hence were of low prevalence. A vessels categorised in the largest vessel group, which on session one has a mean width of $80\mu\text{m}$, may have a mean width of $79.9\mu\text{m}$ on session 2, and hence will be classified in the 40 to less than $80\mu\text{m}$ group. Such an event can produce large difference in the repeatability values. This phenomenon was an unwanted artefact of the vessel width categories chosen, hence, the data from vessels larger than $80\mu\text{m}$ in width was largely ignored. It is noteworthy that the repeatabilities of *WV* and *TV*, are larger than the corresponding indices *W* and *T* respectively. This is because *WV* and *TV* represent variance measures and are calculated from the weighted square of the SD in tortuosity or width of each string (as indicated in chapter 4). Hence, any difference between successive measurement will be exaggerated. However, it was hoped that in conditions of pathological challenge (e.g. cavernous sinus fistula, and diabetes) to the conjunctiva differences in variance would exceed the levels of repeatability found in this chapter.

Indices such as *WV*, *T*, and *TV* are novel measures and hence the mean values quoted in the previous section represent new values to describe conjunctival vasculature. Previous attempts have been made to quantify conjunctival vascularity (Chen *et al*, 1986; Owen *et al*, 1996). However, the *Density* measures given quantify conjunctival vascularity by width calibre. Vessels less than $25\mu\text{m}$ in size represent capillaries and post capillary venules with a mean vascular area of 0.4%, vessels 25 to $< 40\mu\text{m}$ collecting venules with an area of 6%, vessels 40 to $< 80\mu\text{m}$ venules and arterioles with an area of 9%, and vessels $> 80\mu\text{m}$ which refer to anterior ciliary arteries and venules with an area of 0.1%. The combined vascular density for 31 normotensives was approximately 15%. The width classification of vessels allows different populations of vessels to be assessed.

Data for *W*, *WV*, *T*, *TV*, and *Density* showed little change throughout the diurnal series of measurements. Some small statistically significant changes were found, but were not considered clinically important as the limits of inter session repeatabilities were in

excess of these effects. Of interest was the statistically significant association between MAP and pooled vascular density where a 10mmHg increase in MAP was associated with a 2.7% (95% CI between +0.04 to 5.4%) increase in vascular density ($P=0.047$). However, as indicated in the results section this association must be treated cautiously, and was relatively small.

Kovalcheck *et al* (1984) examined photographic conjunctival images of 143 normal patients aged 5 to 70 years. They anecdotally concluded that arteriole, venule, and capillary area increased with age. McMonnies and Ho (1991) subjectively graded vascularity of conjunctival photographs, using a reference scale, of 252 females (aged 1 to 82 years) and 227 males (aged 1 to 89 years). A Spearman rank correlation revealed a statistically significant increase in vascularity with age ($R=0.73$, $P<0.0001$). They also showed that males had greater vascularity than females ($P<0.0001$, Mann Whitney U test) but this small difference was not regarded as being clinically important. Although our sample was considerably smaller no association between age or sex and *Density* for pooled vessel widths, or vessels classified by size, was found. However, for vessels less than $25\mu\text{m}$ in size, the effect of gender was seen to exert a small effect on the *W* index with a 1% (+0.2 to +1.6%) increase in females compared to males ($P<0.001$). As with the findings of McMonnies and Ho (1991) this effect can be considered as not being clinically important. The association between vascular densities age and gender will be examined again in chapter 6 where a larger normal population, with a greater range of age, were examined.

TV for vessels less than $25\mu\text{m}$ in size was found to have a borderline association with MAP ($P=0.040$) where a 0.00006CE^2 increase in *TV* was associated with a 10mmHg rise in MAP. However, as indicated in the results section this increase was extremely small and should be treated with caution.

Evidence for a diurnal variation in MAP was found but the measurement of this value can be confounded by the patients mental and physical status and can be influenced by the patients age, heredity and environment. A univariate analysis revealed that MAP was highest in the morning and decreased throughout the day. This elevation is shown in table 5.11 and may be explained by the physical exertion involved in arriving for the first examination of the day.

In general, the indices measured showed uniform values throughout the day. They are repeatable (except for vessels larger than $80\mu\text{m}$), and offer a more in depth description of the conjunctival vascular bed. Unlike other attempts at general vascularity assessment, the classification of vessels into width categories allows the behaviour of certain populations of vessel to be examined. The 95% CI of inter session repeatability and mean measures of each index measured on the 31 normotensives allows comparisons to be made with those with environmentally or pathologically challenged vasculature. It is noteworthy that the mean of 5 images for each session was considered to be the method of choice for the collection of longitudinal follow-up data, and will be used extensively in chapter 6, where the effects of diabetes on the conjunctival bed will be investigated.

CHAPTER 6

6. Diabetic conjunctival vasculature

6.1 Aim

The purpose of this chapter was to find whether diabetes exerts an effect on vessels within the conjunctiva. The indices discussed in previous chapters were studied on a normal population and compared with those measured on a population of TI and TII diabetics.

6.2 Introduction

The effects of diabetes on retinal circulation are well known and have been discussed at length in chapter 1 (Ditzel, 1954; Stitt *et al* 1995; Klein *et al* 1989; Spencer *et al*, 1992; Kohner and Sleightholm, 1986; Mendivil *et al*, 1995; Patel *et al*, 1992). However, the effects of diabetes on conjunctival vasculature are less documented within the scientific literature and are often based on anecdotal findings (Ditzel, 1954; Ditzel and Saglid, 1954; Landau and Davis, 1960; Dixel *et al*, 1960; Coget *et al*, 1989). Worthen *et al* (1981) endeavoured to use an objective method of studying conjunctival vasculature by superimposing a grid pattern over digitised photographic images, and measuring vessel area. They concluded that diabetic conjunctival microvessels, less than 25µm in diameter, showed a 25% decrease in area. Greer *et al* (1996) used an unspecified automated video technique to show that diabetics had significantly larger vessels and an abnormal vessel organisation. A brief abstract by Chen *et al* (1986) stated that diabetics showed a 20% increase in vascularity compared to normals, whilst hypertensives showed a 10% decrease in vascularity. As indicated in chapter 1 it is difficult to draw conclusions as to the effects of diabetes on conjunctival vasculature. However, it would appear that microvascular drop-out (capillary), macrovascular (venule) dilation accompanied with calibre variation and increased tortuosity are the likely effects of diabetes on conjunctivae. The concept of microvascular drop-out agrees with the documented changes in the kidney (nephropathy), peripheral nervous system (neuropathy), and retina (diabetic retinopathy). The aim of the current study was to verify or disprove these findings using the automated approach outlined in chapter 4. It was hoped that the indices described would give a better indication of conjunctival vessel morphology and morphimetry.

The effects of hypertension and age may confound the effects diabetic conjunctival angiopathy. Hypertensive effects on conjunctival vasculature have been reported (Davis and Landau, 1957; Harper *et al*; 1978). Harper *et al* (1978) found a reduction in the number of bulbar conjunctival arterioles in hypertensive patients, however, these findings were anecdotal. Photographic studies of conjunctival vasculature in 143 'normal' individuals revealed an increase in capillary and venular meandering, and an increase in arteriole, venule and capillary surface area with the onset of age (Kovalcheck *et al*, 1984). McMonnies and Ho (1991) used a photographic scaling technique to grade 252 females (aged 1 to 82 years) and 227 males (aged 1 to 89 years). They showed a small increase in hyperaemia with age ($R=0.73$, $P<0.0001$,

Mann Whitney U test). However these differences were considered as being clinically insignificant. Aliò and Padron (1982) investigated the mean absolute temperature of the anterior segment using ocular thermography in 96 normals, aged 15 days to 80 years and found a negative correlation with age. They concluded that this may indicate a reduction in vascularity with age. This finding appeared to contradict the increase in vascularity with age reported by Kovalcheck *et al* (1984), McMonnies and Ho (1991), but ocular thermography and subjective scaling are far from ideal methods of gauging conjunctival vascularity. However, these findings must be taken into consideration when studying the effects of diabetes on conjunctival vasculature.

6.3 Method

Images of the right bulbar conjunctiva of normal and diabetic individuals were captured using the Nikon FS-2 photo slit-lamp, with a xenon flash power setting of one, with a Wratten 99 and Wratten 96 neutral density filter (0.2 log units) over the illumination turret window. Forty five degrees of nasal ocular rotation was achieved by use of a fixation target, to achieve a maximal view of the conjunctiva without the need for manual lid retraction. Images were recorded using the DCS 100 digital camera, and were imported into a computer via a SCSI card. The image from the green channel of the CCD was extracted using Aldus PhotoStyler version 1.1 (Aldus Corporation, Seattle, USA) software, and archived to a writable CD as an 8 bit, monochrome, 1.38MB portable grey map file. Five images were taken within one session.

Diabetic individuals were recruited from those attending clinics at a hospital eye department (Sussex Eye Hospital) and from those attending the City University Eye Clinic for routine examination. Normal patients were recruited on a volunteer basis from the academic staff, post graduates and undergraduates at the City University. Also staff from a hospital eye clinic (Sussex Eye Hospital) and relatives of attending patients were asked to take part.

A systemic and ocular history were taken. Details of the patients age, sex, and smoking habits were recorded for all individuals. In addition diabetic patients were classified as being TI or TII, and the duration of their diabetes ascertained from medical records. Diabetic medication was recorded under the following broad categories; controlled by diet only, oral hyperglycaemics, or insulin. Patients diagnosed with hypertension, or on hypertensive medications were barred from entry to the study, as were contact lens wearers and those with other significant ocular conditions with a known effect on conjunctival vasculature e.g. glaucoma (Orgül and Flammer, 1995). Fundal examinations were performed after imaging the conjunctiva. Retinopathy was classified under the following headings; no retinopathy, BDR or maculopathy, PPR, PR, or those who had received PRP. These are excepted methods of classification as outlined in section 1.3.2 of chapter 1.

At each examination systolic and diastolic blood pressures were recorded objectively using an auto-sphygmomanometer (Auto-sphygmomanometer UA-251, Copal, USA). MAP was calculated in an identical manner to the method described in chapter 5.

Images obtained underwent Steger's algorithm (1996, 1998) for the detection of curve linear structures using a $\sigma = 3$, as detailed in chapter 4. Mean vessel width (W) and

width variance (WV), mean tortuosity (T) and tortuosity variance (TV), and vascular density were calculated for all vessels measured. Data was then divided into bins where vessel widths $<25\mu\text{m}$ represented capillaries, 25 to $<40\mu\text{m}$ venules, 40 to $<80\mu\text{m}$ arterioles and venules. Note that vessels $\geq 80\mu\text{m}$ representing arterioles and veins were ignored due to the large inter session repeatabilities associated with this measurement as indicated in chapter 5. The above indices (W , WV , T , TV and $Density$) were re-calculated for each vessel bin size giving a total of 20 indices. The final value represented the mean of each index for the 5 images taken.

6.4 Statistical analysis

Demographic details of the sample were obtained, including the number of diabetics, normals, males, females, and smokers. An initial graphical inspection of the raw data was performed to assess any clear pattern of association between any of the variables (such as age, sex, diagnosis, and MAP), and the vessel indices. The distribution of the vessel indices was inspected and an appropriate transformation undertaken if the data appeared skewed. This was followed by univariate linear regression analysis in the first instance to ascertain whether any of the variables listed below are related to the vessel indices calculated for the pooled vessel data and within each vessel bin in both normal and diabetic patients. Variables were recorded in the following manner.

Continuous variables

- Age was recorded in years
- MAP was recorded in mmHg

Grouping / categorical variables

- Smoking status recorded as 1 if a current smoker and 0 if non-smoker
- Sex was recorded as a 0 for male, 1 for female
- Diagnosis recorded as 0 if normal, 1 if TI diabetic, and 2 if TII diabetic

Consider the following equation of linear regression, where y is the outcome of interest i.e. a vessel index, x is one of the explanatory variables e.g. age, or sex, m is the effect per unit increase in x , and c is the intercept term, the value for y when x is zero.

$$y = mx + c$$

For example, considering x as a continuous variables such as age, m is the effect on y for a unit (one year) increase in age. Clearly using the equation above for the continuous variables assumes a linear relationship between y (the vessel index) and x . This is a strong assumption, but the validity of this assumption can be evaluated by examining plots of the data against these continuous variables. Initially age and MAP were divided into quartiles to allow investigation of non-linear relationships with vessel indices. For example for age, all subjects in the youngest quartile were classified as age group 1, those in the second quartile in age group 2, the third quartile age group 3 and the oldest subjects in age group 4, thus creating 4 separate subgroups according to age. By the same method 4 groups for MAP were also constructed. Linear regression analysis with factors / grouping variables is equivalent to an analysis of variance, but allows more flexibility if the simpler model needs to be extended to a more complex model. If the relationship proved to be non-linear then the effect in

each subgroup is presented. However, if there was not a departure from linearity then the effect is given according to years of age or mmHg.

Consider x as the variable sex, where x is coded 0 if male and 1 if female, then m represents the average difference between males and females. Therefore, when $x = 0$, the expression becomes

$$\begin{aligned}y &= mx + c \\y &= m(0) + c \\y &= c\end{aligned}$$

Where c is the value for males. If we now consider the situation for females where $x = 1$, then the expression becomes

$$\begin{aligned}y &= mx + c \\y &= m(1) + c \\y &= m + c\end{aligned}$$

Where $m+c$ is the value for the index in females. From this it is a matter of extension from 2 groups for sex to 4 groups for age (or MAP) where the following equation applies.

$$y_i = m_i x_i + c$$

Where y_i is the value for the index in the i th age group of 4 different age groups, m_i is the effect of being in age group i compared to the baseline age group (which is usually taken as the youngest group), and x_i is the value for the vessel index in the i th age group of 4 different age groups, and x is just an indicator variable which takes the value of 1 if in the i th age group, and zero if not in the i th age group

The univariate model was extended to multivariate linear regression to include those variables identified above as being related to a vessel index in the univariate analysis.

The second stage of the analysis concentrated on the diabetic sample only. The aim here was to ascertain whether duration of diabetes (recorded in years), and the degree of retinopathy reflect the changes, if any, in the vascular indices calculated from diabetic conjunctiva. In addition, the effect of different modes of medication on the vessel indices were investigated. These factors were recorded in the following format.

Continuous variables

- Duration of diabetes was recorded in years

Grouping / categorical variables

- Duration was also factorised into quartiles in a similar fashion to age and MAP
- Retinopathy was recorded as a categorical variable where 0 was the absence of retinopathy, 1 was BR or maculopathy, 2 was PPR, 3 PR, and 4 post PRP
- Medication was recorded as 1 for control by diet only, 2 for oral hyperglycaemics, and 3 for insulin control

6.5 Results

In total 60 normals, 17 TI diabetics and 36 TII diabetics met the inclusion criteria and were studied. Demographic details of the sample are summarised in table 6.1. A total of 113 patients were studied. All observations and measurements were complete except for 2 blood pressure measurements where, due to obesity, sphygmomanometry was impossible.

PATIENT	NORMALS	TI	TII
AGE (YEARS)	49.27±20.26	52.94±17.28	65.50±9.04
DISEASE DURATION	-	28.76±15.19	9.139±6.89
P _S (mmHg)	127.03±18.28	139.5±22.14	146.65±22.09
P _D (mmHg)	77.98±9.97	79.12±12.61	86.24±10.02
MAP (mmHg)	94.33±10.71	99.24±12.70	106.4±12.40
SMOKING			
Non-smokers	55	14	32
Smokers	5	3	4
SEX			
Male	25	10	15
Female	35	7	21
RETINOPATHY			
None	60	6	19
BR / Maculopathy	-	6	13
PPR	-	1	1
PR	-	4	3
TOTAL NUMBER	60	17	36

Table 6.1 lists the demographic details of the sample. Note mean \pm SD are quoted where applicable

Tables 6.2 to 6.4 list the mean values, SD, minimum and maximum values for each index, for the normal, TI and TII diabetics respectively.

DATA FOR 60 NORMAL PATIENTS					
Index	Vessel width bin (vw)	Mean	SD	Minimum	Maximum
<i>W</i>	vw < 25 μ m	20.38	0.707	17.11	21.79
<i>WV</i>	vw < 25 μ m	147.0	18.30	79.49	180.1
<i>T</i>	vw < 25 μ m	0.0111	0.0021	0.0080	0.0218
<i>TV</i>	vw < 25 μ m	0.0017	0.0004	0.0010	0.0035
<i>Density</i>	vw < 25 μ m	0.0032	0.0016	0.0002	0.0080
<i>W</i>	25 μ m \leq vw < 40 μ m	34.18	0.664	32.73	35.43
<i>WV</i>	25 μ m \leq vw < 40 μ m	122.5	16.29	93.34	195.8
<i>T</i>	25 μ m \leq vw < 40 μ m	0.0102	0.0009	0.0083	0.0129
<i>TV</i>	25 μ m \leq vw < 40 μ m	0.0015	0.0002	0.0010	0.0021
<i>Density</i>	25 μ m \leq vw < 40 μ m	0.0475	0.0192	0.0050	0.1080
<i>W</i>	40 μ m \leq vw < 80 μ m	51.75	3.140	45.65	62.50
<i>WV</i>	40 μ m \leq vw < 80 μ m	122.32	17.27	96.33	176.3
<i>T</i>	40 μ m \leq vw < 80 μ m	0.0086	0.0007	0.0065	0.1053
<i>TV</i>	40 μ m \leq vw < 80 μ m	0.0011	0.0002	0.0005	0.0016
<i>Density</i>	40 μ m \leq vw < 80 μ m	0.0937	0.0279	0.0395	0.1864
<i>W</i>	All vessels	43.76	4.908	36.70	60.26
<i>WV</i>	All vessels	123.0	12.95	101.3	169.5
<i>T</i>	All vessels	0.0092	0.0008	0.0064	0.0112
<i>TV</i>	All vessels	0.0012	0.0002	0.0005	0.0018
<i>Density</i>	All vessels	0.1454	0.0326	0.0768	0.2535

Table 6.2 lists the mean, SD, minimum and maximum values for each index measured on 60 normal patients

DATA FOR 17 TI DIABETIC PATIENTS					
Index	Vessel width bin (vw)	Mean	SD	Minimum	Maximum
W	vw < 25 μ m	19.85	1.161	16.35	21.35
WV	vw < 25 μ m	122.9	39.85	51.53	180.0
T	vw < 25 μ m	0.0130	0.0037	0.0082	0.0238
TV	vw < 25 μ m	0.0019	0.0006	0.0011	0.0037
Density	vw < 25 μ m	0.0015	0.0012	0.0001	0.0047
W	25 μ m \leq vw < 40 μ m	33.88	2.729	26.93	36.71
WV	25 μ m \leq vw < 40 μ m	116.6	9.920	98.57	136.7
T	25 μ m \leq vw < 40 μ m	0.0099	0.0009	0.0081	0.0116
TV	25 μ m \leq vw < 40 μ m	0.0014	0.0003	0.0009	0.0019
Density	25 μ m \leq vw < 40 μ m	0.0256	0.0165	0.0004	0.0564
W	40 μ m \leq vw < 80 μ m	54.19	4.259	49.56	66.41
WV	40 μ m \leq vw < 80 μ m	119.0	20.17	86.89	172.8
T	40 μ m \leq vw < 80 μ m	0.0080	0.0008	0.0057	0.0094
TV	40 μ m \leq vw < 80 μ m	0.0009	0.0002	0.00041	0.0012
Density	40 μ m \leq vw < 80 μ m	0.0841	0.0294	0.0411	0.1522
W	All vessels	49.23	6.614	38.84	66.79
WV	All vessels	120.1	16.66	90.91	166.8
T	All vessels	0.0085	0.0010	0.0058	0.0101
TV	All vessels	0.0010	0.0003	0.0004	0.0015
Density	All vessels	0.1126	0.0381	0.0513	0.1821

Table 6.3 lists the mean, SD, minimum and maximum values for each index measured on 17 TI diabetic patients

DATA FOR 36 TII DIABETIC PATIENTS					
Index	Vessel width bin (vw)	Mean	SD	Minimum	Maximum
W	vw < 25 μ m	20.33	1.239	15.74	21.61
WV	vw < 25 μ m	134.4	34.03	61.97	193.0
T	vw < 25 μ m	0.0108	0.0032	0.0020	0.0197
TV	vw < 25 μ m	0.0016	0.0004	0.0006	0.0027
Density	vw < 25 μ m	0.0022	0.0011	0.0003	0.0046
W	25 μ m \leq vw < 40 μ m	33.71	2.078	24.39	35.79
WV	25 μ m \leq vw < 40 μ m	124.6	29.76	75.40	240.0
T	25 μ m \leq vw < 40 μ m	0.0099	0.0021	0.0038	0.0166
TV	25 μ m \leq vw < 40 μ m	0.0014	0.0003	0.0006	0.0024
Density	25 μ m \leq vw < 40 μ m	0.0298	0.0143	0.0028	0.0629
W	40 μ m \leq vw < 80 μ m	53.61	3.391	47.82	63.92
WV	40 μ m \leq vw < 80 μ m	117.4	15.33	90.16	154.9
T	40 μ m \leq vw < 80 μ m	0.0081	0.0007	0.0066	0.0096
TV	40 μ m \leq vw < 80 μ m	0.0009	0.0002	0.0006	0.0013
Density	40 μ m \leq vw < 80 μ m	0.0834	0.0230	0.0393	0.1330
W	All vessels	47.27	5.100	39.81	60.10
WV	All vessels	118.8	13.36	91.51	151.4
T	All vessels	0.0087	0.0009	0.0066	0.0106
TV	All vessels	0.0011	0.0002	0.0006	0.0014
Density	All vessels	0.1162	0.0275	0.0537	0.1695

Table 6.4 lists the mean, SD, minimum and maximum values for each index measured on 36 TII diabetic patients

As indicated in the methodology section age and MAP were used in the linear regression models as both continuous and categorical variables. The quartiles of age

and MAP, enabling them to be recorded as grouping variables, are given in table 6.5 and table 6.6. This type of division of subjects results in approximately equal sample sizes in each subgroup. All indices in all cases demonstrated a skewed distribution which was improved by a logarithmic transformation. In all cases linear regression models were fitted using the logarithmic transformation of the vessel index.

Age group	Age range	Mean age	SD	Number
0	20 to 39 yrs	29.72	6.380	29
1	40 to 59 yrs	51.40	6.360	30
2	60 to 68 yrs	64.15	2.996	27
3	69 to 94 yrs	76.96	6.607	27

Table 6.5 shows the age range, mean age, SD, and patient numbers for each quartile

MAP group	MAP range (mmHg)	Average MAP	SD	Number
0	73.67 to 90.00	84.24	5.208	30
1	90.01 to 97.33	94.26	2.327	27
2	97.34 to 108.00	102.1	2.899	27
3	108.01 to 131.3	116.1	6.645	27

Table 6.6 shows the MAP range, average MAP, SD, and patient numbers for each quartile

All indices measured on the vessels as a whole, and for each vessel bin, did not show any association between sex and smoking. For brevity the results from these models are not given. Univariate analysis was performed on the indices for the pooled vessel data, and for each vessel bin. The results are tabulated under the appropriate headings.

6.5.1.1 Univariate analysis of data from vessels less than 25 μ m in diameter

Table 6.7 summarises the univariate analysis of vessel indices for TI and TII diabetic data compared to normative data, where shaded areas represent statistically significant ($P < 0.05$) effects for vessels less than 25 μ m in diameter. It is noteworthy that none of the vessel indices appeared to show any statistically significant variation between the four age groups ($P > 0.2$ in all cases), neither was there any linear association with age for any index. Plots of vessel indices versus age did not appear to show any relationship and showed a random scatter.

As indicated in table 6.7 most indices showed a reduction in the diabetic groups compared with the normal group. The exception was tortuosity where T appeared to be increased in TI diabetics compared with normals, however, this was of borderline statistical significance ($P = 0.046$). No statistically significant difference was seen in T between TII diabetics and normals. Other indices which did not show statistically significant change from normals included W and TV for both TI and TII diabetics. A statistically significant decrease in WV was observed in both the TI ($P = 0.001$) and TII ($P = 0.026$) diabetic group with a -21.01% (-31.07 to -9.50%), and -11.23% (-20.03 to -1.46%) decrease respectively. The most dramatic effect was the decline in vascular density of approximately -61% (-74.23 to -40.53%) in TI compared with normals ($P < 0.0001$), and -33% (-52.40 to -7.93%) less in TII ($P = 0.014$). The statistically significant decline in indices observed in TI diabetics was larger and of greater significance than for TII when compared with the normal sample.

VESSEL INDEX	DIABETIC TYPE	% CHANGE FROM NORMAL DATA	95% CI	P VALUE
W	TI	-2.70	-5.37 to 0.04	0.053
	TII	-0.37	-2.47 to 1.78	0.730
WV	TI	-21.01	-31.07 to -9.50	0.001
	TII	-11.23	-20.03 to -1.46	0.026
T	TI	16.04	0.28 to 34.27	0.046
	TII	-6.72	-16.61 to 4.32	0.221
TV	TI	7.38	-7.38 to 24.50	0.342
	TII	-8.14	-18.00 to 2.87	0.141
Density	TI	-60.85	-74.23 to -40.53	<0.0001
	TII	-33.20	-52.40 to -7.93	0.014

Table 6.7 lists the effect size, 95% confidence interval (CI), and P value for each index measured on TI and TII diabetics compared to normal data. Shaded areas indicate those indices which are statistically significantly different from normals ($P < 0.05$).

No statistically significant variation of W, WV, T, TV between the quartile groups of MAP was found ($P > 0.2$ in all cases). However, *Density* decreased as the MAP group increased. This indicated a decrease in *Density* with increasing MAP. Hence, MAP was entered into the model as a continuous variable and on average *Density* decreased by -16.55% (-25.85 to -6.09%, $P = 0.003$) per 10mmHg increase in MAP. A plot of vessel density for vessels less than 25 μ m in diameter against MAP is shown in figure 6.1. A plot of the natural logarithm of vessel density for vessel less than 25 μ m in diameter against MAP is shown in figure 6.2. The graphs support the evidence for a linear decline in *Density* with MAP, and the fitted regression line is given in figure 6.2 where the model was fitted.

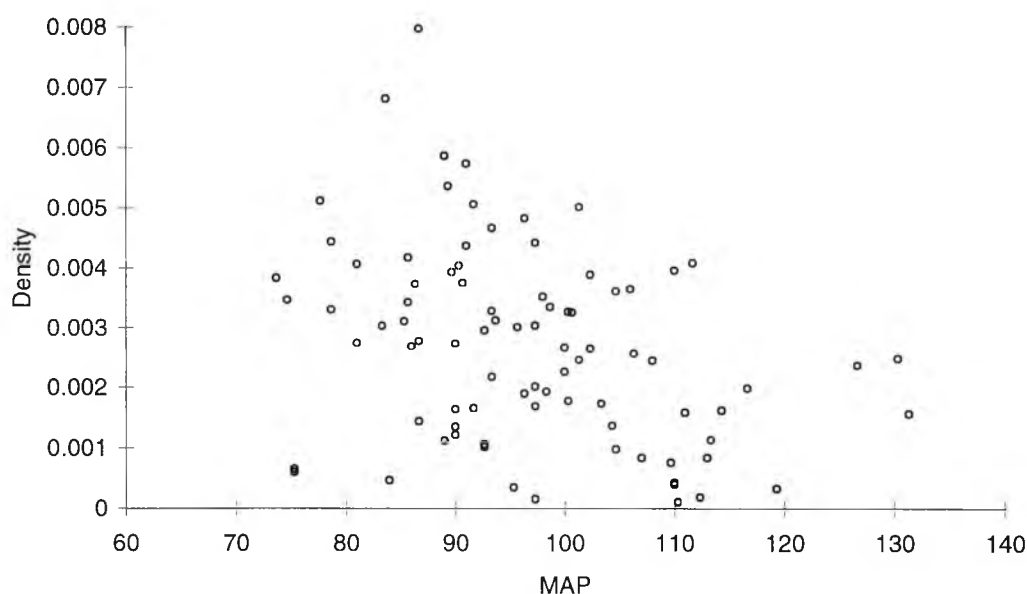


Figure 6.1 shows a scatter plot of MAP against Density for vessels <25 μ m in diameter.

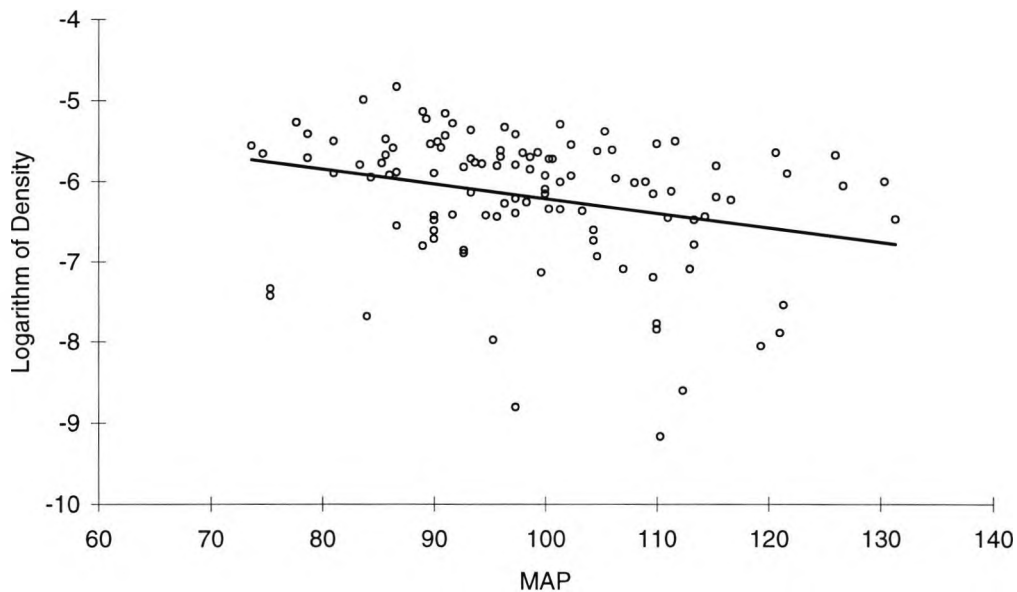


Figure 6.2 shows a scatter plot of MAP against the natural logarithm of Density for vessels $<25\mu\text{m}$ in diameter. The linear regression line shows decreasing density with increasing MAP.

6.5.1.2 Multivariate analysis of data from vessels less than $25\mu\text{m}$ in diameter

As diagnosis code and MAP both showed a statistically significant association with *Density*, a model containing both MAP and diagnosis codes was fitted. The effect of TI on *Density* adjusted for the effect of MAP was -57.12% (95% CI. from -71.96 to -36.76% , $P<0.0001$). Hence, the effect of TI on *Density* reduced slightly but was still considerable. Effect of TII on *Density* adjusted for the effect of MAP was -17.50% (95% CI from -41.71 to 16.64%), however, this did not reach statistical significance ($P=0.273$). The effect of MAP on *Density*, adjusted for diagnosis code, was -13.82% (95% CI -23.71 to -2.65% , $P=0.017$) per 10mmHg rise in MAP.

6.5.1.3 Univariate analysis of data from vessels $25\mu\text{m}$ to $<40\mu\text{m}$ in diameter

Table 6.8 summarises the univariate analysis of vessel indices for TI and TII diabetic data compared to normative data, where shaded areas represent statistically significant ($P<0.05$) effects for vessels $25\mu\text{m}$ to less than $40\mu\text{m}$ in diameter.

There was no evidence of a statistically significant change in W , WV , T , or TV between diabetic and normal populations. Although, a similar decrease in vascular density was found in the $25\mu\text{m}$ to less than $40\mu\text{m}$ vessel group as with the less than $25\mu\text{m}$ group (see table 6.7). The statistically significant reduction in *Density* was approximately -58% (-72.04 to -37.75%) in TI diabetics compared with normals ($P<0.0001$), and -40% (-56.16 to -18.99%) less in TII ($P=0.001$). However, this needs further consideration, because the diabetic group were older than the normal population (as indicated in table 6.1), and the TII group were considerably older than TI. A statistically significant correlation was found between age and the referring diagnosis ($R=0.40$, $P<0.0001$), also age and MAP were correlated ($R=0.50$, $P<0.0001$). Figure 6.3 shows the correlation between age and MAP for all patients where open squares

represent normals, closed squares TI, and crossed symbols TII diabetics. Figure 6.3 indicates a difference in ages between groups.

VESSEL INDEX	DIABETIC TYPE	% CHANGE FROM NORMAL DATA	95% CI	P VALUE
W	TI	-1.21	-4.03 to 1.69	0.407
	TII	-1.59	-3.75 to 0.62	0.157
WV	TI	-4.48	-12.04 to 3.74	0.274
	TII	0.06	-6.08 to 6.59	0.986
T	TI	-2.91	-10.66 to 5.51	0.483
	TII	-4.85	-10.73 to 1.43	0.126
TV	TI	-8.37	-18.12 to 2.54	0.126
	TII	-7.81	-15.43 to 0.50	0.065
Density	TI	-58.28	-72.04 to -37.75	<0.0001
	TII	-40.41	-56.16 to -18.99	0.001

Table 6.8 lists the effect size, 95% CI, and P value for each index measured on TI and TII diabetics compared to baseline - normal data. Shaded areas indicate those indices which are statistically significantly different from baseline ($P < 0.05$).

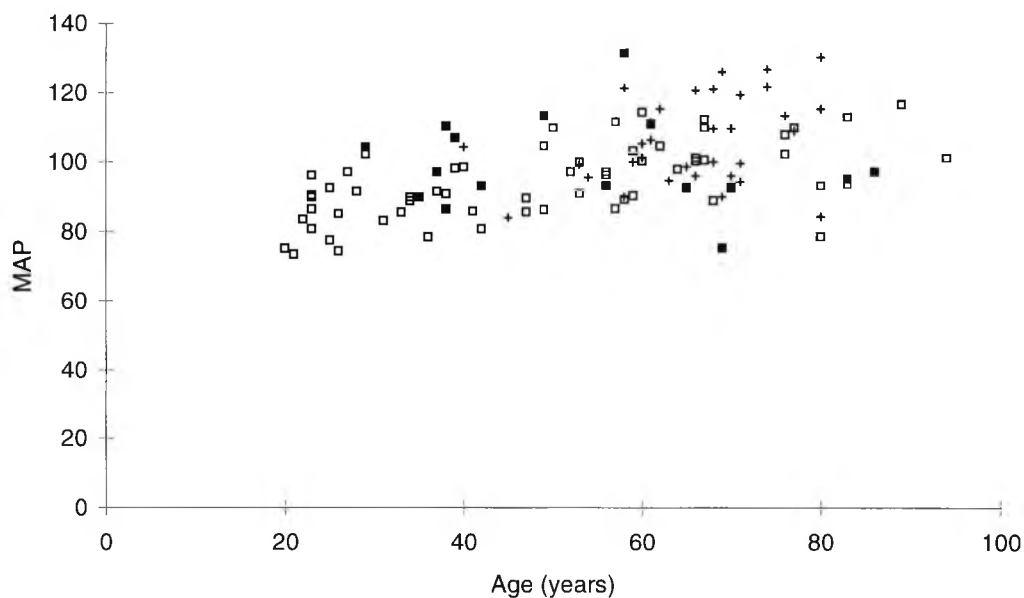


Figure 6.3 shows a scatter plot of age against MAP where open squares represent normals, closed squares TI diabetics, and crossed symbols TII diabetics.

None of the vessel indices appeared to show any statistically significant variation between the four age groups ($P > 0.2$ in all cases), and certainly there was no evidence of any linear association with age for any index when the data was inspected graphically. Although, *Density* showed a marginal effect with age resulting in a -7.07% (-14.29 to 0.76%) decrease in *Density* per decade, this was not statistically significant ($P = 0.08$). No statistically significant variation between W, WV, T, and TV across the 4 MAP groups was found ($P > 0.2$ in all cases). However, as with vessels less than $25\mu\text{m}$ in diameter *Density* demonstrated a decline as the MAP group increased. As there was no significant departure from linearity, MAP was entered into

the model as a continuous variable and on average *Density* declined by -17.13% (-25.77 to -7.42%, $P=0.001$) per 10mmHg rise in MAP. Graphically, raw data is plotted in figure 6.4 and natural log *Density* versus MAP in figure 6.5, along with the fitted regression line.

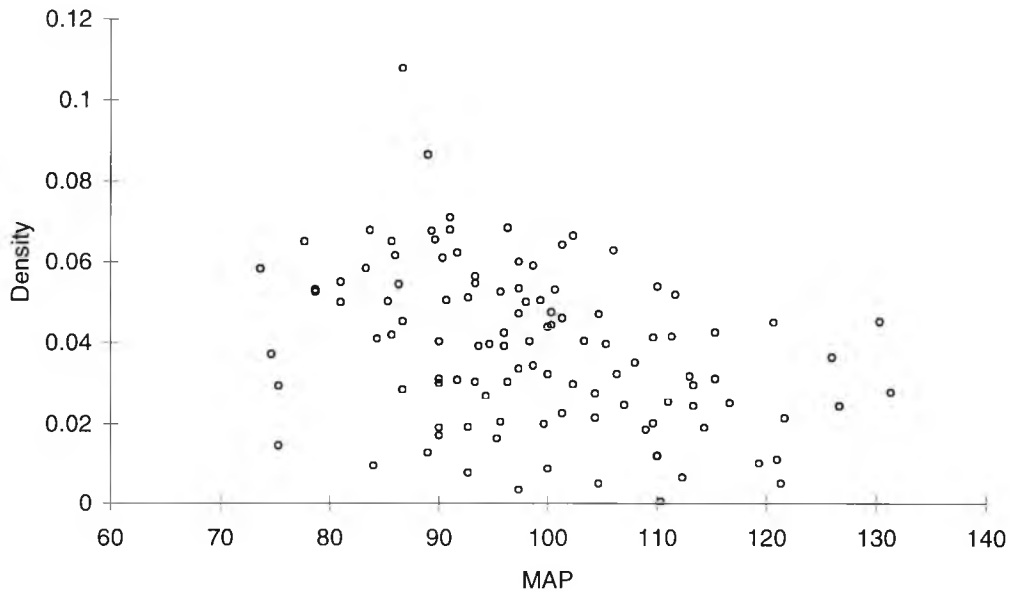


Figure 6.4 shows a scatter plot of MAP against *Density* for vessels 25 μm to <40 μm in diameter.

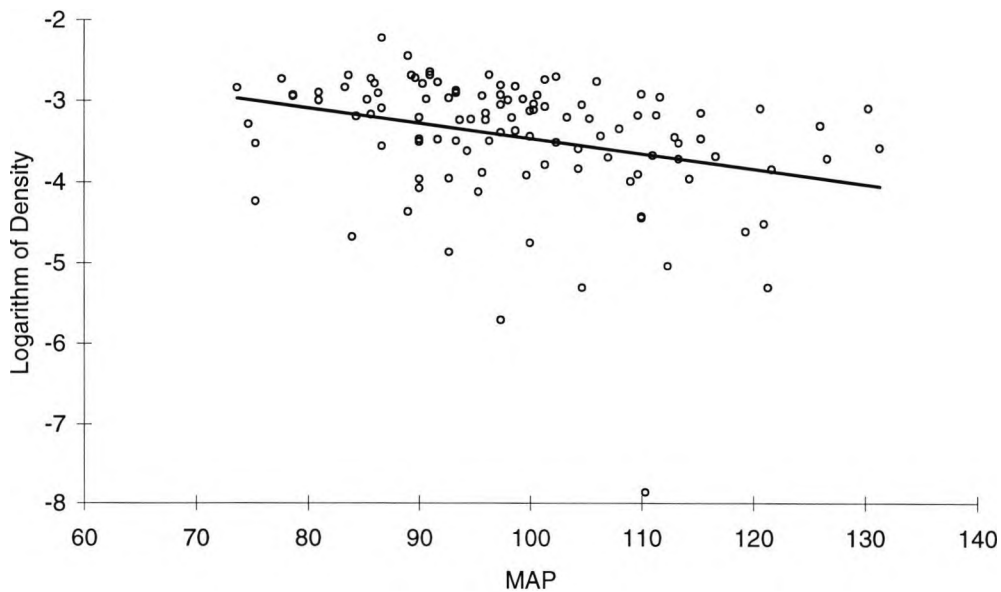


Figure 6.5 shows a scatter plot of MAP against the natural logarithm of *Density* for vessels 25 μm to <40 μm in diameter. The linear regression line shows decreasing density with increasing MAP.

6.5.1.4 Multivariate analysis of data from vessels 25 μ m to < 40 μ m in diameter

Cautious interpretation of the univariate model needs to be exercised when such correlations exist. Hence, a multivariate model including MAP and diagnosis group was fitted to investigate the relationship further between these parameters and vascular density. The effect of TI on *Density*, adjusting for the effect of MAP, was a reduction of -55.31% (-69.55 to -34.42%), thus although the reduction associated with TI is not as marked as the univariate analysis it still constitutes a considerable reduction in vascular density ($P < 0.0001$). The effect of TII on *Density*, adjusting for MAP, was less dramatic, with a reduction of -25.87% (-47.02 to 3.73%), however, this did not reach statistical significance ($P = 0.080$). Effect of MAP on *Density*, adjusting for the effects of diagnosis code, was a reduction of -13.18% (-23.40 to -1.59%, $P = 0.027$) per 10mmHg rise in MAP.

6.5.1.5 Univariate analysis of data from vessels 40 μ m to < 80 μ m in diameter

Table 6.9 summarises the effect sizes and univariate analysis performed, where shaded areas represent statistically significant ($P < 0.05$) effects for vessels 40 μ m to less than 80 μ m in diameter.

VESSEL INDEX	DIABETIC TYPE	% CHANGE FROM NORMAL DATA	95% CI	P VALUE
W	TI	4.62	1.12 to 8.24	0.010
	TII	3.59	0.92 to 6.33	0.009
WV	TI	-3.04	-10.05 to 4.51	0.416
	TII	-3.88	-9.25 to 1.82	0.176
T	TI	-7.03	-11.53 to -2.29	0.004
	TII	-5.34	-8.88 to -1.66	0.005
TV	TI	-15.95	-24.73 to -6.15	0.002
	TII	-11.63	-18.80 to -3.83	0.005
Density	TI	-11.37	-24.95 to 4.68	0.154
	TII	-10.80	-21.49 to 1.35	0.079

Table 6.9 lists the effect size, 95% CI, and P value for each index measured on TI and TII diabetics compared to baseline - normal data. Shaded areas indicate those indices which are statistically significantly different from baseline ($P < 0.05$).

There was no evidence of a statistically significant change in WV between diabetic and normal populations. Although a similar decrease in *Density* was found to smaller vessel groups, this was not statistically significant, neither for the TI or TII group. However, W appeared to increase slightly in both the TI ($P = 0.010$) and TII ($P = 0.009$) diabetic groups compared to the normal sample, with a 4.62% (1.12 to 8.24%) and 3.59% (0.92 to 6.33%) increase respectively. Conversely, T and TV appeared to decrease in the diabetic sample compared to normals. T decreased by -7.03% (-11.53 to -2.29%, $P = 0.004$) in the TI diabetic group, and by -5.34% (-8.88 to -1.66%, $P = 0.005$) in the TII group compared to normal values. TV decreased by -15.95% (-24.73 to -6.15%, $P = 0.002$) in the TI diabetic group, and by -11.63% (-18.80 to -3.83%, $P = 0.005$) in the TII group compared to normal values.

Table 6.10 list the percentage difference in each index per 10mmHg rise in MAP. For all cases, with respect to MAP, no significant departure from linearity was found.

Unlike the findings with smaller vessel groups a statistically significant variation between *W*, *T*, *TV* and MAP was found ($P < 0.0001$, $P = 0.034$, $P = 0.017$ respectively). *W* showed a 1.68% (0.78 to 2.58%) increase per 10mmHg rise in MAP, *T* a -1.51% (-2.89 to -0.12%) decrease per 10mmHg increase in MAP, and *TV* a -3.69% (-6.60 to -0.68%) decrease per 10mmHg increase in MAP. Evidently these effect sizes are very small. Contrary to findings with smaller vessel groups there was no evidence of any statistically significant association between *Density* and increasing MAP in this group of blood vessels.

VESSEL INDEX	% CHANGE IN INDEX / 10MMHG RISE IN MAP	95% CI	P VALUE
<i>W</i>	1.68	0.78 to 2.58	<0.0001
<i>WV</i>	0.90	-1.15 to 2.99	0.389
<i>T</i>	-1.51	-2.89 to -0.12	0.034
<i>TV</i>	-3.69	-6.60 to -0.68	0.017
<i>Density</i>	-1.43	-5.84 to 3.19	0.535

Table 6.10 list the percentage drop in each index per 10mmHg rise in MAP. Shaded areas indicate those indices which show statistically significantly change with increasing MAP ($P < 0.05$).

6.5.1.6 Multivariate analysis of data from vessels 40 μ m to < 80 μ m in diameter

As MAP and diagnosis code demonstrated significant associations with *W*, *T* and *TV* a multivariate model was fitted for these indices. The effect of diagnosis adjusted for MAP, and the effect of MAP adjusted for diagnosis for these indices is given in table 6.11.

VESSEL INDEX	EFFECT	% CHANGE FROM NORMAL	95% CI	P VALUE
<i>W</i>	TI	3.88	0.59 to 7.28	0.021
	TII	1.37	-1.37 to -4.19	0.327
<i>T</i>	TI	-6.64	-11.22 to -1.83	0.008
	TII	-4.40	-8.41 to -0.21	0.040
<i>TV</i>	TI	-14.94	-23.76 to -5.10	0.004
	TII	-8.10	-16.29 to 0.89	0.076

VESSEL INDEX	% CHANGE PER 10MMHG CHANGE IN MAP	95% CI	P VALUE
<i>W</i>	1.45	0.48 to 2.44	0.004
<i>T</i>	-0.83	-2.31 to 0.67	0.275
<i>TV</i>	-2.41	-5.56 to 0.84	0.143

Table 6.11 summarises the multivariate analysis of the effects of diabetes, and MAP on indices *W*, *T*, and *TV* for vessels 40 μ m to <80 μ m in diameter.

Although the average percentage differences in diabetics compared with normals were statistically significant in the cases highlighted it can be seen from table 6.11 that the effect sizes are small. However, *TV* showed a ~15% (-23.76 to -5.10%) reduction in TI diabetics compared to normals.

6.5.1.7 Univariate analysis of pooled data from all vessels

Table 6.12 summarises the effect sizes and univariate analysis performed, where shaded areas represent statistically significant ($P<0.05$) effects for all vessels.

VESSEL INDEX	DIABETIC TYPE	% CHANGE FROM NORMAL DATA	95% CI	P VALUE
<i>W</i>	TI	12.25	5.80 to 19.09	<0.0001
	TII	8.04	3.25 to 13.06	<0.0001
<i>WV</i>	TI	-2.67	-8.28 to 3.27	0.367
	TII	-3.53	-7.82 to 0.97	0.121
<i>T</i>	TI	-8.56	-13.61 to -3.21	0.002
	TII	-6.55	-10.71 to -2.38	0.003
<i>TV</i>	TI	-18.64	-27.91 to -8.18	0.001
	TII	-13.12	-20.82 to -4.67	0.003
<i>Density</i>	TI	-25.20	-35.21 to -13.63	<0.0001
	TII	-20.56	-28.85 to -11.29	<0.0001

Table 6.12 lists the effect size, 95% CI, and P value for each index measured on TI and TII diabetics compared to baseline - normal data. Shaded areas indicate those indices which are statistically significantly different from baseline ($P<0.05$)

Diagnosis code

Evidently more statistically significant changes were observed when the vessel data was taken as a whole. *WV* was the only index which did not show any statistically significant differences between normal values and diabetics. *W* was the only index to show a statistically significant increase compared with normal values, with a 12.25% increase (5.80 to 19.09%, $P<0.0001$) in TI, and an 8% (3.25 to 13.06%, $P<0.0001$) increase in TII diabetics. Indices *T*, *TV*, and *Density* all showed a statistically significant decrease in diabetics compared to normal values. Most of these differences were small, however, the most dramatic of these was for vascular density where TI diabetics showed a 25.20% (35.21 to 13.63%, $P<0.0001$) decrease, and TII a 20.56% (28.85 to 11.29%, $P<0.0001$) decrease compared to normal values. Note that this effect was probably manifested from the reduction in vascular density observed in smaller vessels ($<40\mu\text{m}$ in diameter).

Age

W, *WV*, *T* and *TV* did not show any significant variation with age group. However, density demonstrated an increase with age which appeared to be linear. On average density increased by only 1.26% per decade (0.07 to 2.46%, $P=0.037$), this effect was very small and of borderline significance and in this context is probably not an important factor.

MAP

The effect size in each index associated with a 10mmHg increase in MAP are listed in table 6.13. For all cases, with respect to MAP, no significant departure from linearity was found.

A statistically significant linear association between *W*, *T*, *TV*, *Density* and MAP groups was found ($P<0.0001$, $P=0.028$, $P=0.025$, and $P=0.009$ respectively). *W*

showed a 3.10% (1.44 to 4.78%) increase per 10mmHg rise in MAP, *T* a 1.76% (3.30 to 0.19%) decrease per 10mmHg increase in MAP, and *TV* a 3.79% (6.97 to 0.50%) decrease per 10mmHg increase in MAP. Evidently these effect sizes were very small. The largest difference was found with *Density* where a -5.42% (-9.25 to -1.43%) decrease was found per 10mmHg rise in MAP.

VESSEL INDEX	% CHANGE IN INDEX / 10MMHG RISE IN MAP	95% CI	P VALUE
<i>W</i>	3.10	1.44 to 4.78	<0.0001
<i>WV</i>	0.63	-0.10 to 2.27	0.440
<i>T</i>	-1.76	-3.30 to -0.19	0.028
<i>TV</i>	-3.79	-6.97 to -0.50	0.025
<i>Density</i>	-5.42	-9.25 to -1.43	0.009

Table 6.13 list the percentage drop in each index per 10mmHg rise in MAP. Shaded areas indicate those indices which show statistically significantly change with increasing MAP ($P < 0.05$)

6.5.1.8 Multivariate analysis of data from all vessels

As diagnosis code and MAP both demonstrated a statistically significant association with *W*, *T*, *TV* and *Density*, a model containing both MAP and diagnosis code was fitted for these indices. The effect of diagnosis adjusted for MAP, and the effect of MAP adjusted for diagnosis for these indices is given in table 6.14.

VESSEL INDEX	EFFECT	% CHANGE FROM NORMAL	95% CI	P VALUE
<i>W</i>	TI	10.98	4.86 to 17.46	<0.0001
	TII	4.77	-0.18 to 9.96	0.059
<i>T</i>	TI	-8.16	-13.16 to -2.87	0.003
	TII	-5.56	-9.96 to -0.95	0.019
<i>TV</i>	TI	-17.75	-26.95 to -7.39	0.001
	TII	-9.98	-18.64 to -0.40	0.042
<i>Density</i>	TI	-24.13	-34.19 to -12.52	<0.0001
	TII	-15.88	-25.50 to -5.03	0.006

VESSEL INDEX	% CHANGE PER 10MMHG CHANGE IN MAP	95% CI	P VALUE
<i>W</i>	2.35	0.62 to 4.10	0.008
<i>T</i>	-0.89	-2.54 to 0.79	0.293
<i>TV</i>	-2.20	-5.62 to 1.34	0.217
<i>Density</i>	-2.86	-6.92 to 1.37	0.180

Table 6.14 summarises the multivariate analysis of the effects of diabetes, and MAP on indices *W*, *T*, *TV*, and *Density* for all vessels.

It is interesting to observe that when all vessel are analysed the effect of MAP, adjusted for diagnosis code, in all cases in table 6.14 is relatively small and only statistically significant for *W*. However, the effect sizes associated with type of diabetes, adjusted for MAP, compared to normals are comparatively greater, and

significant in all cases, except for TII diabetics who do not appear to show a statistically significant difference from normals for mean vessel width ($P=0.059$). *T*, *TV* and *Density* are reduced in TI and TII, but *W* is increased in both cases when compared to normals. The effect of type of diabetes on *Density* was of greatest magnitude and statistical significance.

Retinopathy, duration of diabetes and medication

No statistically significant association between grade of retinopathy and any index was found for the vessels as a whole or any sub category of vessels ($P>0.2$ in all cases). Neither was there an association between the duration of diabetes and any vessel index for the vessels as a whole and for any sub category of vessels ($P>0.2$ in all cases). The same was true of type of medication.

6.6 Discussion

A number of statistically significant differences between the diabetic and normal populations were found. However, statistical significance does not necessarily indicate clinical significance. Interpretation of the 95% CI is needed before conclusions can be made. Hence, this discussion will consider effects which show large differences between normal and diabetic values.

Unlike other methods the approach used in this current study enabled populations of vessels, classified on the basis of diameter, to be analysed. Where vessels $<25\mu\text{m}$ represent capillaries, $25\mu\text{m}$ to $40\mu\text{m}$ venules, $40\mu\text{m}$ to $<80\mu\text{m}$ arterioles and venules. In addition the vessels were considered as a whole to formulate a general pattern of vascular changes associated with diabetes. Each of these populations will be considered in turn.

6.6.1 Tortuosity changes

As shown in table 6.7 capillaries of TI diabetics appeared to show a 16.04% (0.28 to 34.7%, $P=0.046$) increase in tortuosity compared to normal values. However, the tortuosity of TII diabetic capillaries were similar to normal values. The presence of increased tortuosity in TI diabetics as opposed to TII could be explained by duration of the disease, however, no statistically significant association between tortuosity and duration was found. On average the duration of TI diabetes was 28.76 ± 15.19 years compared with only 9.14 ± 6.89 years for TII. These findings agree with the anecdotal observations of Ditzel and Saglid (1954) who reported increased tortuosity and angularities in diabetic conjunctival vessels and might be explained by vascular endothelial compromise. Although capillaries showed increased tortuosity in diabetic patients, this was not the case for vessels $25\mu\text{m}$ to less than $40\mu\text{m}$ in diameter. However, the arterial and venule population of vessels ($40\mu\text{m}$ to less than $80\mu\text{m}$ in diameter) showed a slight decrease of -6.64% (-11.22 to -1.83%, $P=0.008$) in tortuosity for TI diabetics and a -4.40% (-8.41 to -0.21%, $P=0.040$) decrease in TII diabetics, compared to normals. This phenomenon of vascular straightening in larger vessels has not previously been reported and its aetiology may be related to the reduction in microvascular density, and hence resembles the tortuosity of larger vessels in the group. It is also of interest that the variance in tortuosity of this population of vessels also decreased in both the TI and TII diabetics by -14.94% (-23.76 to -5.10%, $P=0.004$) and -8.10% (-16.29 to 0.89%, $P=0.076$) respectively, however, the decrease in TII diabetics was of borderline statistical significance.

Evidently, the effect of increased tortuosity with diabetes is specific to the smaller population of vessels. This effect is disguised when considering the vessels as a whole where tortuosity and tortuosity variance are reduced by -8.16% (-13.61 to -2.87%, $P=0.003$) and -17.75% (-26.95 to -7.39%, $P=0.001$) respectively in TI diabetics, and -5.56% (-9.96 to -0.95%, $P=0.019$) and -9.98% (-18.64 to -0.40%, $P=0.042$) in TII, compared to normal values. Note that these figures are adjusted for the effects of MAP. These tortuosity findings may cause confusion when vessels are studied as a whole.

6.6.2 Effects of diabetes on vessel width and vascular density

Diabetic vessels are known to form irregularities in calibre due to basement membrane thickening, pericyte loss, and endothelial changes leading to the formation of microaneurysms and focal calibre changes. However, the variance in width for capillaries (WV) decreased by -21.01% (-31.07 to -9.50%, $P=0.001$) in TI diabetics and -11.23% (-20.03 to -1.46%, $P=0.026$) in TII diabetics compared to normal values. Such findings could be explained by the large reduction in capillary density of -57.12% (-71.96 to -36.76%, $P<0.0001$) in TI diabetics and the borderline -17.5% (-41.71 to 16.64%, $P=0.273$) reduction in capillary density for TII, compared to normal values (figures adjusted for the effects of MAP). Thus, the diversity of vessel sizes within this width category could be largely reduced in the diabetic population. This marked reduction in capillary density agrees with the accepted findings of microvascular drop-out associated with nephropathy, neuropathy, and retinopathy and is in agreement with conjunctival capillary narrowing observed by Landau and Davis (1960). Worthen *et al* (1981) also observed a -25% decrease in vessel area for vessels less than 20 μm in diameter. A dramatic decrease in venular density (vessels 25 to less than 40 μm in diameter) of -55.31% (-69.55 to -34.42, $P<0.0001$, adjusted for the effect of MAP) in TI diabetics compared to normals was also found. The effect of TII diabetes on venular density was a reduction of -25.87% (-47.02 to 3.73%) compared to normal data (adjusted for the effects of MAP), however, this was not statistically significant ($P=0.080$). It is noteworthy that the density of larger vessels (40 μm to less than 80 μm in diameter) was unaffected by diabetes indicating that diabetes is a microangiopathic disorder. In general, considering the vessel as a whole, there was a ~25% decrease in vascular density in TI diabetics ($P<0.0001$), and ~16% decrease in density in TII diabetics ($P=0.006$) compared to normal values which agrees well with the figure published by Worthen *et al* (1981). These figures are adjusted for the effects of MAP. This effect may explain the 10.98% (4.86 to 17.46%, $P<0.0001$) increase in the mean width for all vessels in TI diabetics compared to normals as it is the microvasculature which is lost.

6.6.3 Effects of blood pressure on vascular density

The presence of hypertension in conjunction with diabetes can confound angiopathic findings. Kaup *et al* (1991) demonstrated decreased retinal vessel width and increased tortuosity in hypertensive patients. Macular blood flow studies performed by Wolf *et al* (1994) found perifoveal capillary drop-out, which led them to believe that hypertension could cause a global capillary loss. A brief abstract by Chen *et al* (1986) found a 10% loss in vascularity associated with hypertension. Although our sample did not contain any individual diagnosed with hypertension a -13.82% (-23.71 to -2.65%, $P=0.017$) reduction in capillary density was observed per 10mmHg increase in

MAP (figure adjusted for the effects of diabetes). A similar association between vascular density and MAP was found in the venular population of vessels with a reduction of -13.18% (-23.40 to -1.59%, $P=0.027$) per 10mmHg rise in MAP. However, no association was found with the larger vessels. For all vessels a -2.86% (-6.92 to 1.37%, adjusted for the effects of diabetes) reduction in vascular density was observed per 10mmHg rise in MAP, however this was not statistically significant ($P=0.180$). Evidently the lack of vascular density changes in large vessels disguises the reduction seen in smaller vessel groups. Interestingly, the mean width of all vessels marginally increased by 2.35% (0.62 to 4.10%, $P=0.008$) per 10mmHg rise in MAP (figure adjusted for the effects of diabetes) indicating that the loss of density with increasing MAP may be at a capillary level making these findings more biased towards the macrovessel population. Such findings are worthy of further investigation on a hypertensive sample.

6.6.4 Effects of age on vascular density

It is noteworthy, that there was no statistically significant association between capillary, venular, or larger vessel density with age. However, when the vessels are treated as a whole a marginal 1.26% (0.07 to 2.46%, $P=0.037$) increase in vascular density per decade increment in age was found. This finding is in agreement with McMonnies and Ho (1991), who showed a small increase in hyperaemia with age. Photographic studies of conjunctival vasculature conducted by Kovalcheck *et al* (1984) also reported that arteriole, venule, and capillary surface area increased with the onset of years. However, both papers conclude that the angiopathic effect of age on the conjunctiva is not clinically significant and the same is true of the current study.

6.6.5 Effect of retinopathy and duration of diabetes on vessel indices

Dexel *et al* (1976) subjectively graded the conjunctiva and fundus of 60 diabetic patients and concluded that there was no association between diabetic retinopathy and conjunctival diabetic retinopathy. The findings of the current study support this view. However, it must be acknowledged that our diabetic sample was heavily biased towards those with no retinopathy or background retinopathy (BR) in both the TI and TII diabetic groups (as indicated in table 6.1). A future study should include a greater proportion of those with PPR and PR before this conclusion can be made. Also, there was no statistically significant association between the duration of diabetes and any vessel index, however, a sample with a longer duration of diabetes (especially TII) is needed before an association can be excluded.

6.6.6 Summary

Evidently, all the reported effects of diabetes on conjunctival vasculature are of greater statistical significance and magnitude for TI diabetes compared to TII. As indicated this is probably related to the three fold increase in duration of TI compared to TII within our sample. Conjunctival vascular density at the capillary level is sizeably affected by diabetes with a ~50% reduction in capillary density in TI diabetes and a near ~20% reduction in TII. The ability to discern such differences makes the conjunctiva a useful vascular bed to study the vasculogenesis and sequential changes associated with diabetic angiopathy. It is hoped that the findings of this study could be supported in a much larger population study.

CHAPTER 7

7. Conclusion, summary of results, and future work

7.1 Conclusion and summary of results

Chapter 3 derived the optimal method of imaging conjunctival vasculature. Images of optimal quality are needed to assist image segmentation of vascular structures. The virtues of digital imaging were superior to photographic methods. The concept of exposure density was used to achieve optimal images of bulbar conjunctival vessels using a digital sensor. From knowledge of the spectral sensitivities of the Kodak DCS 100 digital camera, radiant intensity distribution of the Nikon xenon light source, transmittance of the lens optics, and reflectance of oxygenated haemoglobin and conjunctiva, the exposure density of each target area was calculated. By introducing a database of filters the exposure density difference of the two target areas (blood and conjunctiva) was optimised. It was acknowledged that the measurement of the reflectance of conjunctiva and oxygenated haemoglobin was far from ideal, however, for the purposes of this investigation it was considered sufficient. Exposure density calculations predicted a 6.5 times increase in vessel contrast when recording on the green channel of the CCD camera with a Wratten 99 (green) filter over the illumination optics, compared to recording without a filter.

With knowledge of the optical transfer characteristics of the imaging system a vascular model was derived. This tubular model was fitted to densitometric profiles across a sample of 3 conjunctival blood vessels. This model adequately fitted the central portion of the blood vessel and gave the amplitude of the densitometric vessel profile. Images of the same vascular bed, taken through a Wratten 99 (green) filter, on the green sensor of the CCD array were associated with 11 to 29% superior contrast than the same vessel recorded on the green CCD alone, 46 to 65% improvement from those recorded on the combined CCD, and 21 to 48% improvement from those recorded on the combined CCD with a Wratten 99 over the illumination optics. Hence, the use of the DCS 100 digital camera, in association with green filtration, was the method of choice for vascular imaging of the conjunctiva and was used throughout this thesis.

Chapter 4 compared manual, semi-automated, and fully automated methods of establishing vessel width. One hundred and one vessel locations were taken from bulbar conjunctival images of 12 individuals. The widths at these locations using different approaches were calculated for 2 successive images and recorded as session 1 and 2. Manual methods involved the measurement of width from both digitally created and photographic projected images using electronic calibres. Semi-automated measures of width involved fitting Gaussian curves to the vessels densitometric profile, fitted by a least squares principal, and recording both the width at the Gaussian half height and maximum gradient on the curve. In addition cylindrical and tubular models were corrected for the effects of optical defocus, and fitted by a least squares method to the densitometric profile, in order to establish width. Automated measurement of width was done using an algorithm based on the work of Steger

(1996, 1998). The algorithm is fully automated and can be steered to run at different sigma's and thresholds. Correct σ selection is paramount, where unduly low sigma's will under estimate vessel width and large sigma's will over estimate. Hence, Steger's algorithm was applied to conjunctival vascular images, at a selection of sigma's, and vessel width determined at the referenced locations and compared to manual and semi-automated methods.

Manual determination of width, using electronic callipers from projected digitally created photographs were used as the gold standard on the basis of the best intra session repeatability and spread of measurement (95%CI +10.12 to -9.29 μ m, minimum value 14.4 to 140.0 μ m). An inter-method comparison of this method to the automated approach revealed that the algorithm run at $\sigma = 3$ gave the best agreement with the gold standard (MD 1.35 μ m, 95% CI +35.19 to -32.3248 μ m). However, a plot of the differences between methods against their mean revealed that the automated method, run at $\sigma = 3$, slightly overestimated small vessel widths, and underestimated large vessel widths. Hence, sigma's were selected to describe different widths. Sigma = 2 best agreed with widths manually measured as less the 40 μ m in diameter (MD -0.64 μ m, 95% CI +8.37 to -9.64 μ m), and $\sigma = 4$ with those greater than or equal to 40 μ m (MD +0.83 μ m, 95% CI +23.11 to -21.40 μ m). The intra session repeatabilities of these sigmas for their respective vessel populations was good with +5.49 to -6.24 μ m for $\sigma = 2$ and +12.55 to -12.83 μ m for $\sigma = 4$. This compares with the intra session repeatability of $\sigma = 3$ on all vessels of +9.41 to -8.48 μ m. Attempts were made to nurture the algorithm to concurrently measure at two different sigmas, however, this proved to be computationally expensive and was abandoned. Hence, the algorithm was run at $\sigma = 3$.

The use of an automated approach of vessel recognition results in a vast amount of data concerning vessel axis and vessel edge locations. Five indices were derived to describe the vascular bed, including mean vessel width, width variance, tortuosity, tortuosity variance and density. Tortuosity was expressed in units of curve energy in favour of chord to vessel length ratios as this was shown to be a superior method of determining vessel meandering. It is noteworthy that these indices are a novel way of describing a vascular complex. The successful application of these indices to a vascular bed was shown in chapter 4.

The inter session repeatabilities of these indices were derived in chapter 5, on a population of 31 normal patients recruited from the undergraduate, postgraduate, and academic staff of the City University. All indices showed good inter session repeatabilities. Although some appeared to have unduly high levels of repeatability these represented minor differences in relation to the magnitude of the actual measurement. The conjunctiva of 31 normal patients were imaged on 5 occasions throughout the day. Negligible diurnal variation in the indices was found. However, a statistically significant association between MAP and pooled vascular density was found ($P=0.047$), where a 2.7% (95% CI +0.04 to +5.4%) increase in vascular density was associated with a 10mmHg rise in MAP. This effect was found on a small sample size, with a limited MAP range, and hence had to be treated cautiously. However, this association was explored in more detail on a larger sample in chapter 6.

The angiopathic consequence of diabetes is well known in the retina (retinopathy), kidney (nephropathy), and nervous system (neuropathy). Its effects on the peripheral vascular system have been documented in the nail bed of the fingers and toes. However, its effects on conjunctival vasculature has never been adequately quantified. The purpose of chapter 6 was to establish whether the automated approach was capable of discerning between a diabetic and normal conjunctival bed.

Seventeen TI diabetics and 36 TII diabetics were recruited from those attending clinics at a hospital eye department (Sussex Eye Hospital) and from those attending the City University Eye Clinic for routine examination. Sixty normal patients were recruited from the academic staff, postgraduates and undergraduates at the City University and from staff of a hospital eye clinic (Sussex Eye Hospital) and relatives of attending patients.

Although several of the indices measured showed a difference between normals and diabetics for all vessels and sub-categories of vessels, by far the most remarkable was the dramatic change in density at a capillary level (vessels less than 25 μ m in diameter). A -57.12% (-71.96 to -36.76%, $P < 0.0001$) reduction in capillary density was found in TI diabetics compared to normals and a reduction of -17.5% (-41.71 to 16.64%) in TII diabetics compared to normals, however this was not statistically significant ($P = 0.273$). A similar decrease was found in venular density (vessels 25 to <40 μ m in diameter), with a decrease of -55.31% (-69.55 to -34.42, $P < 0.0001$) in TI diabetics compared to normals, and a reduction of -25.87% (-47.02 to 3.73%) in TII diabetics compared to normals, although this was of borderline statistical significance ($P = 0.080$). It is noteworthy that macrovasculature density (vessels 40 to <80 μ m in diameter) was not affected by diabetes. Hence, diabetes principally exerts its effect on the microvasculature of the conjunctival bed.

Another aspect worthy of mention was the association between MAP and vascular density. Although our sample did not contain any individual diagnosed with hypertension a -13.82% (-23.71 to -2.65%, $P = 0.017$) reduction in capillary density (vessels less than 25 μ m in diameter) was observed per 10mmHg increase in MAP, and a reduction of -13.18% (-23.71 to -2.65%, $P = 0.027$) in venular density (vessels 25 to less than 40 μ m in diameter). However, no association between MAP and larger vessel density was found. Considering vessels as a whole the effect was less marked with a reduction of -2.86% (-6.92 to 1.37%), but this was not statistically significant ($P = 0.180$). Evidently, raised MAP exerts an effect on smaller vessels.

The use of an automated measure of quantifying the conjunctival vessel network revealed differences between these normal and diseased peripheral vascular beds.

7.2 Future work

The application of this work is myriad when there are so many conditions causing angiopathic change in the conjunctiva. It would enable the vascular events of certain diseases to be ascertained, and the effect of certain treatment regimes to be monitored. It may also help in the understanding of the vasculogenesis of certain disorders. The current study was conducted with a small number of patients and it is hoped that the findings would be supported in a larger population study.

Although the implementation of the automated program, run at $\sigma = 3$ revealed significant results it was acknowledged that this might overestimate small vessel widths and underestimate larger vessels. Hence, further nurturing of the algorithm to use specific sigma's for vessels of different sizes is needed.

The recent conclusions of the United Kingdom Prospective Diabetic Study (UKPDS) confirmed that hyperglycaemia plays an important role in the development of diabetic retinopathy and its progression (UKPDS 33, 1998). Although glycaemic control is imperative to alleviate diabetic complications increasingly the benefits of concurrently treating hypertension is emerging. The UKPDS (UKPDS 38, 1998) conducted a multicentre randomised controlled trial of diabetics with tightly controlled (blood pressure <150/85mmHg), versus less tightly controlled blood pressure (<180/105mmHg). A 32% (95% CI from 6% to 51%, $P=0.019$) reduction in diabetic related deaths, a 44% (11% to 65%, $P=0.013$) reduction in strokes, and a 37% (11% to 56%, $P=0.0092$) reduction in macrovascular disease was observed in the tightly controlled blood pressure group ($n=758$) compared to the less tightly controlled group ($n=390$). In addition after 9 years of follow up the tightly controlled group had a 34% (99% CI from 11% to 50%, $P=0.0004$) reduction in the proportion of patients with deterioration of retinopathy by two steps and a 47% (99% CI from 7% to 70%, $P=0.004$) reduced risk of deterioration in visual acuity by three lines of the early treatment of diabetic retinopathy study chart, compared to the less tightly controlled group.

The finding of a loss in conjunctival vascular density offers yet another index to show the microvascular complications associated with diabetes. The loss of conjunctival microvascular density with elevated MAP shows that both diabetes and blood pressure exert an effect on this vascular bed. This suggests that in addition to a diabetics hyperglycaemic status, blood pressure also needs to be taken into consideration. An obvious extension of this work would be to use the vessel algorithm to quantify the retinal circulation in a large sample of hypertensive and diabetic patients to determine any association between these conditions. However, unlike the conjunctiva, the magnification effects of the eye must be taken into consideration to ensure that the real size of the retinal vasculature is measured. Also, images of retinal vessels often present with a bright central reflex which would mean modification of the present vessel detection algorithm. Such difficulties could be easily overcome and it is hoped that this will form the subject of future study.

The application of digital imaging and optimal filtering of conjunctival vascular structures has shown accurate measurement over a large proportion of vessels. It has enabled differences between normal and diseased peripheral vascular beds to be found that would have otherwise been laborious by manual methods.

APPENDICES

Appendix A.1

The following figures are supplementary results from chapter 5 and show graphical representations for all indices against age for each visit separately.

For vessels $<25\mu\text{m}$ in diameter

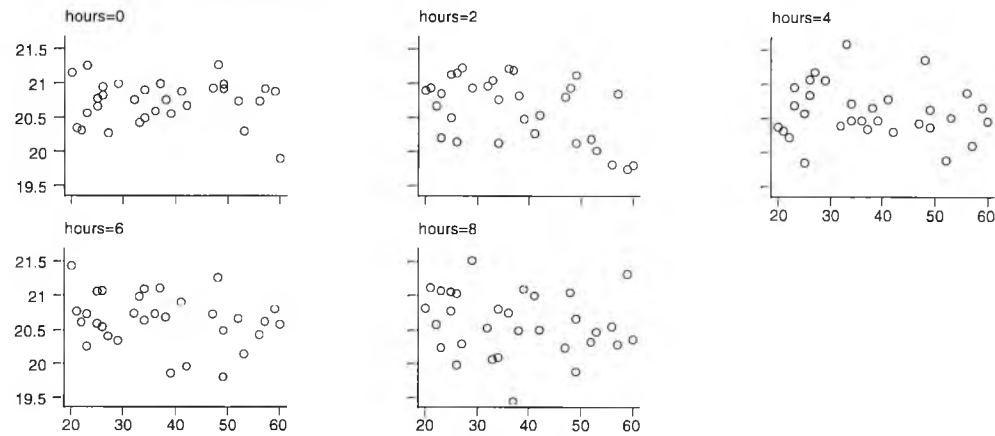


Figure A1.1. W plotted against age at 0, 2, 4, 6 and 8 hours for vessels $<25\mu\text{m}$ in diameter, where W is in microns and age in years

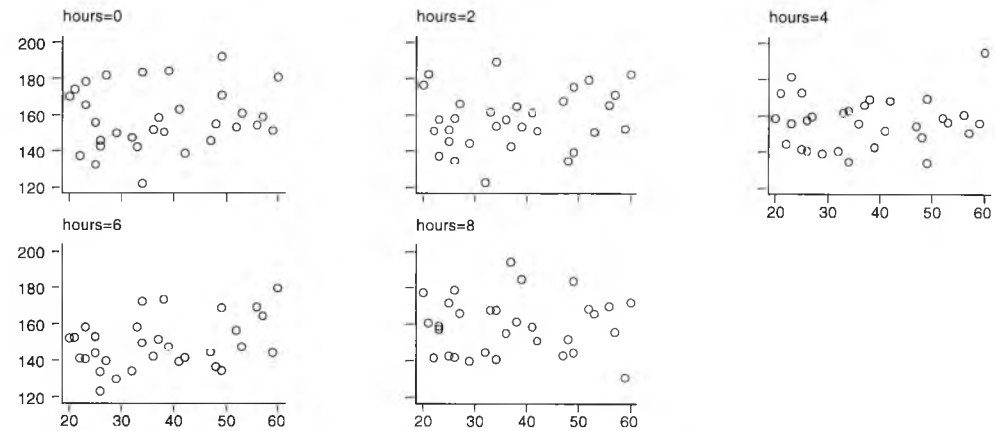


Figure A1.2. WV plotted against age at 0, 2, 4, 6 and 8 hours for vessels $<25\mu\text{m}$ in diameter, where WV is in μm^2 and age in years

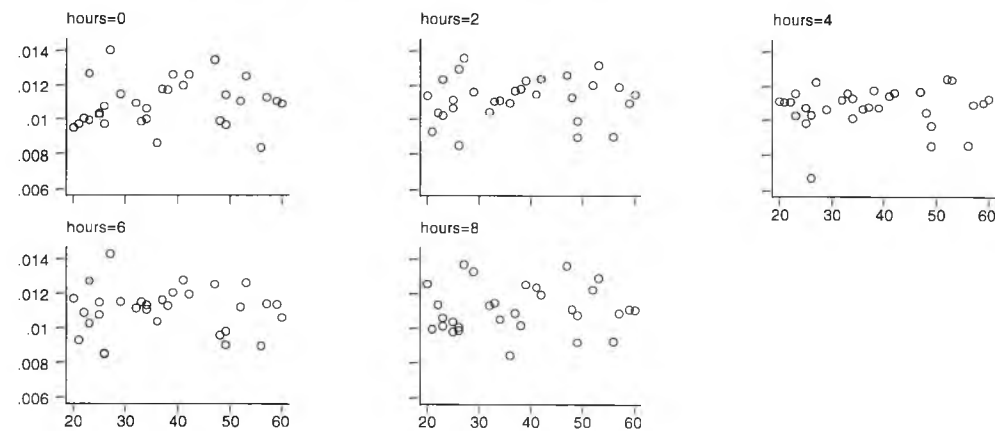


Figure A1.3. T plotted against age at 0, 2, 4, 6 and 8 hours for vessels $<25\mu\text{m}$ in diameter, where T is in units of curve energy and age in years

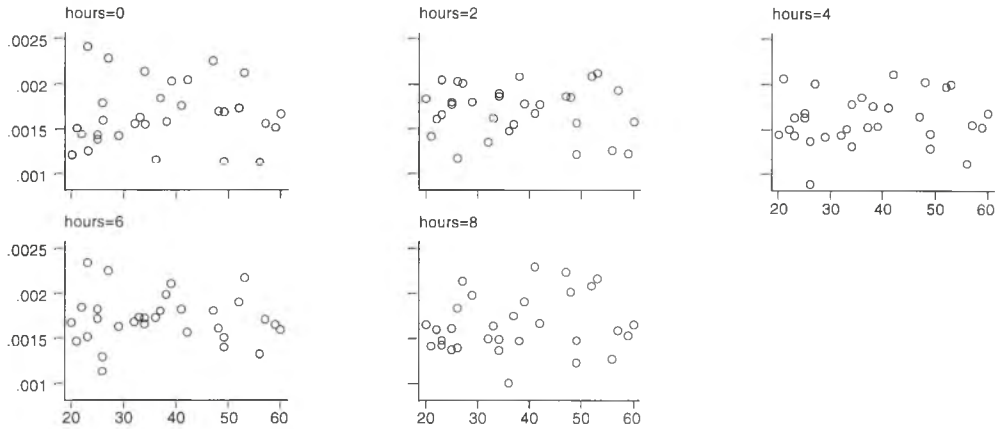


Figure A1.4. TV plotted against age at 0, 2, 4, 6 and 8 hours for vessels $<25\mu\text{m}$ in diameter, where TV is in units of curve energy² and age in years

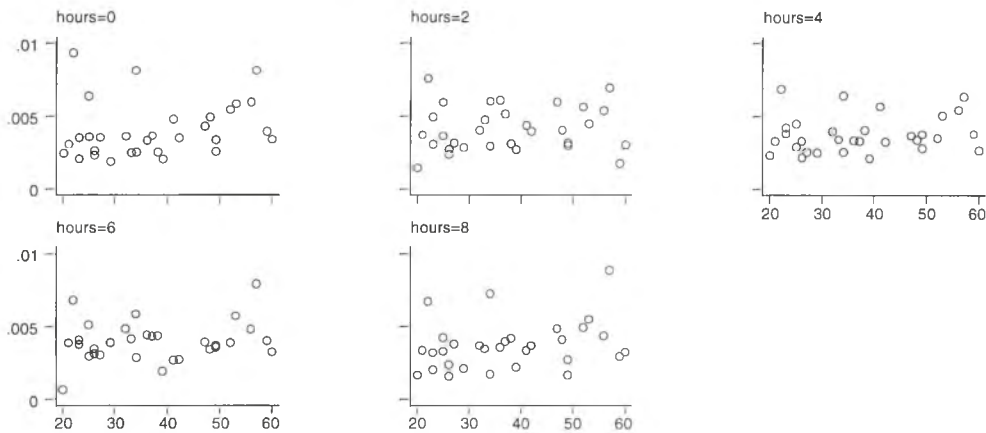


Figure A1.5. Density plotted against age at 0, 2, 4, 6 and 8 hours for vessels $<25\mu\text{m}$ in diameter, where Density is in mm^2 of vessel per mm^2 of conjunctiva and age in years

For vessels $25\mu\text{m}$ to $<40\mu\text{m}$ in diameter

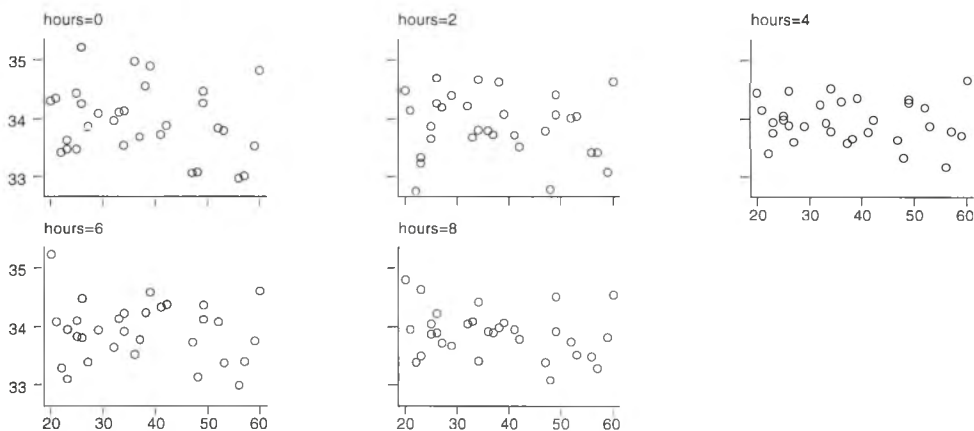


Figure A1.6. W plotted against age at 0, 2, 4, 6 and 8 hours for vessels $25\mu\text{m}$ to $40\mu\text{m}$ in diameter, where W is in microns and age in years

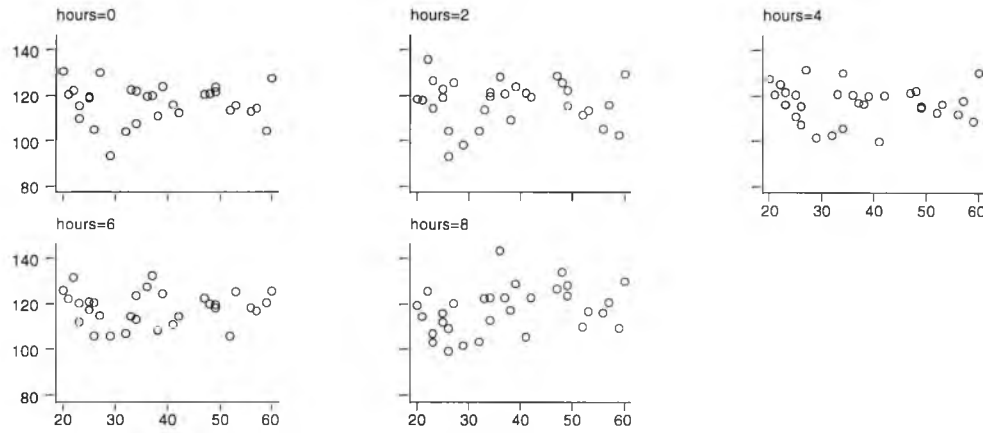


Figure A1.7. WV plotted against age at 0, 2, 4, 6 and 8 hours for vessels $25\mu\text{m}$ to $40\mu\text{m}$ in diameter, where WV is in μm^2 and age in years

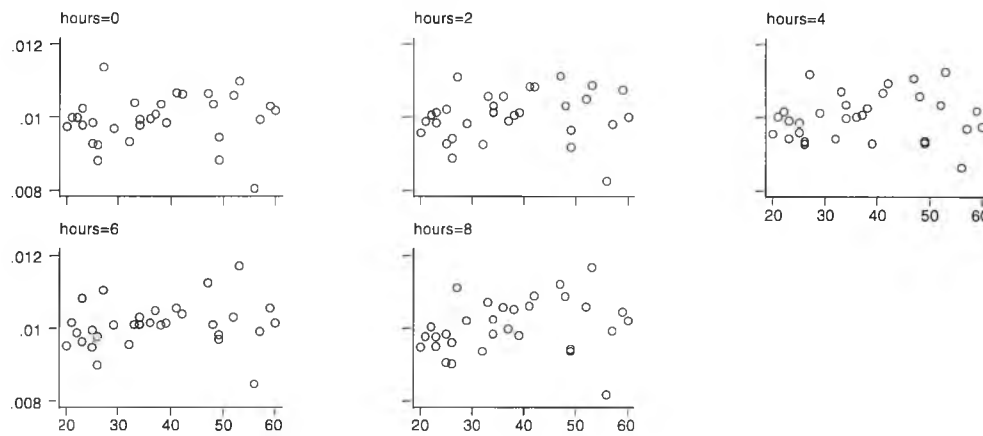


Figure A1.8. T plotted against age at 0, 2, 4, 6 and 8 hours for vessels $25\mu\text{m}$ to less than $40\mu\text{m}$ in diameter, where T is in units of curve energy and age in years

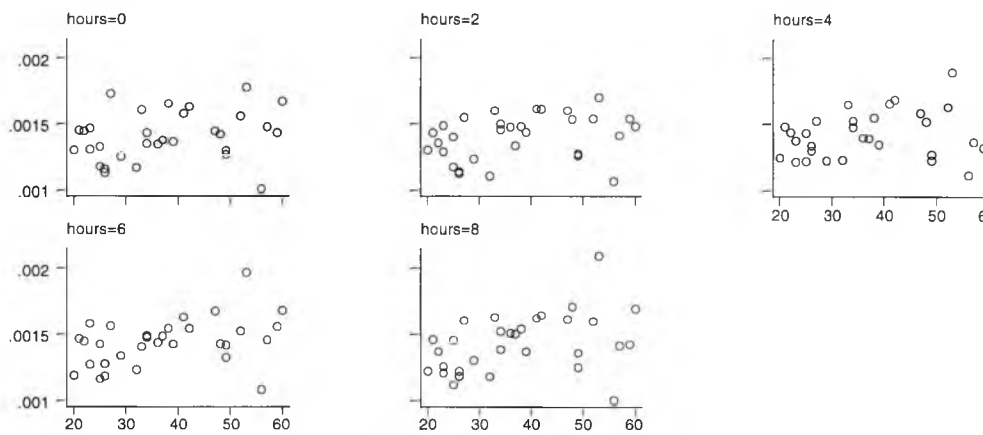


Figure A1.9. TV plotted against age at 0, 2, 4, 6 and 8 hours for vessels $25\mu\text{m}$ to $<40\mu\text{m}$ in diameter, where TV is in units of curve energy² and age in years

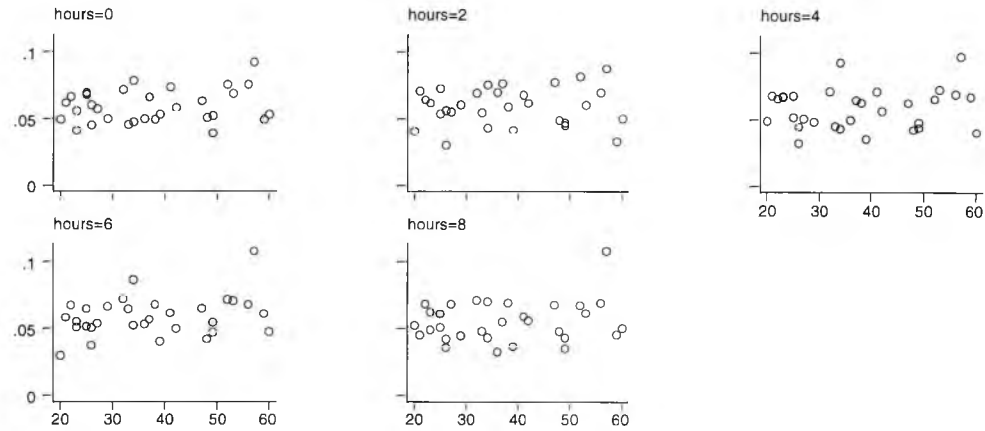


Figure A1.10. Density plotted against age at 0, 2, 4, 6 and 8 hours for vessels 25 μ m to 40 μ m in diameter, where Density is in mm² of vessel per mm² of conjunctiva and age in years

For vessels 40 μ m to <80 μ m in diameter

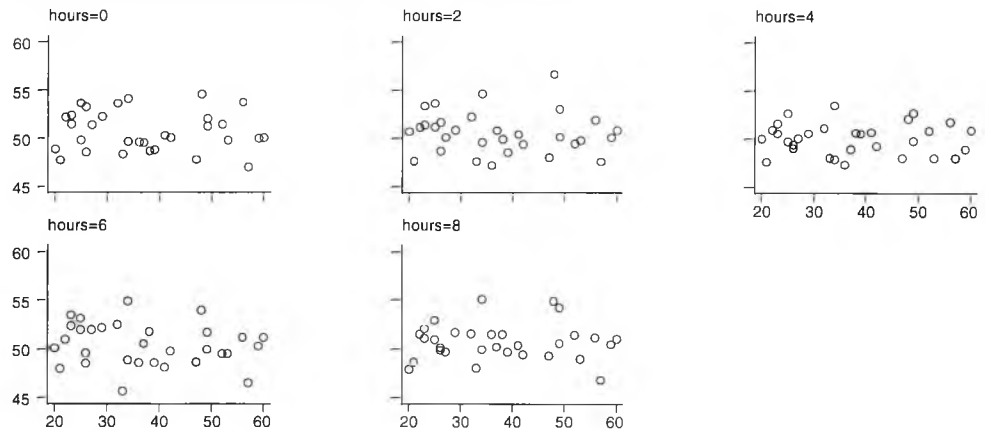


Figure A1.11. W plotted against age at 0, 2, 4, 6 and 8 hours for vessels 40 μ m to 80 μ m in diameter, where W is in microns and age in years

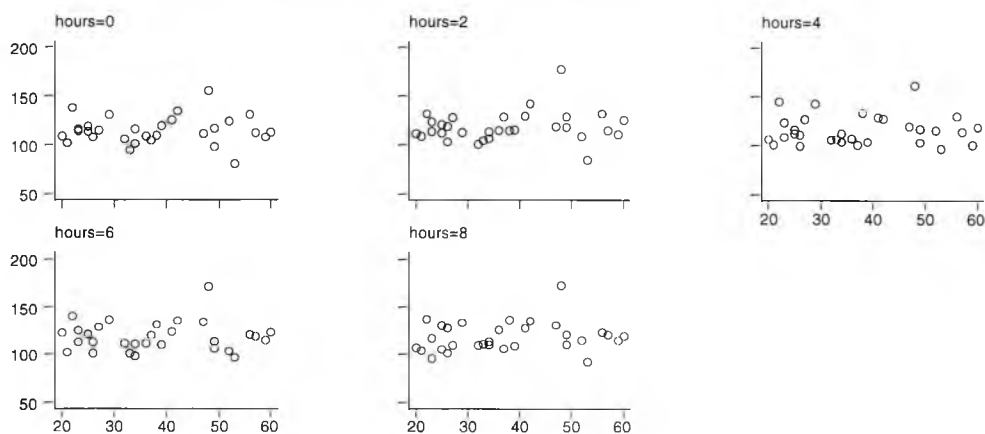


Figure A1.12. WV plotted against age at 0, 2, 4, 6 and 8 hours for vessels 40 μ m to 80 μ m in diameter, where WV is in microns² and age in years

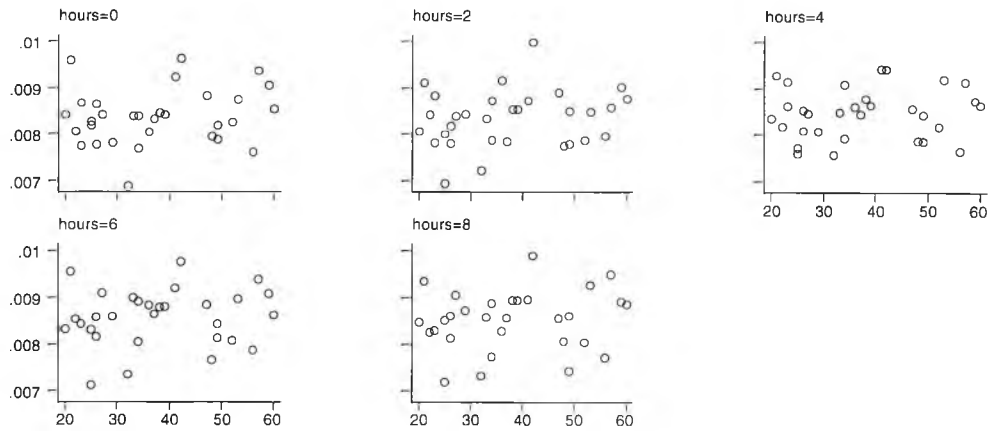


Figure A1.13. T plotted against age at 0, 2, 4, 6 and 8 hours for vessels $40\mu\text{m}$ to less than $80\mu\text{m}$ in diameter, where T is in units of curve energy and age in years

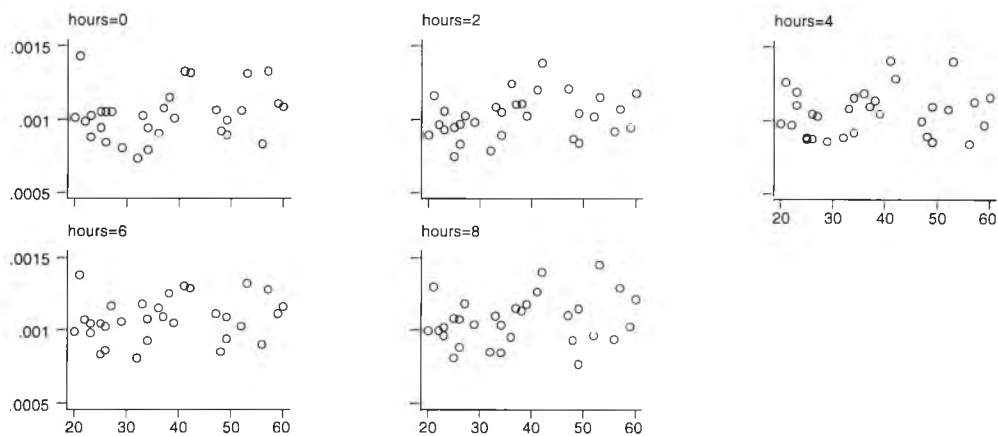


Figure A1.14. TV plotted against age at 0, 2, 4, 6 and 8 hours for vessels $40\mu\text{m}$ to $<80\mu\text{m}$ in diameter, where TV is in units of curve energy² and age in years

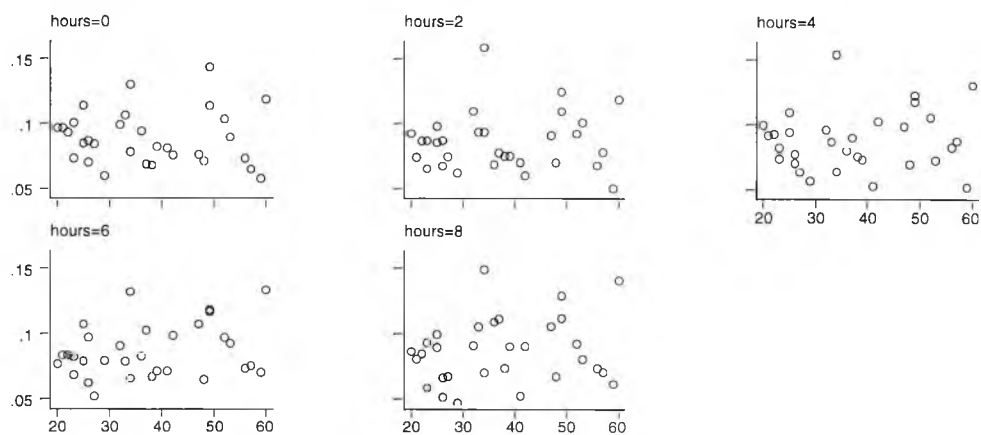


Figure A1.15. Density plotted against age at 0, 2, 4, 6 and 8 hours for vessels $40\mu\text{m}$ to $80\mu\text{m}$ in diameter, where Density is in mm^2 of vessel per mm^2 of conjunctiva and age in years

For all vessels

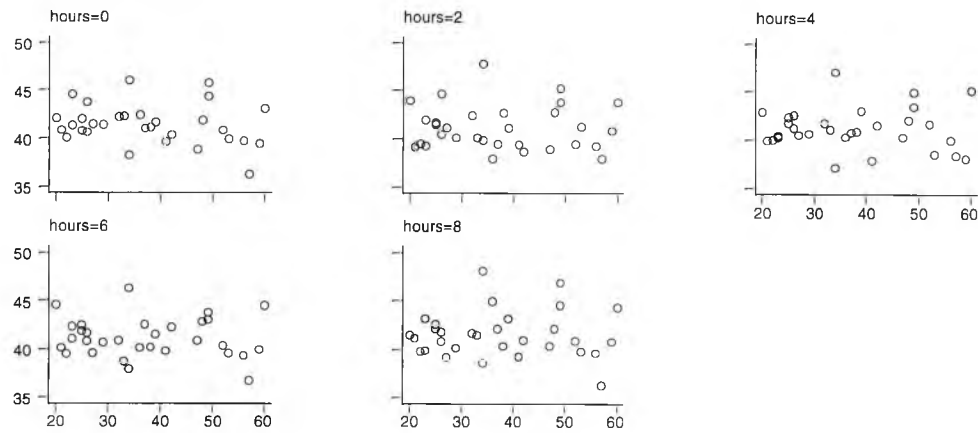


Figure A1.16. W plotted against age at 0, 2, 4, 6 and 8 hours for all vessels, where W is in microns and age in years

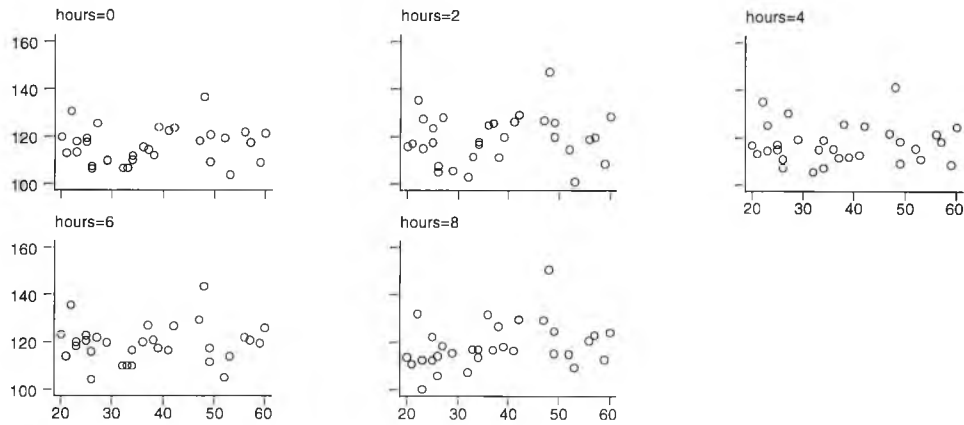


Figure A1.17. WV plotted against age at 0, 2, 4, 6 and 8 hours for all vessels, where WV is in microns² and age in years

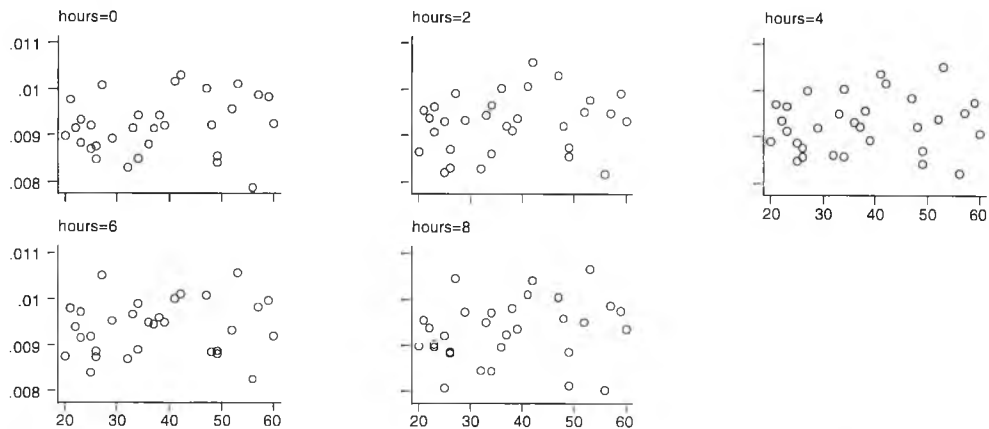


Figure A1.18. T plotted against age at 0, 2, 4, 6 and 8 hours for all vessels, where T is in units of curve energy and age in years

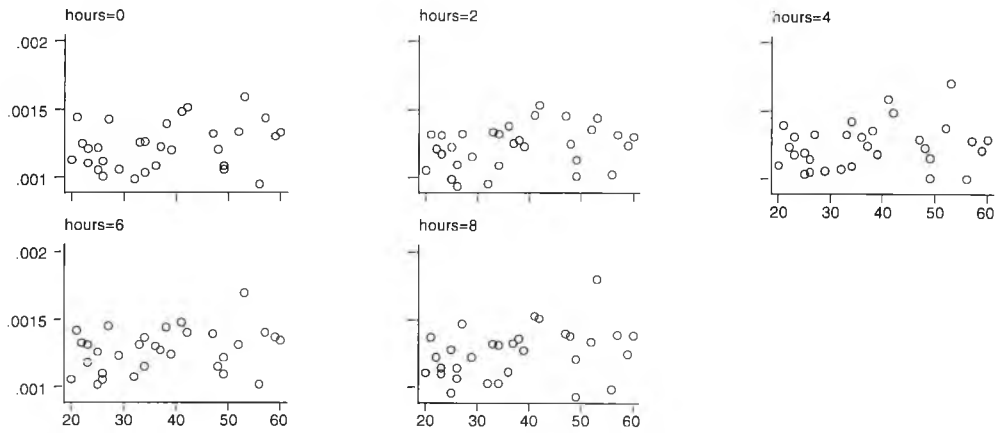


Figure A1.19. TV plotted against age at 0, 2, 4, 6 and 8 hours for all vessels, where TV is in units of curve energy² and age in years

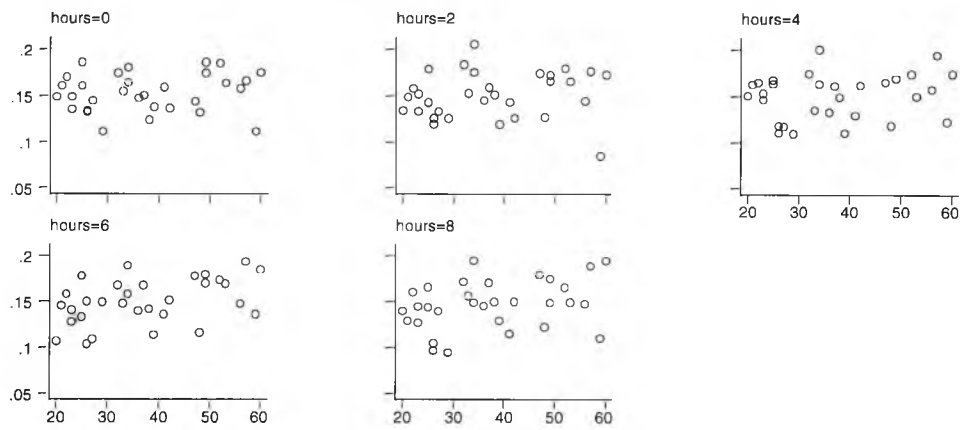


Figure A1.20. Density plotted against age at 0, 2, 4, 6 and 8 hours for all vessels, where Density is in mm² of vessel per mm² of conjunctiva and age in years

Appendix A2

The following figures are supplementary results from chapter 5 and show graphical representation for all indices against MAP for each visit separately.

For vessels $<25\mu\text{m}$ in diameter

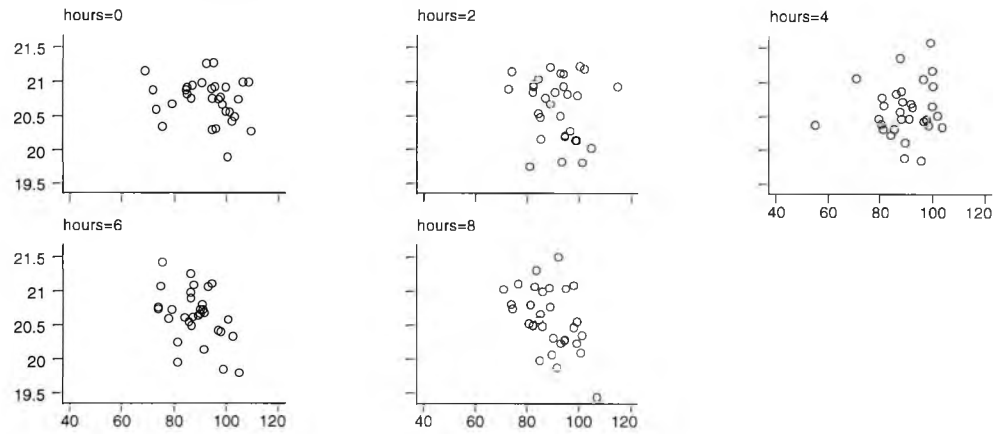


Figure A2.1. W plotted against MAP at 0, 2, 4, 6 and 8 hours for vessels $<25\mu\text{m}$ in diameter, where W is in microns and MAP in mmHg

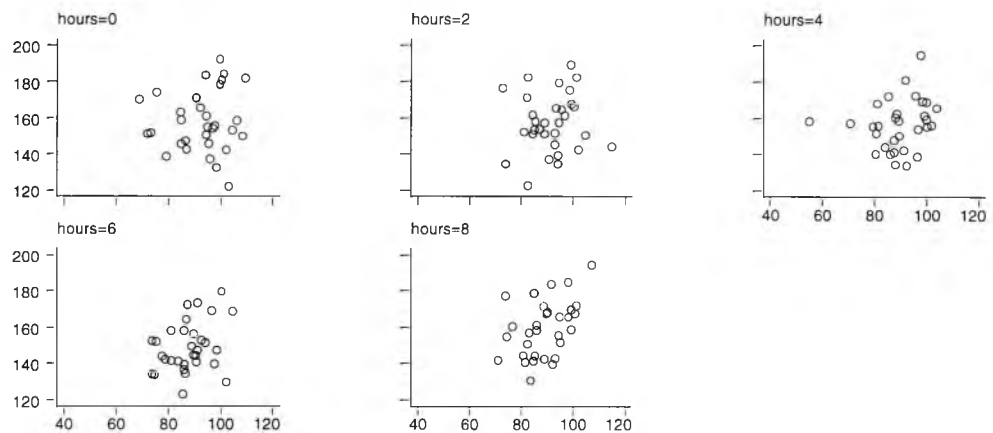


Figure A2.2. WV plotted against MAP at 0, 2, 4, 6 and 8 hours for vessels $<25\mu\text{m}$ in diameter, where WV is in microns² and MAP in mmHg

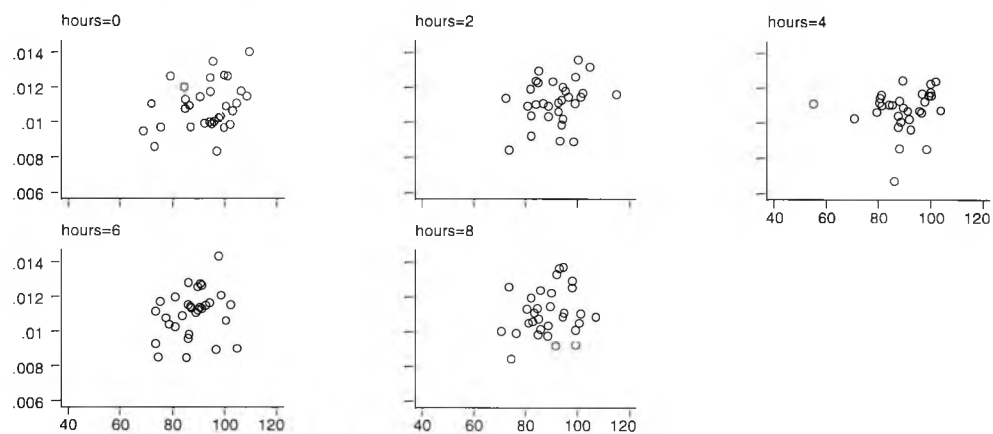


Figure A2.3. T plotted against MAP at 0, 2, 4, 6 and 8 hours for vessels $<25\mu\text{m}$ in diameter, where T is in units of curve energy and MAP in mmHg

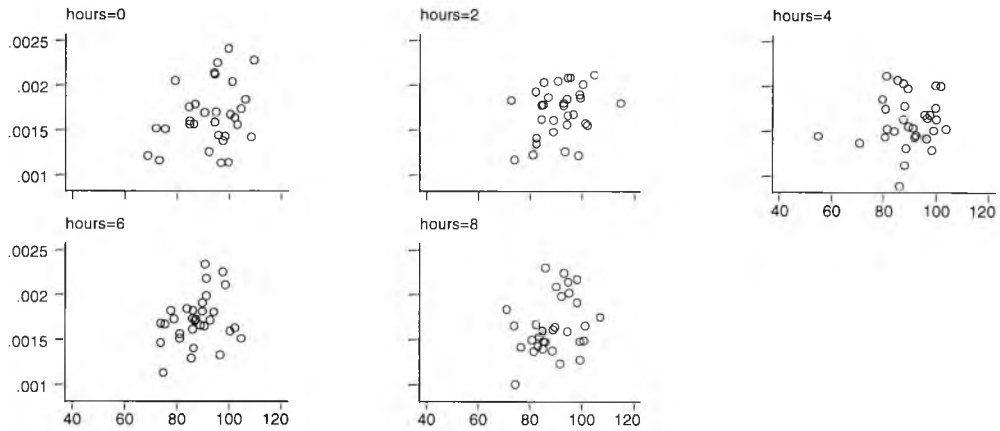


Figure A2.4. TV plotted against MAP at 0, 2, 4, 6 and 8 hours for vessels $<25\mu\text{m}$ in diameter, where TV is in units of curve energy² and MAP in mmHg

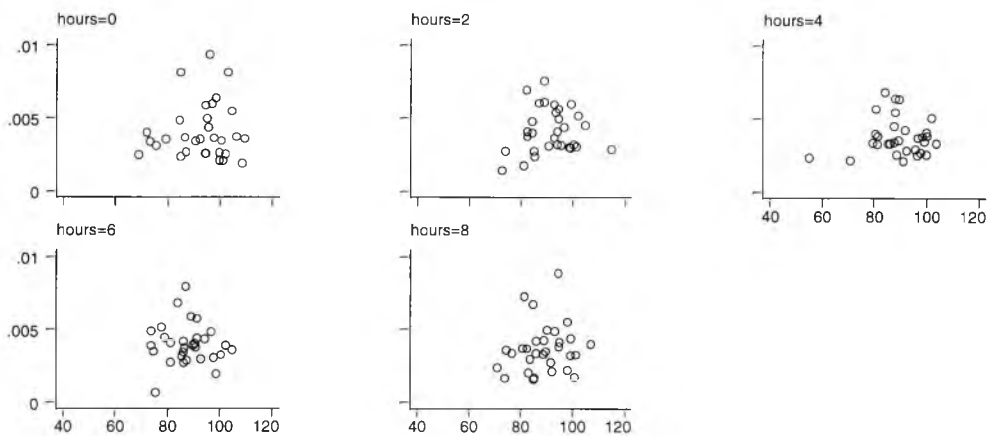


Figure A2.5. Density plotted against MAP at 0, 2, 4, 6 and 8 hours for vessels $<25\mu\text{m}$ in diameter, where Density is in mm^2 of vessel per mm^2 of conjunctiva and MAP in mmHg

For vessels $25\mu\text{m}$ to $<40\mu\text{m}$ in diameter

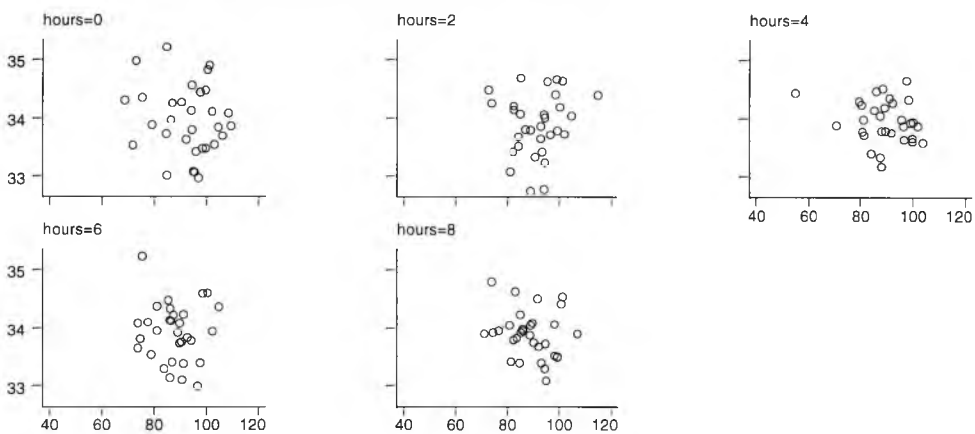


Figure A2.6. W plotted against MAP at 0, 2, 4, 6 and 8 hours for vessels $25\mu\text{m}$ to $<40\mu\text{m}$ in diameter, where W is in microns and MAP in mmHg

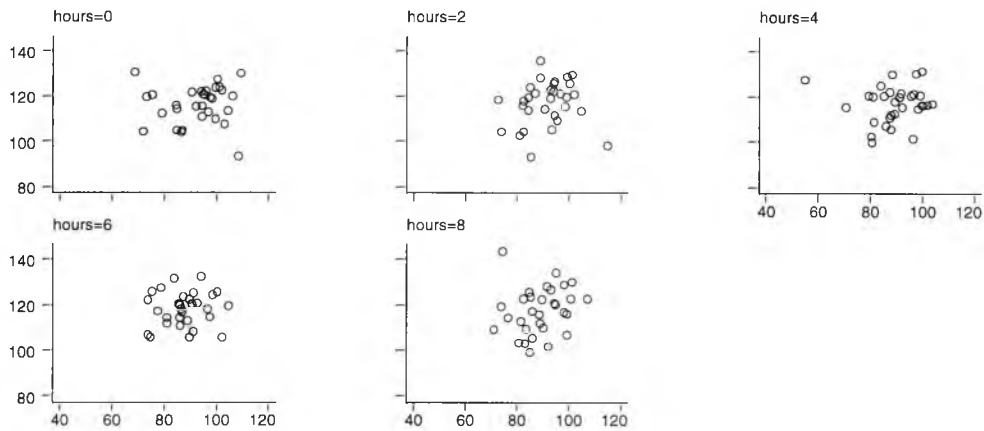


Figure A2.7. WV plotted against MAP at 0, 2, 4, 6 and 8 hours for vessels $25\mu\text{m}$ to $<40\mu\text{m}$ in diameter, where WV is in μm^2 and MAP in mmHg

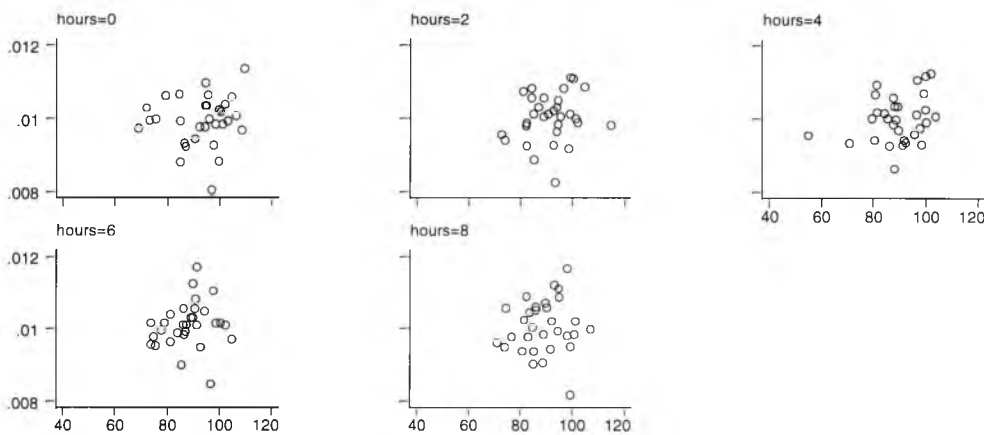


Figure A2.8. T plotted against MAP at 0, 2, 4, 6 and 8 hours for vessels $25\mu\text{m}$ to $<40\mu\text{m}$ in diameter, where T is in units of curve energy and MAP in mmHg

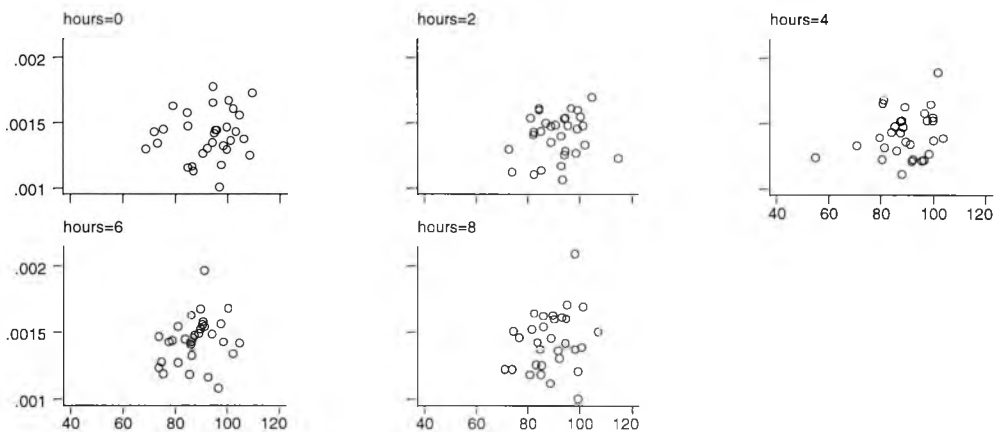


Figure A2.9. TV plotted against MAP at 0, 2, 4, 6 and 8 hours for vessels $25\mu\text{m}$ to $<40\mu\text{m}$ in diameter, where TV is in units of curve energy^2 and MAP in mmHg

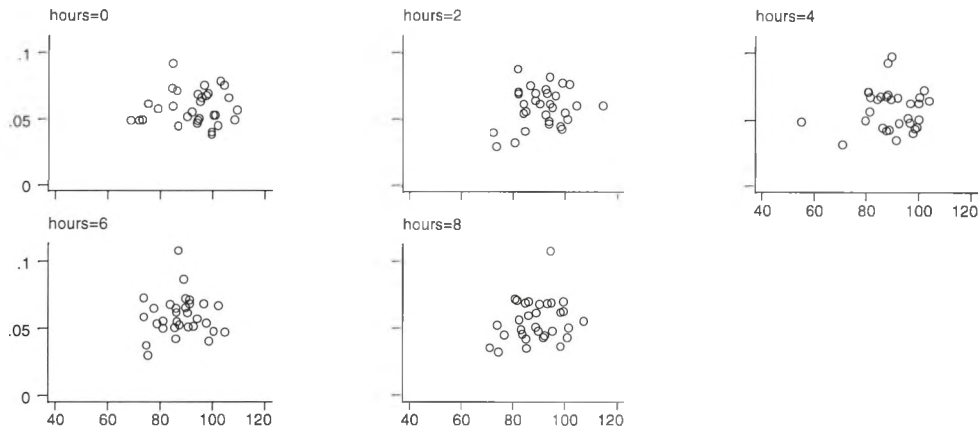


Figure A2.10. Density plotted against MAP at 0, 2, 4, 6 and 8 hours for vessels $25\mu\text{m}$ to $<40\mu\text{m}$ in diameter, where Density is in mm^2 of vessel per mm^2 of conjunctiva and MAP in mmHg

For vessels $40\mu\text{m}$ to $<80\mu\text{m}$ in diameter

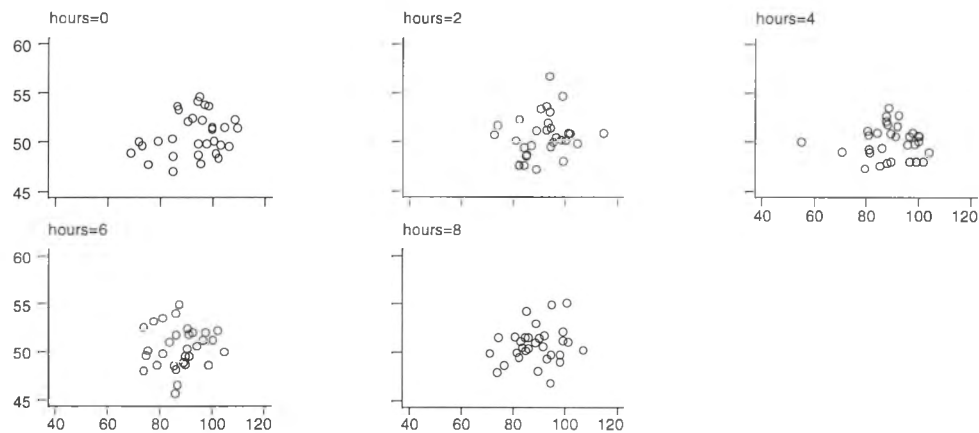


Figure A2.11. W plotted against MAP at 0, 2, 4, 6 and 8 hours for vessels $40\mu\text{m}$ to $<80\mu\text{m}$ in diameter, where W is in microns and MAP in mmHg

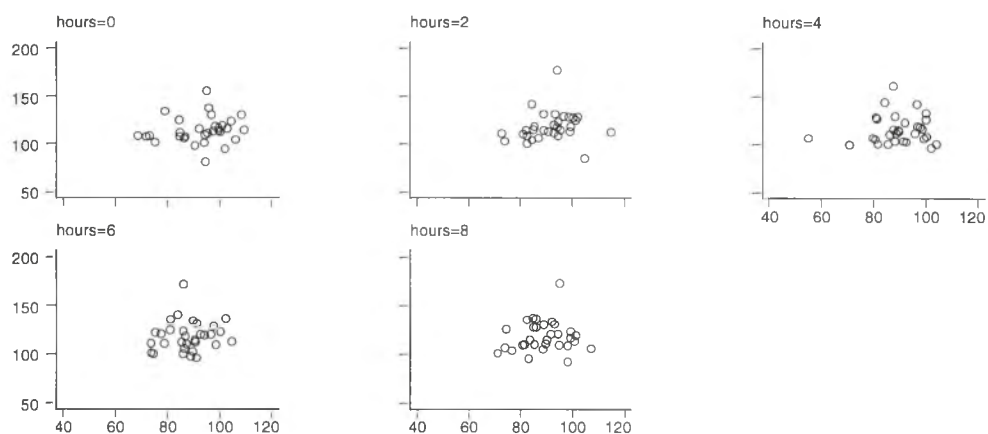


Figure A2.12. WV plotted against MAP at 0, 2, 4, 6 and 8 hours for vessels $40\mu\text{m}$ to $<80\mu\text{m}$ in diameter, where WV is in microns^2 and MAP in mmHg

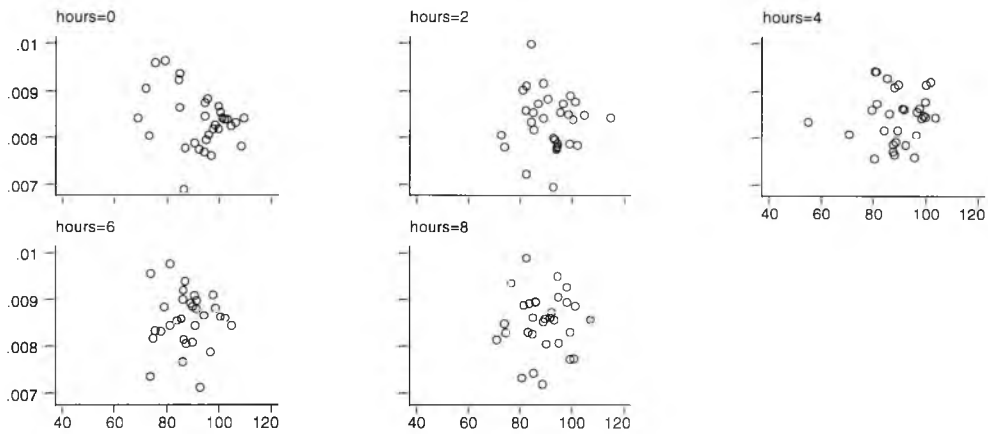


Figure A2.13. T plotted against MAP at 0, 2, 4, 6 and 8 hours for vessels $40\mu\text{m}$ to $<80\mu\text{m}$ in diameter, where T is in units of curve energy and MAP in mmHg

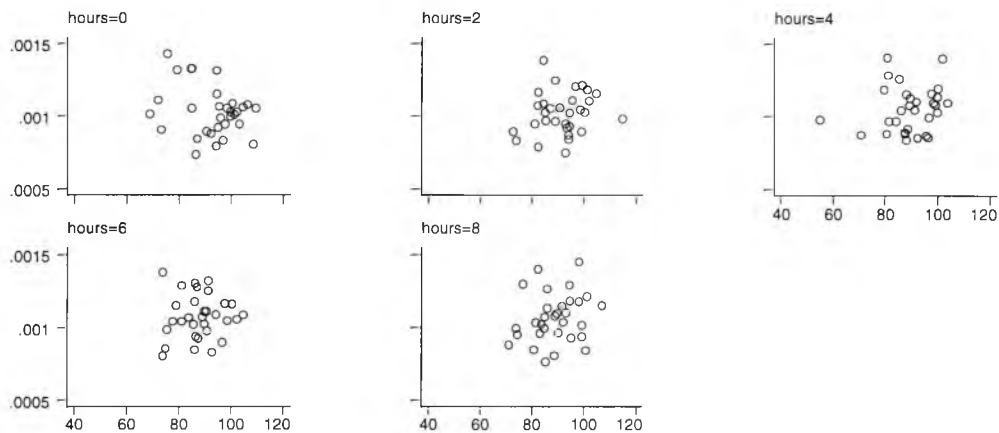


Figure A2.14. TV plotted against MAP at 0, 2, 4, 6 and 8 hours for vessels $40\mu\text{m}$ to $<80\mu\text{m}$ in diameter, where TV is in units of curve energy² and MAP in mmHg

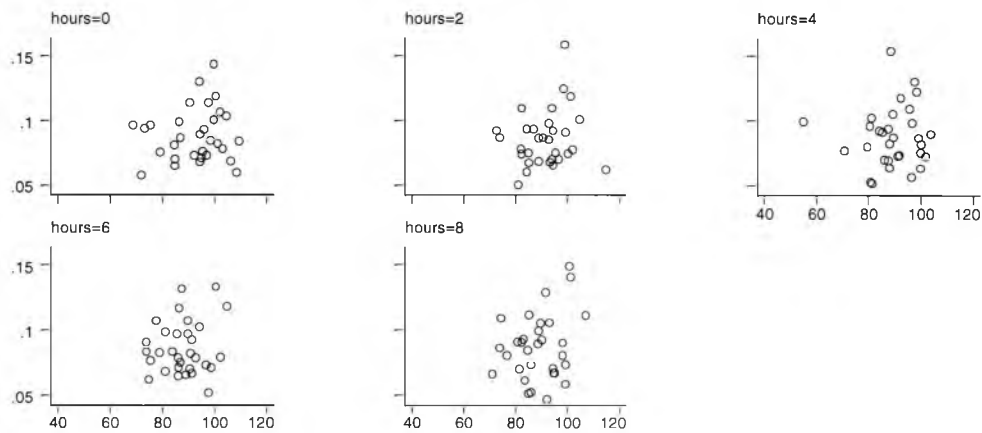


Figure A2.15. Density plotted against MAP at 0, 2, 4, 6 and 8 hours for vessels $40\mu\text{m}$ to $<80\mu\text{m}$ in diameter, where Density is in mm^2 of vessel per mm^2 of conjunctiva and MAP in mmHg

For all vessels

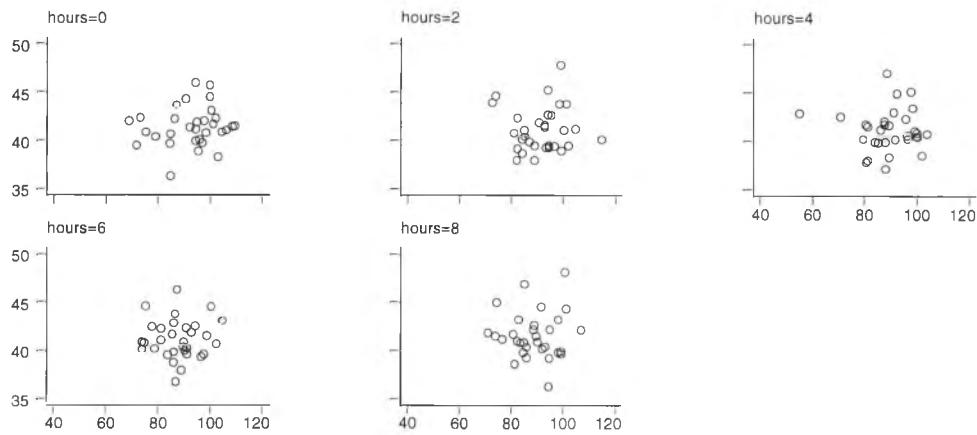


Figure A2.16. W plotted against MAP at 0, 2, 4, 6 and 8 hours for all vessels, where W is in microns and MAP in mmHg

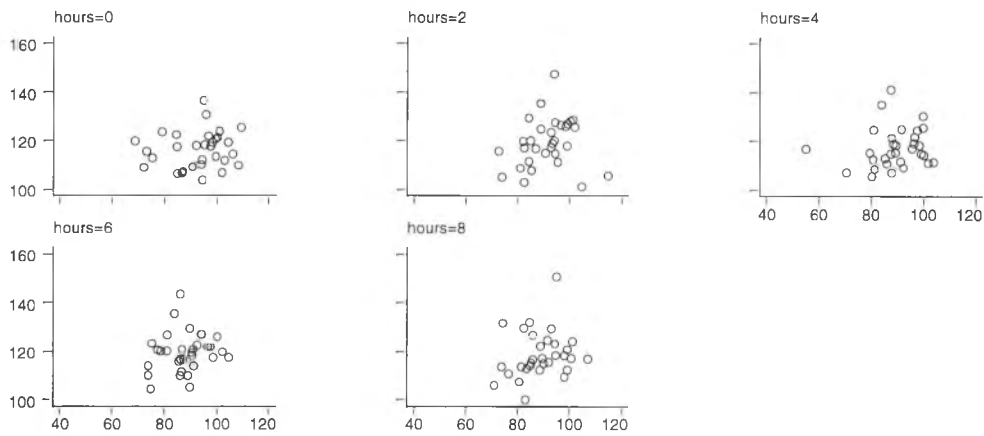


Figure A2.17. WV plotted against MAP at 0, 2, 4, 6 and 8 hours for all vessels, where WV is in microns² and MAP in mmHg

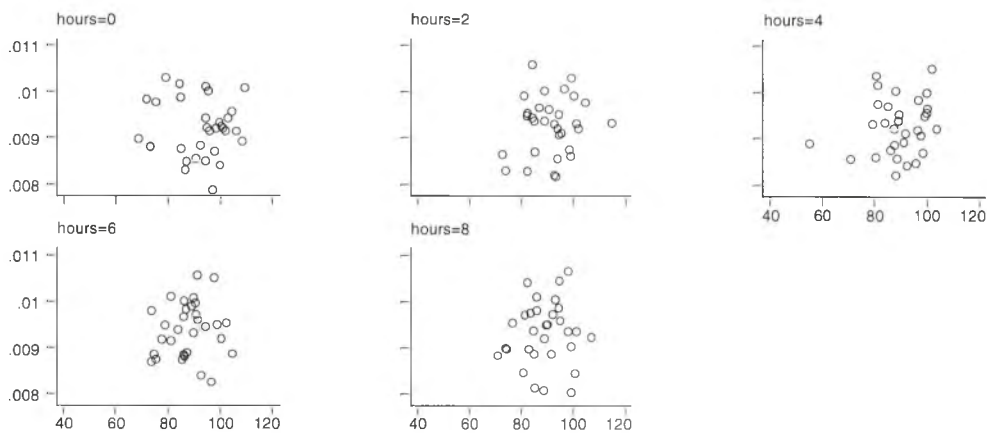


Figure A2.18. T plotted against MAP at 0, 2, 4, 6 and 8 hours for all vessels, where T is in units of curve energy and MAP in mmHg

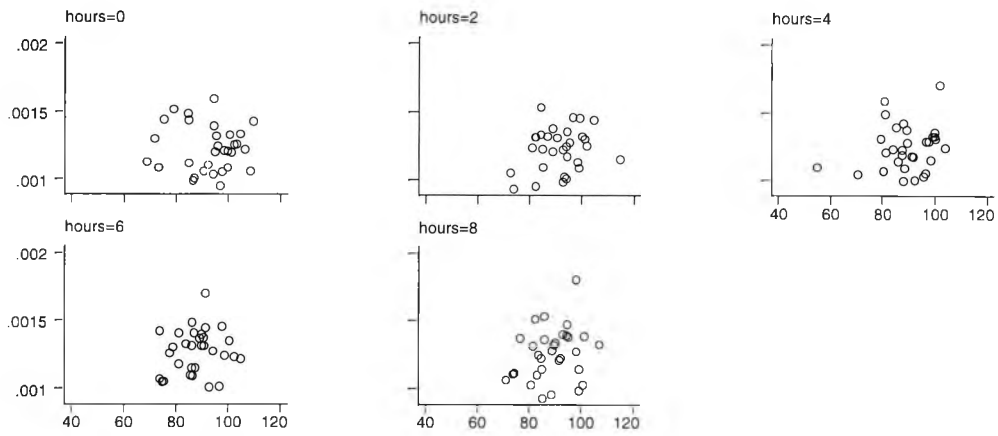


Figure A2.19. TV plotted against MAP at 0, 2, 4, 6 and 8 hours for all vessels, where TV is in units of curve energy² and MAP in mmHg

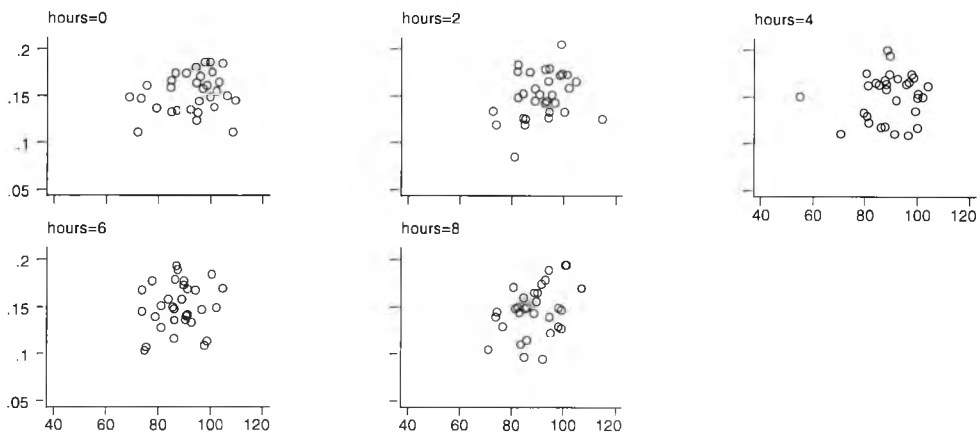


Figure A2.20. Density plotted against MAP at 0, 2, 4, 6 and 8 hours for all vessels, where Density is in mm² of vessel per mm² of conjunctiva and MAP in mmHg

SUPPORTING PUBLICATIONS

Refereed papers

- Palmer, J.R., Owen, C.G., Ford, A.M., Jacobson, R.E., Woodward, E.G. (1996). Optimal photographic imaging of the bulbar conjunctival vasculature. *Ophthalm Physiol Opt* **16**(2): 144-149.
- Owen, C.G., Fitzke, F.W., and Woodward, E.G. (1996). A new computer assisted objective method for quantifying vascular changes of the bulbar conjunctivae. *Ophthalm Physiol Opt* **16**(5): 430-437.
- Owen, C.G., Ellis, T.J., Woodward, E.G. (1998). Automated extraction of morphological and morphometric characteristics of the conjunctival vasculature. **In: Advances in Corneal Research: Selected Transactions of the World Corneal Congress 1996**, ed by J. Lass, (New York: Plenum Press Publications), 73-86.

Refereed conference abstracts

- Owen, C.G., Palmer, J.R., Fitzke, F.W., Woodward, E.G. (1995). A new objective method for quantifying hyperaemic changes of the bulbar conjunctivae associated with contact lens wear in adverse environments. *Invest Ophthalmol Vis Sci* **36**(4): S313.
- Owen, C.G., Ellis, T.J., Woodward, E.G. (1997). Optimal CCD imaging of conjunctival vasculature using colour filtration. *Invest Ophthalmol Vis Sci* **38**(4): S514.
- Ellis, T.J., Owen, C.G., Woodward, E.G. (1997). Measurement of vessel tortuosity on the conjunctiva. *Invest Ophthalmol Vis Sci* **38**(4): S512.

REFERENCES

- Aburn, N.S., Sergott, R.C. (1993). Orbital colour Doppler imaging. *Eye* **7**: 639-647.
- Albanese, C., de Nicola, P. (1987). Small conjunctival vessels and captopril: Microcirculation studies in the elderly. *Curr Therapeutic Res* **42**(4): 557-563
- Aliò, J., Padron, M. (1982). Influence of age on the temperature on the anterior segment of the eye. *Ophthalmic Res* **14**: 153-159.
- Ando, E., Ando, Y., Maruoka, S., Sakai, Y., Watanabe, S., Yamashita, R., Okamura, R., Araki, S. (1992). Ocular microangiopathy in familial amyloidotic polyneuropathy, type 1. *Graefe's Arch Clin Exp Ophthalmol* **230**: 1-5.
- Ando, E., Ando, Y., Okamura, R., Uchino, M., Ando, M., Negi, A. (1997). Ocular manifestations of familial amyloidotic polyneuropathy type 1: long term follow up. *Br J Ophthalmol* **81**: 295-298.
- Arend, O., Wolf, S., Harris, A., Jung, F., Reim, M. (1993). Effects of oral contraceptives on conjunctival microcirculation. *Clin Hemorheology* **13**: 435-445.
- Arnold, J.V., Jargoe, R., Wootton, R., Taylor, K.M. (1994). The measurement of apparent vessel width in retinal images: variation of true dimensions with exposure and development. *Invest Ophthalmol Vis Sci (suppl)* **35**(4): 2089.
- Ashton, N. (1951). Anatomical study of Schlem's canal and aqueous veins by means of neoprene casts. *Brit J Ophthalmol*. **35**: 291-303.
- Ashton, N. (1952). Anatomical study of Schlem's canal and aqueous veins by means of neoprene casts. Part II: aqueous veins. *Brit J Ophthalmol* **36**: 265-267.
- Ashton, N., Smith, R.S. (1953). Anatomical study of Schlem's canal and aqueous veins by means of neoprene casts. Part III: arterial relations of Schlem's canal. *Brit J Ophthalmol* **37**: 577-586.
- Ashton, N., Cook, C. (1953). Mechanism of corneal vascularisation. *Brit J Ophthalmol* **37**: 193-209.
- Bachir, D., Maurel, A., Portos, J.L., Galacteros, F. (1993). Comparative evaluation of laser Doppler flux metering, bulbar conjunctival angioscopy, and nail fold capillaroscopy in sickle cell disease. *Microvascular Research* **45**: 20-32.
- Bailey, I.L., Bullimore, M.A., Raasch, T.W., Taylor, H.R. (1991). Clinical grading and the effects of scaling. *Invest Ophthalmol Vis Sci* **32**(2): 422-432.
- Béchetoille, A. (1996). Vascular risk factors in glaucoma. *Curr Opinion Ophthalmol* **7**(2): 39-43.
- Behrendt, T. (1966). Scanning densitometer for photographic fundus measurements. *Am J Ophthalmol* **62**: 689-693.
- Bell, G.H., Emslie-Smith, D., Paterson, C.R. (1980). The circulation. **In:** *Textbook of Physiology*, (Edinburgh, London, New York: Churchill Livingstone) chapt 11, pp 178-179.
- Berta, A., Tözér, J., Holly, F.J. (1990). Determination of plasminogen activator activities in normal and pathological human tears. The significance of tear plasminogen activators in the inflammatory and traumatic lesions of the cornea and the conjunctiva. *Acta Ophthalmol* **68**: 508-514.
- Bhutto, I.A., Amemiya, T. (1995). Retinal vascular changes during ageing in Wistar Kyoto rats. *Ophthalmic Res* **27**: 249-261.

- Bland, J.M., Altman, D.G. (1986). Statistical methods for assessing agreement between two methods of clinical measurement. *Lancet* **i**: 307-310.
- Bland, J.M., Altman, D.G. (1995). Comparing methods of measurement: why plotting difference against standard method is misleading. *Lancet* **346**: 1085-1087.
- Bracher, D., Dozzi, M., Lotmar, W. (1979). Measurement of vessel width on fundus photographs. *Graefe's Arch Klin Exp Ophthalmol* **211**: 35-48.
- Brewer, W.L., Hanson, W.T., Horton, C.A. (1949). Subtractive colour production: the approximate reduction of selected filters. *J. Opt. Soc. Am.* **39**, 924-927.
- Brinchmann-Hansen, O., Engvold, O. (1986). Microphotometry of the blood column and the light streak on retinal vessels in fundus photographs. *Acta Ophthalmol (suppl)* **179**: 9-19.
- Brinchmann-Hansen, O., Heier, H. (1986). The apparent and true width of the blood column in retinal vessels. *Acta Ophthalmol (suppl)* **179**: 29-35.
- Brinchmann-Hansen, O., Heier, H., Myhre, K. (1986). Fundus photography of width and intensity profiles of the blood column and the light reflex in retinal vessels. *Acta Ophthalmol (suppl)* **179**: 20-28.
- Brinchmann-Hansen, O., Myhre, K., Sandvik, L. (1986). The light reflex in retinal vessels and its relation to age and systemic blood pressure. *Acta Ophthalmol* **65**: 206-212.
- Bron, A.J., Easty, D.L. (1970). Fluorescein angiography of the globe and anterior segment. *Trans Ophthalmol Soc UK* **90**: 339-365.
- Bron, A.J., Mengher, L.S., Davey, C.C. (1985). The normal conjunctiva and its responses to inflammation. *Trans Ophthalmol Soc UK* **104**: 424-435.
- Bruce, A.S., Brennan, N.A. (1990). Corneal pathophysiology with contact lens wear. *Surv Ophthalmol* **35**: 25-58
- Burton, P., Gurrin, L., Sly, P. (1998). Extending the simple linear regression model to account for correlated responses: An introduction to generalised estimating equations and multi-level mixed modelling. *Statist Med* **17**: 1261-1291.
- Butt, Z., McKillop, G., O'Brien, C., Allan, P., Aspinall, P. (1995). Measurement of ocular blood flow velocity using colour Doppler imaging in low tension glaucoma. *Eye* **9**: 29-33.
- Canny, J. (1986). A computational approach to edge detection. *IEEE Trans Pattern Analysis and Machine Intelligence* **8**(6): 679-698.
- Capowski, J.J., Kylstra, J.A., Freedman, S.F. (1995). A numeric index based on spatial frequency for the tortuosity of retinal vessels and its application to plus disease in retinopathy of prematurity. *Retina* **15**: 490-500.
- Chaudhuri, S., Chatterjee, S., Katz, N., Nelson, M., Goldbaum. (1989). Detection of blood vessels in retinal images using two-dimensional matched filters. *IEEE Trans Med Imag* **8**(3): 263-269.
- Chen, H.C., Newsom, R.S.B., Patel, V., Cassar, J., Mather, H., Kohner, E.M. (1994). Retinal blood flow changes during pregnancy in women with diabetes. *Invest Ophthalmol Vis Sci* **35**: 3199-3208.
- Chen, H.C., Patel, V., Wiek, J., Rassam, S.M., Kohner, E.M. (1988). Vessel diameter changes during the cardiac cycle. *Eye* **8**: 97-103.
- Chen, P.C., Li, S.G., Zweifach, B.W. (1986). Comparisons of morphometric alterations in human conjunctiva microvascular network in hypertension and diabetes. *Intern J Microcirculation-Clinical Experimental* **5**(2-3): 200.

- Chen, P.C.Y., Kovalcheck, S.W., Zweifach, B.W. (1987). Analysis of microvascular network in bulbar conjunctiva by image processing. *Int J Microcirc Clin Exp* **6**: 245-255.
- Chew, P.T.K., Watson, P.G., Chee, C.K.L. (1994). Vascular changes over trabeculectomy blebs. *Eye* **8**: 389-393.
- Cogan, D.G. (1949). Vascularization of the cornea: Its experimental induction by small lesions and a new theory of its pathogenesis. *Arch Ophthalmol* **41**: 406-416.
- Coget, J.M., Dupuis-Uvny, C.H., Merlen, J.F. (1989). Intérêde l'étude de la conjonctive oculaire dans le dépistage du prédiabète (Value of the study of the ocular conjunctiva in screening for diabetes). *J des Maladies Vasculaires* **14**: 68-70.
- Cox, I. (1994) Digital imaging in the contact lens practice. *Int Contact Lens Clinic* **22**: 62-66.
- Crawford, J.B. (1986). Conjunctival tumours. **In** *Clinical Ophthalmol: External diseases: The Uvea*, vol IV, ed by T.D. Duane (New York: Harper and Row), chapter 10, pp 1-8.
- Da-Ching, W., Schwartz, B., Schwoerer, J., Banwatt, R. (1995). Retinal blood vessel width measured on colour fundus photographs by image analysis. *Acta Ophthalmol (suppl)* **73**(215): 33-40.
- Davis, J., Landau, E. (1957). Capillary thinning and high capillary blood pressure in hypertension. *Lancet* **272**: 1327-1330.
- Delori, F.C. (1988). Noninvasive technique for oximetry of blood in retinal vessels. *Appl Optics* **27**: 1113-1125.
- Delori, F.C., Gragoudas, E.S., Francisco, R., Pruett, R.C. (1977). Monochromatic ophthalmoscopy and fundus photography: The normal fundus. *Arch Ophthalmol* **95**: 861-868.
- Delori, F.C., Pflibsen, K.P. (1989). Spectral reflectance of the human ocular fundus. *Appl Optics* **28**(6): 1061-1077.
- Deriche, R. (1990). Fast algorithms for low level vision. *IEEE Trans Pattern Analysis and Machine Intelligence* **12**(1): 78-87.
- Dixel, T., Böhme, H., Schmidt, P., Haslbeck, M., Mehnert, H. (1976). Investigation of conjunctival vessels in diabetics with and without retinopathy by means of a microcirculation-index. *Bibl Anat* **16**: 442-444.
- Ditzel, J. (1954). Morphologic and hemodynamic changes in the smaller blood vessels in diabetes mellitus: I Considerations based on the literature. *New Eng J Med* **250**(13): 541-546.
- Ditzel, J., Saglid, U. (1954). Morphologic and hemodynamic changes in the smaller blood vessels in diabetes mellitus: II The degenerative and hemodynamic changes in the bulbar conjunctiva of normotensive diabetic patients. *New Eng J Med* **250**(14): 587-594.
- Ducrey, N.M., Delori, F.C., Gragoudas, E.S. (1979). Monochromatic ophthalmoscopy and fundus photography: The pathological fundus. *Arch Ophthalmol* **97**: 288-293.
- Dumskyj, M.J., Aldington, S.J., Doré, C.J., Kohner, E.M. (1996). The accurate assessment of changes in retinal vessel diameter using multiple frame electrocardiograph synchronised fundus photography. *Curr Eye Res* **15**: 625-632.
- Eaton, A.M., Hatchell, D.L. (1988). Measurement of retinal blood vessel width using computerised image analysis. *Invest Ophthalmol Vis Sci* **29**(8): 1258-1264.

- Eberli, B., Riva, C.E., Feke, G.T. (1979). Mean circulation time of fluorescein in retinal vascular segments. *Arch Ophthalmol* **97**: 145-148.
- Efron, N. (1987). Vascular response of the cornea to contact lens wear. *J Am Optom Assoc* **58**(10): 836-846.
- Efron, N., Brennan, N.A., Hore, J., Rieper, K. (1988). Temperature of the hyperaemic bulbar conjunctiva. *Curr Eye Res* **7**(6): 615-618.
- Enstrom, R.E., Holland, G.N., Hardy, W.D., Meiselman, H.J. (1990). Hemorheologic abnormalities in patients with human immunodeficiency virus infection and ophthalmic microvasculopathy. *Am J Ophthalmol* **109**: 153-161.
- Feather, J.W., Ellis, D.J., Leslie, G. (1988). A portable reflectometer for rapid quantification of cutaneous haemoglobin and melanin. *Phys Med Biol* **33**(6): 711-722.
- Feather, J.W., Hajizadeh-Saffar, M., Leslie, G., Dawson, J.B. (1989). A portable scanning reflectance spectrophotometer using visible wavelengths for the rapid measurement of skin pigments. *Phys Med Biol* **34**(7): 807-820.
- Feke, G.T., Tagawa, H., Deupree, D.M., Goger, D.G., Sebag, J., Weiter, J.J. (1989). Blood flow in the normal retina. *Invest Ophthalmol Vis Sci* **30**: 58-65.
- Fenton, B.M. (1980). Topographical simulation of blood vessels of the human conjunctiva and application to pressure-flow relationships. PhD Thesis, University of California, San Diego, USA.
- Flammer, J. (1996). To what extent are vascular factors involved in the pathogenesis of glaucoma. **In: Ocular blood flow**, ed by HJ Kaiser, J Flammer, P Hendrickson, (Basel, Switzerland: Karger), pp 12-39.
- Flower, R.W., McLeod, D.S., Pitts, S.M. (1978). The effect of blood on ocular fundus reflectance and determination of some optical properties of retinal blood vessels. *Invest Ophthalmol Vis Sci* **17**: 562-565.
- Formaz, F., Riva, C.E., Geiser, M. (1997). Diffuse luminance flicker increase retinal vessel diameter. *Curr Eye Res* **16**: 1252-1257.
- Fryczkowski, A.W., Grimson, B.S., Peiffer, R.L. (1985). Vascular casting and scanning electron microscopy of human vascular abnormalities. *Arch Ophthalmol* **103**: 118-120.
- Gardner, G.G., Keating, D., Williamson, T.H., Elliott, A.T. (1996). Automatic detection of diabetic retinopathy using a artificial neural network: a screening tool. *Br J Ophthalmol* **80**: 940-944.
- George, G.S., Wolbarsht, M.L., Landers, M.B. (1990). Reproducible estimation of retinal vessel width by computerized microdensitometry. *Int Ophthalmol* **14**: 89-95.
- Graaff, R., Dassel, A.C.M., Zijlstra, W.G., de Mul, F.F.M., Aarnoudse, J.G. (1996). How tissue optics influences reflectance pulse oximetry. **In: Oxygen Transport to Tissue XVII**, ed by Ince, *et al*, (Plenum Press, New York), chapt 14, pp 117-132.
- Greer, D.A., Kumagai, L.F., Soeldner, J.S., Cheung, A.T.W. (1996). Computer-assisted quantification of non-insulin dependent diabetic microangiopathy in bulbar conjunctival vessels. *J Invest Med* **44**(1): 102.
- Greiner, J.V., Pearce, D.G., Baird, R.S., Allansmith, M.R. (1985). Effects of eye rubbing on the conjunctiva as a model of ocular inflammation. *Am J Ophthalmol* **100**: 45-50.
- Griffiths, J.D., Hill, D.W., Young, S. (1974). Measurement of apparent vessel width in fluorescence angiography of fundus oculi. *Ophthalmic Res* **6**: 1-5.

- Grunwald, J.E., Piltz, J., Patel, N., Bose, S., Riva, C.E. (1993). Effect of ageing on retinal macular microcirculation: A blue field simulation study. *Invest Ophthalmol Vis Sci* **34**: 3609-3613.
- Grunwald, J.E., Riva, C.E., Kozart, D.M. (1988). Retinal circulation during a spontaneous rise of intraocular pressure. *Br J Ophthalmol* **72**: 754-758.
- Grunwald, J.E., Riva, C.E., Sinclair, S.H., Brucker, A.J. (1986). Laser Doppler velocimetry study of retinal circulation in diabetes mellitus. *Arch Ophthalmol* **104**: 991-996.
- Guillon, M., Shah, D. (1996). Objective measurement of contact lens-induced conjunctival redness. *Optom Vis Sci* **73**(9): 595-605.
- Hajizadeh-Saffar, M., Feather, J.W., Dawson, J.B. (1990). An investigation of factors affecting *in vivo* measurements of skin pigments by reflectance spectrophotometry. *Phys Med Biol* **35**(9): 1301-1315.
- Harper, R.N., Moore, M.A., Marr, M.C., Watts, L.E., Hutchings, P.M. (1978). Arteriolar rarefaction in the conjunctivae of human essential hypertensives. *Microvasc Res* **16**: 369-372.
- Hayreh, S.S. (1996). Systemic arterial blood pressure and the eye. *Eye* **10**: 5-28.
- Hill, D.W., Crabtree, A. (1984). Vascular calibres. *Trans Ophthalmol Soc UK* **104**: 107.
- Hodge, J.V., Parr, J.C., Spears, G.F.S. (1969). Comparison of methods of measuring vessel width on retinal photographs and the effect of fluorescein injection on apparent retinal vessel calibres. *Am J Ophthalmol* **68**: 1060-1068.
- Holden, B.A., Sweeney, D.F., Swarbrick, H.A., Vannas, A., Nilsson, K.A., Efron, E. (1986). The vascular response to long term extended contact lens wear. *Clin Exp Optom* **69**(3): 112-119.
- Isogai, Y., Ikemoto, S., Tanaka, H. (1996). Elevation of viscoelasticity of blood in non-coagulative and coagulative state in diabetes, as indexes of increasing the incidence of aggravation of microangiopathy. *Clinical Hemorheology* **16**(5): 713-735.
- Janssens, M. (1992). Efficacy of levocabastine in conjunctival provocation studies. *Documenta Ophthalmologica* **82**: 341-351.
- Javitt, J.C., Canner, J.K., Sommer, A. (1989). Cost effectiveness of current approaches to the control of retinopathy in type I diabetics. *Ophthalmology* **96**: 255-264.
- Javitt, J.C., Canner, J.K., Frank, R.G. (1990). Detecting and treating retinopathy in patients with type I diabetes mellitus. A health policy model. *Ophthalmology* **97**: 483-494.
- Jensen, V.A., Lunback, K. (1968). Fluorescein angiography of the iris in recent and long-term diabetes. (XVII Scandinavian Ophthalmological Congress, Copenhagen 1967) *Acta Ophthalmol (Kbh)* **46**: 584-585.
- Jonas, J.B., Fernández, M.C., Naumann, G.O.H. (1991). Parapapillary atrophy and retinal vessel diameter in nonglaucomatous optic nerve damage. *Invest Ophthalmol Vis Sci* **32**(11): 2942-2947.
- Jonas, J.B., Nguyen, X.N., Nauman, G.O.H. (1989). Parapapillary retinal vessel diameter in normal and glaucoma eyes. I Morphometric data. *Invest Ophthalmol Vis Sci* **30**(7): 1599-1603.

- Jörneskog, J., Brismar, K., Fagrell, B. (1995). Skin capillary circulation is more impaired in toes of diabetic than non-diabetic patients with peripheral vascular disease. *Diabetic Medicine* **12**: 36-41.
- Jung, F., Korber, N., Kiesewetter, H., Prunute, C., Wolf, S., Reim, M. (1983). Measuring the microcirculation in human conjunctiva bulbi under normal and hyperfusion conditions. *Graefe's Arch Clin Exp Ophthalmol* **220**(6): 294-297.
- Junqueira, L.C., Carneiro, J. (1983). Circulatory system. **In: Basic Histology**, (Lange Medical Publications, Los Altos, California, USA) 4th edition, chapt 12, pp 249-255.
- Kaba, M., Tsushima, N., Sakakura, M., Toikawa, H., Konishi, M., Nakayama, R., Yasunaga, B.W. (1986). Microhemodynamic changes of the human bulbar conjunctiva and hemorheological alterations after insulin administration. *Clinical Hemorheology* **6**(5): 471.
- Kaiser, H.J., Flammer, J., Messerli, J. (1996). Vasospasm - a risk factor for nonarteritic anterior ischemic optic neuropathy. *Neuro-Ophthalmology* **16**: 5-10.
- Kaupp, A., Toonen, H., Wolf, S., Schulte, K., Effert, R., Meyer-Ebrecht, D., Reim, M. (1991). Automatic evaluation of retinal vessel width and tortuosity in digital fluorescein angiograms. *Invest Ophthalmol Vis Sci (suppl)* **32**(4): 863.
- Klaassen-Broekema, N., van Bijsterveld, O.P. (1992). Red eyes in renal failure. *Brit J Ophthalmol* **76**, 268-271.
- Klassen-Broekema, N., Veldkamp, K.E., van Bijsterveld, O.P. (1995). Can hydroxyapatite deposition in the eye cause a neutrophil-related inflammatory reaction? *Docuementa Ophthalmologica* **90**: 325-330.
- Klein, R., Meuer, S.M., Moss, S.E., Klein, E.K. (1989). The relationship of retinal microaneurysm counts to the 4 year progression of diabetic retinopathy. *Arch Ophthalmol* **107**: 1780-1785.
- Kohner, E.M., Sleightholm, M., *et al.* (1986). Does microaneurysm count reflect severity of early diabetic retinopathy. *Ophthalmol* **93**: 586-589.
- Kovalcheck, S.W., Chen, P.C., Zweifach, B.W. (1984). Microvasculature changes with age in bulbar conjunctiva. *Int J Microcirculation-Clinical Exp* **3**(3-4): 530.
- Kylstra, J.A., Freedman, S.F., Capowski, J.J., Hall, J.G. (1995). Measurement of retinal vessel tortuosity as a means of diagnosing plus disease in ROP. *Invest Ophthalmol Vis Sci (suppl)* **36**(4): 18.
- Kylstra, J.A., Wierzbicki, T., Wolbarsht, M.L., Landers, M.B., Stefansson, E. (1986). The relationship between retinal vessel tortuosity, diameter, and transmural pressure. *Graefe's Arch Clin Exp Ophthalmol* **224**: 477-480.
- Landau, J., Davis, E. (1960). The small blood vessels of the conjunctiva and nailbed in diabetes mellitus. *Lancet* **2**: 731-734.
- Landsman, M.L.J., Knop, N., Kwant, G., Mook, G.A., Zijlstra, W.G. (1978). A fiberoptic reflection oximeter. *Pflügers Archiv* **373**: 273-282.
- Libert, J., Toussaint, D. (1982). Tortuosities of retinal and conjunctival vessels in lysosomal storage defects. *Birth Defects: Original Article Series* **18**: 347-358.
- Lotmar, W., Freiburghaus, A., Bracher, D. (1979). Measurement of vessel tortuosity on fundus photographs. *Graefe's Arch Klin Exp Ophthal* **211**: 49-57.
- Manivannan, A., Kirkpatrick, J.N.P., Sharp, P.F., Forrester, J.V. (1994). Clinical investigation of an infrared digital scanning ophthalmoscope. *Br J Ophthalmol* **78**: 84-90.

- Marsh, R.J., Ford, S.M. (1980). Blood flow in the anterior segment of the eye. *Trans Ophthalmol Soc UK* **100**: 388-397.
- Mayrovitz, H.N., Larnard, D., Duda, G. (1981). Blood velocity measurement in human conjunctival vessels. *Cardiovascular Diseases, Bulletin of the Texas Heart Institute* **8**(4): 509-526.
- McCulloch, J.C., Pashby, T.J. (1950). Significance of conjunctival aneurysms in diabetics. *Br J Ophthalmol* **34**: 495-505.
- McLeod, D.S., Goldberg, M.F., Luty, G.A. (1993). Dual-perspective analysis of vascular formations in sickle cell retinopathy. *Arch Ophthalmol* **111**: 1234-1245.
- McMonnies, C.W. (1983). Contact lens-induced corneal vascularization. *Int Contact Lens Clinic* **10**(1): 12-20.
- McMonnies, C.W., Chapman-Davies, A. (1982). The vascular response to contact lens wear. *Optom Vis Sci* **59**(10): 795-799.
- McMonnies, C.W., Chapman-Davies, A. (1987a). Assessment of conjunctival hyperaemia in contact lens wearers. Part 1. *Optom Vis Sci* **64**(4): 246-250.
- McMonnies, C.W., Chapman-Davies, A. (1987b). Assessment of conjunctival hyperaemia in contact lens wearers. Part 2. *Optom Vis Sci* **64**(4): 251-255.
- McMonnies, C.W., Ho, A. (1991). Conjunctival hyperaemia in non-contact lens wearers. *Acta Ophthalmol* **69**: 799-801.
- Mendívil, A., Cuartero, V., Mendívil, P.A. (1995a). Ocular blood flow velocities in patients with proliferative diabetic retinopathy and healthy volunteers: a prospective study. *Br J Ophthalmol* **79**: 413-416.
- Mendívil, A., Cuartero, V., Mendívil, M.P. (1995b). Color doppler imaging of ocular vessels. *Graef's Arch Clin Exp Ophthalmol* **233**: 135-139.
- Meyer, P.A.R. (1988). Patterns of blood flow in episcleral vessels studied by low-dose fluorescein videoangiography. *Eye* **2**: 533-546.
- Meyer, P.A.R. (1989). The circulation of the human limbus. *Eye* **3**: 121-127.
- Meyer, P.A.R., Fitzke, F.W. (1990). Computer assisted analysis of fluorescein videoangiograms. *Br J Ophthalmol* **74**: 275-277.
- Meyer, P.A.R., Watson, P.G. (1987). Low dose fluorescein angiography of the conjunctiva and episclera. *Br J Ophthalmol* **71**: 2-10.
- Miles, F.P., Nuttall, A.L. (1993). Matched filter estimation of serial blood vessel diameters from video images. *IEEE Trans Med Imag* **12**(2): 147-152.
- Mook, G.A., Osypka, P., Strum, R.E., Wood, E.H. (1968). Fibre optic reflection photometry on blood. *Cardiovasc Res* **2**: 199-209.
- Mook, G.A., van Assendelft, O.W., Kwant, G., Landsman, M.L.J., Zijlstra, W.G. (1976). Two colour reflection oximetry. *Proceedings of the Koninklijke Nederlandse Akademie van Wetenschappen, Amsterdam series C* **79**(5): 472-491.
- Moss, S.E., Klien, R., Klein, E.K. (1988). The incidence of vision loss in a diabetic population. *Ophthalmol* **95**: 1340-1348.
- Newsom, R.S.B. (1994). Retinal blood flow and the progression of diabetic retinopathy. MD Thesis, University of London, UK.
- Newsom, R.S.B., Sullivan, P.M., Rassam, S.M.B., Jargoe, R., Kohner, E.M. (1992). Retinal vessel measurement: comparison between observer and computer driven methods. *Graefe's Arch Clin Exp Ophthalmol* **230**: 221-225.
- Nielsen, N.V. (1988). The normal fundus fluorescein angiogram and the normal fundus photograph. *Acta Ophthalmol (suppl)* **80**: 7-30.

- Owen, C.G., Fitzke, F.W., Woodward, E.G. (1996). A new computer assisted objective method for quantifying vascular changes of the bulbar conjunctivae. *Ophthalm Physiol Opt* **16**(5) 430-437.
- Owen, C.G., Ellis, T.J., Woodward, E.G. (1998). Automated extraction of morphological and morphometric characteristics of the conjunctival vasculature. **In: *Advances in Corneal Research: Selected Transactions of the World Corneal Congress 1996***, ed. by J. Lass, (New York: Plenum Press Publications) 73-86.
- Orgül, S., Flammer, J. (1995). Perilimbal aneurysms of conjunctival vessels in glaucoma patients. *German J Ophthalmol* **4**: 94-96.
- Palmer, J.R., Jacobson, R.E. (1994). Determination and enhancement of image contrast using the exposure density concept. *J Photogr Sci* **42**, 35-39.
- Palmer, J.R., Owen, C.G., Ford, A.M., Jacobson, R.E., Woodward, E.G. (1996). Optimal photographic imaging of the bulbar conjunctival vasculature. *Ophthalm Physiol Opt* **16**(2): 144-149.
- Pappas, T.N., Lim, J.S. (1988). A new method for estimation of coronary artery dimensions in angiograms. *IEEE Trans Acoustics, Speech, and Signal Processing* **36**(9): 1501-1513.
- Patel, V., Rassam S., Newson, R., Wiek, J., Kohner, E. (1992). Retinal blood flow in diabetic retinopathy. *Br Med J* **305**: 678-683.
- Paton, D. (1961). The conjunctival of sickle cell disease. *Arch Ophthalmol* **66**: 90-94.
- Phylactos, A. (1991). The lysosomal enzymes of the iris-ciliary body are retained in their organelles and exhibit increased activities during acute uveal inflammation. *Acta Ophthalmologica* **69**: 33-38.
- Rao, G.M.M. (1981). Effect of genetic diabetes on Beta-N-Acetylglucosaminidase activity in plasma, conjunctiva, muscle and kidney cortex of mice. *Biomedicine Express* **35**(5): 159-161.
- Rassam, S.M.B., Patel, V., Brinchmann-Hansen, O., Engvold, O., Kohner, E.M. (1994) Accurate vessel width determination from fundus photographs: a new concept. *Br J Ophthalmol* **78**: 24-29.
- Ravalico, G., Toffoli, G., Pastori, G., Crocè, M., Calderni, S. (1996). Age-related ocular blood flow changes. *Invest Ophthalmol Vis Sci* **37**: 2645-2650.
- Riva, C.E., Grunwald, J.E., Sinclair, S.H., O'Keefe, K. (1981). Fundus camera based retinal LDV. *Appl Opt* **20**(1): 117-120.
- Riva, C.E., Grunwald, J.E., Sinclair, S.H., Petrig, B.L. (1985). Blood velocity and volumetric flow rate in human retinal vessels. *Invest Ophthalmol Vis Sci* **26**: 1124-1132.
- Rohan, T.E., Frost, C.D., Wald, N.J. (1989). prevention of blindness by screening for diabetic retinopathy: a quantitative assessment. *Br Med J* **299**: 1198-1201
- Ruskell, G.L. (1991). The Conjunctiva. **In: *Clinical contact lens practice***, ed by E.S.Bennett and B.A.Weissman, (Philadelphia: J.B.Lippincott Company), chapter 3, pp 1-18.
- Sakai, Y., Maruoka, S., Ando, E., Okamura, R. (1990). Vascular abnormalities (aneurysms) of the bulbar conjunctiva: Studies on healthy subjects and diseased subjects. *Therapeutic Research* **11**(10): 31-36.
- Sanchez-Carrillo, C.I. (1989). Bias due to conjunctiva hue and the clinical assessment of anemia. *J Clin Epidemiol* **42**(8): 751-754.

- Schwenk, J., Cervosnavarro, J., Ferszt, R. (1986). Micro-angiopathic changes of the conjunctiva in chronic diabetes-mellitus. *Clinical Neuropathology* **5**(3): 128.
- Serjeant, G.R., Serjeant, B.E., Condon, P.I. (1972). The conjunctival sign of sickle cell disease. A relationship with irreversibly sickled cells. *J Am Med Assoc.* **219**: 1428-1431.
- Shmueli, K., Brody, W.R., Macovski, A. (1983). Estimation of blood vessel boundaries in X-ray images. *Opt Eng* **22**(1): 110-116.
- Silbert, J.A. (1991). Contact lens-related inflammatory reactions. **In:** *Clinical contact lens practice*, ed by E.S.Bennett and B.A.Weissman, (Philadelphia: J.B.Lippincott Company), chapter 65, pp 1-9.
- Sivak, J.G., Herbert, K.L., Fonn, D. (1995). In vitro ocular irritancy measure of four contact lens solutions: Damage and recovery. *CLAO J* **21**(3): 169-174.
- Skovborg, F., Nielsen, A.V., Lauritzen, E., Hartkopp, O. (1969). Diameter of retinal vessels in diabetic and normal subjects. *Diabetes* **18**: 292-298.
- Smolin, G. (1989). Cellular response to inflammation at the limbus. *Eye* **3**: 167-171.
- Sonnsjö, B., Krakau, C.E.T. (1993). Arguments for a vascular glaucoma etiology. *Acta Ophthalmol* **71**: 433-444.
- Spencer, T., Phillips, R.P., Sharp, P.F., Forrester, J.V. (1992). Automated detection and quantification of microaneurysms in fluorescein angiograms. *Graefe's Clin Exp Ophthalmol* **230**: 36-41.
- Steger, C. (1996). An unbiased detector of curvilinear structures. *Technical Report FGBV-96-03*. Forschungsgruppe Bildeverstehen (FG BV), Informatik IX, Technische Universität München.
- Steger, C. (1998). An unbiased detector of curvilinear structures. *IEEE Trans PAMI* **20**(2): 113-125.
- Stevenson, R.W.W., Chawala, J.C. (1993). Vascular response of limbus to contact lens wear. *J Brit Contact Lens Assoc* **16**(1): 19-23.
- Stitt, A.W., Gardiner, T.A., Archer, D.B. (1995). Histological and ultrastructural investigation of retinal microaneurysm development in diabetic patients. *Br J Ophthalmol* **79**: 362-367.
- Stock, L.E., Roth, S.I., Kim, E.D., Walsh, M.K., Thamman, R. (1990). The effect of platelet-activating factor (PAF), histamine, and ethanol on vascular permeability of the guinea pig conjunctiva. *Invest Ophthalmol Vis Sci* **31**: 987-992.
- Stroman, G.A., Stewart, W.C., Golnik, K.C., Curé, J.K., Olinger, R.E. (1995). Magnetic resonance imaging in patients with low-tension glaucoma. *Arch Ophthalmol* **113**: 168-172.
- Strömland, K., Hellström, A., Gustavsson. (1995). Morphometry of the optic nerve and retinal vessels in children by computer-assisted image analysis of fundus photographs. *Graefe's Clin Exp Ophthalmol* **233**: 150-153.
- Stubiger, N., Erb, C., Thieb, H.J. (1995). Alterations in pericorneal vessels of the conjunctiva in patients with general vascular disease. *Vision Res* **35**(SS): S175.
- Su, E.R., Yu, D.Y., Alder, V.A., Cringle, S.J., Yu, P.K. (1996). Direct vasodilatory effect of insulin on isolated retinal arterioles. *Invest Ophthalmol Vis Sci* **37**: 2634-2644.
- Sullivan, T.J., Clarke, M.P., Morin, J.D. (1992). The ocular manifestations of Sturge-Weber syndrome. *J Pediatr Ophthalmol Strabismus* **29**: 349-356.

- Suzuki, Y. (1995). Direct measurement of retinal vessel diameter: Comparison with microdensitometric methods based on fundus photographs. *Surv Ophthalmol (suppl)* **39**(1): 57-65.
- Tamura, S., Okamoto, Y., Yanashima, K. (1988). Zero-crossing interval correction in tracing eye-fundus blood vessels. *Pattern Recognition* **21**(3): 227-233.
- Tassi, G., Maggi, G., Nicola, P.D. (1985). Microcirculation in the elderly. *Int Angiology* **4**: 275-283.
- Taylor, A.W., Sehu, W., Williamson, T.H., Lee, W.R. (1993). Morphometric assessment of the central retinal artery and vein in the optic nerve head. *Can J Ophthalmol* **28**(7): 320-324.
- Teich, S.A. (1987). Conjunctival vascular changes in AIDS and AIDS related complex. *Am J Ophthalmol* **103**: 332-333.
- Terry, R.L., Schinder, C.M., Holden, B.A., Cornish, R., Grant, T., Sweeney, D., Hood, D.L., Back, A. (1993). CCLRU standards for success of daily and extended wear contact lenses. *Optom Vis Sci* **70**(3): 234-243.
- Trew, D.R., Wright, L.A., Smith, S.E. (1991). Ocular responses in healthy subjects to topical bunazosin 0.3% - an α 1-adrenoreceptor antagonist. *Br J Ophthalmol* **75**: 411-413.
- Ugomori, S., Hayasaka, S., Setogawa, T. (1991). Polymorphonuclear leucocytes (PMN) and bacterial growth of the normal and mildly inflamed conjunctiva. *Ophthalmic Res* **23**: 40-44.
- UKPDS 33. (1998). UKPDS Group. Intensive blood-glucose control with sulphonylureas or insulin compared with conventional treatment and risk of complications in patients with type II diabetes. *Lancet* **352**: 837-853.
- UKPDS 38. (1998). UKPDS Group. Tight blood pressure control and risk of macrovascular complications in type II diabetes. *BMJ* **317**: 703-713.
- van Bijsterveld, B.J., Janssen, P.T. (1981). The effect of calcium dobesilate on albumin leakage of the conjunctival vessels. *Curr Eye Res* **1**(7): 425-430.
- van Kampen, E.J., Zijlstra, W.G. (1983). Spectrophotometry of hemoglobin and hemoglobin derivatives. *Advances in Clinical Chemistry* **23**: 199-257.
- van Kampen, E.J., Zijlstra, W.G., van Assendelft, O.W., Reinkingh, W.H. (1965). Determination of hemoglobin and its derivatives. *Advances in Clinical Chemistry* **8**: 141-187.
- Villumsen, J., Alm, A. (1989). Prostaglandin F_{2α} - isopropylester eye drops: effects in normal eyes. *Br J Ophthalmol* **73**: 419-426.
- Villumsen, J., Alm, A. (1990). Ocular effects of two different prostaglandin F_{2α} esters. *Acta Ophthalmol* **68**: 341-343.
- Villumsen, J., Alm, A. (1992). PhXA34 - a prostaglandin F analogue. Effect on intraocular pressure in patients with ocular hypertension. *Br J Ophthalmol* **76**: 214-217.
- Villumsen, J., Ringquist, J., Alm, A. (1991). Image analysis of conjunctival hyperaemia: A personal computer based system. *Acta Ophthalmol* **69**: 536-539.
- Wells, R., Egerton, H. (1967). Blood flow in the microcirculation of conjunctival vessels of man. *Angiology* **18**(11): 699-704.
- Wilkins, M.R., Fitzke, F.W., Knaw, P.T. (1996). The assessment of conjunctival inflammation using digital photographs. *Invest Ophthalmol Vis Sci (suppl)* **37**(3): 1025.

- Williams, P.L., Warwick, R., Dyson, M., Bannister, L.H. (1989). Angiology. **In: Gray's anatomy**, (London: Churchill Livingstone), chapt 6, pp 682-747.
- Williams, T.J., Peck, M.J. (1977). Role of prostaglandin-mediated vasodilation in inflammation. *Nature* **270**: 530-532.
- Williamson, T.H., Baxter, G.M., Pyott, A., Wykes, W., Dutton, G.N. (1995). A comparison of colour Doppler imaging of orbital vessels and other methods of blood flow assessment. *Graefe's Arch Clin Exp Ophthalmol* **233**: 80-84.
- Williamson, T.H., Harris, A. (1996). Colour Doppler ultrasound imaging of the eye and orbit. *Surv Ophthalmol* **40**(4): 255-267.
- Williamson, T.H., Harris, A., Shoemaker, J.A., Sergott, R.C., Spaeth, G.L., Katz, J.L., Lieb, W.E. (1994). Reproducibility of colour Doppler imaging assessment of blood flow velocity in orbital vessels. *Invest Ophthalmol Vis Sci (suppl)* **35**(4): 1658.
- Williamson, T.H., Keating, D. (1998). Telemedicine and computers in diabetic retinopathy screening. *Br J Ophthalmol* **82**: 5-7.
- Williamson, T.H., Lowe, G.D.O., Baxter, G.M. (1995). Influence of age, systemic blood pressure, smoking, and blood viscosity on orbital blood velocities. *Br J Ophthalmol* **79**: 17-22.
- Willingham, F.F., Cohen, K.L., Coggins, J.M., Tripoli, N.K., Ogle, J.W., Goldstein, G.M. (1995). Automatic quantitative measurement of ocular hyperaemia. *Curr Eye Res* **14**: 1101-1108.
- Wilson, T.M., Constable, I.J., Cooper, R.L., Adler, V.A. (1981). Image splitting-a technique for measuring retinal vascular reactivity. *Br J Ophthalmol* **65**: 291-293.
- Wolansky, L.J., Shaderowsky, P.D., Sander, R., Frohman, L.P., Kalnin, A.J., Lee, H.J. (1997). Optic chiasmal compression by venous aneurysm: Magnetic resonance imaging diagnosis. *J Neuroimag* **7**: 46-47.
- Wolf, S., Jung, F., Korber, N., Reim, M. (1984). Measurement of erythrocyte velocity in the capillaries of human conjunctiva under normal and hyperperfusion conditions. *Int J Microcirc Clin Exp* **3**(3-4): 527.
- Wolf, S., Arend, O., Schulte, K., Ittel, T.H., Reim, M. (1994). Quantification of retinal capillary density and flow velocity in patients with essential hypertension. *Hypertension* **23**: 464-467.
- Worthen, D.M., Fenton, B.M., Rosen, P., Zweifach, B. (1981). Morphometry of diabetic conjunctival vessels. *Ophthalmology* **88**: 655-657.
- Xiu, R.J., Freyschuss, A., Ying, X., Berglund, L., Henriksson, P., Björkhem, I. (1994). The antioxidant butylated hydroxytoluene prevents early cholesterol-induced microcirculatory changes in rabbits. *J Clin Invest* **93**: 2732-2737.
- Zeger, S. L., Liang, K-Y., Albert, P.S. (1988). Models for longitudinal data: A generalised estimating equation approach. *Biometrics* **44**: 1049-1060.
- Zijlstra, W.G., Buursma, A., Meeuwse-van der Roest, W.P. (1991). Absorption spectra of human fetal and adult oxyhemoglobin, de-oxyhemoglobin, carboxyhemoglobin, and methemoglobin. *Clin Chem* **37**: 1633-1638.
- Zhou, L., Rzeszotarski, M.S., Singerman, L.J., Chokeff, J.M. (1994). The detection and quantification of retinopathy using digital angiograms. *IEEE Trans Med Imag* **13**(4): 619-626.